# Design, development and on-field testing of advanced solutions for monitoring, diagnosis and fault mitigation of SOFCs

Marco Gallo


UNIVERSITY OF SALERNO

***Department of Industrial Engineering***

*Ph.D. Course in Industrial Engineering*

*Curriculum in Mechanical Engineering*

*XXXII Cycle*

# Design, development and on-field testing of advanced solutions for monitoring, diagnosis and fault mitigation of SOFCs

Supervisors:
**Ch.mo Prof. Cesare Pianese**
**Ch.mo Prof. Marco Sorrentino**
**Dott. Ing. Pierpaolo Polverino**

Ph.D. Student:
**Marco Gallo**
**8800500037**

Ph.D Course Coordinator:
**Ch.mo Prof. Francesco Donsì**

A.S. 2019-2020

*La mia vita è un'altalena,*
*un attimo sei su e vedi il mondo,*
*un attimo dopo sei giu, pronto a risalire.*

*Le funi sorreggono il peso,*
*sono i miei genitori,*
*saldi, fermi, un punto sicuro a cui potermi aggrappare.*

*L'altalena è ben piantata a terra,*
*quattro incastri ne sorreggono il peso, sono i nonni.*
*Qualsiasi cosa succeda, loro sono lì e reggono l'intera struttura.*

*In altalena non si va da soli, si va in due.*
*Sul sediolino affianco c'è Simona, che guarda il mondo con me.*

*La mia vita dopottutto è semplice,*
*prendi la rincorsa e sali a vedere il mondo,*
*un attimo dopo sei giu, ma poi, subito, risali su,*
*e quanto è bello il mondo da lassù!*

# Contents

# List of Figures

# List of Tables

# Abstract

The work presented in this thesis is aimed at developing an advanced algorithm to monitor the State of Health (SoH) of Solid Oxide Fuel Cells (SOFCs). Then a computational structure has been implemented for the diagnosis of fuel cells faults along with a set of strategies for mitigation actions. The main idea is to apply advanced methods based on Electrochemical Impedance Spectroscopy (EIS) for diagnosis. Then, EIS and Conventional approaches are used to infer on the SOFC system status and to predict its Remaining Useful Life (RUL). Moreover, all those approaches are applied to provide helpful guidelines on possible mitigation countermeasures to be actuated in case of faults.

SOFCs can play a beneficial role in the World's changing energy landscape, being one of the most suitable alternatives to conventional energy production systems for stationary power generation, co-generation and Auxiliary Power Unit (APU). In the last decade, the enhancement of these SOFC-based products has opened perspectives and opportunities that make them valid solutions to contribute to the energy decarbonization scenario. In Europe, their deployment is still limited by high manufacturing costs and limited lifetime due to faulty operations and degradation processes (i.e. leakage, carbon deposition, anode reoxidation, poisoning, etc.), which reduce cell performance during time and can lead to failures in the main components (i.e. the cells). As far as maintenance and warranty expenses are concerned, it is clear that increased reliability and lifetime will contribute to the reduction of SOFCs operating costs and their further market success.

The most common variables that allows faults detection and isolation in the system are mainly current, voltage and temperature. To extract additional information about the SoH of the system, V-I curves and Electrochemical Impedance Spectroscopy (EIS) methodology might help, focusing on the fuel cell electrochemical behaviour. Particularly, the EIS is an advanced diagnostic tool that supports in evaluating the SoH of the stack. It is linked with an Equivalent Circuit Model (ECM) to model the status of the system.

By comparing the data measured in nominal (i.e. unfaulty) conditions to those recorded while the stack is operating, it is possible to identify any change in the spectrum that can be associated to one or more faulty operations that triggers the effect of one or more degradation phenomena respectively. On the other hand, by monitoring the behaviour of the SOFC over time, it could be also possible to identify the impact of the arising degradation phenomena due to the ageing of the cell. In this work an Equivalent Circuit Model (ECM) is used to describe the main processes occurring within the cell and to extract quantitative information as fault and degradation metrics.
One of the results accomplished is the development of a completely generic algorithm named Matching Geometric Fitting Guess (MGFG), based on EIS for detection and isolation of faults in either single cells or stacks. The MGFG algorithm follows an ECM approach, then parameters extraction are performed by means of a UNISA proprietary patented technique. This allows high generalizability and fast fitting of the measured spectrum. The results achieved by applying such methodology to Proton Exchange Membrane Fuel Cells(PEMFC) spectra in the frame of the EU project HEALTH-CODE paved the path toward the application to SOFCs, of which this work aims at defining a general algorithm to extract useful metrics for diagnostic purposes.

The related features (i.e. the metrics themselves, their combination, or the parameters estimated from them) are properly selected as sensitive indicators of the cell/stack State of Health (SoH) and then used to infer on their status. The whole methodology developed was tested and validated upon experimental data coming from the EU projects INSIGHT and SOSLEM. By combining the information derived from ad-hoc experiments with the heuristic knowledge on the phenomena of interest, a Fault Signature Matrix (FSM) was built to correlate the faults to the

symptoms observed during the online monitoring of the stack.
For the purpose of this thesis, fuel starvation phenomenon was considered as fault and the related FSM was populated accordingly. Thresholds were set upon experimental evidences on segmented cells, short stacks and full stacks; then the diagnostic approach was validated on all these configurations as well.

The study on stack ageing towards lifetime estimation was performed via lumped modelling approach and the related validation was carried out with respect to experimental data. This allows simulating the expected nominal conditions, as unfaulty and nominal reference states for the monitoring. Then, a stack aging submodel was implemented by integrating some ECM-based extracted features, enabling the simulation even during natural degraded operations. The results led to a RUL estimation model, successfully validated upon experimental data.

The fault mitigation was investigated to define possible countermeasures to be actuated when a fault occurs. Particularly, the inference on experimental faulty data, provided by the INSIGHT project, and its matching with the heuristic knowledge led to the development of a general methodology for fault mitigation countermeasures.
Moreover, a study was performed to define a sequence of actions that led to a flowchart for maintenance able to support the users to either stabilize or recover the stack from the fault. From the same study the specifications for a mitigation algorithm can be derived as well. Here, the diagnostic algorithm and the related extracted features are used in a kind of "reverse mode" to provide information about the feasibility and effectiveness of the countermeasure applied. In this work the Fuel Starvation case was analysed and the related flowchart was drafted.
Finally, a methodology that combines the diagnostic techniques and a mitigation-oriented control approach was proposed. A case study for fuel starvation caused by hydrogen leakage was performed and the results for the fault mitigation feasibility were discussed.

In summary, a EIS-based algorithm was developed and applied to detect

fuel starvation in solid oxide fuel cells and stacks. A lumped dynamic model successfully simulated the ageing of such systems, aiming at lifetime estimation. Useful mitigation guidelines were provided to increase the market deployment of these devices. These results paved the way for further work aiming at increasing the Technology Readiness Level (TRL) of such Monitoring, Diagnostic and Lifetime Tool (MDLT) for commercial purposes along with a prognostic field to be investigated.

The overall activity has been funded by UNISA under the EU project INSIGHT.

# Pubblications List

Gallo, M., Marra, D., Sorrentino, M., Pianese, C., & Au, S. F. (2017). Development of a dynamic model for diagnosis and control of an integrated stack module based on solid oxide fuel cells. Energy Procedia, 105, 1936-1941.

Gallo, M., Marra, D., Sorrentino, M., Pianese, C., & Au, S. F. (2018). A versatile computational tool for model-based design, control and diagnosis of a generic Solid Oxide Fuel Cell Integrated Stack Module. Energy conversion and management, 171, 1514-1528.

Mougin, J., Morel, B., Ploner, A., Caliandro, P., Van Herle, J., Boškoski, P., Dolenc, B., Gallo, M., Polverino, P., Pohjoranta, A., Nieminen, A., Pofahl, S., Ouweltjes, J., P., Diethelm, S., Leonardi, A., Galiano, F., & Tanzi, C., (2019). Monitoring and Diagnostics of SOFC Stacks and Systems. ECS Transactions, 91(1), 731-743.

Gallo, M., Costabile, C., Sorrentino, M., Polverino., P., Pianese, C. (2019). Comprehensive Model-Based Methodology For Fault Detection, Isolation And Mitigation Of Fuel Cell Powered Systems. Proceedings of 11th International Conference on Applied Energy, Volume IV, Part 3, Sweden, 2019 (ICAE2019)

Gallo, M., Costabile, C., Sorrentino, M., Polverino., P., Pianese, C. (2020). Development And Application of A Comprehensive Model-Based Methodology For Fault Mitigation Of Fuel Cell Powered Systems. Applied Energy, 279, 115698.

Gallo, M., Polverino, P., Mougin, J., Morel, B., Pianese, C. (2020). Coupling electrochemical impedance spectroscopy and model-based aging estimation for solid oxide fuel cell stacks lifetime prediction. Applied Energy, 279, 115718.

Polverino, P., Gallo, M., Pianese, C. (2019). Development Of A Model-Based Algorithm For Online Degradation Estimation Of Solid Oxide Fuel Cells. Presented at the 8th European Fuel Cell Technology & Applications "Piero Lunghi" Conference 2019 - Naples (Italy) & under submission for publication.

# Chapter 1

# Introduction

## 1.1 The Context - A new energy scenario

Over the last century, emissions from fossil fuels have increased the global concentration of carbon dioxide in the atmosphere and caused a corresponding temperature increase. Continued use of carbon-based fuels is leading to a devastating global climate change and the shift to a more sustainable, flexible and environment friendly alternatives is now a necessity; therefore, research activity is strongly pushing in this direction. Among the candidates for clean technologies, Fuel Cells (FC) are spreading for their notable potential for power generation in stationary, portable and transport applications that will support the increasing need for sustainable energy resources. Indeed, FC technology allows combining high efficiency with minimum (or completely null when fuelled by pure hydrogen) harmful emissions (sulphur, nitrogen and carbon oxides, hydrocarbon pollutants and particulate), as well as significantly reducing $CO_2$ emissions. They merge the best aspects of batteries and combustion engines: like engines, fuel cells can produce power as long as fuel is supplied; like batteries, fuel cells convert chemical energy directly to electricity avoiding combustion and, consequently, they don't suffer from the Carnot's limit thus potentially achieving high energy conversion efficien-

cies. Solid oxide fuel cells (SOFCs) are attractive for their high efficiency and fuel flexibility along with the high functioning temperature, making them suitable for co-generation purposes. These devices require, in principle, only five components with no need of noble catalysts: a solid oxide electrolyte, two electrodes (the cathode for oxygen reduction and the anode for fuel oxidation), and interconnect wires to collect current at the electrodes. However, SOFCs haven't achieved a substantial commercial penetration yet. This issue can be mainly ascribed to the high cost of the components required to withstand the high working temperatures and the still reduced lifetime (if compared to the manufacturing costs) with respect to their competitors. However, the global market is currently moving in this direction.

According to the technical report of the EU Joint Research Centre [1], more than 800 MW of large stationary fuel cell systems have been installed globally for distributed generation and combined heat power (CHP) applications, mainly in the US and South Korea. CHP are highly diffused in Asian market, while Back-up applications are highly sold in US. With the renewable energy directive (2009/28/EC), Europe has strongly promoted the use of energy from renewable energy sources, particularly integrating them into the transmission and distribution grid and the use of energy storage systems for integrated variable production of energy from renewable sources [2]. However, the European investments for SOFC-based power generation and CHP are still low and the main market deployment barriers are the reliability (in terms of availability and lifetime performance) and the manufacturing cost of the fuel cells.

Investing in technology development and in research activity would definitely boost the market deployment of such technology, particularly overcoming some of the remaining barriers, specifically lowering cost and improving reliability and durability.

## 1.2 Degradation in SOFC

The most significant barriers to improve the market deployment of SOFCs are the very limited durability, low reliability and cost. The first two are significantly impacted by the degradation phenomena that can occur during SOFC operations, due to contaminants in fuel, thermo-

mechanical stress, chemical undesired reactions and sealing issues. The most challenging activities on which research activity is spending many efforts are understanding the physics behind these phenomena, the way to early detect them and possible countermeasures to limit their effects. SOFC performance degradation is generally ascribed to the deterioration of single components as well as to mutual interactions among the cells. Moreover, in nominal conditions the stability of the system can be affected by several detrimental phenomena that can lead the system to die. Some degradation mechanisms are reversible, particularly at an early stage, like sulphur poisoning or carbon deposition, whereas others are not recoverable, as leakage, electrode delamination and electrolyte cracking. Their physics and the causes behind them are several, as well as the countermeasures that can be adopted; however, the effect on cell performance over long-term degradation is common to most of them: a loss in the available potential at constant current load. Indeed, it is not possible to clearly distinguish a specific degradation mechanism among those that could occur by just monitoring the changes in the cell potential. Therefore, it is fundamental to implement a diagnostic technique to identify the degradation mechanisms and properly envisage a mitigation strategy. For this purpose an interesting literature survey on the main degradation phenomena has been conducted, especially focusing on their effects on the SOFC and their detectability with both conventional and advanced measurements (e.g., EIS).

The degradation mechanisms that have the greatest impact on the deterioration of the cell/stack performance are listed below. Even though several of them are usually strictly correlated among themselves, a proper classification has been provided below to investigate them for the modelling purposes:

- **Thermomechanical stress**
  The high working temperatures of a SOFC make this technology highly affected by temperatures oscillations, particularly for the used materials. Any shut-down and start-up phase is detrimental to the cell itself, since thermal transients may induce some cracks in the structure of the cell components, in the sealing surrounding the cell and at the interfaces. Moreover, such cracks could further evolve and lead to additional failures, as a flow leakage. This prob-

lem is attributed to the low thermal shock resistance (TSR) of the ceramic electrolyte and in changing of the Thermal Expansion Coefficient (TEC) that varies between the different components of the fuel cell [3]. Thus the understanding of thermal stresses distribution results a crucial step to interpret the mechanism of mechanical failures, which is particularly helpful for the design of the cells and to broaden the field of potential applications [4]. Hanasaki et al. [5] systematically investigated start-up and shut-down modes proposing alternative procedures to avoid rapid performance degradation by thermal cycling. In [6] Khan et al., studied the degradation trend of a SOFC cathode as a function of applied current density during thermal cycling; to avoid such phenomena, Schluckner et al. [7] investigated the influence of co-, counter-, and cross-flow configurations, along with various electrical contact positions on the current density distribution and temperature evolution within the cell. On the other hand Xu et al. [8] studied the thermal stress in SOFCs and stated that the thermal stress at different operating conditions results from the mismatch of its components; this indicates that the major principal stress at free fixed constraint situation in the SOFC is tensile. Other details relating to the effects of Thermal Cycling stresses and on their distribution in different SOFCs configurations can be found in [9], [10] and [11].

- **Nickel Oxidation**
  Redox-instability of Ni/YSZ electrodes can lead to severe malfunctioning of a stack due to a fast electrochemical degradation and a local increase of oxygen partial pressure, with an high performance degradation and, usually, a mechanical failure. An undesired redox-process causes a change in the cermet's microstructure, with consequent cracks in the electrolyte. Sometimes a temporary improved Ni/YSZ morphology can be seen due to a redistribution of the microstructure; nevertheless, it is often followed by a fast degradation [12]. Different faults may induce re-oxidation, as air leakage due to sealant failure and high fuel utilization. Furthermore, control actions could induce such degradation phenomenon as well, like an emergency system shutdown or the application of mitigation strategies to recovery the system in case of a fault (i.e.,

strong air treatment of the fuel electrode for carbon deposition). A detailed literature analysis and a mechanical overview can be found in [13]. In [14], Kawasaki et al. investigated the degradation and performance fluctuation of SOFC Ni anode under high fuel utilization, particularly focusing on the Ni oxidation phenomenon, whereas in [15] Shang et al., developed an oxidation-induced stress model to investigate the mechanical behavior of anode-supported SOFC under various oxidation mechanisms. More details about this degradation phenomenon, along with its relation with other faults can be found in [16], [17], and [18], where authors focused on different degradation mechanisms clearly related to Ni Oxidation.

- **Anode/Cathode delamination**
  Delamination occurs directly at the electrode-electrolyte interface, with a detachment of the individual layers and a related reduction in the mechanical stability and performance loss. The void between the layers blocks the charge conductive path, thus making useless the electrochemical reaction sides nearby the delaminated areas, especially at the oxygen-electrode-electrolyte interface. Due to high working temperatures of SOFCs [19], differences in TECs of adjacent layers [20] and, generally speaking, thermomechanical stresses (i.e., repeated thermal cycling) could cause delamination [21]. More details about the effects of delamination on the electrochemical performance, on their thermic effects and on the detection of delamination defects via pulsed thermography can be found in [22], [23], [24] and [25]

- **Nickel coarsening**
  The Ni-YSZ-based anode side could suffer from microstructural changes during operations. Particularly, the Ni is often affected by degradation phenomena due to its electrochemical reactivity. Some degradation phenomena related to Nickel are the coarsening [26], due to solid diffusion processes and/or Ni surface and vapour transport [16], Ni connectivity loss [27], along with the aforementioned Ni-based morphology changes [28]. Several operating parameters can induce Ni-based degradation mechanisms, mainly temperature, humidity and fuel gas contaminants that can lead to changes in

the initial microstructure of the anode. These effects result in a rapid performance reduction as well as the Triple Phase Boundary (TPB) length [29], with a sensible decrease in the number of active electrochemical sites (and the electroactive area as well) when the cell is operated for extended times. In [30] the authors carried out long-term experimental tests to study the impact of Nickel (Ni) coarsening on the performance of Solid Oxide Cell, in both fuel cell and electrolysis mode confirming the related significant loss of active TPB length. Zhu et al. [31] performed multi-physics numerical simulations to monitor the effects of Ni-particle coarsening on the SOFC anode conductivity and TPB length. Khan et al. [32] used a simplified modelling approach to predict SOFCs performance degradation upon Ni grain growth and providing deep insight into Ni agglomeration behavior over time along with its impact on the electrochemical performance degradation of the anode.

More details about Nickel coarsening effects in the degradation of Ni–YSZ anodes and studies on the local morphological changes of Nickel can be found in [33], [34], [35], [16] and [36].

- **Interconnect oxidation**
  During SOFC operation, a chromium oxide could form on the ferrite stainless steel interconnects, reducing the electrical conductivity at the interface [37]. This is usually due to the oxygen reaction with the chromium present in materials and usually implies an increase in the ohmic losses [38]. Thus, for practical applications, protective coatings are needed, particularly at the cathode side to reduce the chromium evaporation. The scientific community is thus moving toward the selection of proper materials to avoid this strong oxidation of the interconnects without sensibly reducing performance.

  More details about the past researches on SOFC cathode/interconnect contact materials can be found in [39].

- **Carbon deposition**
  The direct use of hydrocarbon fuel instead of pure hydrogen easily leads to a more evident cell degradation. For Ni-based fuel

electrodes, the most detrimental phenomenon is known as coking, which is the deposition of solid Carbon on the electroactive sites that causes their deactivation [40]. Nevertheless, hydrocarbon cracking seems to be the favoured reaction at high temperatures. The deposited carbon induces different kind of deactivations, like the chemisorption of carbon as monolayer, the blockage of the gas diffusion channels or the dissolution of the carbon into the metal, with a related volume expansion. It is not very easy to predict where the solid carbon can be formed, as shown by Sasaki et al. [41]. The major factors determining coking are surely temperature [42] and polarization [43]. Considering the high fuel versatility of SOFCs, research activity is spending much effort in studying the effect of Carbon deposition and the solutions to overcome this issue. The most recent works in this field can be found in [44] where Perovskite is studied as promising anode material that is immune to coke formation and sulphur poisoning when using hydrocarbon fuels. In [45], da Silva et al. investigated novel materials for SOFC to avoid carbon deposition. In [46] Yue et al. described the latest engineering approaches on anode coking along with the recent engineering approaches to enhance electrode durability under carbon-related atmosphere.

- **Anode poisoning**
  Hydrocarbon-based fuels usually presents several additives and impurities whose presence in SOFC cells can lead to poisoning effects particularly at the Ni-YSZ based anode side. Among them, sulphur-containing species are the ones of major concern [40]. Indeed, sulphur has a detrimental effect on Nickel, since it chemisorbs on the surface, thus highly reducing the catalytic activity. Moreover, the Sulphur contaminating the anode side could easily react with the hydrogen to form $H_2S$ that covers the electroactive area, blocking in turn the TPBs and highly reducing the cell performance. As a consequence, a fast performance decay is observed, along with a further long-term degradation process [47], [48]. In hydrocarbon-based fuels the poisoning effect at the anode side can be observed even in Open Circuit Voltage (OCV) condition [49], [50], [51]. This requires even a particular attention on the possible

counteractions to mitigate the detrimental effect; it is usually a common solution to put the system in OCV operation, to achieve in a sort of standby condition. Long term effects of the anode poisoning are less studied. Indeed, scientific community agrees on the possible enhancement of Ni agglomeration due to the sulphur dissolution in the Ni bulk structure [52] or a Ni-diffusion away from the anode/electrolyte interface with a related percolation loss [53]. As already presented for carbon deposition, the poisoning-tolerant anode materials are under investigation by the scientific community as one can see in [54], [55], [56], [57] and [58]. Methods to remove impurities at the anode side are investigated in [59], where a oxidative regeneration method is proposed to remove the adsorbed sulphur and sulfurin sulfide in a short time, releasing more active anode reaction sites. In [60], Mehran et al. proved that the sulphur poisoning of Ni catalyst can be avoided by applying pulsed current cycling conditions and higher humidity. They envisaged the possibility to achieve a stable SOFC operation at lower $H_2S$ concentration by combining the optimization of operating conditions and modification of the anode microstructure. More details about sulphur poisoning and, generally speaking, anode poisoning can be found in [61], [62], [63] and [64], where their effects on the performance, their modelling approach and some hints of countermeasures for recovery are considered .

- **Cathode chromium poisoning**
  SOFC cathode is usually subjected to poisoning by chromium species contained in the interconnect material [65]. Indeed, volatile Cr-containing species, as $CrO_3$ and $CrO_2(OH)_2$, are generated over the chromia scale on the interconnect surface [66]. This gas species, transported to the cathode active layer, could poison it through an oxygen reduction reaction and then lead to a sensible performance loss. In the literature, different proposed mechanisms on chromium poisoning of SOFC cathodes can be found. From a thermodynamic stability point of view, Yokokawa et al. [67] considered the $Cr_2O_3$ deposition or formation of $CrMn_2O_4$ at the TPB as the direct cause of chromium poisoning at the Lanthanum strontium manganite (LSM)/Yttria Stabilized Zirconia (YSZ) in-

terface at the cathode side. Badwal et al. [68] stated that the deposition of Cr is mainly due to the electrochemical reduction of Cr-containing gaseous species. Indeed, Taniguchi showed in [69] a correlation between the polarization losses and the accumulation of chromium at the LSM/YSZ interface. Konysheva et al. [70] suggested that the causes of chromium poisoning could be either the deposition of chromium oxide blocking oxygen diffusion and transportation to active TPBs or a reaction of Cr-containing gaseous species with cathode materials forming poorly conductive phases, such as $SrCrO_4$. More details about cathode poisoning and corrosion, coatings for interconnects and mechanism of chromium poisoning in SOFCs can be found in [71], [72], [73], [74] and [75].

- **Leakage**
  During normal operations the SOFC can present internal leakages between anode and cathode or external leakages between the cell itself and the surrounding. Leakages are driven by the pressure and by the different concentrations between both cathode and the anode sides, which push the fuel or the air to cross the electrolyte and reach the other side to react with fresh air or the fuel respectively [76], [77]. Being it a physical break of the material mainly at sealant level, the mitigation counteraction is usually ineffective. As Rautanen [78] reported, leakages can cause cell degradation by means of several mechanisms, e.g. increased thermal gradients [79], local shortage of fuel, oxidation of the anode and increased chromium evaporation [80] due to higher water vapour content at the cathode. According to Bram et al. [81], internal leakage can lead to nickel re-oxidation especially with mixture characterized by high dilution, thus leading to exothermic reaction and then causing severe damages due to the formation of the so called hot spots. Nevertheless, leakages might cause fuel starvation due to the increasing in the fuel utilization [82]. Further investigations on sealant designs and materials, with a focus on the evaluation of their thermal and structural stability can be found in [83], [84] and [85].

- **Fuel starvation**
  Fuel starvation is a very limiting factor of SOFC when power fol-

lowing manoeuvres are required. Indeed, during the operations, either stationary or transients, the current could electrochemically consume the fuel reactants more rapidly than the fuel provided, thus limiting the performance and causing a sharp decline in voltage with a related possibility to damage the cell [86]. This condition may cause a local oxidizing environment leading to the formation of NiO [87].

The fuel starvation can be caused by different malfunctioning (i.e., a leakage, an issue in the BoP or in a strong deactivation of TPB at the anode side) and it is commonly considered as a fault itself, due to the detrimental effects that causes on the cell performance. Usually, when fuel starvation occurs during a real SOFC operation, an electrochemical oxidation of Ni in the anode can be caused by the strong increase in the polarization losses of the cell [88]. Moreover, the Nickel oxidation causes irreversible mechanical degradation with a crack at the electrolyte-electrode interface. It was demonstrated that the fuel starvation can be caused by rapid load increase and its effects can cause significant changes in microstructure morphology, as stated by da Silva and Heck [89]. In turn, the starvation can be the effect of a strong anode reoxidation or a leakage in the fuel pipeline, thus causing a detrimental chain reaction as well. It is thus important to detect early any phenomenon/process that causes degradation to immediately counteract to recover from the performance losses. Thus, to avoid or at least manage such malfunctioning, different methods have been investigated to prevent fuel depletion within the fuel cell. Laurencin et al. [90] investigated the effects of anode reoxidation due to a direct oxidation in air throughout a damage model. Angeloni et al. [91] developed a SOFC model relying on partial differential equations to simulate the behaviour of the local gas starvation with both high fuel and high oxidant utilization. They affirmed that an increase in the electrode porosity might allow a reduction of local gas starvation. From a diagnostic point of view, the fuel starvation could be a generic fault caused or causing other degradation/detrimental phenomena directly correlated to it. On the other hand it can occur during transient with a complete nat-

ural recovery when the FC reaches a new stable condition. All these consideration lead the interest of the scientific community toward the study of its effects on the FC performance [92] and the research for new materials to improve SOFC durability at higher fuel utilization [93].

## 1.3 The Diagnosis

To support the successful deployment of fuel cells, meaningful information on the actual State-of-Health (SoH) of the stack and the balance-of-plant (BoP) components are fundamentals. A comprehensive view supports an advanced management aiming at achieving improved performance, maintenance scheduling, higher reliability and increased system lifetime. Fuel cell operations are influenced by several physical phenomena occurring inside the cell. Abnormal operating conditions may introduce system faults and worse degradation mechanisms. These critical behaviours force the research activities to develop new monitoring and diagnosis techniques to ensure optimal system management and improve fuel cell performance and durability [94].

Fault diagnosis consists in the determination of fault type, size, location and time of detection (when possible). The diagnostic procedure is based on the observed analytical and heuristic symptoms and the heuristic knowledge of the process. Particularly, three main processes are usually required, as shown in Figure 1.1, that are data acquisition and treatment, fault detection and isolation (FDI).

Figure 1.1 schematically shows the diagnostic procedure: the measure collected by different technologies is preliminary treated to remove spurious points and outliers, and useful metrics are then extracted as representative parameters for SoH assessment. Then a fault detection process is performed, usually through a comparison of the expected (i.e., nominal un-faulty) conditions and the measured ones, to reveal a possible malfunctioning occurring in the system. The further step is the isolation of such malfunctioning to locate the problem and correlate the experimental evidence to one or more phenomena occurring. Thus, a decision making process starts to adopt countermeasure to recovery or simply mitigate the detrimental condition.

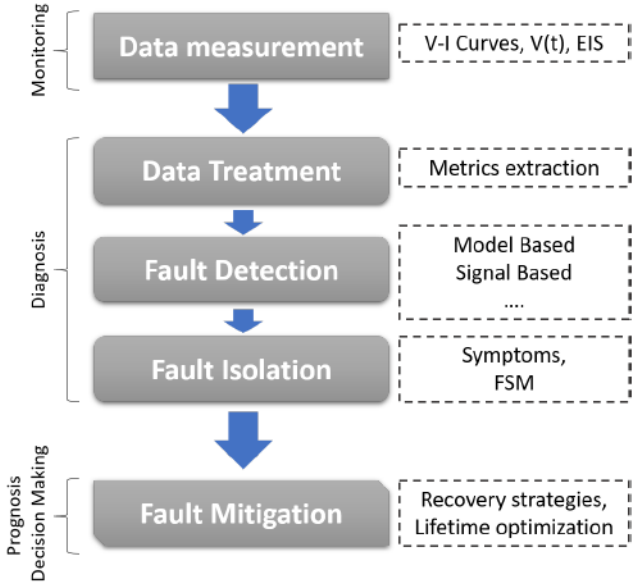


**Figure 1.1:** Diagnostic process scheme.

The diagnostic approach can be divided into model-based methods, signal-based methods or combined ones [95]. While the signal-based methods monitor and detect malfunctioning occurring using only measured values, model-based approaches rely on the redundancies offered by the modelling, which is intended to predict the behaviour of such systems through physical equations and whose detail and computational burden depends on the expected accuracy. In both cases redundancies are used to generate residual values (i.e., actual values measures or model outputs with respect to the expected ones in nominal unfaulty conditions) to observe abnormal system behaviour; here, investigated residual patterns can be used to classify possible faults, matching similar effects and thus isolating the malfunctioning occurring [96]. A suitable diagnostic tool aims at identifying the system faults in real time. Indeed, even if some faults are quite easy to detect, their isolation is sometimes hard to perform and requires detailed information. Fault detection is based on the on-line comparison between measured data and reference ones evaluated in normal system behaviour [97]. In parallel with system diagnosis, re-

searches are also focusing on Prognostic and Health Management (PHM) activities [98] and on the evaluation of the system remaining useful life (RUL) studying the system ageing, planning recovery action and then, reducing the risk of failures. Particularly, PHM is oriented to predict the voltage degradation depending on the history of the system mission profile. The system response evolution caused by ageing is a sensible point to consider in diagnosis algorithms development. Models required for condition assessment are largely available in the form of qualitative rules based on metrics derived from experimental evidence [99]. Metrics are characteristic quantities obtained by signal processing and strictly linked to the operational functioning points of the system [100], then representative of the SOFC SoH. They can be defined as a measure, an indirect variable or a modelling parameter that may report on the performance of various processes and provide information on the SoH of the monitored system. Thus, the metrics are used for a double purposes: to monitor the Fuel Cell State of Health aiming at promptly activating an alarm in case of unexpected condition and to guide the Fault Detection and Isolation Process toward the isolation of the malfunctioning occurring. Metrics can be qualitative or quantitative; particularly, these latter are fundamental to evaluate the state of the degradation processes causing loss of cell performance. Fuel cells monitoring is usually achieved by observing their electrical behaviour under different operating conditions. The most used methods to characterize the fuel cell performance are based on electrochemical techniques, namely polarization curves, Electrochemical Impedance Spectroscopy (EIS), current sweeps, current interruption, etc.. As aforementioned, the durability of fuel cells is significantly affected by several degradation mechanisms, which reduce cell performance during time and can lead to failures in the stack. Methods to directly observe degradation phenomena aiming at the evaluation of loss of performance and to measure their behaviour over time are difficult to implement. Usually, indirect SoH indicators, related to the decay of the voltage over time and coupled with temperature trend monitoring with respect to the current density and functioning time are adopted [101]. Indeed, the effect of operating parameters, as temperature, voltage and current density has been studied in literature, in order to provide a reference for the development of specific methods for advanced control and automatic on-line diagnosis. These latter can efficiently detect and

isolate malfunctioning at both stack and system levels [102]. Moreover, a fast diagnostic algorithm able to detect the occurring malfunctioning at its early stage might reveal to be fundamental to promptly act and recover the healthy state if the fault is recoverable (i.e., Sulphur poisoning, whose negative effects could be cancelled if an ad-hoc strategy is applied in an early phase of the fault, thus restoring the un-faulty condition of the cell). Therefore, a suitable diagnostic algorithm should be fast, accurate and capable of discerning several faults by means of a reduced number of sensors that need to be installed on board, in a trade off view between accuracy, computational burden and costs [103]. This work focuses on model-based diagnosis in order to have an acceptable accuracy coupled with a reduced needs of experiments.

Fault diagnosis consists in four main tasks, as shown in figure 1.1 monitoring of the main variables describing the system state, detection of an abnormal behaviour of the system, isolation of the fault and the affected auxiliary elements and identification of its magnitude and evolution in time [99]. According to a model-based approach, by comparing the measured variables with their value in unfaulty condition (through a reliable simulation of the system), if a sensible deviation (residual) exceeds suitable thresholds, a symptom arises (its value changes from the unfaulty state "0" to the faulty one "1") [102]. By collecting the symptoms for each main variable selected (i.e. metric chosen), a binary array of 0 and 1 values, known as State vector, can be built. In order to correlate the State Vector with the fault itself, a Fault Signature Matrix needs to be developed, according to the heuristic knowledge of the phenomena considered. This latter matrix is derived from a Fault Tree Analysis, which depicts the causal relationship among faults and symptoms [104]. This approach, based on the comparison of measured data with simulated ones, aims at preventing a potential critical breakdown. Moreover, this will help in setting a new operating point, according to the current system state of health, as done by Costamagna et al. [105], to improve its Remaining Useful Life (RUL). Thus, for each fault considered, a proper choice of its representative features with respect to the measurable variables, is the key point for a reliable diagnostic tool. This choice can be made upon the experimental analysis on the selected fault so as to identify the most susceptible parameters that changes with respect to the detrimental effect magnitude.

### 1.3.1 Conventional approach - modelling

The main indicator of fuel cell performance is the voltage, which provides a lumped information on the cell state of health. Thus the mostly used diagnostic approach focus on a proper voltage estimation, through physical modelling of the most relevant electrochemical effect from microscale to macroscale. The needed model accuracy depends on the requirement specifications of the model-based tool purpose and implies a related computational burden in both terms of calculations and time. For diagnostic purposes, the voltage estimation is often not enough and the model has to be improved to provide more outcomes (i.e., temperature, flows,. pressures, etc.). Indeed, the effect on cell performance over long-term degradation is common to most of the degradation phenomena occurring within the cell, caused by abrupt malfunctioning or detrimental effect, which imply a loss in the available voltage at constant current load. Indeed, it is not possible to clearly single out a specific degradation mechanism among those that could occur by just monitoring the changes in the cell potential. For SOFCs, degradation can be related to the cell/stack internal mechanisms, to external phenomena or malfunctions of some balance of plant (BoP) components or a combination of both. Among those investigated in the literature and those experienced by SOFC manufacturers, it emerged that the most relevant degradation phenomena are nickel oxidation or coarsening, carbon deposition and anode poisoning, fuel starvation, anode and cathode delamination, chromium poisoning, interconnect oxidation and thermomechanical stresses [106], as discussed in detail in section 1.2. All these issues can cause in the cell/stack a performance reduction, which could last as long as the malfunction persists (if such phenomenon is reversible) or lead to an irreversible effect increasing with time. On the other hand, some burdensome and stressful operations (i.e., high current, high fuel utilization or high temperature) can lead to microstructural changes and a fast aging of the cell/stack with a related time-increasing reduction in voltage. Offer and Brandon [107] studied experimentally the effect of temperature and current density on carbon deposition degradation mechanism, showing that, under not extreme current density values, carbon deposition does not affect seriously the electrochemical performance of

the anode electrode. Nakajo et al. [108] investigated the distribution and the evolution of the degradation under practical operating conditions by means of polarization curves characterizations performed at fixed operating times, observing an underestimation of the severity of the degradation due to temperature effects. De Haart et al. [109] studied the degradation behaviour over 3000 h of continuous operation of several stacks subject to different current densities and to chromium poisoning. In particular, they affirmed that degradation evolution is highly affected by the fuel utilization. Zaccaria et al. [110] developed a simplified real-time model of degradation due to current density, temperature, and total resistance of the cell. They analysed the local degradation effects on the different parts of the cell, which degrade at different time rates and with different dynamics. However, after 12000 h, they found that the degradation rates start to be fairly uniform along the cell. Yan et al. [111] investigated SOFC degradation for more than 750 h under a fixed current density in order to evaluate the behaviour of the cells and detrimental mechanisms of sealing, contact resistance and oxidation of metal interconnect, which might lead the cell to performance losses.

Numerical simulation is fundamental to support the development of SOFC prototypes in a wide range of operating points and nominal conditions, instead of performing time-consuming and costly experimental campaigns [112]. Thus, the research field on models for simulations of SOFC systems is extremely dynamic. Al Moussawi et al. [113] developed an electrochemical model to simulate a trigeneration system for residential applications; Xenos [114] et al. presented a flexible mathematical model for planar SOFCs to simulate the dynamic conditions, particularly in critical operating points as start-up, load change or inlet temperature drastic changes of the streams; likewise Bae et al. [115] studied the transient behavior of thermodynamic variables in a physical 3-D model of a SOFC upon electrical load change, in order to provide useful guidelines to develop new design concepts that can soften degradation processes arising from dynamic operating conditions. Moreover, they stressed the need of a real-time model-based control system to improve the reliability of cell microstructure and stack configuration. Recent research activities mainly focused on three-dimensional modelling of SOFCs to investigate the temperatures flow distribution and to study electrochemical properties. Hussain et al. [116] developed a 3-D model

in COMSOL Multiphysics for a planar intermediate temperature (IT) SOFC and carried out a parametric study to analyze the SOFC performance; particularly, they studied the change in the SOFC performance with the variation of different parameters, electrolyte materials and configurations. Ilbas et al. [117] investigated the parameters affecting the performance of a cathode and an electrolyte supported SOFC through a Finite Element method applied to a SOFC 3D model. Indeed, they observed a minor influence of the thickness of a cathode-support layer with respect to that of of the electrolyte-support layer. Prokop et al. [118] proposed a three-dimensional, multiphase, micro-scale SOFC model of anodic transport phenomena, coupling it with a numerical code for constructing three-dimensional, triple phase numerical grids employing active recognition of geometric features to enhance the FIB-SEM tomography results analysis. On the other hand, 1-D and 0-D models allow increase model speediness and lump relevant parameters, significant for the modelling purposes. Kupecki et al. [119] investigated the internal reforming of the methane in 60-cell SOFC stack through a 1-D numerical model; they studied the effects of varying the composition of the gas at the anode inlet with a particular focus on the nickel reactions. Barelli et al. [120] developed a dynamic model of a hybrid SOFC coupled with a gas turbine system (SOFC/GT); Ferrari et al. [121] analyzed pressurized hybrid SOFC/GT systems; Sorrentino and Pianese [122] developed a control-oriented model for simulating a hybrid APU equipped with a SOFC; Cao and Li in [123] proved the importance of relying on accurate SOFC models to develop robust PID controller aimed at enhancing thermal management. Santarelli et al. [124] investigated a natural gas fueled APU by a zero-dimensional SOFC model for flight applications. Arpino et al. [125] presented a zero-dimensional model for the simulation of a SOFC-based micro-CHP power system for residential applications, fed by natural gas. Baldinelli et al. [126] demonstrated the importance of relying on accurate models to perform long-term experimental investigation of unreformed biogas-fed SOFC systems. Bao et al. [127] investigated the state of the art of macroscopic SOFC models and model-based control of SOFC/GT hybrid systems, whereas in Marra et al. [128] several approaches for SOFC systems modeling are presented and discussed, in view of their subsequent, needed deployment and implementation within design, control and diagnostic procedures and tools.

If on the one hand many studies focus on control-oriented modeling approaches, on the other hand a few contributions are available concerning with diagnostic tools suitable for SOFC systems. To improve the remaining useful life, Arsie et al. and Polverino et al. proposed suitable coupling of an SOFC system model with Fault Tree Analysis method, so as to develop a strategy to detect, identify and isolate an incipient fault [104]- [102]. The approach is based on the comparison of measured data with simulated ones, thus preventing an eventual breakdown and setting the optimal operating point according to the current system state of health, as done by Costamagna et al. [105] as well.

### 1.3.2 Advanced approach - EIS

Among fuel cell characterization methods aiming at monitoring performance behaviour, Electrochemical Impedance Spectroscopy (EIS) is proved one of the most powerful techniques able to investigate the main phenomena occurring in electrochemical cells (PEMFC, SOFC, Li-ion batteries, etc.) for on-line prognostic purposes and SoH monitoring thanks to non-invasive features [129]. EIS provides a wealth of information about the analysed system. It is a non-destructive tool extremely useful to give an insight on the SoH of the cell and to evaluate how a degradation process could affect the overall performance losses [130]. Moreover, it allows detecting the occurrence of incipient faults several minutes before they evidently arise [131]. Indeed, this method allows analysing electrochemical reactions, charge and mass transfer as well as thermal phenomena for a single cell or a complete stack [132]. The EIS working principle is based on the injection of a sinusoidal current stimulus and then recording its voltage response at several frequencies. The ratio between voltage response and injected current represents the impedance spectrum, which gives for each frequency an information on the main phenomena occurring within the stack. An overview can be found in [133], where Huang et al. investigated 150 journal papers dealing with AC impedance modelling for SOFC diagnosis. Nechache et al. [134] showed how EIS can be applied to Solid Oxide Electrolyser Cell (SOEC) systems to characterize performance mechanisms, study the degradation mechanisms for different cell configurations and monitoring overall SOEC performance for diagnostic applications. Nechache et al. [135] combined

EIS, polarization curve and deconvolution technique to analyse SOEC technology and study the electrochemical behaviour of commercial cells. They proved that these methodologies represent a key-tool for monitoring in-situ performance and elaborate control-aided strategies. With respect to Polymer Electrolyte Membrane Fuel Cells (PEMFCs) EIS-Based diagnosis, Petrone et al. [129] presented a detailed review on model-based diagnosis methodology, focusing on Equivalent Circuit Modelling (ECM) derived from EIS data and aiming at reaching a good compromise between accuracy and efforts in computation, extremely needed for on-board applications [1]. Several approaches are exploited to extract from EIS measurements specific features able to detect and isolate undesired events in fuel cells. Among them, ECM correlates specific circuit components to the investigated physical phenomena. This aspect represents the main advantage of combining EIS with ECM, since suitable impedance contributors (e.g., ohmic resistance, charge-transfer resistance, etc.) can be identified by analysing circuit parameters [136]. From the evaluation of the ECM parameters, it is possible to discern between normal and faulty conditions [137]. It is worth remarking that the choice of the most effective ECM is related to the type of fault to be detected. However, to develop flexible and generalizable diagnostic tools, it is preferable to employ comprehensive ECM able to account for a large number of possible faults and different kind of system configurations (as the model proposed in Figure 1.2).

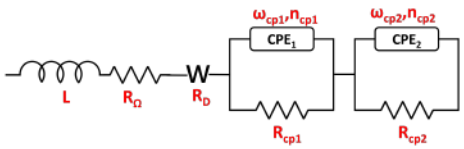


**Figure 1.2:** Exemplary scheme of an Equivalent Circuit Model. The meaning of each element will be further explained in Chapter 2.

[1] It is worth commenting that for on-board application, the reader should refer to any kind of direct application on the real system running on-line. This means that an on-board application is, for example, an algorithm running in parallel with the real system and directly installed on it (e.g., a plug-in embedded portable device) without any kind of connection to laboratory devices

Electrical elements used for the impedance modelling are clearly described by Khan and Rizvi [138], who proposed ECMs for diverse kinds of SOFC cathode materials. Hissel and Perà [139] summed up recent developments and experimentations in efficient diagnostic and SoH estimation methodologies. Although the literature concerning EIS is vast, only few works seek to investigate monitoring and diagnosis approaches for SOFC technologies involving EIS. For this reason, great attention should be given to diagnostic methodologies derived from impedance measurements, which allows testing the system in real-time in a non-invasive way, to develop an on-line diagnostic tool for SOFC. In the work of Barelli at al. [140], the authors performed a literature survey on failure causes and relative diagnostic systems for SOFC technologies. The main degradation phenomena occurring during SOFCs normal operation have been analysed. Similarly, Lee et al. [141] investigated mechanisms and symptoms of several simulated failure modes, especially fuel starvation, air-depletion and wet and dry cycling modes. Monitoring the behaviour of a technology requires a complete knowledge about in-situ phenomena occurring in the cell, and how they are related to electric parameters, which might be derived from the EIS measurements. Sometimes, when experimental campaigns lack of information, physical model represents the correct approach to simulate the real fuel cell behaviour. For these reasons, Hofmann and Panopoulos [142] developed a mathematical model for planar SOFC to simulate steady state performance characteristics and in particular to simulate electrochemical impendence. The model was applied in a detailed parametric analysis of the losses in order to deconvolute the impedance spectrum, by relating each main transport process to an impedance arc. Parametric analysis of EIS was performed by varying characteristic parameters as porosity, tortuosity, anode thickness, anodic exchange current density and so on. Similarly, Zhu et al. [143] investigated through modelling approach the influences of detailed surface chemistry within SOFC composite anode structures on EIS. By developing a 6-elements ECM based on physical parameter models, they computed qualitative trends of frequency shifts measured on the complex impedance of SOFCs operating on hydrogen, carbon monoxide and syngas mixtures. On the same line, Fadaei and Mohammadi [144] exploited physical models to perform a parametric study on the effects of overvoltage, inlet fuel concentration, temperature, anode

thickness, inflow velocity and porosity on the impedance spectrum. Lang et al. [145] tested SOFC short stacks with sintered anode-supported cells and identified the nature of losses by fitting the impedance spectra to an ECM based on five elements. Finally, Montinaro et al. [146] tested an SOFC with Lanthanum Strontium Cobalt Ferrite (LSCF) cathode at different operating conditions (e.g., changing gas partial pressure or cell temperature, inducing $H_2S$ poisoning, etc.) through EIS, in order to identify the main mechanisms contributing to the polarization resistance, especially at the anode side. In particular, they presented the evolution of VI curves and Nyquist plots under different conditions of S/C ratio, $H_2S$ poisoning, voltage and raw materials.

EIS technique is a key tool to monitor the behavior of the polarization losses during time, to identify the causes of system degradation in a short time with no relevant effect on the fixed operation. This application, fast and non-invasive, might represent the basis to implement a fault detection and identification process on-board. Indeed, many work dealt with the application of such technique to infer on the SOFC degradation.

Comminges et al. in [147] monitored the impedance spectra of 5-cell SOFC stack in order to analyse the evolution of ohmic and polarization resistances during 10000 h; they found that stack degradation was mainly attributed to the increased ohmic resistance by means of possible interconnect corrosion, reduced effective contact areas between cells and interconnects and partial re-oxidation of the anode.

Shy et al. [148] investigated how flow distributors could improve significantly the degree of flow uniformity of a planar SOFC and then its performance by reducing ohmic and polarization resistances. Electrochemical impedance measurements through a 5-elements equivalent circuit model was used to describe the evolution of ohmic and polarization resistances both in a cell with guide vanes and in a classic one. In this latter case, an anode-reoxidation phenomenon was detected. A finite element model was applied by Gazzari and Kesler[149] to investigate the degradation mechanisms of a SOFC, in particular the electrode delamination, which causes significant changes in the impedance spectrum. In this study an impedance model was developed to simulate degradation mechanisms of anode and cathode delamination, Sulphur poisoning, chromium deposition and their effects on the spectra in terms of arcs dimensions and peak frequencies. Papurello et al. [150] investi-

gated the performance of anode supported SOFCs under different trace compounds. In particular, they deconvolute the impedance spectra of the SOFC through EIS in order to identify the main losses under $H_2S$, HCl and other compounds poisoning. They found that $H_2S$ poisoning minimally affects the ohmic contribution, while the polarization losses increase due to the TPB decrease. Similarly in [62] they showed how $H_2S$ poisoning doesn't affect the ohmic resistance, but it leads to an increase of the high frequency circle of the EIS spectra due to a deactivation of Ni by the sulphur. As result, the low frequency arc is also affected, due to a slower gas conversion phenomenon [62].

Tanasini et al. [151] studied the effect of particle coarsening in SOFC electrodes. They performed EIS at fixed operation times for 4 identical cell tests. In this way they found that *"the activation period"* of nickel coarsening led to a reduction of the low frequency arc, while ohmic resistance remained constant. At the same time, the high frequencies intercept shifted towards smaller values and the polarization resistance increased even if water saturation could have falsified the analysis. Kubota et al.[152] investigated the effects of redox treatments on performance of Ni-based anode SOFC due to floating temperatures. They found that the changes in anode micro-structure led to an increase of polarization resistance due to TPB length reduction, particularly the ohmic resistance increased slightly together with cycles with an increase of the high frequency impedance arc.

Due to the high complexity of the systems, the individual impedance-related process cannot be easily separated by the semi-empirical equivalent circuit models evaluated by the Complex Nonlinear Least Square (CNLS) fitting, due to overlapping, and because different arrangements of the circuit elements can yield the same impedance curves [153]. For these reasons, the Distribution of Relaxation Time (DRT) approach has proved to be a complementary tool to identify and target the processes with the highest polarization losses in order to improve cell performance. In this approach, the system is modelled through a quasi-infinite series of resistive-capacitive elements without specific consideration about the occurring phenomena, thus eliminating the need of a priori circuit model choice [154]. Individual processes are separated by means of their typical time constants and allows separating different polarization losses in order to develop a physical model for the ECM analysis. In [155] Kromp

showed that unlike the imaginary part of the complex impedance curve, where the individual polarization processes overlap, four peaks can be distinguished clearly in the DRT, otherwise unrecognisable (see Figure 1.3).

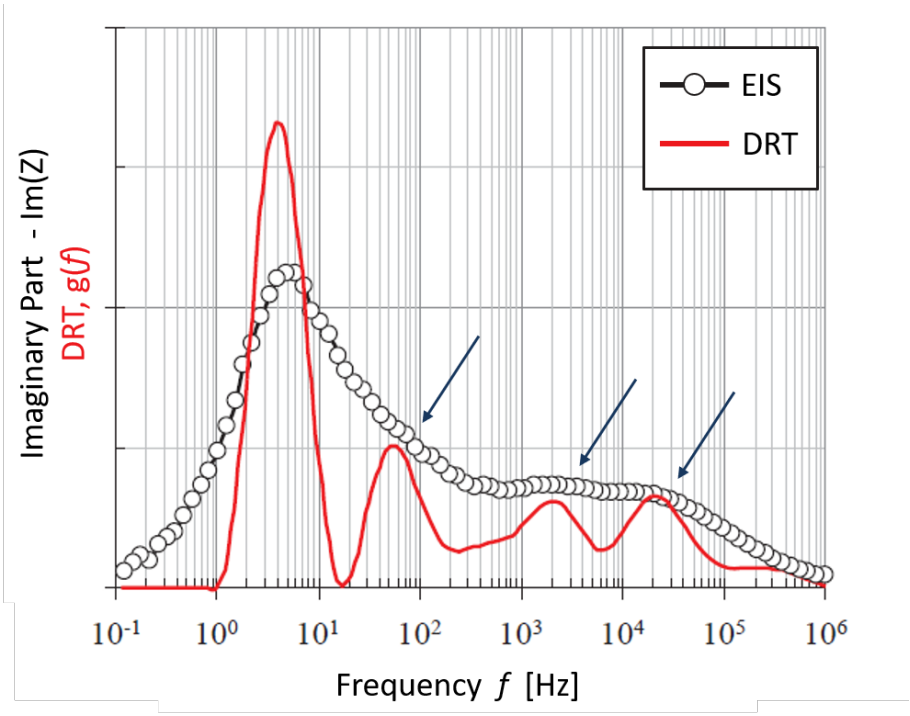


**Figure 1.3:** Imaginary part of an impedance spectrum along with the corresponding Distribution of Relaxation Times (in red). It is clearly visible how the DRT approach allows analysing single peaks related to relevant phenomena otherwise unrecognisable. Adapted from [155].

Furthermore, by exploiting this approach it is possible to identify the characteristic frequencies of the individual polarization processes and a qualitative information about their contribution to the overall polarization resistance. In [156] Leonide et al. analyzed anode-supported SOFC experimental data through a DRT approach. This latter allows identifying five different processes contributing to the total polarization loss that an EIS might not do. By means of a CNLS fitting, an equivalent

circuit model was developed, by modelling all polarization loss processes identified. By doing so, oxygen surface exchange kinetics, diffusivity of oxygen in the bulk, gas-phase diffusion in the cathode, gas diffusion in the anode substrate, charge transfer reaction and ionic transport at the anode side were identified and modelled [157]. Wei$\beta$ et al.[158] studied the application of the Distribution of Relaxation Times approach in the analysis of the impedance spectra of high-temperature fuel cells, in order to separate polarization losses by means of their typical time constants without any a-priori knowledge about the physics of the system. This methodology, coupled with the EIS, allows individuating the most appropriate ECM describing the real system. More detailed information about the DRT can be found in [157], [159] and [160].

To resume, the EIS is a powerful technique, widely applied in studies of electrochemical systems, such as batteries, material corrosions, etc. [161], that allows to get insight on the electrochemical device with a perturbation that do not compromise the current operation of the system. Thus, it is very interesting for on-board applications of fuel cell systems. Moreover, it provides several information on the electrochemical phenomena acting within the Fuel Cell, depending on their relaxation time. With respect to the voltage monitoring, this technique provides information on possible losses that can be ascribed to different electrochemical processes, thus revealing to be extremely useful in the fault isolation process. The main issue is to correlate what emerges from impedance spectroscopy to the physical phenomena occurring in the system, to extract significant parameters to be monitored. Their deviation over well-defined thresholds cause the arising of an alarm that could lead to the identification of a fault. To do so, a diagnostic algorithm has to be coupled with EIS monitoring approach.

## 1.4 Remaining Useful Life

Real-time lifetime estimation techniques, to directly observe degradation phenomena aiming at the evaluation of performance losses and to measure their behaviour over time are difficult to implement. Usually, indirect State-of-Health (SoH) indicators are adopted, since they link voltage decay to temperature trend monitoring with respect to the

current density and operation time [101]. The effect on cell performance over long-term degradation is common to most of the degradation phenomena occurring within the cell, caused by abrupt malfunctioning or detrimental effect, which imply a loss in the available voltage at constant current load.

Lifetime prediction can represent a key methodology to foster SOFC market deployment since it allows scheduling a proper maintenance actions, set the operating condition with respect to the technology applications and avoid unplanned shut-downs. Relatively little work has been done in the field of remaining useful life (RUL) prediction of SOFCs. Indeed, SOFC prognostic is a quite novel field the scientific research is focusing on, as a natural further step after monitoring and diagnosis [162], to improve SOFC durability. Wu et al. [163] combined Elman neural network state prediction model with multivariable dynamic response of SOFC system to predict the residual SoH of the stack. Moreover, Xiao et al. [164] studied the impact of shut-downs and standby on SOFC lifetime. Wu et al. [165] proposed a prognostic-based dynamic optimization strategy to increase SOFC lifetime without significantly reducing its efficiency. They quantified the lifetime of an SOFC under Ni-based degradation processes and tried to sort out a reliable mitigation counteraction to manage the occurring detrimental phenomenon. Wu et al. [166] developed a prognostic model for SOFC RUL prediction by combining a hidden semi-Mark model (HSMM) with an empirical model validated on six groups of SOFC experimental data, achieving good results in terms of prediction accuracy and forecasting speed. Dolenc et al. [167] proposed an integrated Area Specific Resistance (ASR)-based approach for SoH estimation, finding a time-based mathematical relation of the ASR increase, validated upon experimental data to estimate the RUL. They used a linear Kalman Filter and Montecarlo simulation to predict the future time evolution of the ASR to obtain the RUL, thus confirming the ASR as a reliable SoH indicator for the SOFC.

It is clear that a diagnostic algorithm might be fundamental to detect reversible incipient faults. Therefore, a reliable tool should be fast, accurate and capable of discerning several faults by means of a reduced number of sensors that need to be installed on board, with a good trade-off between accuracy, computational burden and costs [103]. For diagnostic purposes, lumped modelling is a suitable option to simulate the nominal

state of the system to have a real-time reference of the system characteristic parameters. Electrochemical Impedance Spectroscopy (EIS) proved to be a suitable technique providing a wealth of information on electrochemical phenomena taking place inside the stack. EIS can be applied to extract useful metrics for stack modelling and fault diagnosis by means of an Equivalent Circuit Modelling (ECM) approach.

## 1.5 Mitigation

Fault mitigation for SOFC is an interesting field, on which the scientific community is currently advancing its first steps. Mitigation could be seen as the follow up of diagnosis and has a key role towards the improvement of SOFCs performance enhancement.

For Proton Exchange Membrane fuel cells (PEMFC), some work were pioneers. Among other, Jia et al. [168] described some mitigation strategies for hydrogen starvation and studied their effectiveness by measuring variations of local current densities and temperatures under various load change scenarios; Wu and Zhou [162] developed a fault tolerant control strategy to make the system robust with respect to unexpected faults, such as membrane drying and flooding. Bilondi et al. [169] investigated both transient and steady-state operations while providing contaminated hydrogen fuel. They studied the mitigation techniques on the CO poisoning, injecting a small amount of air (or oxygen) into the contaminated anode, by analysing the impact on fuel cell performance. Zhai et al. [170] studied the effects of acetylene contamination and envisaged a way to reduce the performance losses. Shabani et al. [171] proposed several mitigation strategies to increase the fuel cell tolerance towards impurities and to reduce the detrimental effects of anode poisoning. In [172] it is possible to find an interesting overview on mechanical failure of PEM fuel cell membranes and practical strategies to reduce the related degradation rate.

Scientific literature provides not so many works on the countermeasures to apply when a fault is detected in a SOFC. Among them, Jia et al. [168] described a novel method for the mitigation of chromium poisoning by capturing chromium vapours using Cr "getters". Uddin et al. [173] showed that getter coating in direct contact with the cathode or sepa-

rated from the cathode can mitigate the Cr poisoning. Wu and Gao [174] developed an optimal fault-tolerant control strategy with a fault diagnosis module, a switching module, two backup optimizers and a controller loop; whereas, Yu et al. [175] proposed a control strategy to mitigate the voltage oscillations and deviations during electrical faults. Sreedhar et al. [176] studied the mitigation methods for corrosion in SOFC, particularly focusing on $CO_2$ contamination, Humidity, Chromium, Silicon, Sulphur, Chlorine compounds and carbonaceous gases. Kupecki et. al [177] proposed a control system oriented towards the mitigation of the effects caused by a sudden reduction in fuel flow as well as during oxidant leakage. They presented an interesting comparison of the stack behaviour with and without the proposed counteractions. Wang et al. [178] demonstrated the mitigation capability of $CuMn_{1.8}O_4$ spinel coating on metallic interconnect upon Cr-poisoning, while in [179] the authors investigated the influence of $CO_2$ in dry $CH_4/CO_2$ anode feeds with regard to degradation issues, and particularly its mitigation effect on the carbon formation in Ni-based anode-supported SOFC.

It is clear that a proper mitigation strategy depends on the specific fault event or degradation phenomenon occurring; indeed, any effective solution has to be tailored to the specific malfunctioning by reducing its impact on the fuel cell performance and, eventually can help in recovering the performance itself. As a consequence, a generic approach does not exist. It results in a very challenging field to explore, since the countermeasure for a fault solve that problem, but might induce further different unexpected effects. On the other hand, an early application of a proper mitigation countermeasure could lead the system toward a full recovery, or at least a stabilization, before the increase in the magnitude of the fault occurring, not more reversible otherwise.

## 1.6 Motivation and Objectives

On the basis of the state of art presented in the previous sections, it is clear the need of improving the diagnosis, the monitoring techniques, the lifetime, and the mitigation, which is the most critical and even crucial step toward the market deployment, while guaranteeing the expected performance required by the market.

This thesis addresses to all this points, with the aim of improving the SOFC performance by implementing innovative solutions looking toward the increase of reliability of such technology. The achievement of these objectives is reached here combining in a proper way modelling approaches and advanced real time measurements. Accuracy, low computational burden and non intrusive measurements are thus required for a robust and reliable on-line algorithm continuously running along with the stack.

Among the achievable measurements for SOFC monitoring, thanks to the recent work in EU-funded projects D-CODE, HEALTH CODE and INSIGHT, it has been demonstrated the possibility of implementing EIS measurements while the system is working. This allows extracting information on the electrochemical processes occurring within the cell during its normal functioning. Based on heuristic knowledge and experimental evidences the features extracted through an ECM approach could allow distinguishing from nominal (i.e. unfaulty) condition and abnormal one, thus detecting and isolating the fault.

A fast-lumped model capable of reproducing the real system behaviour with an acceptable error is extremely useful for the monitoring phase of the ongoing operations, providing with reference values (i.e. nominal and unfaulty conditions) for the main variables that can be compared to real system ones to evaluate real-time residuals. Moreover, the combination of conventional signals (i.e. voltage, temperature, pressures, etc.) with EIS measurements could improve the number of symptoms that can characterize the fault detection phase; nevertheless, the Fault Signature Matrix can be improved adding extra features that cannot be directly extracted from measurements.

The model could be valid support for the EIS based fault detection and isolation and might be a starting point for both a fault mitigation strategy and a lifetime estimation tool. It allows merging all information derived from EIS and conventional signals into an aggregate model exploitable for prognostics and advanced control.

Moreover, such model could be the framework of a lifetime estimation algorithm and a valid support for the FDI algorithm as well, being it a flexible structure in which the Equivalent Circuit Model derived from EIS measurements and the degradation sub models can converge. The concept is described in Figure 1.4, where the integration between EIS-

based algorithm and conventional model is presented.

The model can be coupled with ECM/EIS applications to improve the reliability of the fault detection and isolation. Moreover, the features from the EIS-based algorithm can help in the identification of the specific polarization loss affected by the fault. By doing so, the lumped model can be tuned to adapt its results to the real system in faulty conditions. On the other hand, the Fault Detection and Isolation algorithm might be able to recognize the fault and directly enable one or more related degradation sub-models. These latter sub models are strictly correlated to physical parameters, influenced by the magnitude of the fault. Thus, the model will be able to simulate the faulty stack and to perform an estimate of the parameters (i.e. voltage, temperature, etc.) trends in time and to provide useful data for eventually countermeasures.

This approach can be exploited for both lifetime estimation and eventually mitigation actions. Indeed, the lifetime estimation, along with the fault identification progress, would help in the Remaining Useful Life (RUL) prediction, which could suggest possible mitigation actions that an advanced control tool might apply. These latter actions depend on the nature of the fault and on the lifetime estimation results at the "new" operating conditions at the following time step (sketched in Figure 1.4 as i(t+1)).

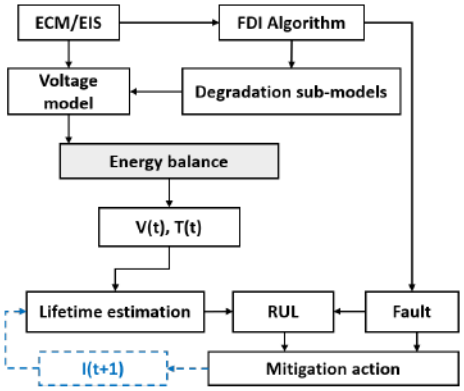


**Figure 1.4:** The concept – Correlation between the lumped stack model, the degradation sub-models, the Equivalent Circuit Model for features extraction and the FDI algorithm.

The main goal of this thesis can be resumed in the following remarks:

- Development of a fast reliable and robust ECM-based algorithm to automatically extract features from EIS measurements
- Development of lumped dynamic model to simulate the electrochemical reaction occurring within the SOFC for voltage, outlet flows and temperature estimation
- Build Fault Detection and Isolation algorithm to detect and isolate the occurring malfunctioning
- Development of a remaining useful life model that predicts the nominal behaviour of the SOFC over the time
- Provide useful guidelines for fault mitigation of such technology to pave the way towards advanced prognostic applications that combine the diagnosis and the countermeasure to extend the SOFCs reliability

# Chapter 2

# The advanced approach EIS-based diagnosis

One of the goal of this work is to develop a diagnostic algorithm based on Electrochemical Impedance Spectroscopy for Detection and Isolation of faults in both single cell and stack. The diagnostic algorithm follows an Equivalent Circuit Modelling (ECM) approach through which significant parameters are identified upon Electrochemical Impedance Spectroscopy (EIS) measurements. Parameters extraction is performed by means of an adaptation of a UNISA proprietary patented technique [180], which allows high generalizability and fast fitting performance. EIS is a powerful diagnostic and non-destructive testing method for electrochemical devices that provides some useful information about the electrochemical phenomena occurring at either low and high frequency. Indeed, through a perturbation in the load signal it allows acquiring the response of the electrochemical system. Each resulting impedance obtained at the corresponding perturbation frequency brings useful information that can be linked to the main electrochemical reactions. Therefore some features can be extracted and used to appraise whether the cell is in either normal or faulty states.

For diagnostic purposes, the parameters of an equivalent circuit model obtained after fitting the EIS data recorded are used to derive the features. The challenge is to correlate the phenomena occurring in the cell with relevant circuital elements. It is worth remarking that any EIS

spectrum could be fit by several Equivalent Circuital models because of its own strong non-linear behaviour. The shape of the spectrum shown via Nyquist plot and Bode diagrams usually presents two o three arcs, which are related to the main electrochemical phenomena. It is expected that one arc shows a single peak in the Bode representation, though this is not always experienced, making the model parameters identification troublesome. In such cases, the information that can be extracted from the EIS data set could lead to an incomplete circuit modelling identification. To approach that problem, Zhang et al. [160] and Boukamp et al. [181] proposed the Distribution of relaxation times (DRT) approach, which investigates the time constants corresponding to the dynamics of the electrochemical processes taking place within the cell. In a SOFC, as described in [153], usually 6 processes can be distinguished via DRT analysis, showing in turn 6 peaks in the distribution function-frequency diagram, which can be easily correlated to a 6-elements circuit. Then, these characteristic frequencies are used as key metrics. According to Leonide[157], each phenomenon has a characteristic frequency that helps to distinguish it among others. Although, the DRT approach might help in selecting a complete ECM capable of representing each process, the computational burden required is not suitable for on-board [1] uses.

The aim of this thesis is the development of algorithms that can be implemented on-board for the purpose of monitoring, diagnosis and lifetime estimation. Therefore, a particular attention to the computational burden (both time and memory usage) is a strict constraint to be accounted. The monitoring algorithm aims at extracting the ECM parameters for diagnostic purposes. The main idea, as represented in Figure 2.1 and Figure 2.2, is to exploit the EIS experimental measurement to identify a suitable Equivalent Circuit model that fits the spectra by analysing the Nyquist plot and Bode diagrams as well. Particularly, Figure 2.1 shows the parameter extraction from the EIS measurement. Indeed, by injecting a sinusoidal stimulus (i.e., current), the system response (i.e., voltage) will be sinusoidal as well. The ratio between such response and the perturbation is a complex number, whose representation in the Nyquist plot is a kind of arcs-based shape. The algorithm

[1] Hereafter, on-board application means the use of any algorithm that is embedded on control devices implemented on a SOFC system running in a real environment.

will take this measurements aiming at identifying the best circuital model which fits the geometrical shape of the Nyquist. This will allow extracting quantitative informations (i.e., the ECM parameters) from a qualitative EIS representation, which will be monitored as representative of the FC State of Health.

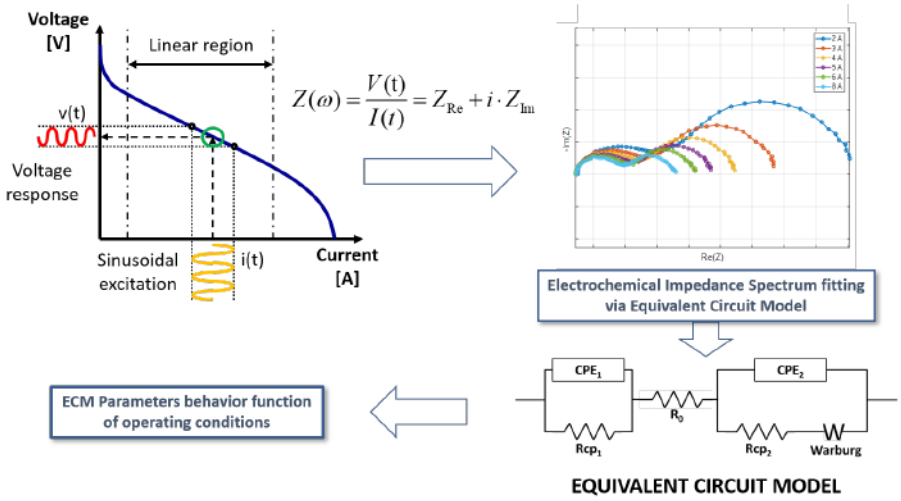


**Figure 2.1:** Scheme of the diagnostic approach 1/2. By injecting a signal perturbation it is possible to generate a Nyquist spectrum. This latter is fitted by means of an Equivalent Circuit Model, whose parameters are used as indicators of the State of Health of the system.

The right choice of the circuit is the first and the main step towards the right parameters extraction, which are named as features (i.e. $R_\Omega$, $R_{TOT}$, $\omega_n$, $R_{cp}$, or a combination of them). The features can be identified when the SOFC is running in nominal conditions at different loads. A map of the parameters can be built to have a set of reference values, which are said nominal or unfaulty herein. As sketched in Figure 2.2, when a fault occurs, the algorithm receives the EIS spectrum data and returns a set of identified features that deviate from the expected nominal ones. For any feature significantly deviating from the expected value, a related symptom changes its value from "0" (nominal) to "1" (faulty). The collection of all these symptoms defines the symptom pattern, describing the State of Health (SoH) of the SOFC.

During the monitoring, the continuous comparison of the symptom vector with the set of vectors correlating the features to all faulty conditions (i.e. Fault Signature Matrix) allows detecting the current abnormal condition. Indeed, when the symptom pattern matches a row of the matrix (built upon experimental evidences), the fault is correctly detected and isolated.

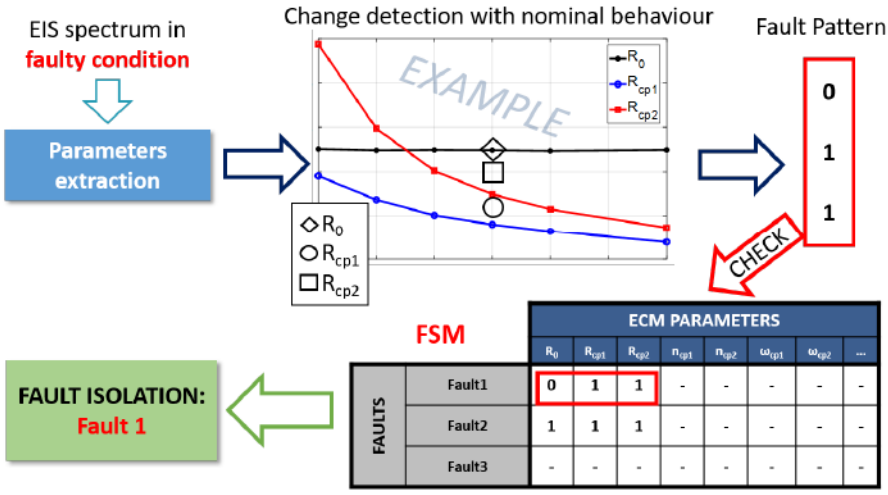


**Figure 2.2:** Scheme of the diagnostic approach 2/2. The extracted features are monitored continuously. From ad hoc experiments, the expected behaviour of such parameters under defined conditions is collected in the Fault Signature Matrix. When this behaviour is detected in the system under investigation, the related fault is thus isolated.

## 2.1 The ECM approach

The Equivalent Circuit Modelling (ECM) approach is usually adopted for fuel cell EIS-based diagnosis. Ideal equivalent circuits are often constructed to simulate the electrochemical processes taking place within the cell. The main idea is to model each element of the ECM as a lumped parameter model to simulate the main physical and electrochemical phenomena, relating to, for example, electrolyte resistance, electrochemical reaction conductance, mass transfer, electron transfer. Moreover, ECM

approach allows extracting quantitative information from the shape of the EIS spectrum. The information derived from EIS measurement is mainly related to two variables: The impedance $Z$ and the frequency $f$. The first one can be plit in real , $Re_Z$, and imaginary, $Im_Z$, parts respectively, while the frequency gives an information linked to the relaxation time of the phenomena occurring. As Leonide [157] states: the term "relaxation time" refers to the return of a system into a state of equilibrium after an imposed perturbation, and it is the time constant at which the specific physical process is dominant. SOFC are usually characterized by the simultaneous overlapping of various process that could cause a loss in performance. In turn, the capability of analysing their relaxation times could help the State of Health analysis, being possible to identify the dynamics of each single process. According to Kromp [155], in SOFC it is possible to identify the typical frequency of each phenomenon occurring, as shown in Figure 2.3.

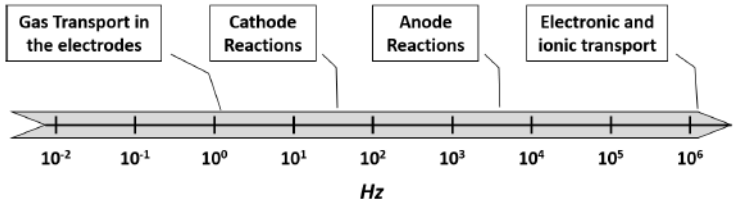


**Figure 2.3:** Characteristic frequencies of the electrochemical losses occurring in a SOFC. Adapted from [155].

The frequency measured via EIS ranges from 0.1 to $10^{5-6}Hz$ and it can be further detailed in 4 different decades and two extreme intervals, according to the following peak distribution [182]:

- **P1 -** $f < 1Hz$: fuel electrode diffusion under reformed gas operation and/or oxygen electrode adsorption/desorption;
- **P2 -** $f \approx 1\breve{}10Hz$: gas conversion;
- **P3 -** $f \approx 10\breve{}100Hz$: overlap of oxygen and transport related processes in the fuel electrode;

- **P4 -** $f \approx 100\check{}1000Hz$: overlap of oxygen and transport related processes in the fuel electrode;
- **P5 -** $f \approx 1\check{}10kHz$: Charge transfer in the fuel electrode;
- **P6 -** $f > 10kHz$: no consensus in literature, probably something related to the electronic and ionic transport.

While the Distribution of Relaxation Times (DRT) allows singling out all these phenomena, from Bode diagrams only the most dominant ones are visible, while the remaining are superimposed and not clearly distinguishable. However, when the State of Health changes, some phenomena start being more significant, so the spectrum is expected to vary in the shape and, sometimes, even in the number of visible arcs as well. The rise of a new arc in the spectrum is related to a new clear distinguishable peak in the Bode representation, due to a clear shift in frequency of the phenomenon.

With a well identified ECM, the impedance of a fuel cell can be described as the sum of the impedances of the single circuital elements. Thus, each element could be considered as one or more (if wrapped) losses in the cell and brings information about the Area Specific Resistance, the characteristic time constant and its frequency of occurrence along with its distribution.

### 2.1.1 The main elements

In ECM approach it is possible to distinguish some basic elements, whose combination in a circuit can reproduce the behaviour of the electrochemical devices. Many of them depend on the angular frequency $\omega$, defined as:

$$\omega = 2\pi f \tag{2.1}$$

where $f$ *[Hz]* is the frequency.
The main elements of the Equivalent Circuit modelling approach are:

- **Resistance -** $R[\Omega]$ It is used to describe the ohmic resistance in terms of electron and ion conduction. In the frequency domain, the resistance has only a real part:

$$Z_R = R \tag{2.2}$$

- **Inductance - $L$** $[H]$ It is used to describe the high frequency inductance. It is the magnetic field generated when a current pass through an inductor and it is often caused by the device used to test the system, by the cabling and the wires influence. In the frequency domain, the inductance is given as:

$$Z_L = j\omega L \tag{2.3}$$

- **Capacitance - $C$** $[F]$

  It is used to describe the double layer capacitance [2] at the electrode-electrolyte interfaces and the chemical capacitance linked to the concentration impedance. In the frequency domain, the capacitance is purely imaginary:

$$Z_C = \frac{1}{j\omega C} \tag{2.4}$$

  The graphical representation of these three aforementioned circuital elements is sketched in Figure 2.4.

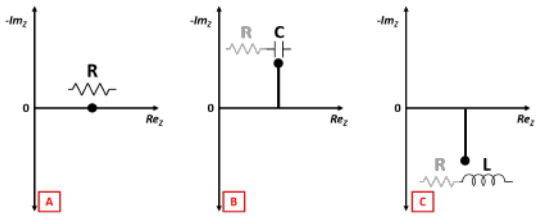


**Figure 2.4:** Graphical representation of the impedance elements. From the left the following elements are shown: A) $R$ - Resistance, B) $C$ - Capacitance and C) $L$ - Inductance. Please note that for sake of clarity, $L$ and $C$ representation is shifted by a certain $Re_Z$ (as they are connected in series with a Resistance).

[2] An electrical double layer is an electron layer at the electrode-electrolyte interface. It behave as a capacitor, in which the ions from the solution adsorb into the electrode surface. The reader is addressed to [183]

- **Warburg -** $W$ $[\Omega s^{-1/2}]$ It is a frequency dependent resistance used to simulate the mass transfer in an electrochemical process. The Warburg element can be written as follows:

$$Z_W = \sigma\omega^{-1/2} - j(\sigma\omega^{-1/2}) \tag{2.5}$$

where $\sigma$ is the mass transfer coefficient due to the contribution of the reactants in the reaction within the stack. It can be considered as a resistance ($R_W = \sigma\omega^{-1/2}$) in series with a capacitance ($C_W = \sigma\omega^{-1/2}$). Due to its formulation (eq. 2.7), the Warburg element is a 45° line at the end of the low frequency arc.

- **Constant Phase Element -** $CPE$ $[\Omega^{-1}s^{n_Q}]$ Also known as Q-element, it is a frequency dependent element useful to represent the response of a real electrode (or generally speaking device). A CPE element assumes a specific distribution of time constants as a function of its $n_Q$ parameter. The impedance associated to the CPE element is described as follows:

$$Z_{CPE} = \frac{1}{Q \cdot (j\omega)^{n_Q}} \tag{2.6}$$

where $Q$ and $n_Q$ are parameters that need to be identified.

The CPE element is a very versatile and useful circuital element, being it capable of reproducing different shapes depending on $n_Q$, which can vary from -1 to +1 values. Table 2.1 shows the different meaning that the CPE can assume:

| $n_Q$ | **CPE meaning** | **Q** |
|---|---|---|
| 0 | Resistance | $R^{-1}$ |
| 0.5 | Warburg | $\sigma^{-1}$ |
| 1 | Capacitance | $C$ |
| -1 | Inductance | $L^{-1}$ |

**Table 2.1:** Physical meaning of the CPE element. Adapted from [130].

In summary, Table 2.2 groups the main circuital elements that, connected in series and parallel, can be used to reproduce the EIS spectra of a typical electrochemical device.

| Element | Name | Parameter(s) | Units |
|---|---|---|---|
| ***R*** | Resistance | R | $\Omega$ |
| ***C*** | Capacitance | C | $F = \Omega^{-1}s$ |
| ***L*** | Inductance | L | $H = \Omega s$ |
| ***W*** | Warburg | $\sigma$ | $\Omega s^{-1/2}$ |
| ***CPE*** | Constant Phase Element | $Q$ | $\Omega^{-1}s^{n}$ |
| | | $n_Q$ | [/] |

**Table 2.2:** Equivalent circuit elements parameters. Adapted from [130].

Impedance models are built by suitably combining elements to simulate the concerned electrochemical phenomena. The proper combination of elements allows matching the simulated shapes of the EIS spectrum with the measured one. For SOFCs, the elementary block is built by connecting in parallel a Resistance and a Capacitance. This "RC" group is known as Voigt element, and its complex impedance can be written as:

$$Z_{RC} = \frac{R_{RC}}{1 + j\omega RC} = \frac{R_{RC}}{1 + j\omega\tau} \tag{2.7}$$

where $\tau = RC$ is the time constant of this building block and its representation on the Nyquist plot is a semicircle of diameter $R_{RC}$, as shown in Figure 2.5:

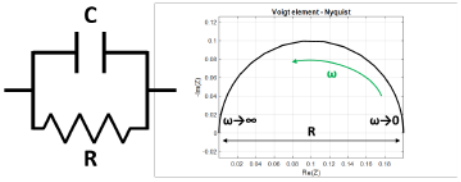


**Figure 2.5:** Voigt element representation. On the left side the RC equivalent scheme is presented, while on the right side its representation on the Nyquist plot is sketched.

Usually, a more generic element is used to match the real shape of the spectra. Thus, the RC element is replaced with a RQ element, where a $CPE$ element is used in spite of the capacitor $C$, see. In this case if the $n_Q$ parameter is 1, the RQ element behaves like the Voigt element. Figure 2.6. describes the variation of the Voigt shape when a RQ element is used at different values of the $n_Q$ parameter.

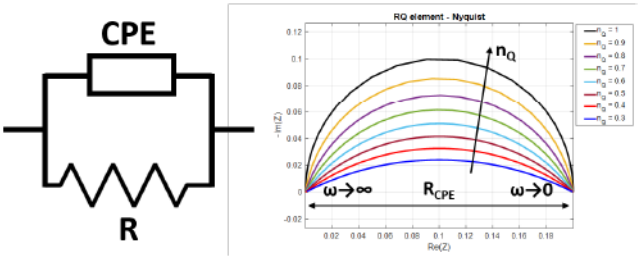


**Figure 2.6:** RQ element. On the left side the RQ equivalent scheme is presented, while on the right side its representation on the Nyquist plot at different values of $n_Q$ is shown.

## 2.2 The MGFG Algorithm

The Matching Geometric Fitting Guess (MGFG) algorithm derives from a patented approach developed for PEM technologies. In the framework of the INSIGHT project, this approach has been suitably modified, extended and applied for the first time to SOFC technologies, with good and accurate results. The algorithm was conceived and developed to be fast, accurate and not computationally demanding, to allow a diagnostic procedure for detection of faults. It was validated upon measurements from both INSIGHT and SOSLEM EU-funded projects. This latter data set proved to be fundamental for the tuning phase of the algorithm and to prove its low computational burden, robustness and reliability. As shown in Figure 2.7, the algorithm works sequentially.

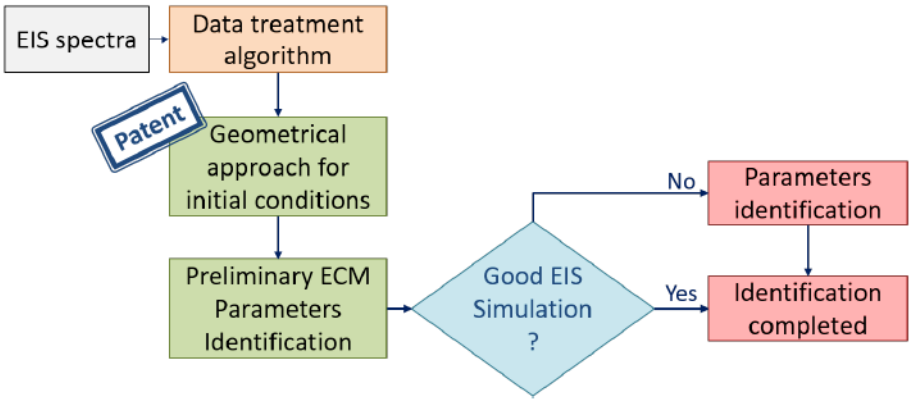


**Figure 2.7:** MGFG identification algorithm flow chart. From the measured spectrum, the algorithm analyses the data, defines a suitable initial condition upon the geometrical approach developed and then, if necessary, applies an identification routine

The first step consists in loading the impedance spectrum information in terms of frequency $f$, real $Re_Z$ and imaginary $Im_Z$ parts of the impedance vectors, along with the number of cells and the electroactive area. Afterwards, the raw EIS spectrum is treated to remove spurious points. Significant points - such as the intercepts with x-axis - are then extracted to identify geometrical shapes and help defining the initial conditions for ECM parameters identification. Indeed, these geometrical shapes recall the features shown by ECM parameters (or certain combination of them) on the Nyquist plot. The approach enables, therefore, a preliminary rough identification of the parameters values to perform a proper identification procedure with reasoned initial conditions. Thus, if the EIS spectrum is well represented by a model running with the preliminary estimation of ECM parameters, they can be used as final identification of the considered metrics. Otherwise, a more robust parameters identification is needed. The fitting is performed by applying a minimization algorithm with a cost function based on the difference between the measured and simulated real and imaginary part of the impedance. Afterwards, the parameters are identified, and their values are associated to the specific operating condition at which the spectrum was measured. It is worth noting that the ECM structure (and thus the number of the

electrical components) is not defined a priori, but it adapts according to the geometrical features extracted with the geometrical approach [3]. Indeed, the circuital structure presented in Figure 2.8 can easily apply to a two-arcs spectrum. However, in case the algorithm recognizes three or more arcs, it automatically changes the ECM structure to better fit the shape of the spectrum by adding more circuital elements with a certain arrangement (e.g., series, parallel, etc.) as explained later on. This feature allows a flexible use of the proposed metrics extraction algorithm for different conditions and spectrum shapes. The Equivalent Circuit model designed built by the algorithm is presented in Figure 2.8. The elements of the blue area are enabled by default, being them responsible for the intercept at high frequencies and the first arc of the Nyquist plot. The elements of the green area are usually enabled if in the spectrum some physical parameters are recognized (e.g. the inductive-element is activated when at high frequencies points at positive imaginary part are observed, thus revealing an inductive effect mostly-likely related to the cabling or the test bench). The violet area contains elements that are automatically enabled to match the shape of the spectrum in case of additional arcs. It is worth remarking that the algorithm selects the circuit arrangement and the elements automatically.

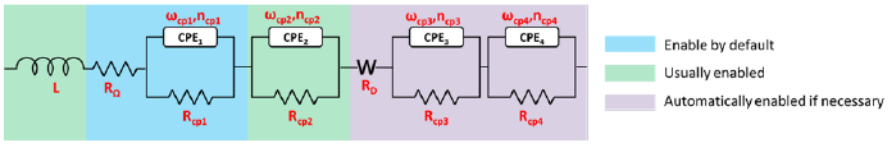


**Figure 2.8:** Scheme of the Equivalent Circuit Model identified by the MGFG Algorithm. The common ECM is usually made of at least an ohmic resistance and one or two R/Q elements. If some inductive effects are recognized, the inductance is added.

For sake of clarity, a typical inductive effect that leads the algorithm to activate the related circuital element, namely inductance $L$, is shown in figure 2.9. Here, the yellow area empathizes the EIS points highly

[3]It is worth noting that the algorithm applies with no a priori ECM structure for the specific system and technology; however, a basic initial circuit for each specific technology (i.e., PEMFC, SOFC, etc.) would improve the speediness of the tool and the accuracy of the results.

affected by an inductive effect, with a positive value on the Imaginary part of $Z$. When the algorithm detects such behaviour, the element in green area of figure 2.8 is added to the ECM and its value is estimated upon the identification procedure.

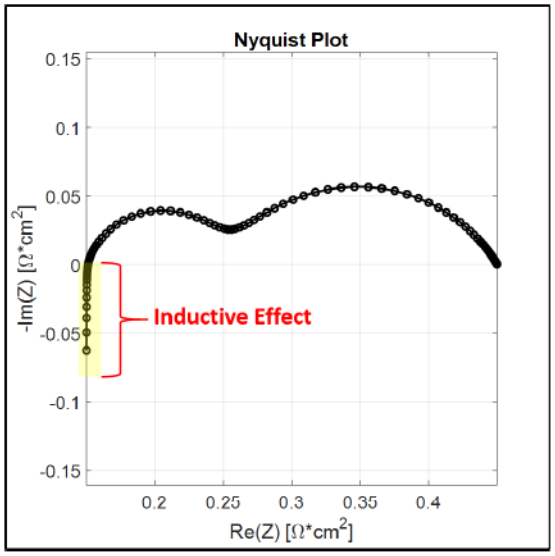


**Figure 2.9:** Geometrical representation of the inductive effect on the shape of a typical SOFC Nyquist plot.

### 2.2.1 The geometrical approach

One of the most common problems occurring while working with noisy experimental data is the presence of outliers or discontinuities, which may cause instabilities and errors during the identification process. To make a smooth spectrum and to perform an effective mathematical parameter identification, a filtering process is implemented.

The data need to be treated to remove all non-coherent points. This can be performed in many different ways, e.g. applying the Kramers Kronig routine, or identifying the spectrum with a large number of RQ elements. Indeed, at this step the main goal is to have a model or a function that allows approximating the impedance $Z$ (both for Real and Imaginary parts) with respect to the frequency as well, even if it doesn't

contain any kind of physical information about the electrochemistry of the system. The analytical function is then a basis for the EIS significant point extraction. As sketched in figure 2.10, the intercept of the Nyquist with the $Re_Z$ axis at high frequencies is directly identified and then associated to the $R_\Omega$. The other intercept at low frequencies, $Re_{Z_{end}}$, called $R_{TOT}$, is thus exploited to evaluate the well-known polarization resistance $R_{pol}$, whose calculation is shown in eq. 2.8:

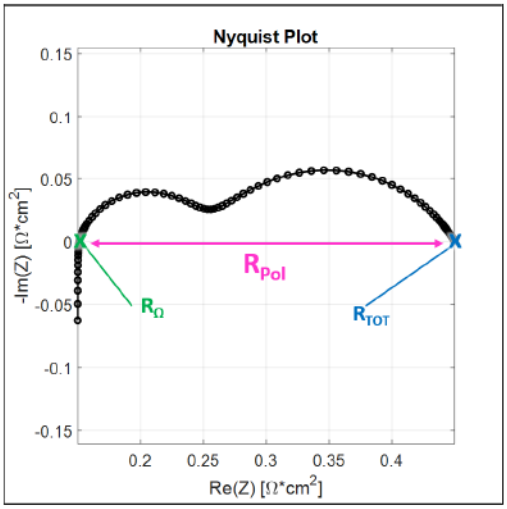


**Figure 2.10:** Definition of the evident ECM resistances on a Nyquist plot

$$R_{pol} = R_{TOT} - R_\Omega \tag{2.8}$$

By considering the geometric shape of the spectrum in the Nyquist Plot, which reminds to a combination of elementary geometrical figures (e.g., semicircles, ellipses, and lines, at least), it is possible to exploit analytical functions to derive key-features of the EIS graphical representation such as local maxima $Max_n$, minima $min_n$, flexes $flex_n$ and real axis intercept points. These data are exploited to define a preliminary set of spectrum features, which in turn are used as initial conditions for the ECM parameter identification process. Moreover, in the Bode diagram ($Frequency/-Im_Z$) the frequency of the relevant points is extracted and correlated to the key-features derived from the Nyquist representation.

The basic circuit used to represent a typical SOFC spectrum is shown in Figure 2.11. Therefore, each circuital element provides a typical geometry of the spectrum. The inductance is used to simulate the inductive effect of the wired cable and implies the spectrum to have a positive part in the $Im_Z$, typically at $Re_Z < R_\Omega$. If negligible in the measured spectrum, the inductance $L$ is set to 0. $R_\Omega$, as already mentioned, stands for the resistance of the electrolyte and it is directly evaluated in the Nyquist plot. The Warburg element $W$ simulates the diffusion resistance $R_D$; it is worth recalling that its effect on the shape of the spectrum is not easy to recognize in a SOFC. Indeed, Warburg element simulates the ideal charge-transfer resistance and a double layer capacitance. Usually, it can be seen as a linear relationship on the log of a Bode plot ($log|Z|$ versus $log(\omega)$) with a slope of value $-1/2$. If such behaviour is not recognized in the Bode Plot, the $R_D$ can be set to zero and the Warburg element neglected. The last circuital component is a R-Q element composed by a Resistance and a CPE. It simulates, with an acceptable approximation, almost all the predominant electrochemical processes, like anodic charge transfer, double layer capacitance or cathodic processes of gas conversion. As detailed in section 2.1.1, the RQ elements geometrically represent semicircles in the Nyquist plot, with a variable shape depending on the parameters $Q$ and $n_Q$. Thus, if more than two arcs are found, the ECM is immediately extended adding an extra RQ element, as shown in Figure 2.12.

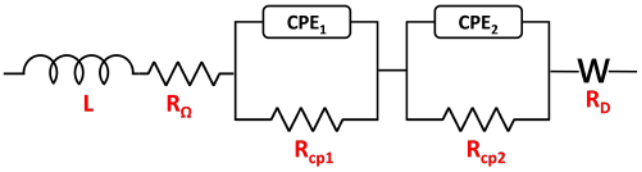


**Figure 2.11:** Basic Equivalent Circuit Model

As far as the model implementation and the identification of its parameters concerns, the main issue deals with the mathematical complexity whose non-linearities may lead to, among others, multiple solutions and high computational burden. These issues may easily occur for a SOFC where the matching of all the main electrochemical processes requires a series of at least five circuital elements ($L-R-W-R/Q-R/Q$),

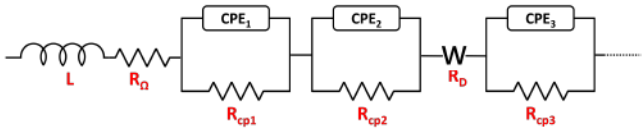


**Figure 2.12:** Extended Equivalent Circuit Model

as sketched in Figure 2.11. Indeed, the same circuit with a different set of parameters or different circuit layouts can simulate the same spectrum. To have a strong adherence with the measurements and the electrochemical phenomena, some information, like the $R_\Omega$ are to be directly extracted from the EIS data. Moreover, great attention has to be given to the modelling of the RQ elements and therefore they are herein defined in a not common way so as to directly set the characteristic frequency upon the experimental data set. Staring form the common used form of the $R/Q$, which has the following formulation:

$$Z_{RQ} = \frac{RQ}{R+Q} \tag{2.9}$$

$$Q = \frac{1}{(j\omega)^{n_Q} \cdot Y_Q} \tag{2.10}$$

A new formulation was built adapting the one of Leonide [157], as described below. This formulation explicitly correlates $Re_Z$ and $IM_Z$ of the Nyquist plot with the frequency taken from the Bode plots. It is worth recalling that while the $R$ could be easily estimated by analysing the geometrical shape of the semicircle in the Nyquist Plot, the $n_Q$ and the $Y_Q$ have to be searched by means of a mathematical identification. By introducing $\frac{1}{\tau}$ as the characteristic frequency peak of the RQ element, which can be directly observed as the maximum in the Bode diagram ([157]), the eq. 2.9 can be rewritten as:

$$Y_Q = \frac{\tau^{n_Q}}{R} \tag{2.11}$$

where $\tau^{n_Q} = R \cdot Y_Q$ is the time constant. Thus, the impedance of the RQ element from eq. 2.9 turns into:

$$Z_{RQ} = \frac{R}{1 + \frac{R}{Q}} = \frac{R}{1 + R \cdot Y_Q \cdot j\omega^{n_Q}} \tag{2.12}$$

Considering eq. 2.11 it is possible to single out the characteristic frequency peak:

$$Z_{RQ} = \frac{R}{1 + \tau^{n_Q} \cdot j\omega^{n_Q}} = \frac{R}{1 + (j\frac{\omega}{\omega_c})^{n_Q}} \tag{2.13}$$

where $\omega_c$ is the frequency peak of the associated arc on the Bode diagram.

The approach might apparently fail when two phenomena have closed characteristic frequencies thus leading to a curve where two peaks appear as merged in a single one. As a consequence, the model fitting can be achieved with a single R-Q element, instead of two (i.e., one per peak/arc).

It is worth reminding that the requirement of reduced computational burden, both memory and speed, implies a trade-off between number of RQ elements (which entails the number of parameters) and accuracy. Moreover, the main goal of the conceived diagnostic approach is to determine an unexpected fuel cell behaviour by means of both a quantitative and qualitative comparison of the spectrum in nominal and current conditions. Thus, even if the algorithm fails in the perfect matching of the spectrum geometry, it is able to select a set of clearly identified key points. They guarantee the same model outputs (e.g., the ECM identified parameters) at the same Fuel Cell operations. In this sense, when an unexpected event occurs, the identified circuital model will show a sensible change in the parameters, revealing in turn the occurrence of a possible malfunctioning.

### 2.2.2 The Montecarlo analysis on the Geometrical guess

The MGFG algorithm was developed within the EU-funded project INSIGHT. Its application was carried out on the experimental dataset provided by that project along with those made available by the other EU-funded project Soslem whose measurements were used for the training phase. As a first step, to test the robustness of the geometrical approach adopted to identify the ECM upon experimental data, a Montecarlo analysis was performed to check the variability of the results with

respect to the change of the initial values as identified by the geometrical approach. The analysis consisted in starting from an equivalent circuit model (i.e., reference ECM) whose shape is resembling to the one provided by the experiments, in a frequency range between $10^{-5}Hz$ and $10^{6}Hz$. The generated spectrum was given as input to the MGFG algorithm with a double purpose: to understand if the choice of the circuital elements was right and to check the quality of the minimization as well. An exemplary result is provided in Figure 2.13, where a simulated spectrum has been identified via MGFG algorithm.

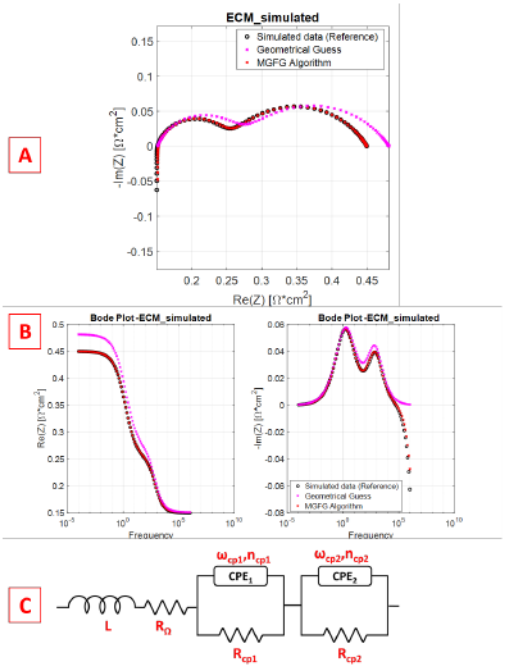


**Figure 2.13:** MGFG algorithm trial on a simulated spectrum. A) shows the Nyquist plot, B) the Bode diagrams whereas in C) the identified ECM is sketched. In the plots, the black markers represent the simulated spectrum, input of the algorithm, the pink circles are the initial geometrical guess and the red ones are the final identification achieved.

It is interesting to note how the initial geometrical guess of the ECM parameters provides a quite similar shape of the spectrum, with respect

to the reference ECM. It is up to the algorithm to refine the accuracy of the identified parameters. Moreover, being the shape (i.e., initial condition) already well-defined, the minimization problem is less burdensome resulting in a more reliable solution. This is due to the fact that the initial conditions of the parameter set for the minimization of the MGFG algorithm have been selected without a random guess as usually done for conventional optimization procedures. The Equivalent Circuit Model used to simulate the spectrum and identified by the MGFG algorithm is shown in Figure 2.13-C). Here the two arcs are simulated by two RQ elements connected in series with a resistance $R_\omega$. The two characteristic frequencies of the RQ elements are identified through the two peaks shown by the Bode Diagrams in the right side of 2.13-B), whereas the $R_\omega$ [4] is the first intercept of the real axis in the Nyquist plot of Figure 2.13-A), whereas the $R_{tot} = \sum R_i$ Since some points at $Im_Z > 0$ are found, a related inductance $L$ is activated. The identified ECM results in 4 element and, in turn, in 9 features, which are: $L_0$, $R_0$, $R_{cp_1}$, $n_{cp_1}$, $\omega_{cp_1}$, $R_{cp_2}$, $n_{cp_2}$, $\omega_{cp_2}$ and $R_{tot}$. Once identified the 9 circuital features of the simulated spectrum via MGFG algorithm, and taking them as reference, the analysis has been performed by varying each parameter per time with a hundred random selection within a range of 100% $\pm$ 30% with respect to its reference value. As said before, the variation was applied to the parameters identified by the geometrical approach to be used as initial condition for the optimization problem. As a sample of the analysis performed, the figures 2.14, 2.15 and 2.16 show the effect of the $\pm$30% change of the aforementioned approach of $R_{cp1}$, $\omega_{cp1}$ and $n_{cp1}$ on the minimization error, respectively. This three figures reported below show the comparison ( in figure $* A$ ) between the 9 parameters values used to build the simulated EIS spectrum and the 9 parameters values identified by the MGFG algorithm. Moreover figure $* B$ shows the variability of the identification for each parameter (the $R_0$ is neglected since it is directly evaluated on the spectrum) due to $\pm$30% variation of the chosen element (highlighted in red) in the initial condition (i.e., the result of the geometrical approach and before the minimization). The overall fitting error is then presented in figure $* C$.

[4] For the purpose of this work $R_\omega$ and $R_0$ have the same meaning and can be used alternatively.

A

| | $R_m$ [Ω/m²] | $L_0$ [Ω/m²] | $R_{cp1}$ [Ω/m²] | $\omega_{cp1}$ [Hz] | $n_{cp1}$ [/] | $R_{cp2}$ [Ω/m²] | $\omega_{cp2}$ [Hz] | $n_{cp2}$ [/] | $R_{TOT}$ [Ω/m²] |
|---|---|---|---|---|---|---|---|---|---|
| Simulated | 0,15 | 1e-8 | 0,10 | 5000 | 0,80 | 0,20 | 10 | 0,65 | 0,45 |
| **Identified** | **0.15** | **7.75 e-9** | **0.10** | **4643.73** | **0.80** | **0.20** | **9.78** | **0.65** | **0.45** |

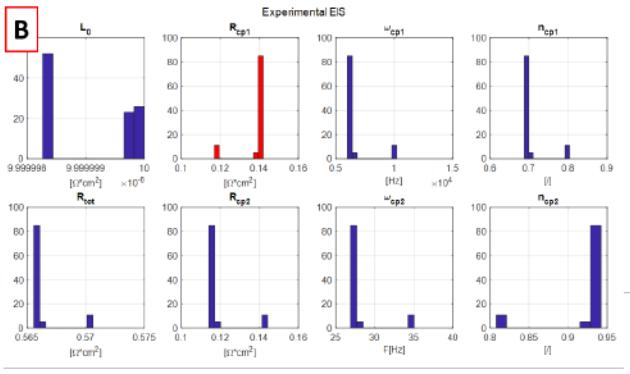


**Figure 2.14:** Montecarlo analysis - simulated spectrum. ±30% variation of the $R_{cp1}$ parameter (red highlighted) in the geometrical initial guess. The Table A) shows the comparison between the simulated data used to generate the spectrum and the identified parameters; the bar-plots in B) present the effect on the identified parameters of the variation in the initial condition of the defined one (in red). The green bars in C) are the related fitting errors for the 100 tests performed.

A

| | $R_m$ [Ω/m²] | $L_0$ [Ω/m²] | $R_{cp1}$ [Ω/m²] | $\omega_{cp1}$ [Hz] | $n_{cp1}$ [/] | $R_{cp2}$ [Ω/m²] | $\omega_{cp2}$ [Hz] | $n_{cp2}$ [/] | $R_{TOT}$ [Ω/m²] |
|---|---|---|---|---|---|---|---|---|---|
| Simulated | 0,15 | 1e-8 | 0,10 | 5000 | 0,80 | 0,20 | 10 | 0,65 | 0,45 |
| **Identified** | **0.15** | **7.75 e-9** | **0.10** | **4643.73** | **0.80** | **0.20** | **9.78** | **0.65** | **0.45** |

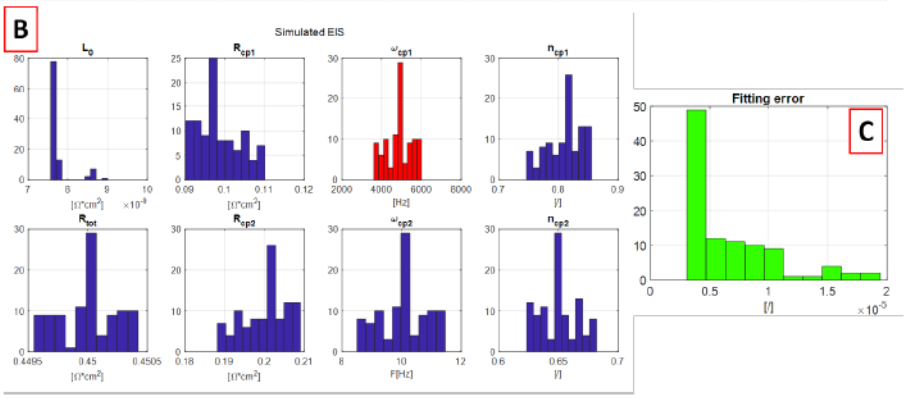


**Figure 2.15:** Montecarlo analysis - simulated spectrum. ±30% variation of the $\omega_{cp1}$ parameter (red highlighted) in the geometrical initial guess. The Table A) shows the comparison between the simulated data used to generate the spectrum and the identified parameters; the bar-plots in B) present the effect on the identified parameters of the variation in the initial condition of the defined one (in red). The green bars in C) are the related fitting errors for the 100 tests performed.

It is interesting to note that both $R_{cp1}$ and $n_{cp1}$ variations have a very reduced effect on the overall fitting error. On the other hand, the algorithm seems to be more sensitive to the change of the characteristic frequency $\omega_{cp1}$. However, the fitting error doesn't change its magnitude, thus proving the consistency of the algorithm with respect to the simulated spectrum.

A

| | $R_m$ [Ω/m²] | $L_0$ [Ω/m²] | $R_{cp1}$ [Ω/m²] | $\omega_{cp1}$ [Hz] | $n_{cp1}$ [/] | $R_{cp2}$ [Ω/m²] | $\omega_{cp2}$ [Hz] | $n_{cp2}$ [/] | $R_{TOT}$ [Ω/m²] |
|---|---|---|---|---|---|---|---|---|---|
| Simulated | 0,15 | 1e-8 | 0,10 | 5000 | 0,80 | 0,20 | 10 | 0,65 | 0,45 |
| **Identified** | **0.15** | **7.75 e-9** | **0.10** | **4643.73** | **0.80** | **0.20** | **9.78** | **0.65** | **0.45** |

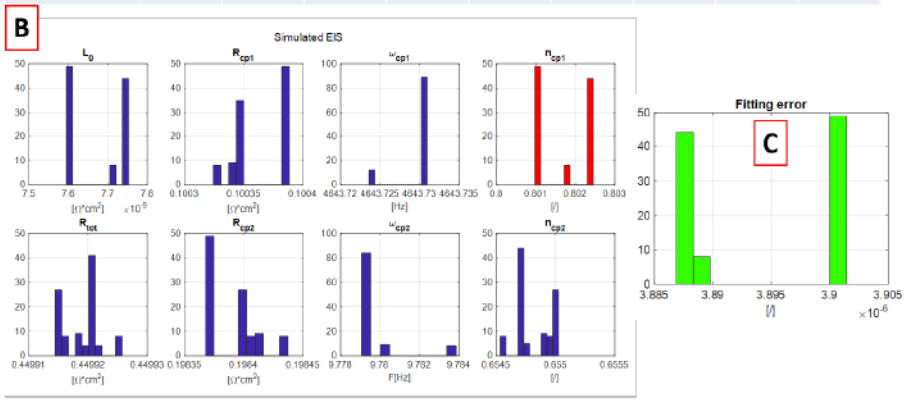


**Figure 2.16:** Montecarlo analysis - simulated spectrum. ±30% variation of the $n_{cp1}$ parameter (red highlighted) in the geometrical initial guess. The Table A) shows the comparison between the simulated data used to generate the spectrum and the identified parameters; the bar-plots in B) present the effect on the identified parameters of the variation in the initial condition of the defined one (in red). The green bars in C) are the related fitting errors for the 100 tests performed.

For sake of comparison, all the fitting error variations are reported in Figure 2.17 with the related parameter changing.

| | $R_0$ [Ω/cm²] | $L_0$ [Ω/cm²] | $R_{cp1}$ [Ω/cm²] | $\omega_{cp1}$ [Hz] | $n_{cp1}$ [/] | $R_{cp2}$ [Ω/cm²] | $\omega_{cp2}$ [Hz] | $n_{cp2}$ [/] | $R_{TOT}$ [Ω/cm²] |
|---|---|---|---|---|---|---|---|---|---|
| Simulated | 0,15 | 1e-8 | 0,10 | 5000 | 0,80 | 0,20 | 10 | 0,65 | 0,45 |
| **Identified** | **0.15** | **7.75 e-9** | **0.10** | **4643.73** | **0.80** | **0.20** | **9.78** | **0.65** | **0.45** |

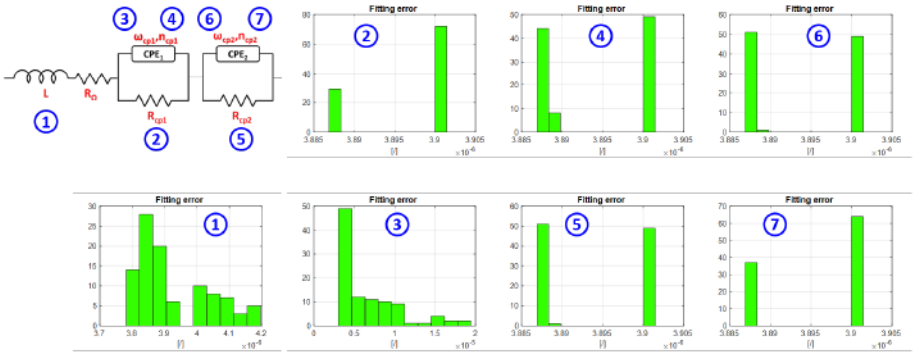


**Figure 2.17:** Montecarlo analysis - simulated spectrum. Comparison of the 9 fitting errors related to the change of the 9 ECM parameters along with the comparison between the simulated data used to generate the spectrum and the identified parameters.

Finally, it is worth remarking that the most effective change is ascribed to the $\omega_{cp1}$, which is the characteristic frequency peak of the high frequency spectrum.

### 2.2.3 Training

The training phase was performed on experimental data set provided by the Soslem Project, which consisted in more than 40 spectra acquired on a SOFC segmented cell. In this set-up the active area is segmented in several small electrically insulated measurement points, namely segments, in addition to a main segment, to acquire measurements of local current-voltage characteristics, gas composition and temperature with repeatability and reduced experimental costs. For the sake of completeness, it is worth nothing that as far as the shape of the spectra concerns, the objective is to achieve a good quality of the ECM fitting, without accounting for the actual operations or the configurations of the SOFCs

under measurement.

An example of EIS spectra used for ECM parameters identification is reported in Figure 2.18, where six EIS spectra have been acquired and provided by HTCeramix S.A. (HTC) in the framework of the EU project SOSLeM at different operating current levels, ranging from 2 A to 8 A.

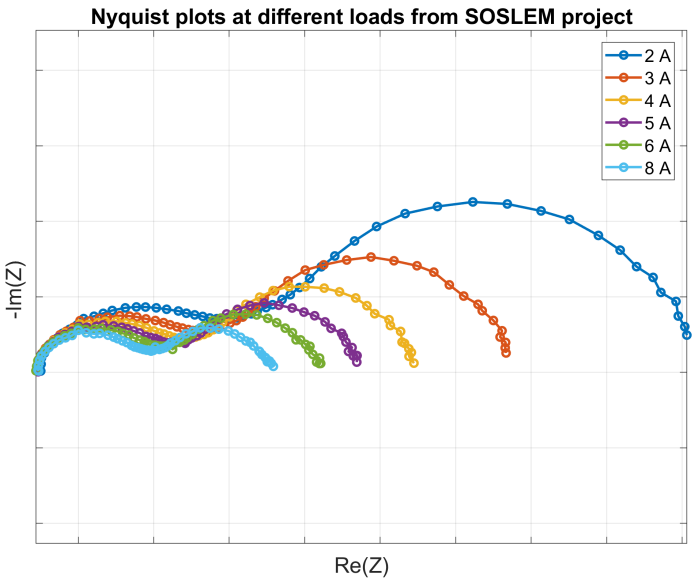


**Figure 2.18:** Example of EIS spectra used for MGFG identification algorithm performance assessment and validation. These spectra have been acquired within the EU project SOSLeM and provided by HTC for the specific purpose.

It can be immediately observed that the spectra present two visible arcs at varying current levels with a reducing area when current rises. Moreover, the real axis intercept at high frequencies (left side of the spectra) seems not to change at different operating conditions. From this analysis it is expected a change in the identified parameters which should vary consistently with shape changes in the spectra.

The results of the fitting process of the EIS spectra are presented in Figure 2.19 for all investigated currents. It can be observed that all spectra are correctly simulated by the ECM identified model (with the

structure shown in Figure 2.8 ).

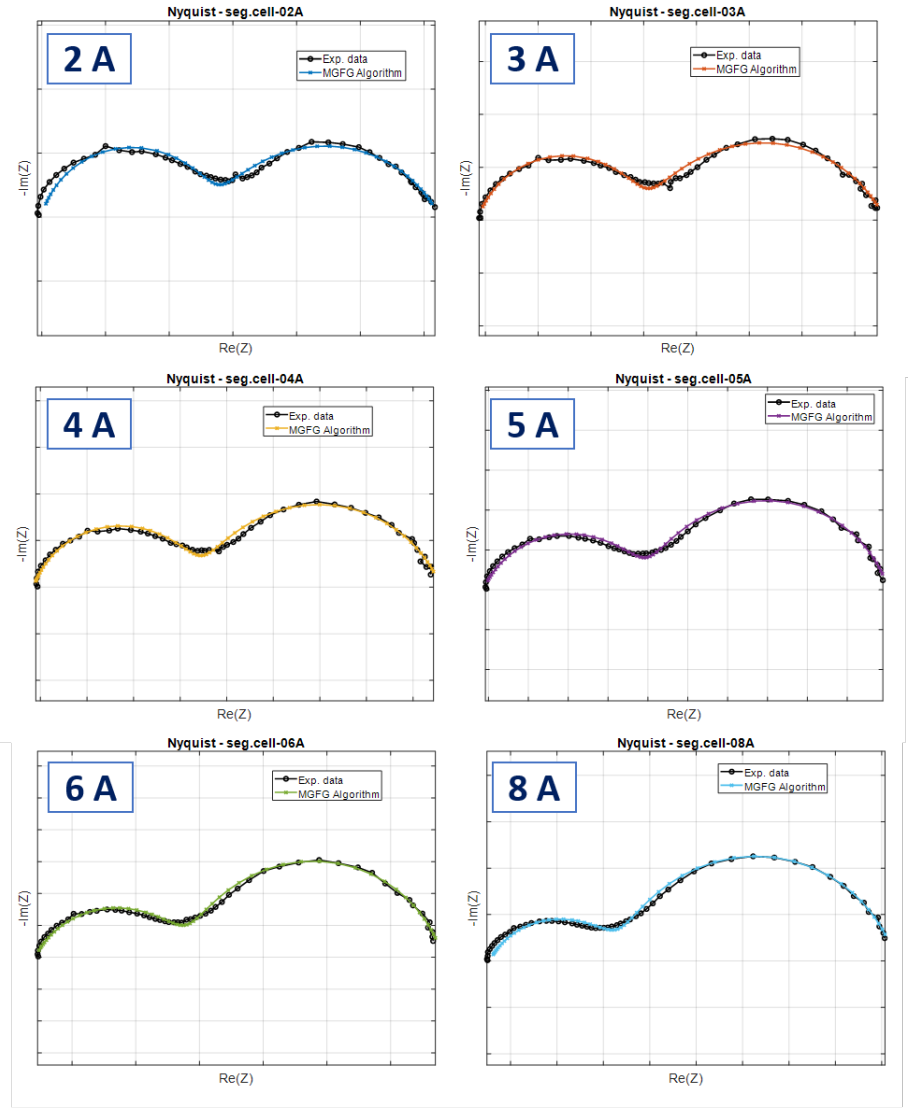


**Figure 2.19:** Results of ECM fitting on the EIS spectra provided by the EU SOSLeM project - Nyquist plots.

The same considerations can be done for the Bode representation of the aforementioned dataset, as shown in Figure 2.20

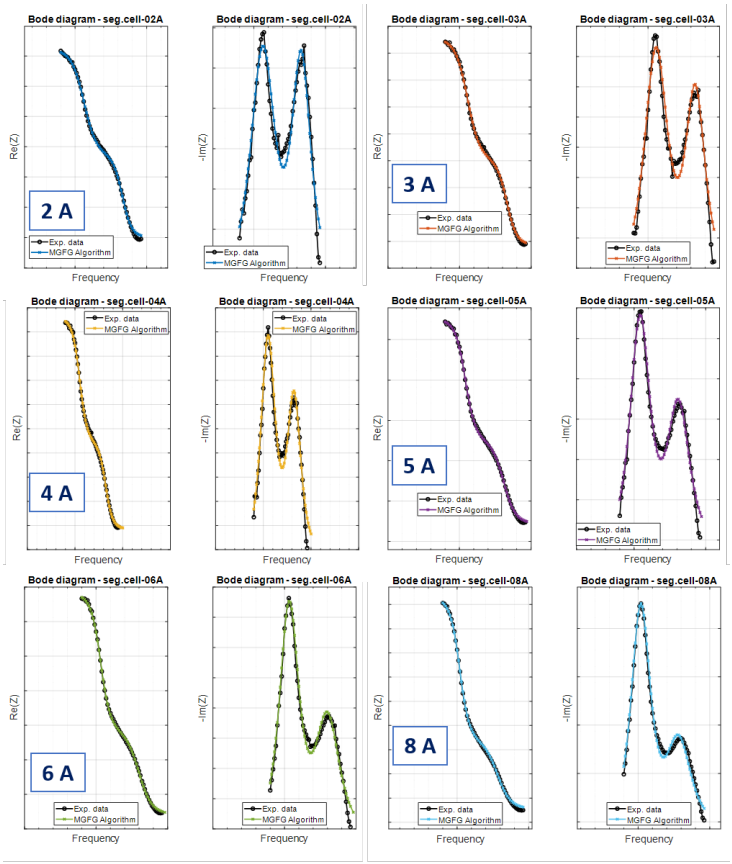


**Figure 2.20:** Results of ECM fitting on the EIS spectra provided by the EU SOSLeM project - Bode Diagrams.

Again, the algorithm was applied to several measurements performed on segmented cells operated at HTc facilities for different temperature, fuel flows and loads, as shown in Figure 2.21. The figures confirm the consistency of the results obtained by applying the algorithm with respect to different EIS shapes measured. For sake of simplicity, some spectra have been shown in figure 2.21.

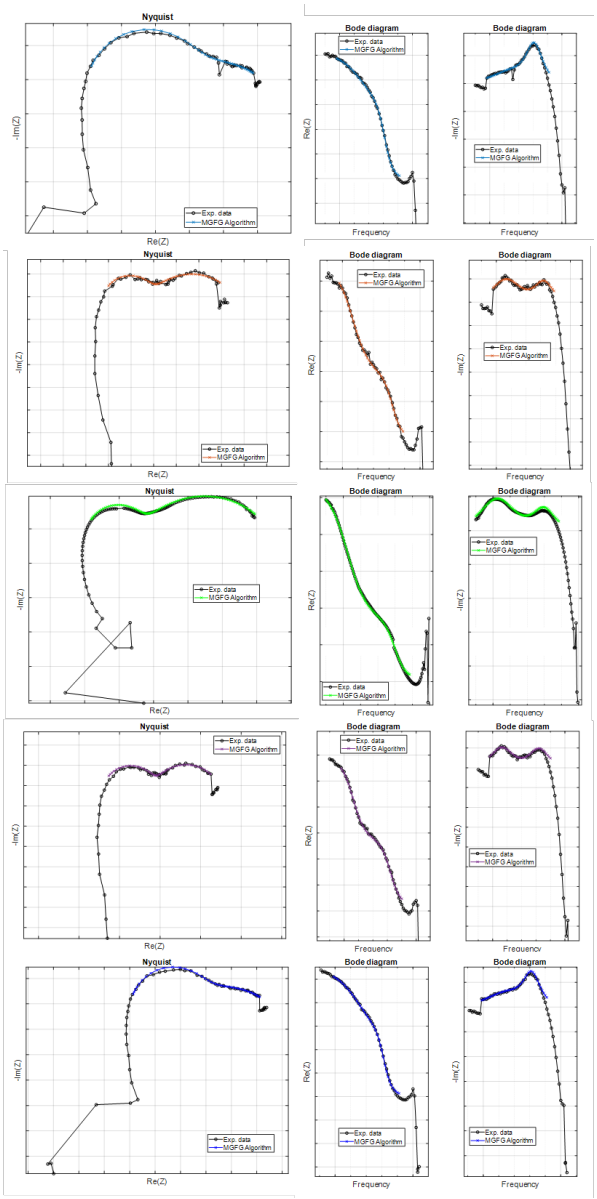


**Figure 2.21:** Results of ECM fitting on the EIS spectra provided by the EU SOSLeM project - exemplary measurements

It is interesting to add a comment on the shape of the spectra of figure 2.21. All the measurements suffer from an inductive effect due to the cabling, which implies the need of a $L$ element in the ECM; however, this effect does not sensibly change the shape for $Im_Z \leq 0$ (i.e., on the upper side of the real-axis), which is clearly recognizable via one or two RQ elements. Some outliers need to be clearly neglected to have a smooth shape of the two arcs. Nevertheless, the algorithm provides a good fitting with an increasing error/divergence at the edges of the spectra, where the measurements are highly affected by a not physical behaviour.

Finally, even in this case, the Montecarlo analysis, already introduced in section 2.2.2, has been performed on a single spectrum taken from SOSLEM database instead of a simulated one. Again, this analysis allows checking the variability of the results with respect to the change of the initial values of the 9 model parameters selected by the geometrical approach. The results are reported in Figure 2.22, where the circuit is sketched along with the Nyquist and Bode plots.

Here two visible arcs are seen with an inductive effect that causes a sensible distortion in the high frequency arc of the spectrum. Indeed, the inductance is not the theoretical one described as a straight line parallel to the Imaginary axes; here some non linearities let the high frequency arc to move with the inductance, like a weight hanging from the high frequency region.

This is further highlighted by the Bode diagram $f/Re_Z$, where at high frequencies the shape is not the expected one (usually that diagram should have an horizontal asymptote at both low and high frequencies). Moreover is interesting to note how the two peaks are well defined in the Bode diagram $f/-Im_Z$. The Nyquist plot shows how the two arcs have similar sizes, this allows having a flat shape at middle frequencies.

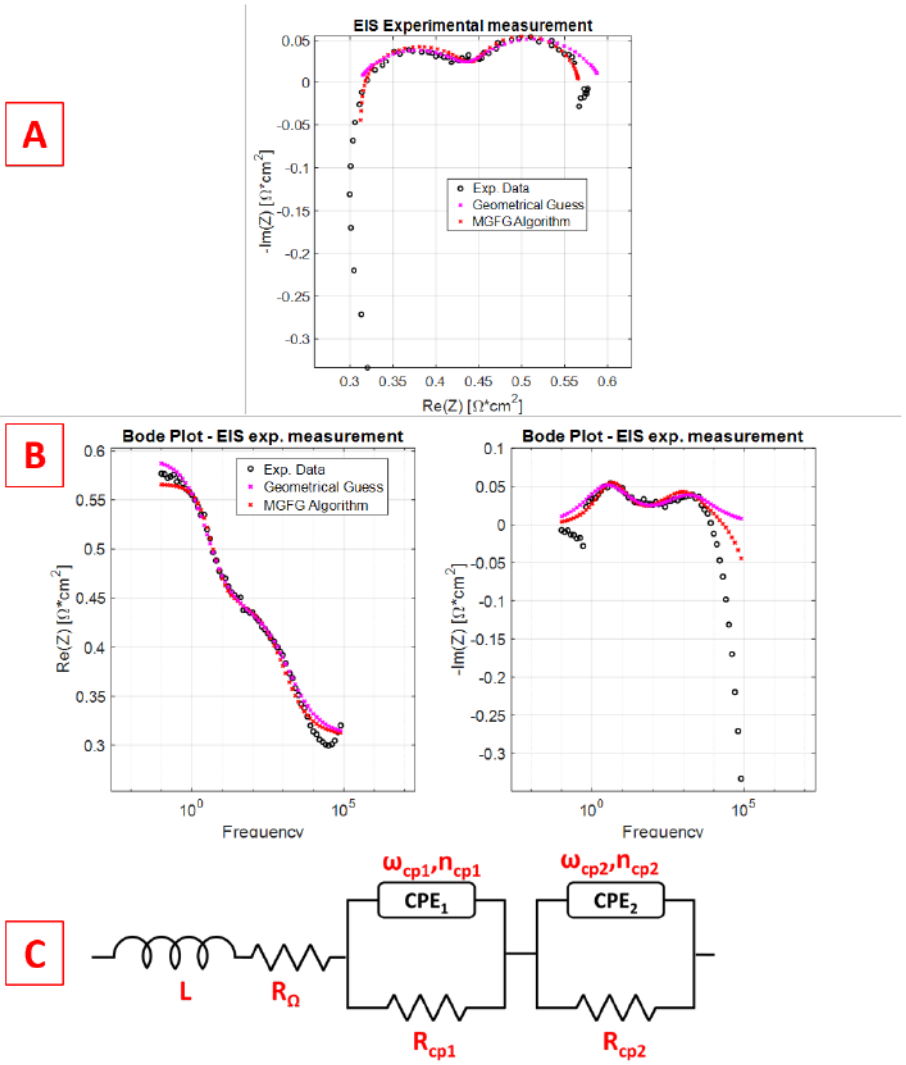


**Figure 2.22:** MGFG algorithm test on a measured spectrum provided by SOSLEM project on segmented SOFC cell. A) shows the Nyquist plot, B) the Bode diagrams whereas in C) the identified ECM is sketched. Here, the black markers are the measured spectrum, input of the algorithm, the pink circles are the initial geometrical guess and the red ones are the final identification achieved.

The EIS measurement was performed on a segmented SOFC cell after 7000h of operation, whose anode was fed by a mixture of dry $60\%H_2 - 40\%N_2$ while the cathode was fed with air at $750°C$. Figures 2.23, 2.24 and 2.25 show the effect of the $\pm 30\%$ changing of the $R_{cp1}$, $\omega_{cp1}$ and $n_{cp1}$ respectively. For the sake of conciseness, only the results of the Montecarlo analysis performed on these three parameters are reported. This three figures reported below show the 9 identified parameters values upon the EIS measurement ( in figure $* A$ ). Moreover figure $* B$ shows the variability of the identification for each parameter (the $R_0$ is neglected since it is directly evaluated on the spectrum) due to $\pm 30\%$ variation of the chosen element (highlighted in red) in the initial condition (i.e., the result of the geometrical approach and before the minimization). The overall fitting error is then presented in figure $* C$.

A

| | $R_0$ [Ω/cm²] | $L_0$ [Ω/cm²] | $R_{cp1}$ [Ω/cm²] | $\omega_{cp1}$ [Hz] | $n_{cp1}$ [/] | $R_{cp2}$ [Ω/cm²] | $\omega_{cp2}$ [Hz] | $n_{cp2}$ [/] | $R_{TOT}$ [Ω/cm²] |
|---|---|---|---|---|---|---|---|---|---|
| **Identified** | **0.309** | **1 e-7** | **0.137** | **6675,8** | **0.710** | **0.119** | **28,164** | **0.92** | **0.565** |

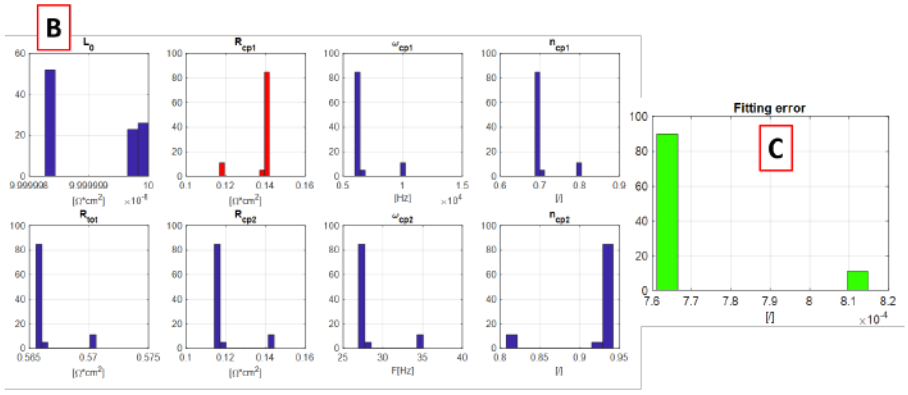


**Figure 2.23:** Montecarlo analysis - measured spectrum. $\pm 30\%$ variation of the $R_{cp1}$ parameter (red highlighted) in the geometrical initial guess. The Table A) shows the identified values of the ECM parameters; the bar-plots in B) present the effect on the identified parameters of the variation in the initial condition of the defined one (in red). The green bars in C) are the related fitting errors for the 100 tests performed.

A

| | $R_0$ [Ω/cm²] | $L_0$ [Ω/cm²] | $R_{cp1}$ [Ω/cm²] | $\omega_{cp1}$ [Hz] | $n_{cp1}$ [/] | $R_{cp2}$ [Ω/cm²] | $\omega_{cp2}$ [Hz] | $n_{cp2}$ [/] | $R_{TOT}$ [Ω/cm²] |
|---|---|---|---|---|---|---|---|---|---|
| **Identified** | 0.309 | 1 e-7 | 0.137 | 6675,8 | 0.710 | 0.119 | 28,164 | 0.92 | 0.565 |

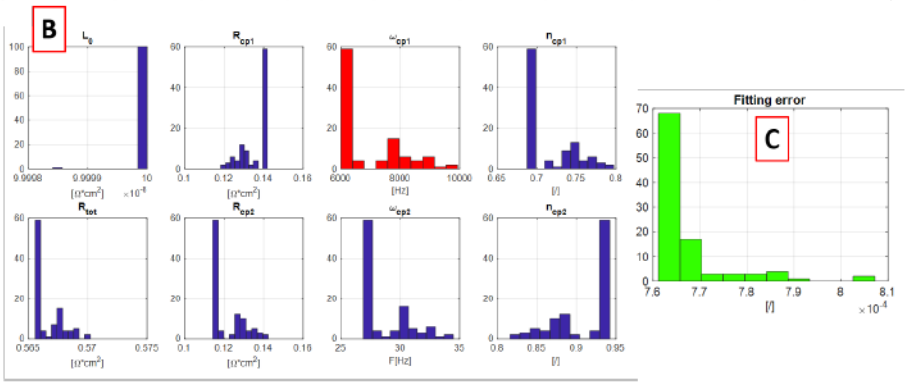


**Figure 2.24:** Montecarlo analysis - measured spectrum. ±30% variation of the $\omega_{cp1}$ parameter (red highlighted) in the geometrical initial guess. The Table A) shows the identified values of the ECM parameters; the bar-plots in B) present the effect on the identified parameters of the variation in the initial condition of the defined one (in red). The green bars in C) are the related fitting errors for the 100 tests performed.

A

| | $R_0$ [Ω/cm²] | $L_0$ [Ω/cm²] | $R_{cp1}$ [Ω/cm²] | $\omega_{cp1}$ [Hz] | $n_{cp1}$ [/] | $R_{cp2}$ [Ω/cm²] | $\omega_{cp2}$ [Hz] | $n_{cp2}$ [/] | $R_{TOT}$ [Ω/cm²] |
|---|---|---|---|---|---|---|---|---|---|
| **Identified** | 0.309 | 1 e-7 | 0.137 | 6675,8 | 0.710 | 0.119 | 28,164 | 0.92 | 0.565 |

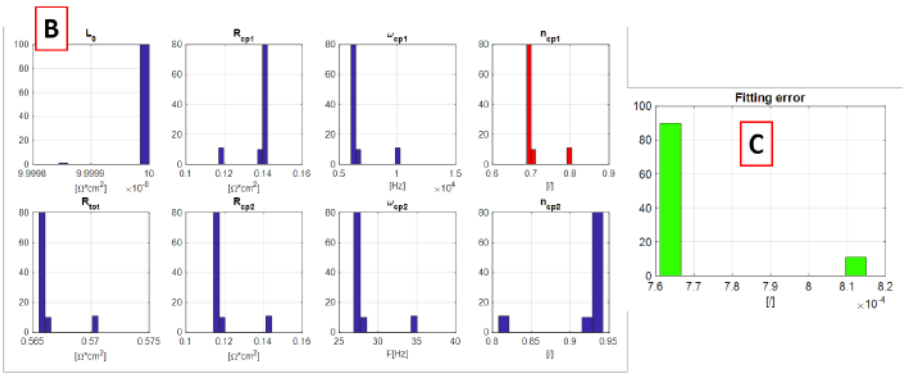


**Figure 2.25:** Montecarlo analysis - measured spectrum. ±30% variation of the $n_{cp1}$ parameter (red highlighted) in the geometrical initial guess. The Table A) shows the identified values of the ECM parameters; the bar-plots in B) present the effect on the identified parameters of the variation in the initial condition of the defined one (in red). The green bars in C) are the related fitting errors for the 100 tests performed.

The variability of the three circuital parameters have a very reduced effect on the overall fitting error, which varies between $7.6 \cdot 10^{-4}$ and $8.1 \cdot 10^{-4}$. It is worth noting that the identified values of $\omega_{cp1}$ exhibit a small change within that range; this behaviour is opposite to the one found for the simulated case (see Figure 2.15).

At end of this analysis, a positive comment on the reliability of the algorithm can be made. Indeed, it has been shown its capability to successfully perform even in case of experimental raw data; its intrinsic uncertainties does not affect the convergence of the identification procedures towards a unique solution in a bounded interval. The Figure 2.26 reports the variability of fitting errors when the Montecarlo procedure is applied to each single parameter.

| | $R_0$ [Ω/cm²] | $L_0$ [Ω/cm²] | $R_{cp1}$ [Ω/cm²] | $\omega_{cp1}$ [Hz] | $n_{cp1}$ [/] | $R_{cp2}$ [Ω/cm²] | $\omega_{cp2}$ [Hz] | $n_{cp2}$ [/] | $R_{TOT}$ [Ω/cm²] |
|---|---|---|---|---|---|---|---|---|---|
| Identified | 0.309 | 1 e-7 | 0.137 | 6675,8 | 0.710 | 0.119 | 28,164 | 0.92 | 0.565 |

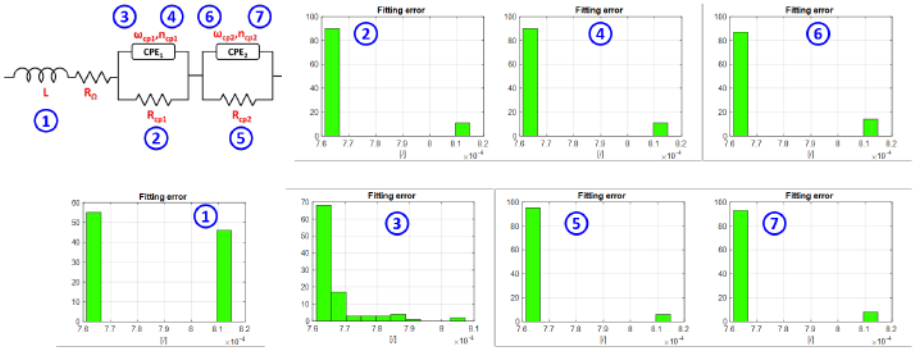


**Figure 2.26:** Montecarlo analysis - measured spectrum. Comparison of the 9 fitting errors related to the change of the 9 ECM parameters chosen.

In summary, thanks to the completeness of the dataset provided by the SOSleM project, the development of the fitting algorithm was successfully achieved. Indeed, several EIS curves were used to tune the geometrical initial conditions to reproduce different spectrum shapes and extracting relevant metrics (i.e. ECM parameters). Afterwards, the algorithm has been tested on a set of both nominal and faulty data available within the INSIGHT project. This activity led to the final algorithm, which has been used as the basis for the diagnostic features extraction as shown in chapter 3.

### 2.2.4 Testing

The MGFG algorithm has been applied to different SOFC set-ups provided by SOLIDPower within the EU-funded project INSIGHT: *i)* single element of a segmented cell, whose experimental tests were performed by EPFL, *ii)* single cells, tested by DTU and CEA, and *iii)* full stack (64 cells), tested by VTT.

For the single cell tests, two different stimuli were used as perturbation, which are a conventional sinusoidal stimulus and a Pseudo Random Binary Signal (PRBS) one; the former set of experiments were performed by DTU, whereas the latter by CEA.

- **Segmented Cells**
  The algorithm has been applied to a preliminary Fuel Starvation test provided by EPFL on SOFC segmented cells and the results on SEG10 are shown in Figure 2.27. The experiments have been carried out for three different values of fuel utilization (i.e., 0.85, 0.90, 0.95) at the beginning and at end of a test completed in a time interval of roughly one day. In this case, the MGFG algorithm output consists in an ECM made of two R/Q elements and an inductance (both blue and green highlighted elements shown in Figure 2.8). In the Figure the upper set of plot refers to the beginning (with the tag *"b"*), while the lower one (with the tag *"e"*) is the ending of the test. For further details about the structure of the segmented cells, the reader is addressed to [182]. Overall, the algorithm well fits the experimental data, though a slight discrepancy is found mainly at high frequencies; here the inductive behaviour due to the cabling may affect the shape of the spectrum. It is well-know that the inductance is mainly related to the wires and it is not representative of the State of Health of the cell, as suggested in [184]. Therefore, though the shape derived from the identified ECM is not accurate enough in the high frequency region, the identified parameters still can be reliably used for the monitoring of the fuel cell status and then applicable for FDI purposes. It is worth commenting that the shape of the low frequency arc region increases with the fuel utilization, and results are very similar for *"b"* and *"e"*.

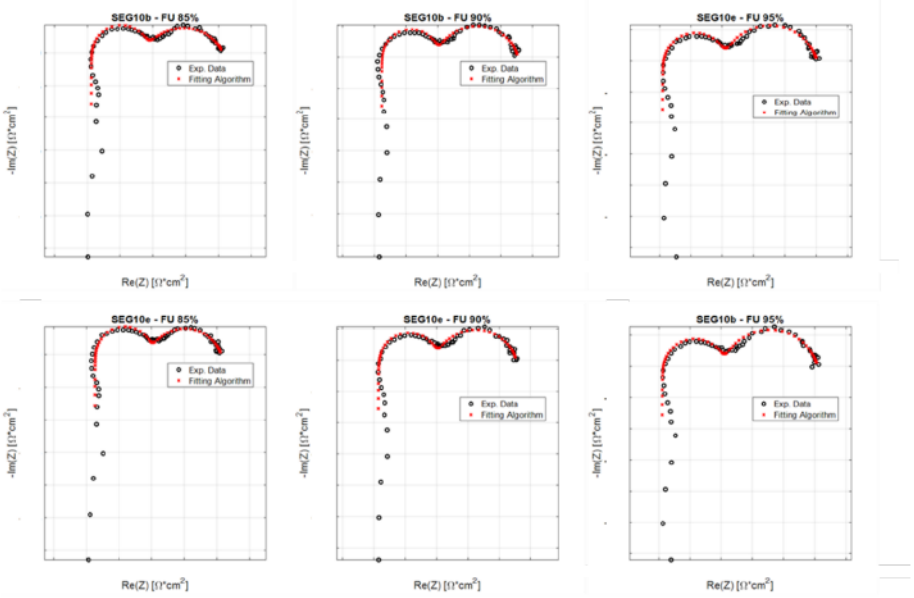


**Figure 2.27:** MGFG algorithm testing on a SOFC segmented cell. EPFL SEG10 Fuel Starvation test. Here the tag "b" stands for "beginning" while the tag "e" is "ending".

- **Single cell – sinusoidal stimulus**
  The set of data provided by DTU on single cell were referred to some operating conditions generating carbon deposition. As shown in Figure 2.28 the algorithm achieves a successful fit of the spectrum. As described in [185], when carbon deposition occurs, a typical big high frequency arc is visible. Indeed, Chen et al. [42], state that the carbon could deposit on the triple phase boundaries (TPBs), stop the electrochemical reactions and, in turn, the fuel diffusion to the anode. Moreover, the increasing in the high frequency arc can be explained also with the decrease of anode conductivity, which could hinder the charge transfer process of the electrochemical reactions. The results for this case are shown in Figure 2.28 where two arcs are clearly distinguishable without a remarkable inductive effect. It is worth remarking that the EIS measurement was achieved by injecting a conventional sinusoidal stimulus superimposed on the constant current set point.

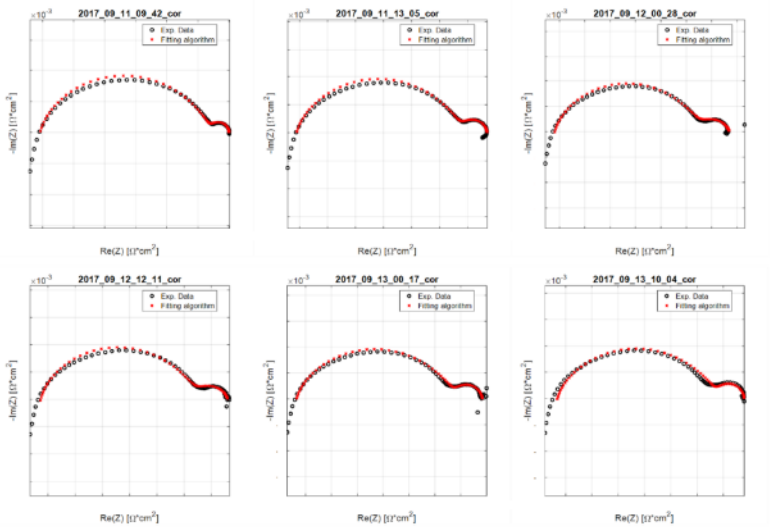


**Figure 2.28:** MGFG algorithm testing on a SOFC segmented cell. Preliminary Carbon Deposition tests on single cell performed by DTU.

- **Single cell – PRBS stimulus**
  The MGFG algorithm was applied to measurements performed by CEA on SOFC single cells with Pseudo Random Binary Signal (PRBS) stimulus at different time periods. In principle PRBS should guarantee an improved resolution of the impedance and an *"almost"* continuous spectrum (with an increased number of points derived from the stimulus) with respect to the conventional EIS measurement. Moreover, the approach results in a strong reduction of experimental time with an increase in the computational one for data treatment and spectrum extraction. More information about PRBS can be found in [186] and [187]. Thanks to the opportunity made available by the INSIGHT project experiments, the MGFG algorithm was tested also for PRBS-generated spectra allowing a further a check of its correctness even for non conventional EIS measurements. For the purpose of this analysis the algorithm was applied to some preliminary PRBS spectra and results are presented in Figure 2.29, where the algorithm proved to be reliable in the spectrum fitting, even though the raw data required a light

manipulation. Indeed, first a K-K test (black markers) has been applied to remove spurious points from the measurements, then the uncertainties found in the high frequency region are replaced with extrapolated data (blue circles). It is worth noting that the extrapolation identified a clear intersection with the Real-axis, which can help the identification of the parameters. Further comments are available in the next section. As described in [188], the CEA tests were performed on a 6-cells short stack, in which each Single cell was measured via impedance spectroscopy. The results presented show the fitting capability of the algorithm to match the different shapes of the cells, whose exemplary spectra are herein reported at different times of the experiment. It is worth commenting that the measurements present the not-closing low frequency arc due to the sensitivity of the instrument and to the highly-demanding time for the stimulus. Nevertheless, using PRBS excitation, the Kramers Kroning related analysis has removed some spurious points even at very low frequency, thus cutting a part of the arc.

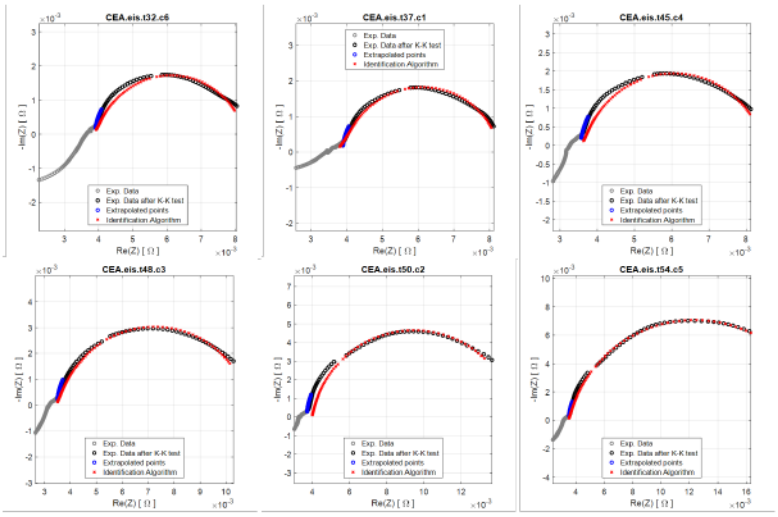


**Figure 2.29:** MGFG algorithm testing on a single cell by CEA. EIS measurement is performed via PRBS excitation and the so called *"Partial analysis"* was performed, as further described in the next paragraph.

- **Full stack**
  The algorithm has been applied to the EIS measurements on a 64-cells Stack tested by VTT at different Fuel utilization values and results are shown in Figure 2.30. Even in this case, the ECM automatically enabled from the algorithm is a double RQ-element (blue and green area of Figure 2.8). From the spectrum it is evident that the number of arcs is not directly correlated to the number of the circuital elements of the ECM. Indeed, the representative frequencies of the main phenomena occurring might have the same scale and, thus, it can result in an overlapping in the shape of the Nyquist plot.

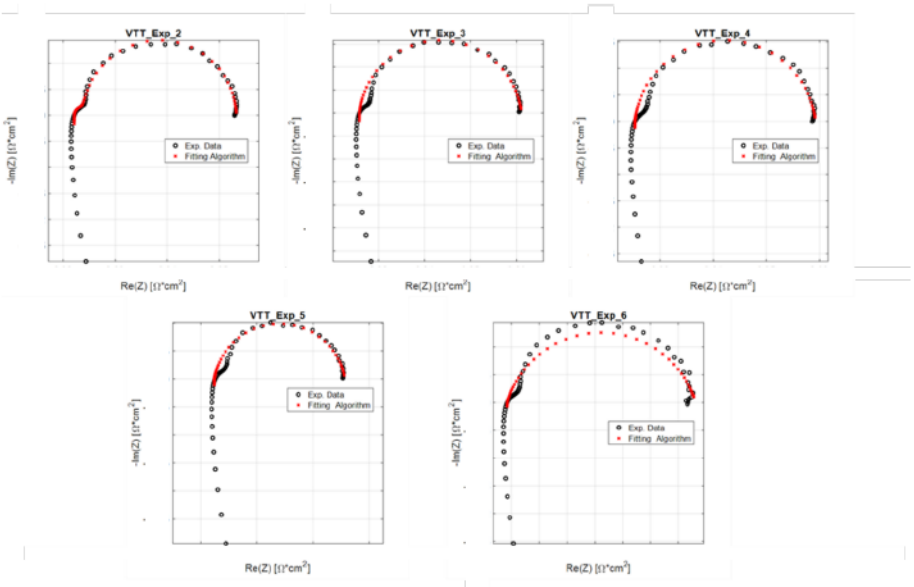


**Figure 2.30:** MGFG algorithm testing on a SOFC stack. VTT preliminary EIS data on SOFC Stack provided by SP.

## 2.3 The inductive problem and the *"Partial analysis"*

As for the experimental campaigns performed in the framework of the INSIGHT project, strong inductive effect affected several spectra at high frequencies. Indeed, the measurements performed by DTU and CEA on single cells present some not coherent behaviour at high frequency that hinder the right extraction of informations from the experiments. As a consequence, the high frequency part of the spectrum presents a shape that, in turn, could bias the diagnosis. Figure 2.31 shows two spectra acquired on a single cell by DTU and CEA, respectively. Both of them present a high inductive effect due to the cabling that clearly deforms the high frequency arc on the Nyquist plot. It results in an issue in the proper ECM selection, being this effect not related to the SOFC, but to the test bench. Usually, the most adopted solution is to neglect the not coherent part of the spectrum, which can be easily achieved by applying the Kramers-Kronig (K-K) technique ([158], [189]). However, the simple cut of not consistent part of the spectrum might result in a partial one that could not show the real-axis intercept at high frequencies, which could make difficult the ohmic resistance $R_{ohm}$ detection. Moreover, depending on the frequency defined by the K-K test, the identification algorithm can follow different arc shapes, especially when more phenomena occur in the same frequency range. This results in an issue in the right ECM selection, weakening the robustness and repeatability of the algorithm application as well. In the examples given in Figure 2.31 the high inductive effect causes a strong distortion in the shape of the spectra near its intercept with real axis. It could be easily argued that the use of ECM approach to reproduce such a shape can lead to a selection of both number and type of circuital elements, difficult to handle for a good representation of the phenomena behind. They, in turn, could not be related to the cell physics, thus making the ECM parameters not suitable for diagnostic purposes. In summary, the outcome of the overall identification procedure would generate a perfect fitting but a meaningless model.

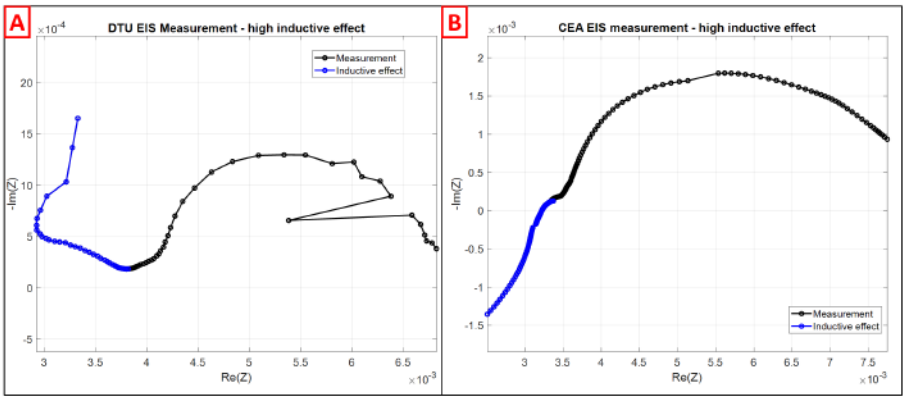


**Figure 2.31:** Inductive effect on two exemplary EIS measurements performed at two different test benches. A) is a EIS spectrum acquired by DTU on a cell of a 6-cells short stack; B) is a EIS spectrum acquired via PRBS stimulus at CEA labs on a cell of a similar short stack. Both spectra show an high inductive effect due to the cabling.

To avoid all these issues a different approach, named *"partial analysis"*, has been proposed in this work.

The objective is to provide a technique implementable on real systems, where the manual intervention is not possible, to achieve as much as possible reliable information also in case of strong side effects due to external factors that highly affects the measurement. This allows extracting useful, even though partial, information from a wrong measurement instead of completely discarding it.

It consists in isolating the low frequency arc from the spectrum, which is not affected by inductive phenomena. The frequency limit at which the spectrum is assumed unaffected by inductive-based distortion is defined through a K-K test. Afterwards, the ECM is identified at lower frequencies data, leading to the identification of an intercept, whose value can be interpreted as a resistance (called $R_{cut}$). For the aim of this analysis a spectrum measured on a VTT 64-cells SOFC stack operating at I = 29 A and T = $734°C$, with a reduced inductive distortion is sketched in Figure 2.32.

Then, the *"Partial analysis"* is applied to the low frequency part of the spectrum, whose fitting is shown in Figure 2.32 – *A)* along with the

identified parameters $R_{cut}$, $R_{LF}$ and $R_{TOT}$. The complete ECM identification analysis is then applied, leading to the fitting shown in Figure 2.32 – *B)*, where the main resistances $R_0$, $R_{HF}$,$R_{LF}$, $R_{Pol}$, and $R_{TOT}$ are shown as well. It is worth commenting that in the *"Partial analysis"* only one RQ element is selected instead of the two identified with the complete spectrum. However, the extracted parameters related to the low frequency arc are the same in both cases. On the other hand, the total amount of the information is limited with respect to the complete analysis; nevertheless, this kind of approach allows extracting information from a not-reliable measurement. In this approach, the $R_{cut}$ is a parameter in which the information relating high frequency behaviour are lumped, and its formulation is shown in the following equation:

$$R_{cut} = R_0 + \sum R_{HF} \tag{2.14}$$

It is worth noting that the information related to the ohmic resistance ($R_0$) cannot be split from the high frequency arc, thus limiting the study. The *"Partial analysis"* proved to be a valid approach, applicable both for low and high frequency part of the spectrum, particularly when something unexpected occurs during experiments and could highly affect the measurement. The only information needed is the frequency cut, at which the algorithm has to start the identification. This value can be given by the user via K-K test or found as the local minimum on the Nyquist spectrum.

It is worth remarking that if the *"Partial analysis"* is performed, the identified spectrum is expected to "close" at the $R_{cut}$ value. This means that the representation of the identified ECM intercepts the x-axis at $R_{cut}$ while the real measurement presents a different behaviour. However, this is expected, since the high frequency phenomena affect that region, making the spectrum to show some strange and not expected shapes.

As shown in Figure 2.32, the comparison of the *"Partial analysis"* with the complete approach returns the same values for the low frequency region (indeed, the spectrum was cut at a defined frequency). This supports the claim that the algorithm can be used even when the measurement is incomplete or highly biased.

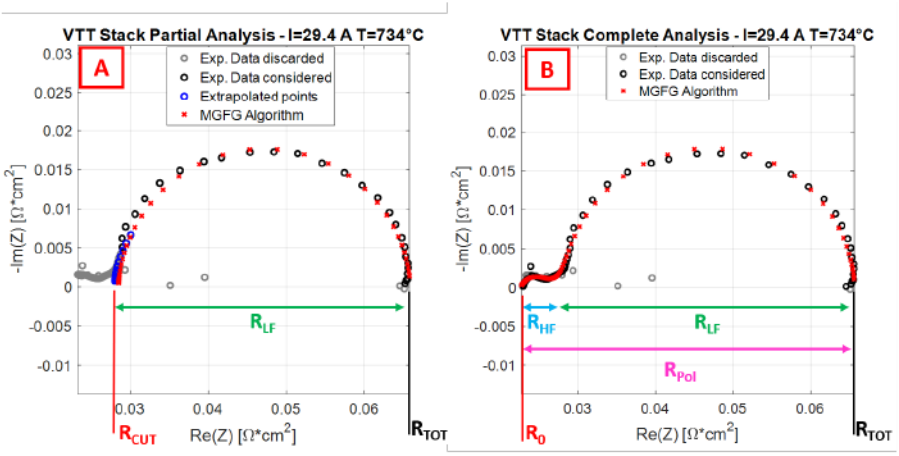


**Figure 2.32:** Comparison between partial (on the left-hand side – *A)*) and complete analysis (on the right-hand side – *B)*) of the spectrum and features extracted from data coming from VTT experimental campaign on a 64-cell SOFC stack. The Figure clearly shows how the *"Partial analysis"* provides the same parameters related to the low-frequency arc of the complete one, while at high frequency all the information are concentrated into the lumped parameter named $R_{cut}$.

## 2.4 Features extraction

To summarize, the MGFG, algorithm presented in this Chapter proved to be reliable after the testing on different SOFC set-ups and in case of two kind of EIS stimuli (sinusoidal and PRBS excitations). The algorithm, applied for the first time to the SOFC technologies, automatically adapts the ECM against the EIS data with no a priori knowledge. The list of all ECM parameters, which can be identified either via complete or *"Partial analysis"* is shown in Table 2.3.

They could be used as monitoring features, according to parameter-based diagnostic approach [99], [102] and exploited for the Fault Signature Matrix building process (see section 3.3.2); moreover, the parameters can also be exploited to set proper thresholds for the design of the diagnostic algorithm.

| Metric | Unit | Description |
|---|---|---|
| $R_0$ | $\Omega \cdot cm^2$ | Resistance related to the high frequency real intercept |
| $R_{cut}$ | $\Omega \cdot cm^2$ | Lumped resistance of the *"Partial analysis"* related to the high freq. behaviour |
| $R_{cp1}$ | $\Omega \cdot cm^2$ | Charge transfer resistance of the high frequency arc |
| $R_{cp2}$ | $\Omega \cdot cm^2$ | Charge transfer resistance of the low frequency arc |
| $R_w$ | $\Omega \cdot cm^2$ | Warburg element resistance |
| $\omega_w$ | $rad \cdot s^{-1}$ | Warburg element characteristic frequency |
| $n_{cp1}$ | - | CPE coefficient of the high frequency arc |
| $\omega_{cp1}$ | $rad \cdot s^{-1}$ | CPE characteristic frequency of the high frequency arc |
| $n_{cp2}$ | - | CPE coefficient of the low frequency arc |
| $\omega_{cp2}$ | $rad \cdot s^{-1}$ | CPE characteristic frequency of the low frequency arc |
| $R_{cpn}$ | $\Omega \cdot cm^2$ | Charge transfer resistance of the $n^{th}$ element (if enabled) |
| ... | ... | ... |
| $\omega_{cpn}$ | $rad \cdot s^{-1}$ | CPE characteristic frequency of the $n^{th}$ element (if enabled) |
| $n_{cpn}$ | - | CPE coefficient of the $n^{th}$ element (if enabled) |
| $R_{tot}$ | $\Omega \cdot cm^2$ | Total resistance of the spectrum |
| $R_{pol}$ | $\Omega \cdot cm^2$ | Polarization resistance (defined as $R_{tot}$ - $R_0$) |

**Table 2.3:** List of ECM parameters features (i.e., metrics) extracted from the MGFG algorithm

The obtained results show that the algorithm is able to identify the ECM parameters in a reduced time frame, that is less then 10 seconds for a model with 16 parameters if run on a laptop computer equipped with an Intel Quad Core i7 – 4700 HQ, 2.4 GHz. Moreover, the convergence of the identification process is guaranteed by the patented approach, which properly pre-selects the right values, as shown in section 2.2.1. This avoids the occurrence of errors and biases that can easily affect the results, when conventional optimization-based identification processes are implemented. The main issue found is linked to the inductive phenomena occurring at high frequencies. It is worth commenting that the inductive part of the spectrum is strictly correlated to the wires of the test bench and, in perspective, this issue should be carefully addressed when implementing the EIS-based monitoring and diagnostic tools on real systems.

Indeed, the inductive behaviour could hinder some state of health indicators of the instrumentation and not directly related to the stack. This information could be however considered during the monitoring to check for possible cabling faults. This entails a thorough and ad-hoc analysis to discriminate among several inductive effects caused by different wiring, configuration, size, materials, connections, etc.

# Chapter 3

# Fault Detection and Isolation

## 3.1 The Concept

This Chapter aims at providing a full description of the Fault Detection and Isolation (FDI) process performed via EIS-based features extracted through the MGFG algorithm.
The overall diagnostic scheme is represented in Figure 3.1. It should be distinguished between algorithm design and application. The former is performed offline (left side of the figure), while the latter entails online (i.e., on-board) application (right side of the figure).

The offline algorithm design involves three main steps. The first one corresponds to the proper parameter extraction under all the investigated operating conditions (i.e., both nominal and faulty). This process is thoroughly described in Chapter 2 and particularly in section 2.2. Then, once defined the reference value of each parameter in unfaulty operating conditions, a threshold for fault detection is set. Then, data from ad hoc faulty experiments, performed in the frame of the INSIGHT project, have been used to define the expected parameters trends and thresholds. The offline process ends with the building of the Fault Signature Matrix (FSM), which links the parameters to the investigated faults, through some variables, called symptoms (see Figure 2.2, [102]).

The online algorithm application involves three main steps. The first one consists in the parameter extraction from EIS spectra measured. The identified parameters are then compared to the thresholds (previ-

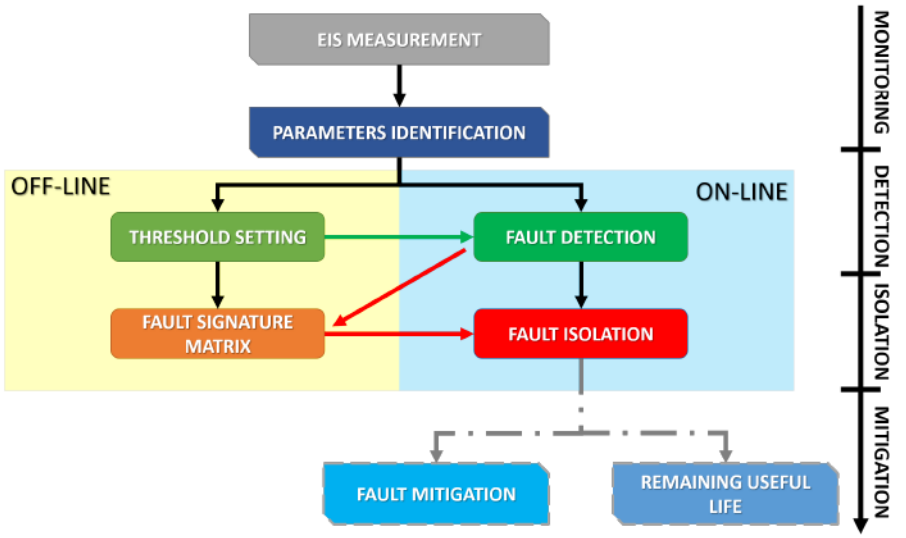


**Figure 3.1:** Schematic representation of the diagnostic algorithm design (offline) and online application (on-board).

ously defined offline) and the symptoms patterns are collected. Their matching with the FSM leads to the State of Health (SoH) assessment and the possible Fault isolation if one specific behaviour is monitored. In this case, a proper mitigation strategy can be further applied and the monitoring approach can be exploited to verify whether the countermeasure adopted could reach the mitigation goal (e.g., recovery, stabilization or other actions). Furthermore, the information extracted from the FDI algorithm might help in tuning a submodel to be integrated within a dynamic Fuel Cell model for remaining useful life (RUL) appraisal.

## 3.2 Experimental dataset

Towards the development of the Monitoring and Diagnostic Lifetime Tool (MDLT) to increase the reliability of Solid Oxide Fuel Cells, which is the main objective of the INSIGHT project, the material provided by the company SOLIDPower (SP) has been tested by project's partners listed below. Segmented Cells, Single Cells in Short Stacks and Full stacks were tested under different operations to infer on the nominal status and for fuel starvation detrimental conditions. The data were collected in a database built "ad hoc" and identified with the "tag" of the partner who performed the measurements as reported in the following list:

- **EPFL** segmented cell tested by EPFL. Here the active area was segmented in 20 small electrically insulated measurement points, namely segments, to acquire local measurements of local electrochemical characteristics [1]. EIS measurements were performed in the section referring to the inlet (SEG6), middle (SEG8) and outlet (SEG10) gas path within the cell. The conditions investigated are: nominal ones at OCV, fuel starvation test at variable F.U. from 80%, 85% and 90%. Particularly after each measurement at the specific F.U. level, the segmented cell is always put in OCV to measure the overall system state; so as to have a measurement under load and at OCV for each condition, alternatively. More details on the EPFL segmented cell set-up can be found in [190].

- **DTU** 6-cells short stack tested by DTU. EIS measurements were performed along with conventional measurements (used for the development of the lumped model as described in Chapter 4). The conditions investigated are three: nominal conditions at different current values (from 8A to 40A) – namely "characterization" tests – to monitor the change in the stack/cell parameters at different loads , nominal condition (reference: 32 A - F.U. 77%) kept constant for a defined time-period – namely "durability" tests – to

[1] For more details about the segmented cell set-up, the reader is addressed to the INSIGHT Website *http://insight-project.eu/* and specifically to *https://projectnetboard.absiskey.com/viewdocument/ec22a5-e6db53-749d78-013beb-000134* (Last access: 2020-05-01).

check the stack/cell behaviour over time and to restore the nominal condition after the imposed malfunctioning; two fuel starvation test, with a F.U. stepwise increase from 77% to 93% performed by lowering the $H_2$ flow rate (test n.1) and increasing the current (test n.2);

- **CEA** 6-cells short stack tested by CEA. EIS measurements were performed via Pseudo Random Binary Signal (instead of the sinusoidal one) for each cell, along with conventional measurements (used for the development of the lumped model as described in Chapter 4). The investigated conditions are: nominal conditions at 32 A - F.U. 77%; two fuel starvation tests, with a F.U. stepwise increase from 77% to 93% performed by lowering the $H_2$ flow rate (test n.1) and increasing the current (test n.2); a 2500 h long term "durability" test at nominal conditions;

- **VTT** 64-cells stack tested by VTT. EIS measurements were performed at the complete stack level, connected with the BoP. The conditions investigated are 30A with a F.U. from 67% (nominal) to 82%;

- **SP** 64-cells stack tested at SP facilities on a real-environment - On-Field Test. EIS measurements were performed directly on-board through a portable instrumentation designed by Bitron Company within the INSIGHT project. Two tests were performed. The first one at 25A, 2500 W - F.U. 62% (nominal condition) and a Fuel Starvation test with a stepwise increase from F.U. 62% to 72%. The second one was performed after a stack replacement, at 9.3 A, 1000 W - F.U. 60% (nominal condition) and a Fuel Starvation test with three F.U. levels, 60%, 65% and 72%.

The algorithm was applied to the above described experimental data to extract the features for the fuel starvation investigated at different magnitudes and for different set-ups. The identified features trends were used to build the FSM.

Figure 3.2 shows some EIS spectra on which the algorithm has been applied. Particularly, the first row (A) is dedicated to EPFL experimental campaign performed on a segmented cell, the second one contains

experimental data from DTU short stack (B). The third one presents the application of the algorithm on spectra derived from Pseudo Random Binary Signal (PRBS) stimulus performed during the experimental campaign at CEA labs on a 6-cells short stack (C), while the fourth one (D) is related to EIS measurements on the full stack at VTT lab. The last row (E) shows some spectra acquired on SP on-field real system with the measurement performed on-board. The algorithm performs a preliminary removal of non-coherent points, observed through cut-frequency analysis, highly influenced by inductive and non-linear effects. Then, an extrapolation routine models some extra points when needed to identify the intercepts on the real-axis of the Nyquist plot. Finally, the MGFG algorithm selects the equivalent circuit that best represents the spectrum and then identifies the significant features, according to the scheme presented in figure 2.7 of section 2.2

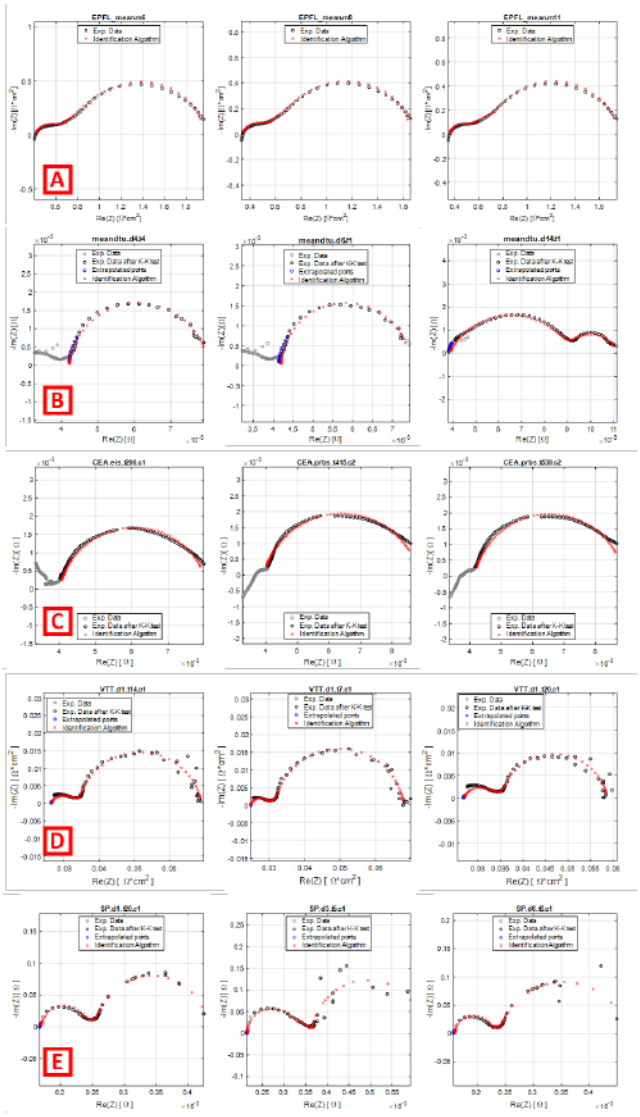


**Figure 3.2:** Application of the MGFG algorithm on the experimental data provided by INSIGHT partners: A) refers to EPFL experiments, B) refers to DTU ones, the third one (C) presents CEA experiments, and the D) to VTT measurements respectively. the last row (E) contains some spectra of the 64-cells stack tested in a real environment during the on-field test at SP facilities. It is worth remarking that the spectra herein presented are intended to show the applicability of such algorithm to different EIS shapes and different SOFC configurations.

For the purpose of the FDI tool development, two disjoint datasets where used. The first one allowed to define the thresholds and to fill the FSM. The second one was used to check the results of the tool. Particularly, the DTU dataset was used for the development of the diagnostic procedure to sort out a qualitative trend of the features at different fuel utilizations. Moreover, the thresholds for the nominal/faulty limits were extracted and the Fault Signature Matrix was built accordingly. Afterwards, the FDI approach has been applied to all the experimental data set provided by the partners for the validation. Moreover, other conditions but different from fuel starvation operations and the nominal ones have been analysed with the same approach. In this case, successful results were achieved, thus confirming the capability of the diagnostic tool to provide useful information on the SOFC State of Health.

## 3.3 Fuel Starvation

Fuel starvation is a very limiting factor of SOFC when power following manoeuvres are required. Indeed, during the operations, either stationary or transients, the current could electrochemically consume the fuel reactants more rapidly than the fuel provided, thus limiting the performance and causing a sharp decline in voltage with a related possibility to damage the cell [86].

The fuel starvation can be caused by different malfunctioning, and it is commonly considered as a fault itself, due to the detrimental effects that it causes on the cell performance.

Usually, when fuel starvation occurs during a real SOFC operation, an electrochemical oxidation of Ni in the anode can be caused by the strong increase in the polarization losses of the cell [88]. In turn, the starvation can be the effect of a strong anode re-oxidation or a leakage in the fuel pipeline, thus causing a detrimental chain reaction as well. It is thus important the early detection of any phenomenon/process that causes degradation to immediately counteract to recover from the performance losses. EIS provides information related to the electrochemical processes at stack level, so a change in the spectrum during an hydrogen depletion may occur.

Particularly, a fuel starvation effect is expected in the frequency range

in which the stack impedance is dominated by the gas concentration,with a frequency peak around 4-10 Hz (see Figure 2.4). Here the high dependence of the gas diffusion in the anode substrate is predominant [157]. Indeed, with respect to the nominal conditions the increase in the low frequency arc along with a shift of the low frequency peak toward lower values is then expected as a clear hint of fuel shortage.

### 3.3.1 Thresholds definition

The algorithm was applied to DTU and CEA 6-cells short stack measurements. Here, due to the strong influence of inductive effect seen on the test bench, the application of *"partial analysis"* approach was adopted. The thresholds setting was carried out to identify the two regions of the parameters' domain representing either nominal (i.e., unfaulty) or faulty operations. Therefore, the dataset was used to devise a trend in the parameters with respect to the fuel utilization levels.

Figure 3.3 shows the trend of the extracted features from the DTU dataset during different experiments: "characterization", "durability" and the two fuel starvation tests.

In figure 3.3 A), the resistances named $R_{cut}$, $R_{LF}$ and $R_{TOT}$ are shown along with the $\omega_{LF}$ in figure 3.3 B). The $n_{LF}$ has been found to have large oscillation which help in reproducing the shape of the plot, but it is not representative of the State of Health of the cell.

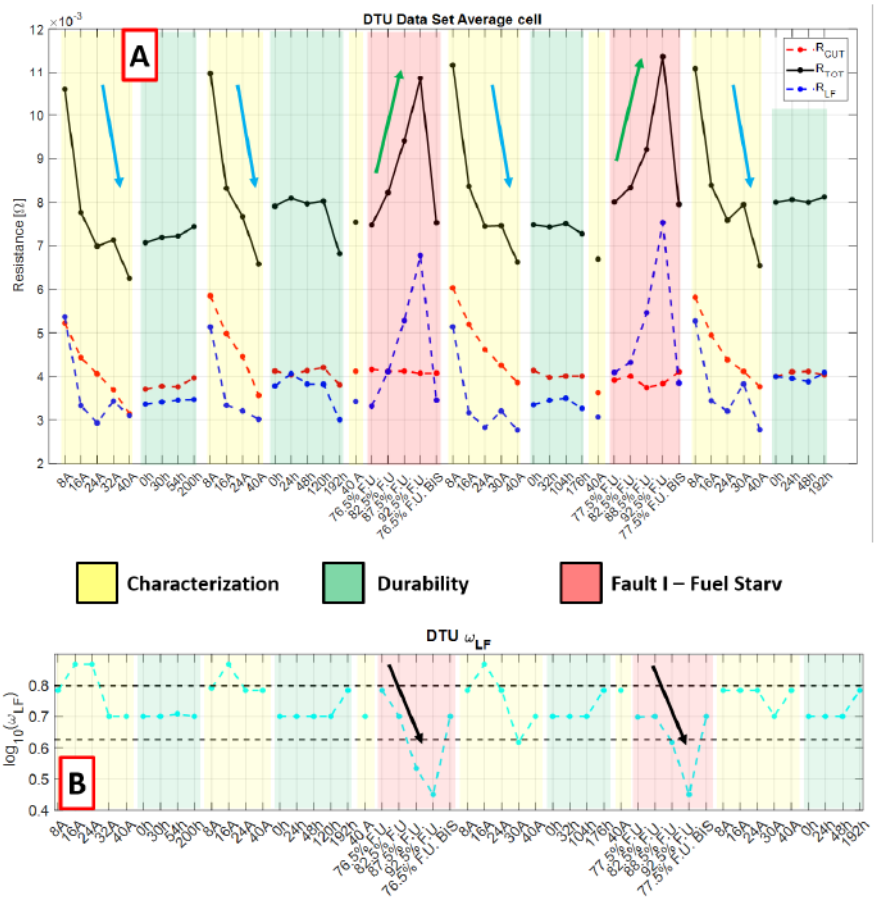


**Figure 3.3:** DTU experimental data – Average cell. Features extraction by means of the *"Partial analysis"* approach. A) shows the behaviour of $R_{cut}$, $R_{LF}$ and $R_{TOT}$, whereas B) reports the $\omega_{LF}$ one.

As aforementioned, the test protocol consisted in "characterization" and "durability" tests to identify the nominal condition, considered as reference and to investigate the ageing of the stack as well. Moreover, two Fuel Starvation tests have been performed in different conditions. The first one was caused by stepwise throttling of the fuel supply by 5%, with regular monitoring of each step, while the second simulation was caused by increasing the current during operation, while maintaining constant

fuel flow. The faulty tests have been followed by a "characterization" and "durability" phase to perform a slight recovery of the stack. Particularly, the former is a test at different loads (8A, 16A, 24 A, 32 A and 40A) at constant F.U. of 77% (i.e., un-faulty value), while the latter is constant operation in nominal condition (32 A, 77% F.U.) to let the stack recover from the imposed malfunctioning. Figure 3.4 shows the application of the MGFG algorithm via *"Partial analysis"* on the Fuel starvation test n.1. The experimental dataset (in the left side of the figure) are modelled through an ECM whose Nyquist plot is sketched on the right side. As expected from consideration based in 3.5, the low frequency arc area increases with the fuel utilization, leading to an increase of the $R_{LF}$. On the other hand, the high frequency part of the spectrum (lumped in $R_{cut}$ derived from the *"partial analysis"* approach) doesn't reflect any change while fuel utilization increases. In turn, the $R_{tot}$, being the sum of all resistance contribution and the ohmic resistance, increases according to the $R_{LF}$, since $\Delta R_{cut} \approx 0$. When considering the characteristic low frequency peaks of the circuital elements is interesting to note how the $\omega_{LF}$ moves toward lower values with the F.U. increase: the peak moves rightwards on the Nyquist plot.

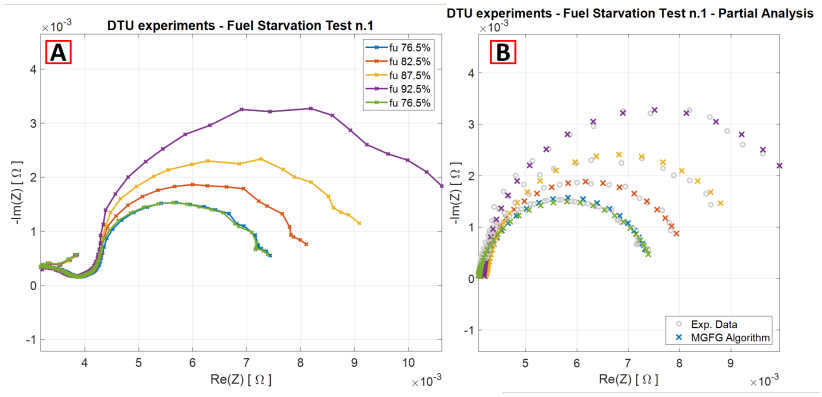


**Figure 3.4:** DTU experimental data – Fuel Starvation Test n.1. Raw data and features extraction by means of the *"Partial analysis"* approach. A) shows the increase in the low frequency arc of the Nyquist plot with the fuel utilization with a constant behaviour at high frequencies. B) shows the application of the MGFG algorithm with the *"Partial analysis"* approach

For sake of clarity an example of threshold definition has been reported in figure 3.5, which describes how the threshold on the $R_{LF}$ has been set. Here, the data have been normalized with respect to the average value that $R_{LF}$ assumes in the measured nominal conditions (blue markers). Defined the F.U. limit for unfaulty state at 85%, the closest measurement under starvation is at F.U. 87.5%. Consequently, the threshold for $R_{LF}$ has to be defined so as this measures must be beyond such threshold. Thus, considering the normalized value of the y-axis, the threshold is defined 1.4 times the nominal value (that is 1, being it normalized). In turn, assuming a symmetrical threshold, while the upper one is 140% of the reference value, the lower threshold is at 60% of the reference value as well.

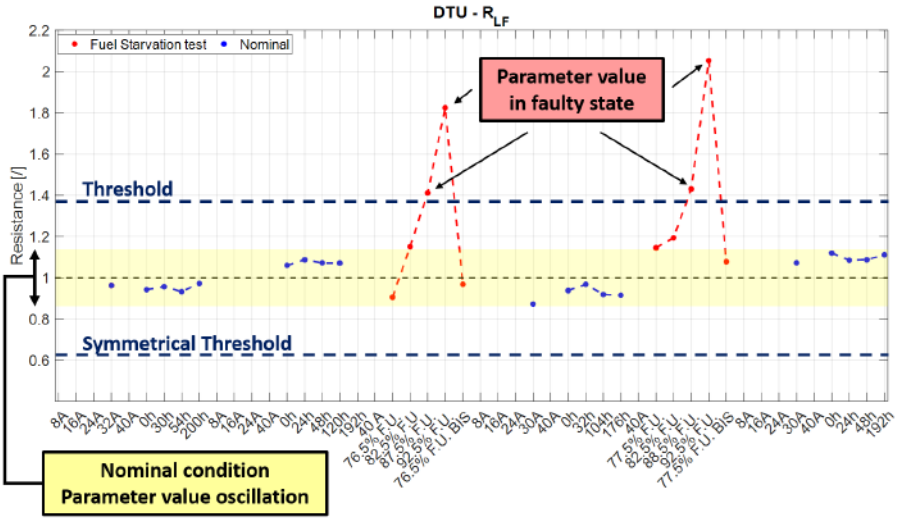


**Figure 3.5:** Threshold definition for the $R_{LF}$. the nominal conditions during both "characterization" and "durability" tests are reported in blue, whereas the fuel starvation test values are reported in red. The yellow area is the oscillation of the nominal values. Thus a symmetrical threshold is set upon a well defined parameter's value in faulty state.

Table 3.1 presents the thresholds defined for the characteristic features to monitor for the fuel starvation detection, defined upon DTU experimental evidences:

| Feature | Upper Threshold | Lower Threshold |
|---|---|---|
| $R_0$ | 110% | 90% |
| $R_{HF}$ | 120% | 80% |
| $\omega_H F$ | n/u | n/u |
| $R_{CUT}$ | 115% | 85% |
| $R_{LF}$ | 140% | 60% |
| $\omega_L F$ | 115% | 85% |
| $R_{POL}$ | 130% | 70% |
| $R_{TOT}$ | 120% | 80% |

**Table 3.1:** Thresholds definition for the extracted features. It is worth nothing that the threshold value is considered as the percentage with respect to the nominal (i.e., un-faulty) reference value.

The experimental tests performed by CEA were obtained by applying a similar test protocol as implemented by DTU. The measurements were performed of each cell of the 6-cells stack with PRBS excitation stimuli, and the reconstructed EIS spectra were analysed by MGFG algorithm through *"partial analysis"*. The Figure 3.6 shows the extracted parameters, namely $R_{cut}, R_{TOT}, R_{LF}$ as a function of time from the CEA dataset, during the fuel starvation test. Particularly, the fuel starvation test consists in a preliminary durability part with fixed nominal condition (32 A, 77% F.U.) followed by a fuel utilization stepwise increase up to 93% (starvation test n.1) by lowering the $H_2$ flow rate. Again a durability part is operated to have a recovery of the malfunctioning and a subsequent fuel utilization increase by changing the current is actuated (starvation test n.2). At the end of the fuel starvation test, a shut-down for $H_2$ shortage occurred. After the restart a 2500h durability test at the nominal condition is performed.

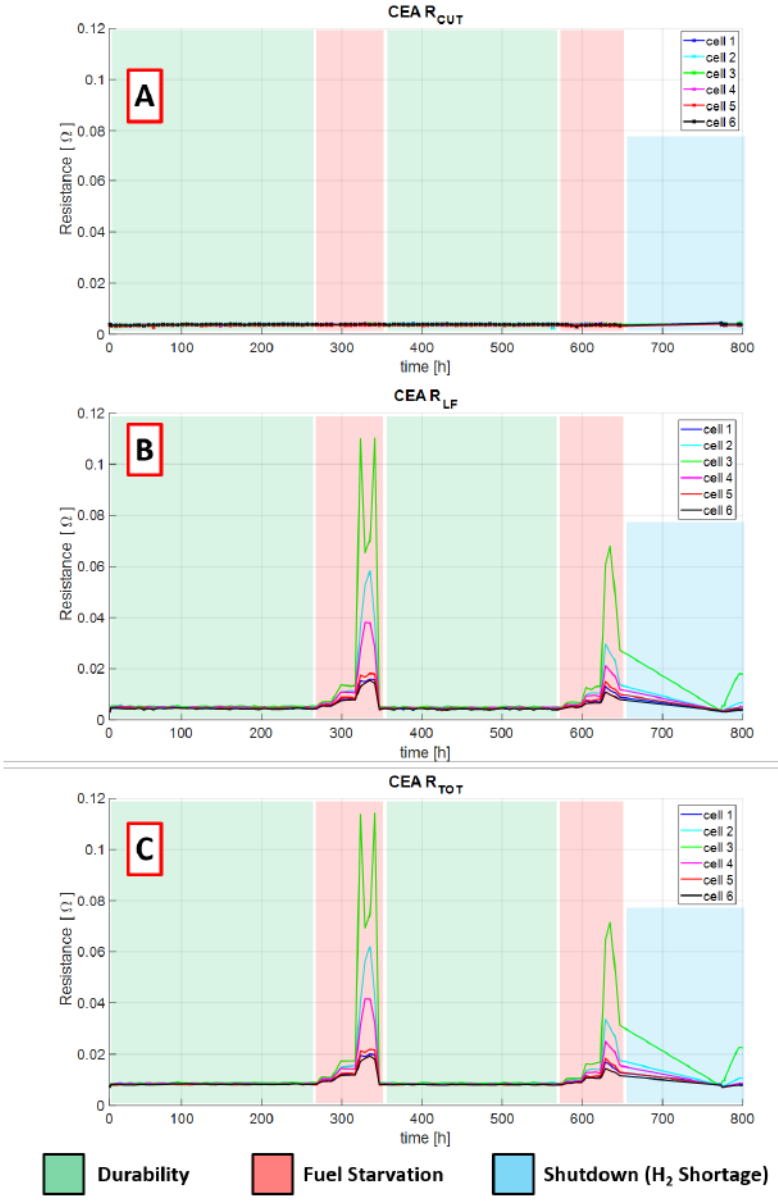


**Figure 3.6:** CEA experimental data – 6 cells. Features extraction by means of *"Partial analysis"* approach. The durability test (32 A 77% F.U.) is highlighted in green, the two starvation tests in red and the shut-down in blue.

It is worth commenting that while the $R_{cut}$ has a constant behaviour during both the durability and the fuel starvation tests, both $R_{LF}$ and $R_{TOT}$ values increase with the fuel utilization; this is a clear hint of how the fuel starvation affects the phenomena correlated to the low frequency part of the spectrum, thus resulting in a change in the related $R_{LF}$ and $R_{TOT}$ parameters.

### 3.3.2 Fault Signature Matrix

The Fault Signature Matrix has been thus completed by exploiting DTU experimental evidences. Table 3.2 shows the qualitative Matrix filled with symbols that represent the current FC status and adapted from the approach presented in [103], [92] and [191]. Indeed for the purpose of this work, instead of using 0 and 1 values, which represent unfaulty and faulty states respectively, the FSM values are completed by adding signs $+$, $-$, which account for the trends of the activated fault symptoms as well. The list below describes the meaning of the complete set of FSM symbols used:

- **"0"**: the feature does not sensibly change with respect to the fault magnitude;
- **"+1"**: the feature increases with respect to the fault magnitude;
- **"-1"**: the feature decreases with respect to the fault magnitude;
- **"n/u"**: the feature was not used because they could be either not relevant or not available for the analysis applied.

The fuel starvation row of the Fault signature matrix for a "complete analysis" could be easily derived from the one related to the "partial analysis" by considering the behaviour of the $R_{CUT}$ under that malfunctioning. Indeed, as shown in figures 3.3 A) and 3.6 A), the $R_{CUT}$ does not change with the fuel utilization. According to eq. 2.14, the $R_{CUT}$ is defined as the sum of the $R_0$ and all the resistances at high frequencies; therefore, it is possible to reach a constant value if both $R_0$ and $R_{HF}$ are constant or if their values balance, always resulting in a constant sum value. The former hypothesis is the most-likely one. Thus, during the fuel starvation, both $R_0$ and $R_{HF}$ are expected to be constant.

| | $R_0$ | $R_{cut}$ | $R_{HF}$ | $R_{LF}$ | $\omega_{HF}$ | $\omega_{LF}$ | $R_{pol}$ | $R_{TOT}$ | $HFArc_{Area}$ | $LFArc_{Area}$ |
|---|---|---|---|---|---|---|---|---|---|---|
| **Partial Analysis** | n/u | 0 | n/u | + | n/u | - | n/u | + | n/u | + |
| **Complete Analysis** | 0 | n/u | 0 | + | + | - | + | + | 0 | + |

**Table 3.2:** Qualitative Fault Signature Matrix for fuel starvation test

In order to activate the values of each symbols, the following logics is implemented:

$$\left\{\begin{array}{l} for \quad i = 1 : n \\ \\ \quad if \qquad r_i > r_{nom,i} \cdot T_i \\ \quad s_i = +1 \\ \\ \quad elseif \qquad r_i < r_{nom,i} \cdot (1 - T_i) \\ \quad s_i = -1 \\ \\ \quad elseif \qquad r_{nom,i} \cdot (1 - T_i) \leq r_i \leq r_{nom,i} \cdot T_i \\ \quad s = 0 \\ \quad end \\ \\ end \end{array}\right\} \tag{3.1}$$

where $r_i$ is the value of the "i-th" extracted feature, $r_{nom,i}$ is its nominal (i.e., reference) value previously identified upon experiments performed in the defined nominal conditions, whereas $s_i$ is the the symptom associated to such feature. It is worth remarking that the thresholds for all features ($T_i$) were defined as a percentage increase of the reference condition and set upon DTU experiments. This makes the diagnostic approach general and applicable to different set-ups.

The FSM is used during on-line monitoring to check possible changes in symptoms values. In order to perform a FDI process, the first step is to check whether the FC is in nominal conditions (i.e., a zeroes-vector). Then, if the symptom pattern matches one row of the FSM, the related fault is identified; otherwise a "general alarm" is activated.

It is worth to note that the main concerns in diagnostics are the occurrence of either false or missed alarms. The first case occurs when a faulty condition is detected while the system is operating in nominal conditions, the second one is the opposite instead. This may be ascribed

| | **Conventional measurements - Fuel Starvation** | | | |
|---|---|---|---|---|
| | **V** | **T** | $\Delta P$ | $V_{fluctuation}$ |
| **Cell** | -1 | +1 | n/u | +1 |

**Table 3.3:** Conventional measurements Fault Signature Matrix for fuel starvation test

to a limited number of symptoms or to a not reliable measurements set. An increase in redundancy in both symptoms and measurements might be beneficial for the reliability of the diagnostic approach. Moreover, because of the strong dependency of symptoms from experimental data, it is mandatory to give strong attention to the quality of the measurement itself. For example, unstable measurements near threshold value could give a misleading information on the FC status [102]. Two recommendations are suggested: extend the FSM with more monitoring variables if additional sensors are available; on the other hand the frequency of measurements should be improved when a possible fault is envisaged. The first can provide more information about the effects of the malfunctioning on the system with a trade-off between symptoms and costs, while the second one allows understanding the persistence of abnormal behaviour over time.

To increase the number of symptoms, the FSM can be extended by introducing conventional measurement-based ones, which are presented for the fuel starvation case in Table 3.3. Particularly, the voltage fluctuation is an interesting information derived from the tests performed that can give a qualitative hint of the fault as well [101]. This measurements could trigger the diagnostic procedure and perform the EIS.

To validate the approach summarized in this section, the diagnostic algorithm has been applied to the experimental dataset performed under induced fuel starvation operation, as described in the following section.

## 3.4 Detection & Isolation

Once defined the thresholds upon DTU experimental campaign, the validation of the diagnostic tool is carried out by using the experimental evidences derived from the application of the *"partial analysis"* on EPFL, CEA, and of the complete procedure on VTT and SP measurements.

1. **EPFL – segmented cell**

   For the validation of the EPFL segmented cell, the inlet, middle and outlet sections measurements values were averaged to limit the uncertainties caused by the non homogeneous distribution of the load, temperatures, fuel, etc. among the cell segments. It is worth remarking that the thresholds were set after DTU Starvation experiments of section 3.3.1.

   Figure 3.7 shows the monitored features extracted under malfunctioning operations and their values are compared against the threshold limits. The features are extracted via *"partial analysis"* and the symptoms are collected into the corresponding vector to be compared with the rows of the FSM for the fault isolation.

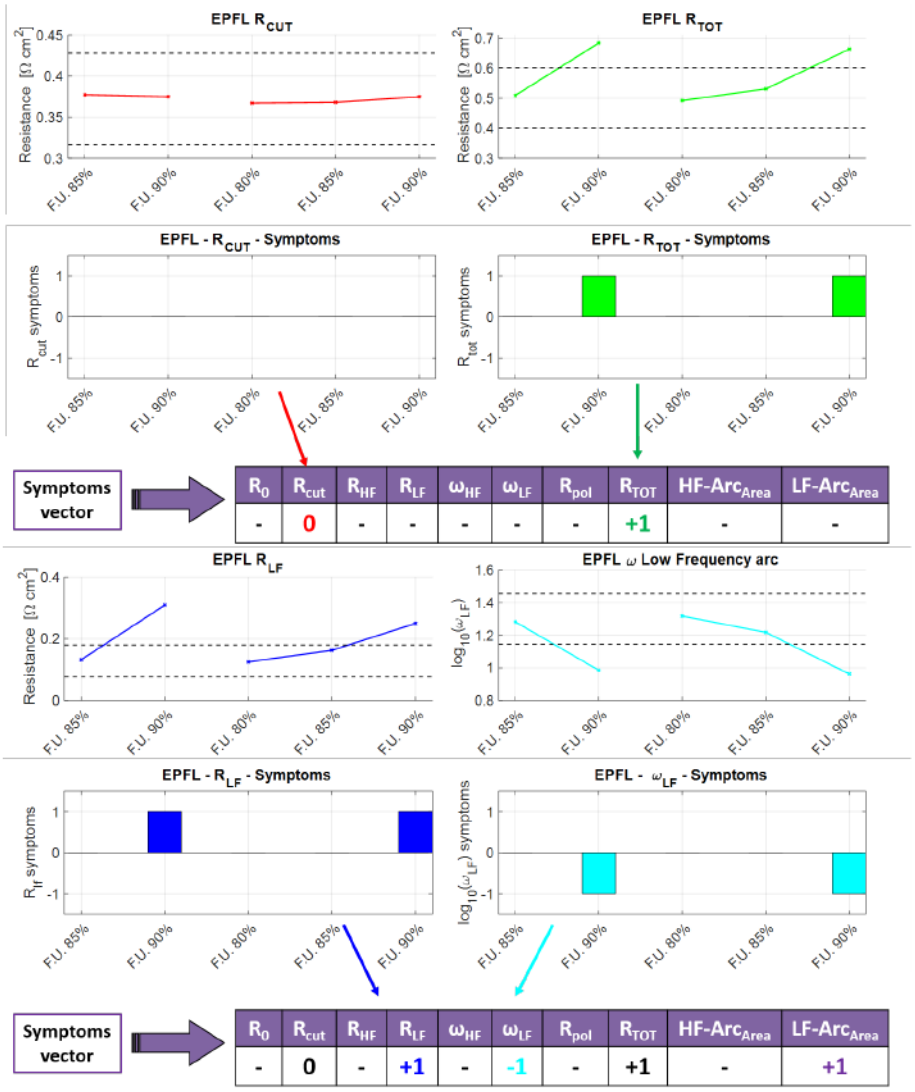


**Figure 3.7:** Validation - EPFL experimental Campaign - Segmented cells. The parameters deviations are collected into the symptoms vector.

It is interesting to note how the high frequency elements of the spectrum are not affected by the induced fault and the related symptoms (i.e., $R_{cut}$) do not change their values with respect to

the nominal behaviour, whereas the low frequency arc presents a sensible increase with the fuel utilization. Indeed, when the F.U. goes over 85% the $R_{LF}$ exceeds the threshold as well as the $R_{TOT}$. Moreover, the characteristic frequency peak of the low frequency arc moves towards lower values as the fuel utilization increases; this reflects in a rightward shift of the maximum of this arc in the Nyquist representation (see Figure 3.7) and in a change of the related symptom $s_{\omega_{LF}} = -1$.

Figure 3.7 shows the symptom pattern building by checking each feature with respect to its threshold.

The comparison of the symptoms vector with respect to the fuel starvation FSM row is then presented in Figure 3.8, to validate the detection (i.e, the change in some symptoms from 0 to $\pm 1$) and the isolation of the fault (i.e., the exact matching of the symptoms vector at high F.U. with the Fuel Starvation FSM row). Particularly, in figure 3.8 the relevant symptom patterns collected when the segmented cell is operated at $F.U. < 90\%$ (i.e., the Nominal state) and at $F.U. \geq 90\%$ (i.e., under fuel starvation) are compared with the defined fuel starvation row built in section 3.3.2. In case of fuel starvation the symptom pattern matches exactly the FSM, thus proving the successful isolation of the fault.

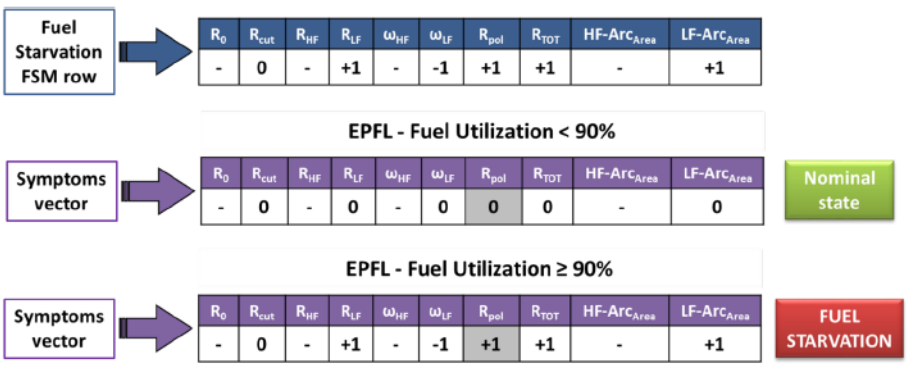


**Figure 3.8:** Validation - EPFL segmented cell. Detection and Isolation phase. Comparison of the symptoms vector in nominal and "faulty mode" with the Fuel Starvation FSM row.

It is worth recalling that the *"partial analysis"* does not allow identifying the Polarization resistance $R_{pol}$, since some information at high frequencies are lumped into $R_{cut}$. However, as justified by the eq. 3.2, if the $R_{cut}$ is constant and both $R_{LF}$ and $R_{TOT}$ increase, it could likely occur that $R_{pol}$ would increase as well. This reflects in a $R_{pol}$ with a related symptom "+1".

$$R_{pol} = R_{TOT} - R_0 = \sum R_{HF} + R_{LF} \approx R_{TOT} - R_{cut} \qquad (3.2)$$

Thus, for EPFL segmented cell (averaged), it is possible to state that the Fuel Starvation is clearly detected and isolated when the F.U. is higher than 90%. This high value of F.U. is justified for the segmented cell as described in [108] and [192].

2. **CEA – 6-cells short stack**
The CEA 6-cells short stack EIS measurements were performed via PRBS stimuli applied to each cell. Again, the thresholds were taken from the experiments performed by DTU as described in section 3.3.1. The nominal (i.e., reference) condition was set at 32 A, 77% F.U. and kept constant for about 300 h ("durability test" - green area); afterwards the two fuel starvation tests ("red-highlighted areas") were performed, separated by a further durability one to let the stack recover from the malfunctioning. At the end of the second starvation test, a shut-down occurred for $H_2$ shortage (Blue area). The remaining part of the experiments consisted in a long-term durability test ("green area") of about 3200 h; here further shut-down (blue areas) occurred.
Figure 3.9 and Figure 3.10 show the monitored features extracted under malfunctioning operations and their values are compared against the threshold limits. The features are extracted via *"partial analysis"* and the symptoms are collected into the corresponding vector to be compared with the rows of the FSM for the fault isolation.

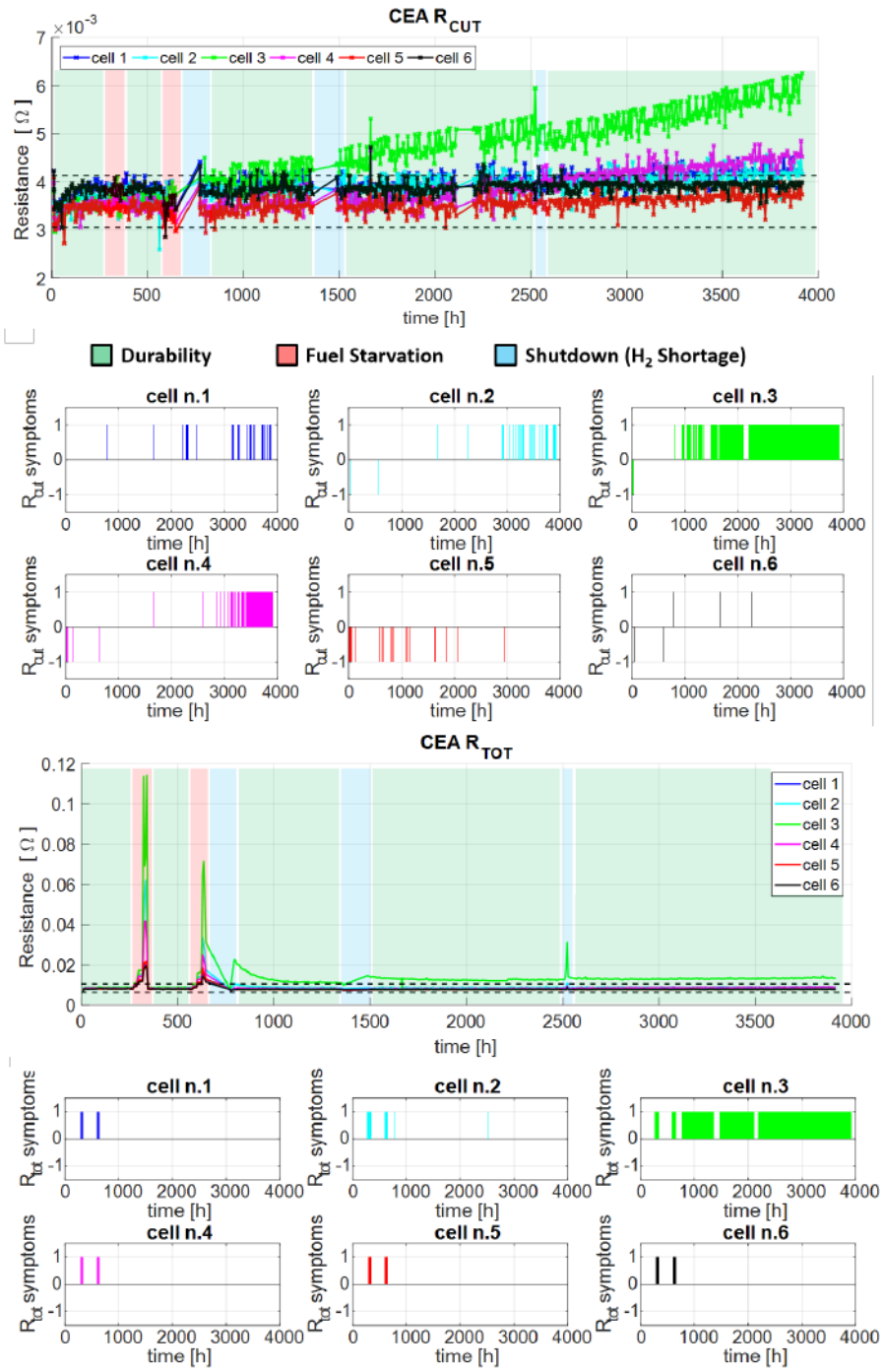


**Figure 3.9:** Validation - CEA experimental Campaign - 6 cells short stack. The features deviations of the 6 cells are collected into the symptoms vector. Here, the $R_{cut}$ and $R_{tot}$ trends are presented.

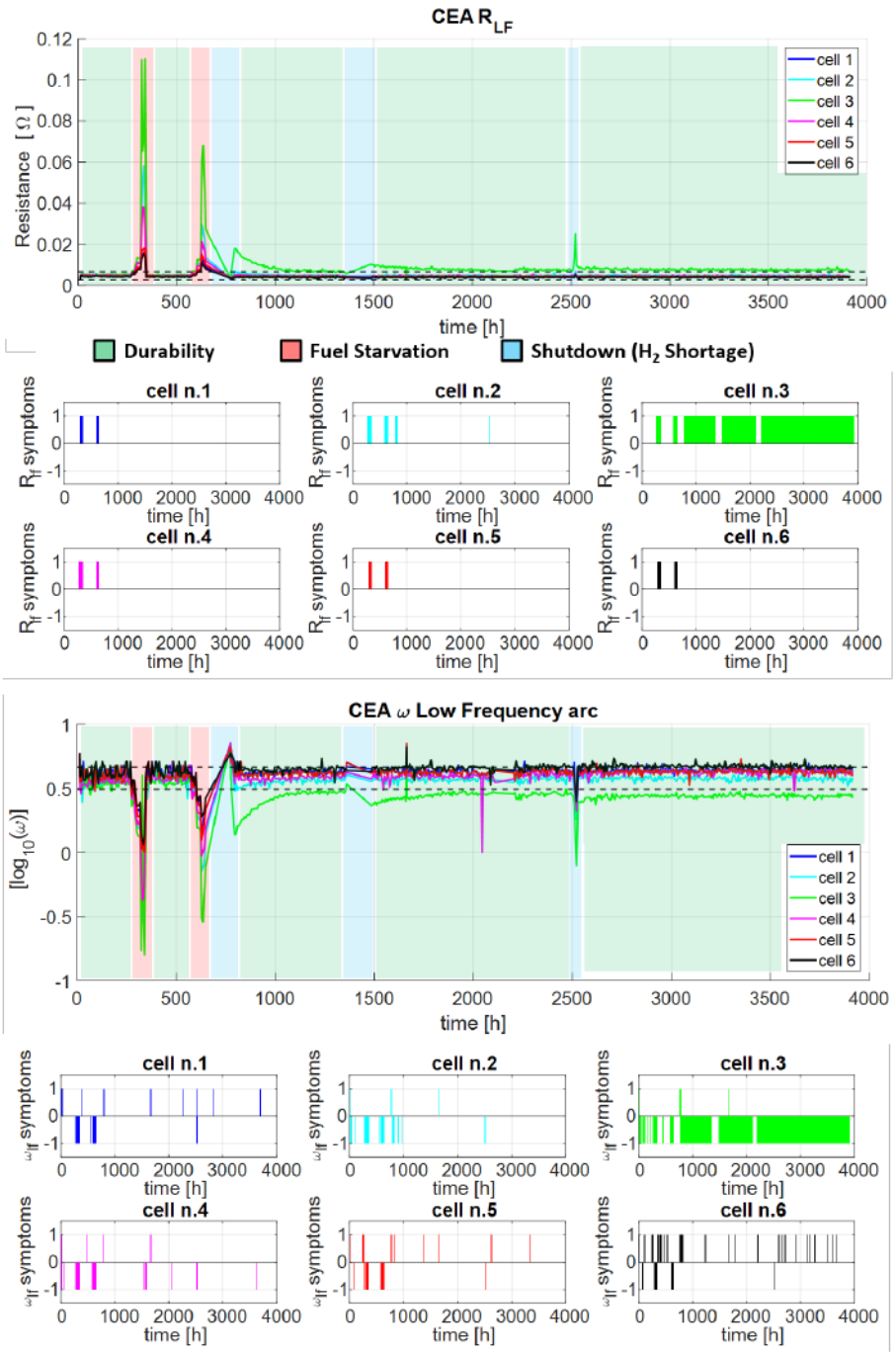


**Figure 3.10:** Validation - CEA experimental Campaign - 6 cells short stack. The features deviations of the 6 cells are collected into the symptoms vector. Here, the $R_{LF}$ and the low frequency arc characteristic frequency ($\omega_{LF}$) behaviours are presented.

Figure 3.11 shows the symptom pattern building by checking each feature with respect to its threshold. This has been performed for each cell of the short stack.

It is interesting to point out that the approach suitably works with a PRBS-based [2] measurement (i.e., not sinusoidal stimulus). The symptoms collection shows how all cells change their behaviour with respect to the increase of the fuel utilization. Moreover, even in this case, the polarization resistance $R_{pol}$ can be added as indirect extracted feature, according to the eq. 3.2. It can be noted that when the stack is set at a fuel utilization higher than 82% the algorithm detects the change in the nominal behaviour and the comparison with the FSM row exactly matches the behaviour observed for the fuel starvation in all cells. Thus, the fuel starvation detection and isolation is clearly validated at $F.U. > 82\%$, as shown in Figure 3.11.

[2] As already reported in the "Single cell – PRBS stimulus" of section 2.2.4, the PRBS stimulus is a not conventional sinewave based stimulus that should guarantee an improved resolution of the impedance and an *"almost"* continuous spectrum (with an increased number of points derived from the stimulus) with respect to the conventional EIS measurement. More information about PRBS can be found in [186] and [187].

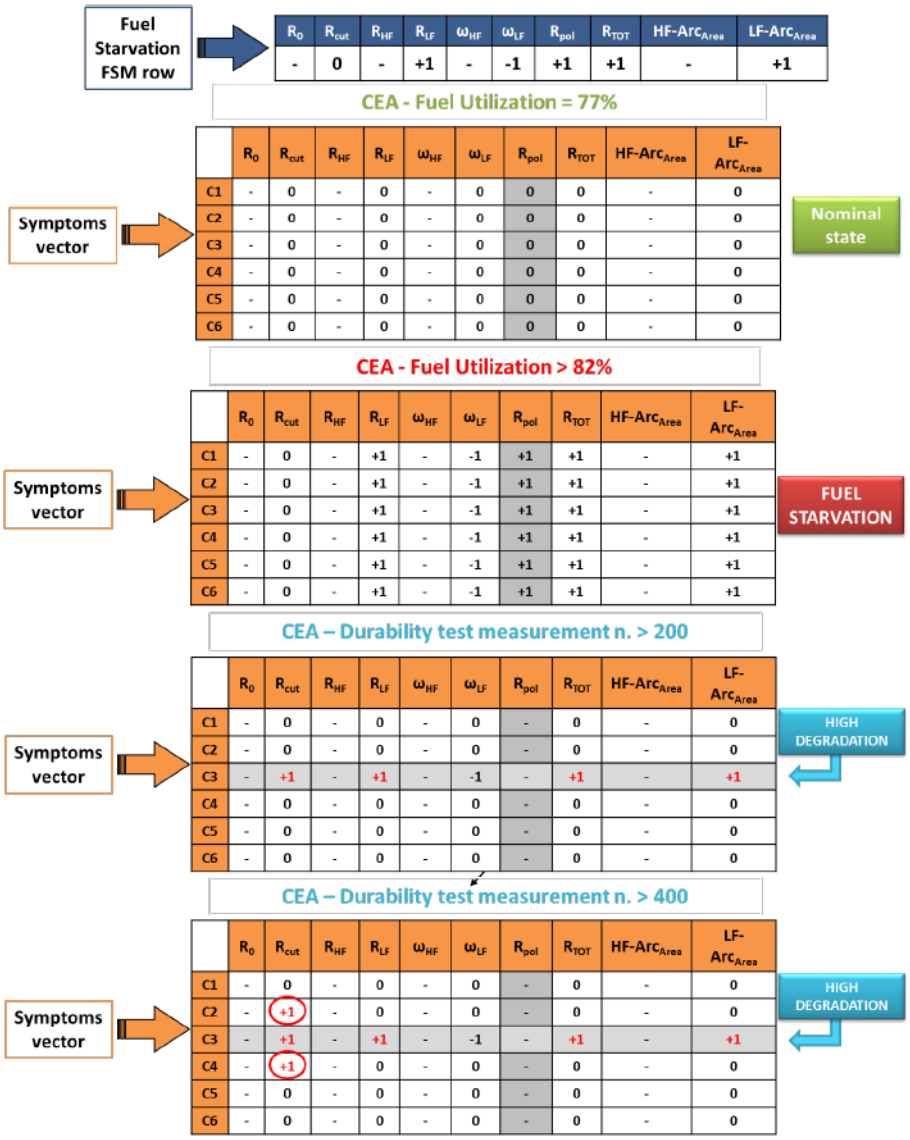


**Figure 3.11:** Validation – CEA 6 cells stack. Detection and Isolation phase. Comparison of the symptoms vector in nominal, "faulty mode", and long-term degradation with the Fuel Starvation FSM row.

Further interesting comments can be provided by analysing the stack behaviour during the 2500h long term test, which has been performed in nominal conditions with 77% F.U. Considering that after the two starvation tests the system was shut-down due to $H_2$ shortage, a re-oxidation or a leakage might have occurred, affecting the operation of the cell n.3; this is confirmed by the voltage monitoring curves as will be commented afterwards. Regarding the EIS-based features monitoring, it is possible to note that after 1500 h the symptom vector of cell n.3 is significantly far from the nominal expected behaviour (whose symptom vector is of all zeros) and the fuel starvation condition as well. Indeed, an appreciable increase in the $R_{CUT}$ along with the $R_{LF}$ and the $R_{TOT}$ is found, as usually expected for high degradation.

According to figure 3.9, the cell n.3 after 1500 h presents an increase in both $R_{CUT}$ and $R_{LF}$, leading to the activation of the relevant symptoms. Therefore a "+1" value is inserted into the corresponding cell of the FSM. The other cells don't exhibit any changes. The total resistance of the spectrum of the cell n.3 sensibly increases with a behaviour not identifiable from the experiments performed (see figure 3.9). Indeed, it is a different detrimental phenomenon detected, far from the fuel starvation herein investigated that cannot be isolated because its pattern is different from that one extracted from the exploited experimental dataset. Moreover, after the 2500h the cells n. 2 and n. 4 seem to be affected by the abnormal behaviour as cell n. 3; indeed $R_{CUT}$ starts exceeding the threshold, leading to a switch in the symptom from "0" to "+1". This correlation in time between cell n.3 and its neighbours drives to the conclusion that likely a local phenomenon occurred and increased in time; such behaviour has been named "high degradation".

As a final remark on the CEA 6-cells short stack diagnosis, it is possible to comment that the Fuel Starvation is clearly detected and isolated when the F.U. is higher than 82%. Moreover, a strong degradation over time is detected after 1200h. According to experimental evidences and the the authors' experience, such behaviour could be attributed to a leakage occurring in the cell n.3, which,

in turn, affects the behaviour of the two neighbouring cells, whose performance decrease in time with a continuous but less evident behaviour. Further comments regarding such conclusions are provided in chapter 5 about the Remaining Useful Life analysis along with other remarks highlighted in the next subsection.

3. **DTU – 6-cells short stack**
   The EIS measurements performed by DTU on the 6-cell short stack were averaged to smooth the EIS curves and reduce the impact of possible outliers and inductive-based distortion effect on the spectrum. The thresholds for each feature were set upon DTU Starvation experiments, as reported in section 3.3.1. The reader is addressed to this section, to recall the explanation of the results on the diagnostic analysis performed. It is evident that the Fuel Starvation isolation process is implicitly validated, being these experiments used to set the nominal thresholds for all cases described in this work. Furthermore, it is interesting to infer on the reliability of such thresholds when applying the FDI algorithm to such cases where faults are not expected to occur, namely "characterization" and "durability" tests described in section 3.2. For all cases, the figures 3.12 and 3.13 report the monitored features extracted during all experiments collected by DTU. These features were identified via *"partial analysis"* and the symptoms collected into the corresponding vector have thus been compared with the rows of the FSM for fault isolation, as shown in figure 3.15.

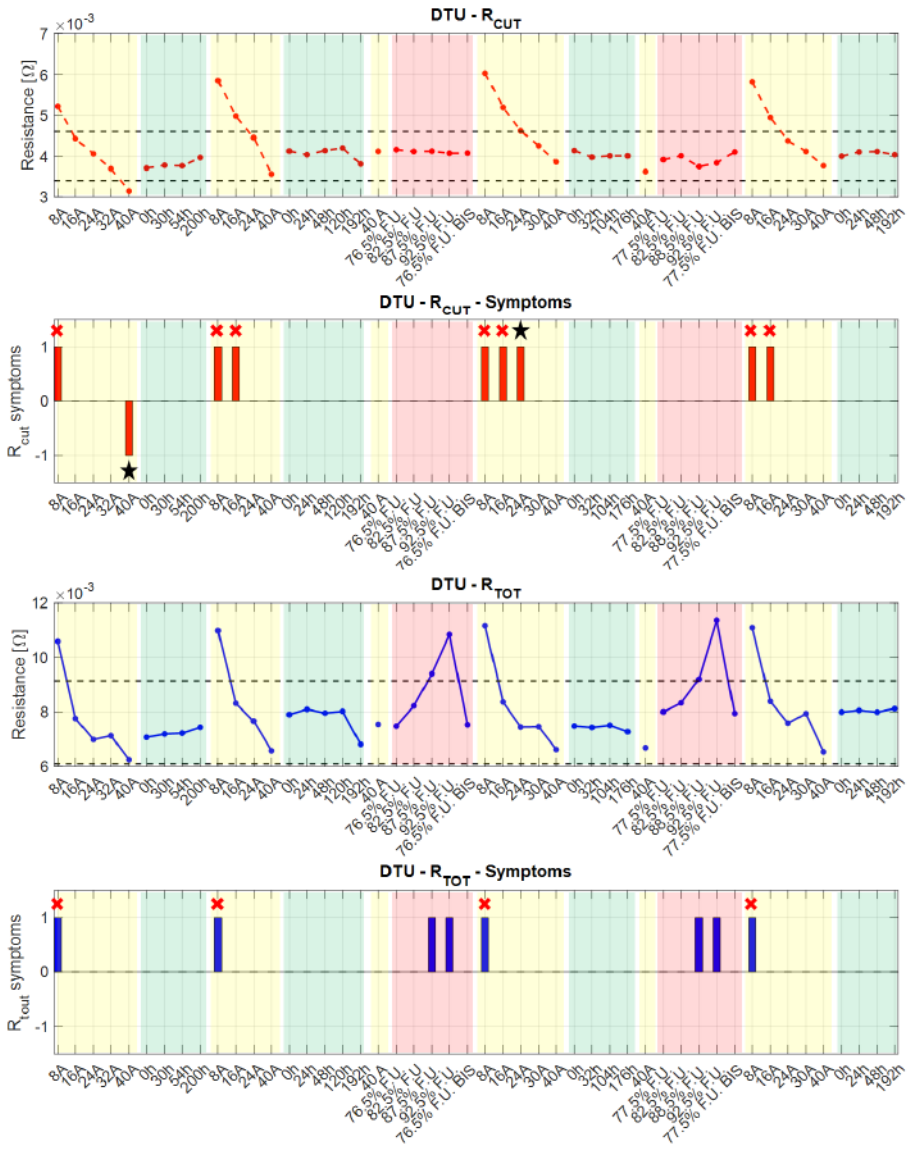


**Figure 3.12:** Validation - DTU experimental Campaign - 6 cells short stack - averaged cell. The parameters deviations are collected into the symptoms vector. Here, the $R_{cut}$ and $R_{tot}$ trends are presented. The black stars indicate an outlier (i.e., false alarm)

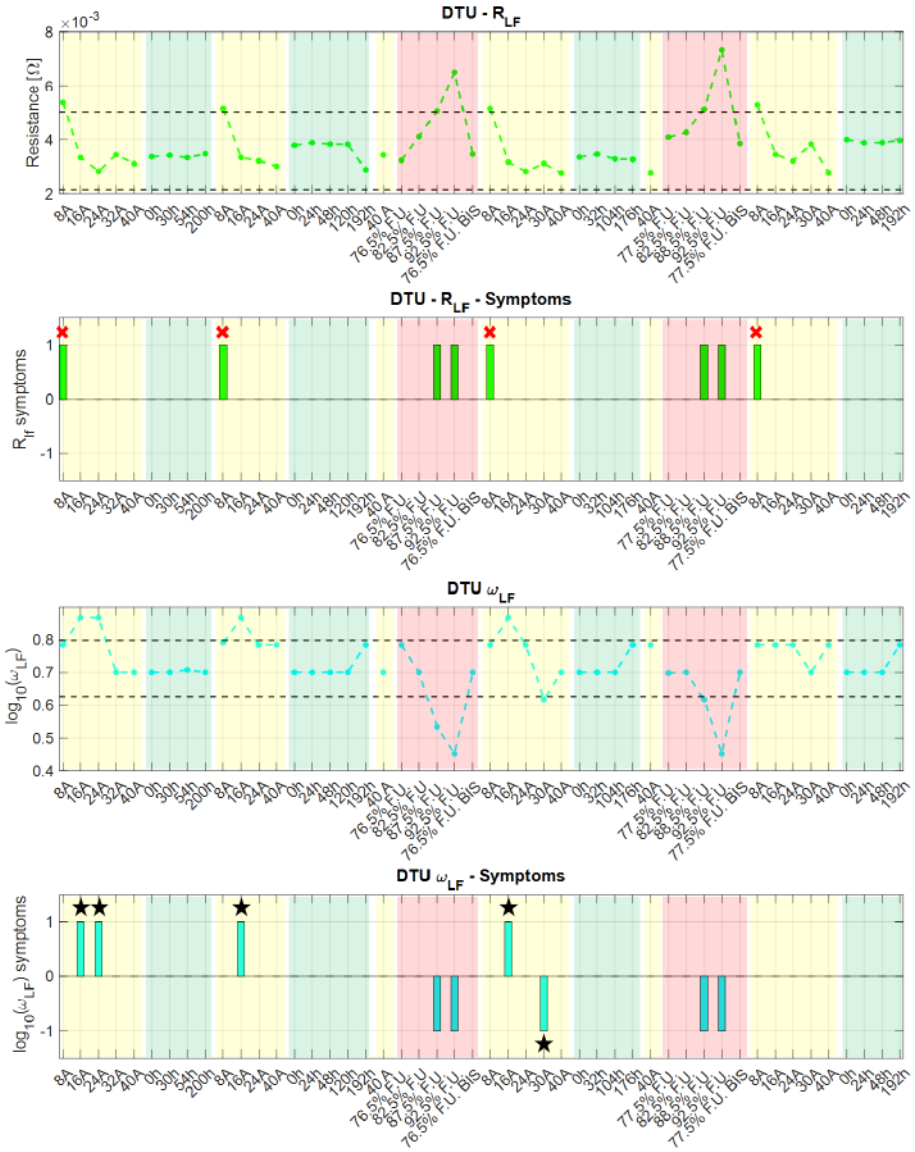


**Figure 3.13:** DTU experimental Campaign - 6 cells short stack - averaged cells. The parameters deviations are collected into the symptoms vector. Here, the $R_{LF}$ and the low frequency arc characteristic frequency ($\omega_{LF}$) behaviours are presented. The black stars indicate an outlier (i.e., false alarm)

The results show that the symptoms change their values in several experiments. During the fuel starvation tests (red highlighted areas) the symptoms are activated, as expected after the building of the FSM row, which was derived from the same dataset. It is worth to note that the symptoms linked to $R_{cut}$ and $R_{TOT}$ (figure 3.12) are activated though the stack is properly operating without faults during the "characterization" tests (yellow highlighted areas). This may be classified either as a "false alarm" (i.e., when a symptom reveals a malfunctioning that does not actually occur) or as a "general fault" (i.e., a faulty behaviour detected but not identifiable). To clearly distinguish between these two possible malfunctioning, further measures in the same condition could help. Generally speaking, a "false alarm" is a result that indicates a condition exists, when it does not; indeed, it could be either an alarm that matches one row of the FSM (though a fault hasn't occurred) or a generic pattern that does not match any FSM row (either a detected malfunctioning that is not known or a malfunctioning that does not really occur). On the other hand, a "general fault" could be defined as an unknown symptom vector that is always detectable in that kind of condition (a recurring behaviour). Particularly, the former is a seldom not expected behaviour (i.e., a sort of outlier), while the latter is a typical pattern of the system in that condition, which is detected as malfunctioning but not possible to isolate. Figure 3.14 summarizes how an activated symptom (i.e., $\neq 0$) might lead to an isolated fault, a generic fault or a false alarm. Particularly, the matching of the symptom pattern with one row of the FSM can lead to a correct isolation of the fault or to a false alarm if not occurring. On the other hand, if the symptom pattern is unknown and persists in time at the same condition, the most-likely system state is a malfunctioning not accounted within the FSM; otherwise, a seldom occurrence of such pattern is a false detection of a fault.

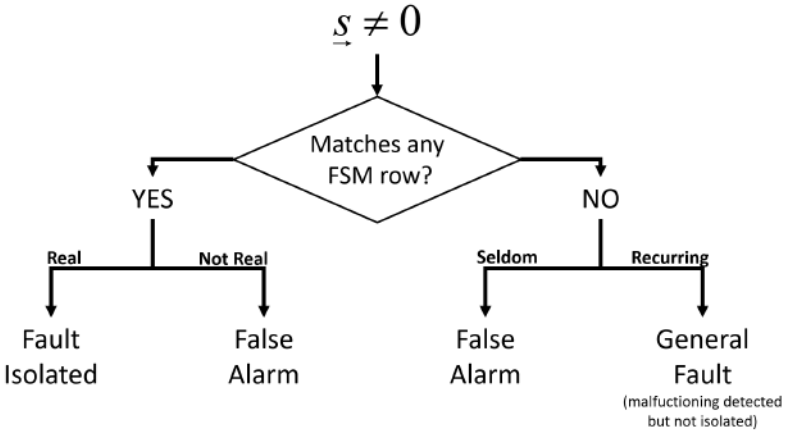


**Figure 3.14:** Tree diagram of the possible outcomes from an activated symptom.

An example of "false alarm" is provided in figures 3.12 and 3.13, where a fluctuation in some relevant/corresponding parameters around the threshold at the same conditions is reported with black star marks. Indeed, during the "characterization" (yellow area) at 24 A and at 40A, the $R_{cut}$ is at least three times out of four within the nominal range limited by the threshold (i.e., the related symptom is "0") whereas just in one case, pointed out by a black star (see figure 3.12), is in a faulty state. The same comment can be made for the $\omega_{LF}$ (see figure 3.13), whose value oscillates around the threshold during the "characterization" at 8A and 16A. These "false alarms" are likely due to errors in measurement or to a not-yet-reached stable condition of the system, whose dynamics related to the change of the operating condition has not expired yet.

Moreover, according to the thresholds' definitions described in section 3.3.1, it is clear that the nominal range for each parameter is strictly linked to the reference condition investigated (see eq. 3.1). This means that, when the FC is operated at different loads, the thresholds need to be re-tuned as a function of the new nominal (i.e., un-faulty) operations; indeed, the diagnostic approach could detect a not well defined faulty condition (i.e., an unknown symp-

tom pattern) instead of a nominal one, which is not investigated/ detected, otherwise.

Moreover, when the nominal operation changes, the reference value of the extracted features has to change accordingly. This suggests the need of defining a map of the nominal operating conditions leading to the setting of threshold values for each condition to improve the tool applicability. It is worth commenting that, when the load changes for a malfunctioning outside the FC (i.e. a problem in the BoP of the system that causes a reduction in the current/power), the "general fault" detected by the algorithm could reveal a not expected behaviour of the system. This would suggest a double check on the load to understand if something outside the FC (i.e., in the BoP) caused this issue. On the other hand, if the change in the load is intentionally operated, the algorithm needs to be updated with the new reference condition, being it not calibrated for that operation. This is not an issue on the real system and it only requires the mapping of the FSM with respect to the operating conditions. However, if such exercise is not performed, the diagnostic tool might be not applicable for such new conditions, since they have not been considered while building the FSM; this is shown in figures 3.12 and 3.13 with red cross markers. Here, when the current load goes below 16 A (whereas the nominal one taken as reference is 32 A) the FSM is activated and a "general fault" arises. Here, some symptoms exceed the thresholds in a not expected way. It results in a detection of a faulty state whereas the stack is working properly but at different load/power.

As seen in Figure 2.18, when the current decreases, the EIS spectrum of a SOFC is expected to enlarge its shape in both high frequency and low frequency arcs whereas the ohmic resistance ($R_0$) should not change (this mean that the $R_{cut}$ is expected to increase with the $R_{HF}$). Looking at figures 3.12 and 3.13, when the current is lower then 16 A, the $R_{cut}$ increases along with $R_{LF}$ and, in turn, $R_{tot}$, whose related symptom change to "+1". Moreover, a strong fluctuation of $\omega_{LF}$ around the threshold is found, revealing that this parameter might not be reliable for such an analysis. Another symptom expected to change is the $\omega_{HF}$, which is not available

for the *"Partial analysis"* here adopted, since Figure 2.19 suggests an increase in the High Frequency peak with a related shift towards low frequencies. Considering the presented condition as an unexpected one, the diagnostic algorithm defines a new FSM row, presented in Figure 3.15, where a "general fault" is revealed. Since the experimental test plan suggests that this operation is a nominal condition with reduced power, this symptom pattern can be defined as "Load change". A further comment can be added considering the results presented in figure 3.11. The symptom pattern of the CEA "high degradation" condition is the same of the DTU "Load Change", but for the $\omega_{LF}$ that is not reliable in this case as previously discussed. On the other hand, while for DTU that behaviour is due to a different current (i.e., 16 A $<$ 32 A – nominal reference –), for the CEA dataset the nominal condition was not affected by intentional or accidental changes. It is interesting to note how the CEA cell n.3 behaves like a cell in a different load condition despite being still the nominal (i.e., reference) one. This underlines how the cell n.3 is affected by a local detrimental phenomenon that leads the cell to behave as it would if it were at a lower load condition. These comments can thus support the initial hypothesis of an internal leakage, which causes a local reduction of the fuel in cell n.3, and in turn, letting the cell work in a limited power-condition. Furthermore, this effect increases in time and affects the neighbour cells (i.e., cells n.2 and 4). Thus, even for DTU 6-cells short stack (averaged), it is possible to state that the Fuel Starvation is clearly detected and isolated when the F.U. is higher than 85%. Moreover, a change in the load, even in nominal (i.e., un-faulty) condition is detected with a different symptom pattern.

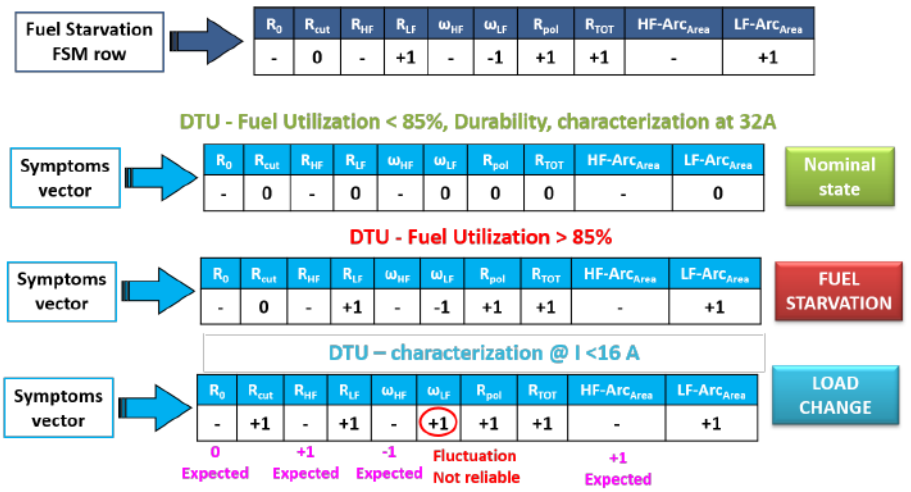


**Figure 3.15:** Validation – DTU 6 cells stack. Detection and Isolation phase. Comparison of the symptoms vector in nominal, "faulty mode", and "characterization" at a different load with the Fuel Starvation FSM row. For this latter vector, some expected behaviours are highlighted in pink and red font.

4. **VTT – 64 - cells stack** The 64-cells full stack were tested by VTT by applying the conventional sinusoidal stimulus for EIS analysis. Again, the thresholds were taken from the experiments performed by DTU as described in section 3.3.1.

   Here a complete full stack was tested by VTT with EIS measurements performed at increasing fuel utilization from 66.9% to 81.9%. In this case the stack was connected to the BoP and the measures were taken on the full stack. Since the spectra didn't show high inductive effects, the MGFG algorithm was applied by means of the "complete analysis" approach. This allowed validating the FSM row for the "complete analysis" at a reference condition of 32 A and 70% F.U. Figure 3.16 shows some EIS measurement along with its fitting derived from the MGFG algorithm application at increasing fuel utilization.

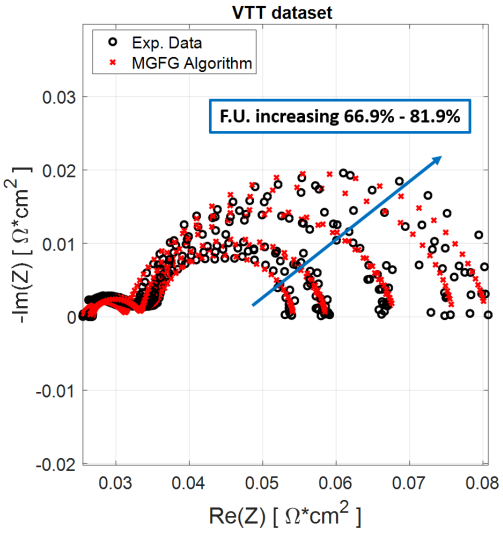


**Figure 3.16:** VTT experimental Campaign - 64 cells stack. Measured Nyquist plots along with the corresponding fitting obtained by MGFG algorithm application. Here some EIS measurement at different Fuel Utilization values are superimposed to show the changes in the spectra.

Figures 3.17, 3.18, 3.19 show the monitored features extracted under malfunctioning operations and their values are compared against the threshold limits. The symptoms were collected into the corresponding vector to be compared with the rows of the FSM for the fault isolation. Particularly, Figure 3.17 describes the trend of the $R_0$ and $R_{TOT}$ along with the change in the related symptoms, Figure 3.18 presents all the features related to the low frequency arc, whereas Figure 3.19 describes the behaviour of $R_{HF}$ and $R_{pol}$. Since the VTT dataset consisted in a more detailed test at different step-wise increasing fuel utilization values, with respect to the fuel starvation tests presented so far, a mathematical trend has been identified and here superimposed to the measured points (i.e., the extracted features), to define a function of such features with respect to the fuel utilization. Results show a parabolic behaviour of $R_{TOT}$, $R_{POL}$, $R_{LF}$ and $\omega_{LF}$; on the hand a quasi-linear trend in $R_0$ and $R_{HF}$ is observed.

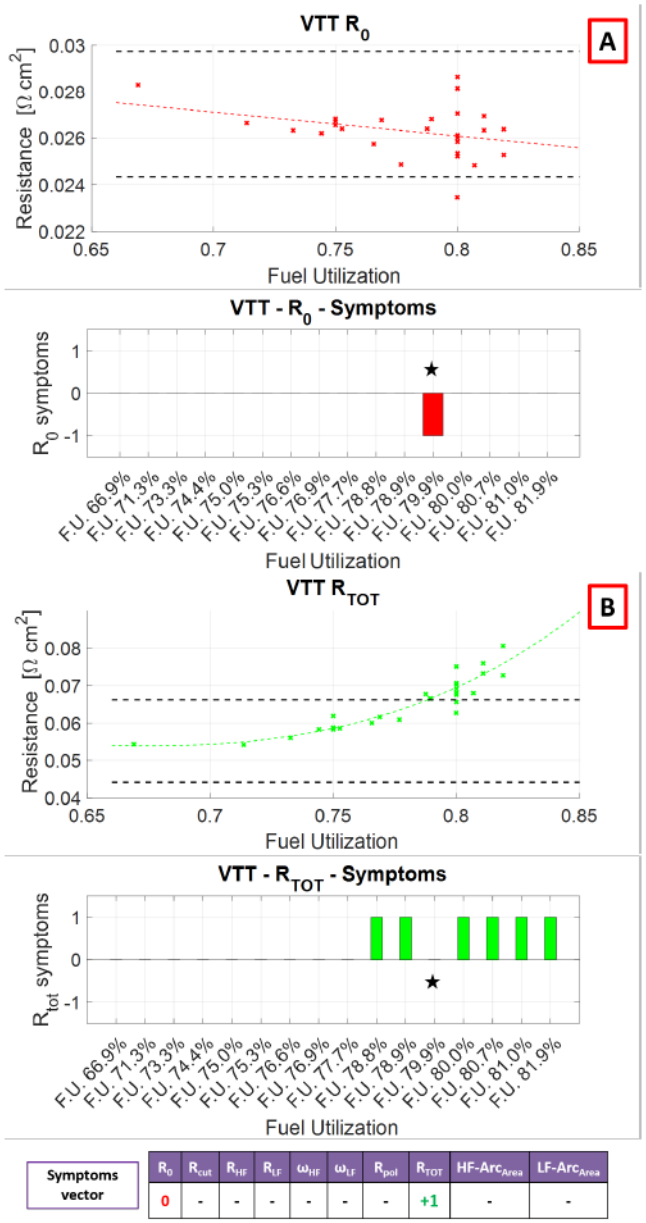


**Figure 3.17:** Validation - VTT experimental Campaign - 64 cells stack. The parameters deviations are collected into the symptoms vector. In the Figure, the $R_0$ and $R_{TOT}$ behaviours are presented in figure A and B, respectively.

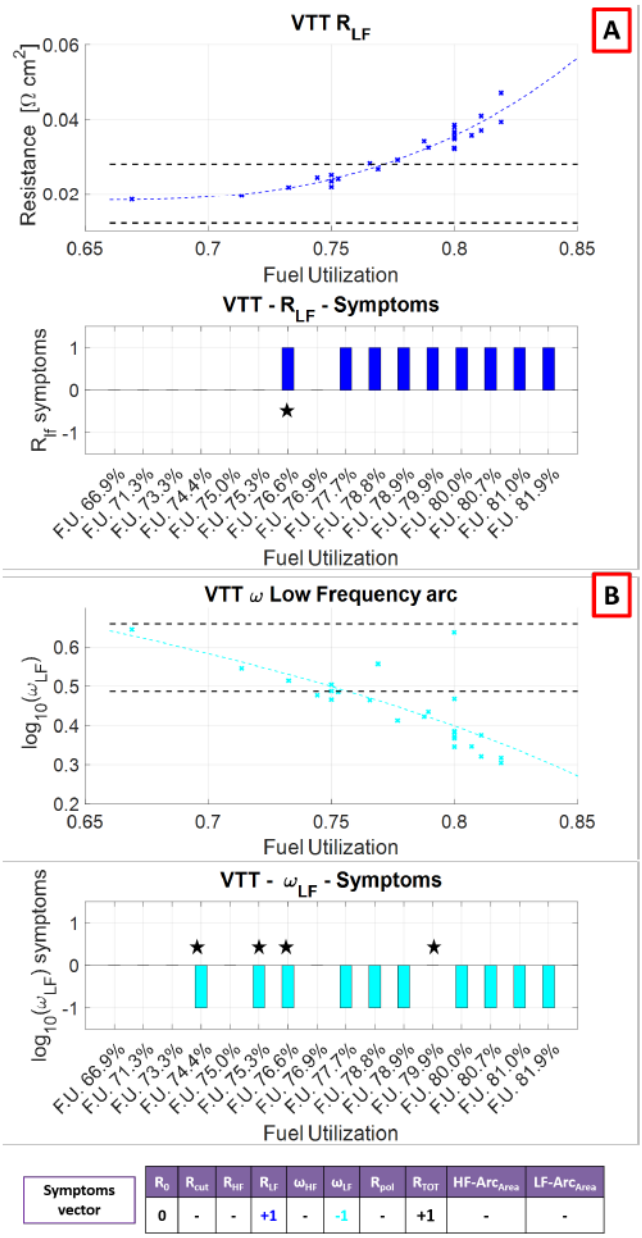


**Figure 3.18:** VTT experimental Campaign - 64 cells stack. The parameters deviations are collected into the symptoms vector. In the Figure, the $R_{LF}$ and low frequency arc characteristic frequency $\omega_{LF}$ behaviours are presented.

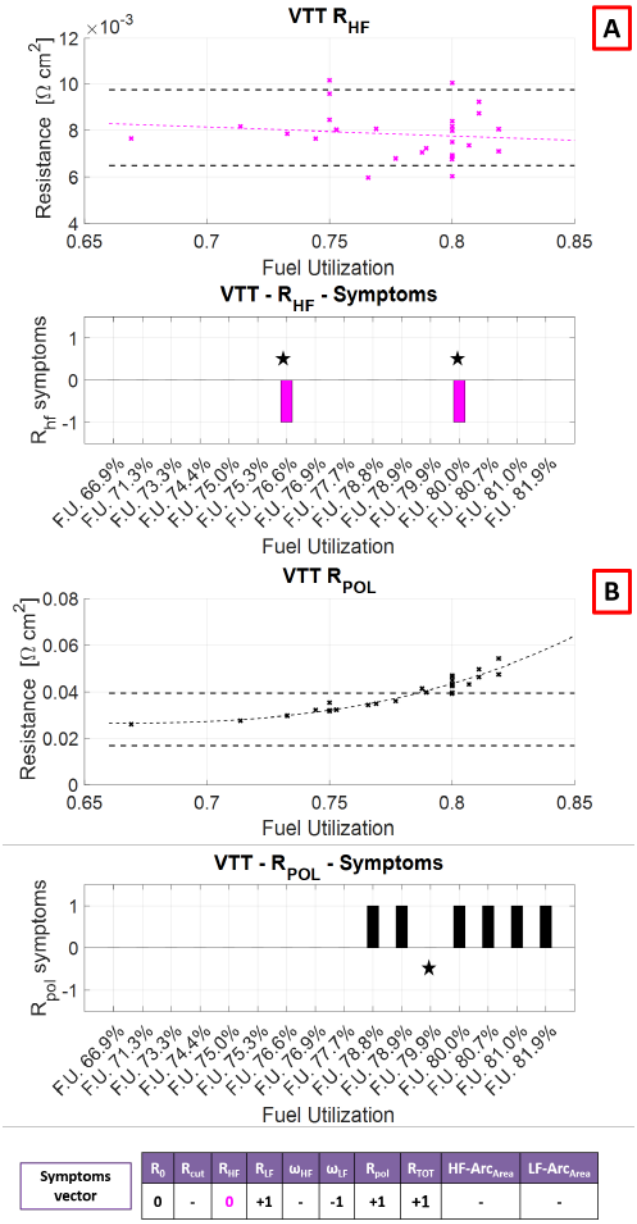


**Figure 3.19:** Validation - VTT experimental Campaign - 64 cells stack. The parameters deviations are collected into the symptoms vector. In the Figure, the $R_{HF}$ and $R_{POL}$ behaviours are presented.

It is interesting to note how the ohmic resistance doesn't present any significant change at high fuel utilization, while the total resistance is systematically increased for F.U. higher than 77%. Moreover, the low frequency arc and the related extracted features confirm the results expected after the analysis performed on the short stacks, as explained before for DTU and CEA cases. Therefore, the limit value for the nominal behaviour can be here defined at the F.U. 77%. This is expected because the layout of the single cell implements the same components (i.e., pipeline, supply and return manifolds) of a full stack, which, in turn, suffers from a major fuel depletion particularly at the outlet side.

The high frequency resistance $R_{HF}$ doesn't show any kind of sensible changes with the increasing fuel utilization, while the $R_{pol}$ exceeds the threshold when the F.U. reaches the value of 77%. This is expected since the fuel starvation mainly affects the low frequency region of the spectrum, as already discussed. Moreover, it is worth adding a comment on the evaluation of $R_{cut}$, which has been defined as the sum of the $R_0$ and $R_{HF}$ as described in eq. 2.14, not available for the application of the *"complete analysis"*. Being both $R_0$ and $R_{HF}$ in the nominal (i.e., unfaulty) region limited by the corresponding thresholds, they don't change significantly their values during the fuel starvation, leading to a symptom value of "0". According to eq. 2.14, the $R_{cut}$ is the sum of two constant values, so, in turn, it is a constant value as well, easily allowing setting the symptom to "0". Thus, also the symptom related to $R_{cut}$ can be added to the vector for the comparison to the FSM row. The comparison between the FSM fuel starvation row and the symptom pattern extracted from VTT data is presented in Figure 3.20, where for $F.U. \geq 75\%$ it is possible to state that fuel starvation is correctly detected and isolated.

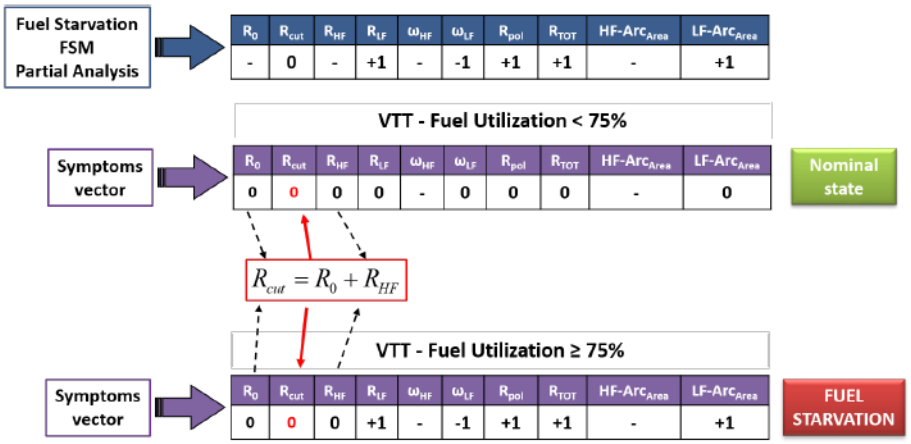


**Figure 3.20:** Validation – VTT 64 cells stack. Detection and Isolation phase. Comparison of the symptoms vector in nominal and "faulty mode" with the Fuel Starvation FSM row.

## 3.5 The on-field test

In the frame of the INSIGHT project, the developed diagnostic tool was applied to a commercial SOFC in a real environment to test its applicability. Indeed, one of the aims of the INSIGHT project in which this work has been developed was to validate the tool on a operating full stack in a real environment. The goal was to improve the Technology readiness level [3] of the diagnostic tool from level 5 (Technology validated in relevant environment - industrially relevant environment in the case of key enabling technologies) to level 6 (Technology demonstrated in relevant environment - industrially relevant environment in the case of key enabling technologies). Thus, the company SolidPOWER (partner of the project INSIGHT) provided a SOFC module with one 64-cells stack (EnGen-2500) installed in a real environment (see Figure 3.21). Indeed, the durability lab of SOLIDpower in Trento (IT) was chosen

[3]For more details about the Technology Readiness Levels (TRL) the reader is addressed to the website www.fch.europa.eu or to https://ec.europa.eu/research/participants/data/ref/h2020/other/wp/2016-2017/annexes/h2020-wp1617-annex-ga_en.pdf - Annex G. Last access 06 June 2020

for the expected conditions similar to that ones of a standard customer's installation site, in terms of functionalities, limitations and requirements.

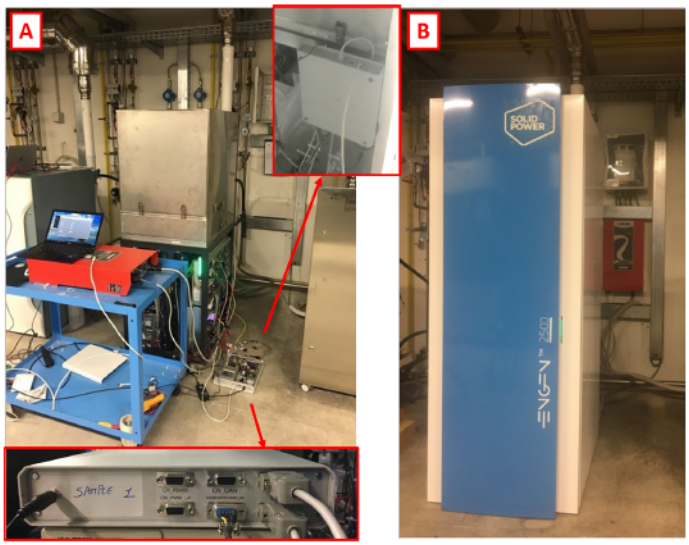


**Figure 3.21:** On-field test – Final test configuration for EnGen-2500 INSIGHT system. A) shows the environmental installation of the Engen-2500 during the development with some pictures of the board and its connections; B) shows the final system with the integrated board.

EIS measurements were performed (with both sinusoidal and PRBS-based stimuli) by means of a hardware developed by Bitron company, named Bitron box [4]. In this product an Analog Front-End (AFE) board commands the converter to superimpose a defined stimulus to the electrochemical device operating in stable conditions. A beaglebone board acts as controller and sends the data to a second embedded board on which the diagnostic algorithm runs for monitoring, detection and isolation purposes. The preliminary tests performed have been used to define a nominal reference condition (i.e., 25 A, 2500 W, F.U. 62%) and a fuel starvation test with a stepwise increase in fuel utilization from 62% to 72% at 25 A, 2500 W by changing the fuel flow. The fuel utilization steps have been shown in Figure 3.22.

[4]For more details the reader is addressed to the website http://insight-project.eu/

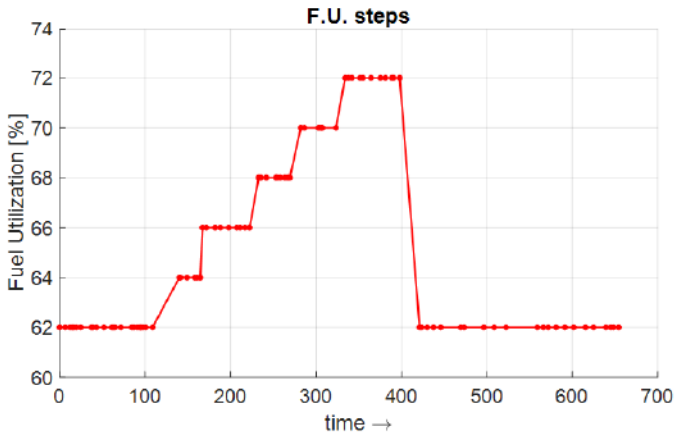


**Figure 3.22:** On-field test – SP 64 cells stack. Fuel utilization steps.

The EIS measurements of the 64-cells full stack were performed via sinusoidal stimuli and analysed by means of the "complete analysis", whose results are presented in the following. Figure 3.23 shows about 30 EIS spectra collected at nominal reference condition. As expected, the on-field test presented many spectra with shapes that exhibit a rough shape, particularly in the low frequency region. Such a behaviour could be explained by considering the non-controlled environment experiment which led to high fluctuations in the signals. Indeed, particularly at low frequencies, the recorded EIS points show a deviation most-likely due to the influence of the instrumentation, cabling and limitations in the converter response. From the figure 3.23 two arcs are visible with no relevant inductive effects. Looking at the low frequency, the simple cut of the EIS points was not considered, because it might have hindered any information about the fuel starvation detectability, being the low frequency arc the mostly affected one by such fault. Thus, repeating measurements were necessary to at least define a trusty-region of the measured points. Nevertheless, despite the high amount of outliers, the MGFG algorithm revealed to be capable of identifying the spectra with a ECM made of 4 RQ elements, of which two represented the two visible arcs in the Nyquist plot and the remaining helped in refining the shape of the low frequency one. These latter RQ elements presented the similar characteristic frequency peak of the low frequency arc one and a very

reduced resistance value at least one order of magnitude lower than the $R_{LF}$ and $R_{HF}$. Thus, for the analysis of the relevant extracted parameters, this two RQ elements were considered to be not significant for the state of health identification; however their values helped in smoothing the computed spectra instead.

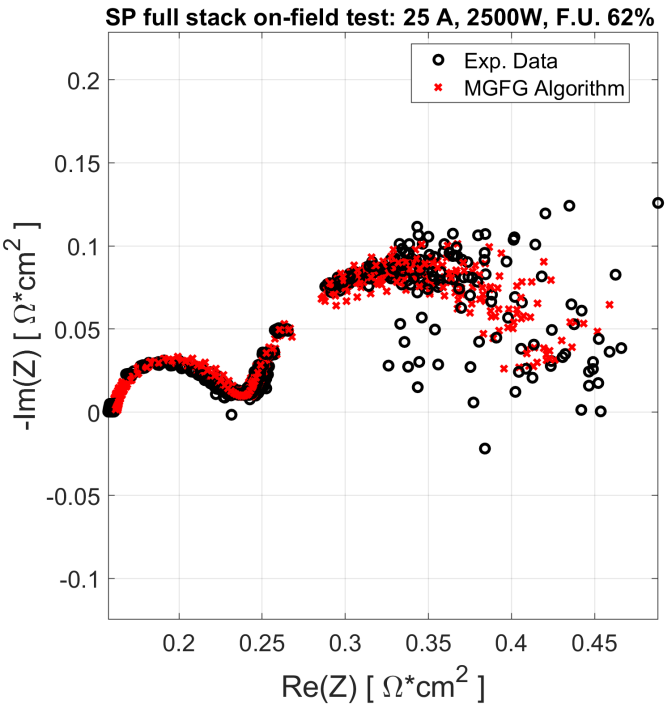


**Figure 3.23:** On-field test – 22 Nyquist plots of the nominal conditions at F.U. 62% superimposed. Here in black circles are shown the experimental points while in red crosses the identified points via MGFG algorithm are reported. It is clearly visible noise at low frequencies.

Since the MGFG algorithm proved to be reliable in identifying a coherent circuit with the same elements for each measurement of Figure 3.23, the diagnostic approach was validated on the fuel starvation with the same FSM and threshold definition used in section 3.4. Indeed, Figures 3.24, 3.25 and 3.26 show the monitored features extracted under

malfunctioning operations and their values are compared against the threshold limits. The features are extracted via *"complete analysis"* and the symptoms are collected into the corresponding vector to be compared with the rows of the FSM for the fault isolation. Particularly, Figure 3.24 presents the trend of the $R_0$ and $R_{TOT}$ along with the change in the related symptoms, Figure 3.25 presents all the features related to the low frequency arc, whereas Figure 3.26 describes the behaviour of $R_{HF}$ and $R_{pol}$.

Here, the ohmic resistance doesn't present any significant change at high fuel utilization with respect to the reference condition, while the total resistance is systematically increased over 70% F.U. It is interesting to note that the system is affected by a detrimental effect that increases in time. Even though the threshold is not exceeded, there is an indication of changing in the ohmic behaviour that should be taken in consideration as a possible incipient fault. This is more evident in the $R_{TOT}$ trend after the highest value of fuel utilization (72%), which leads to the occurrence of some outliers leading to a "false alarm" in the last part of the experimental test; this is pointed out by the black star markers in figure 3.24.

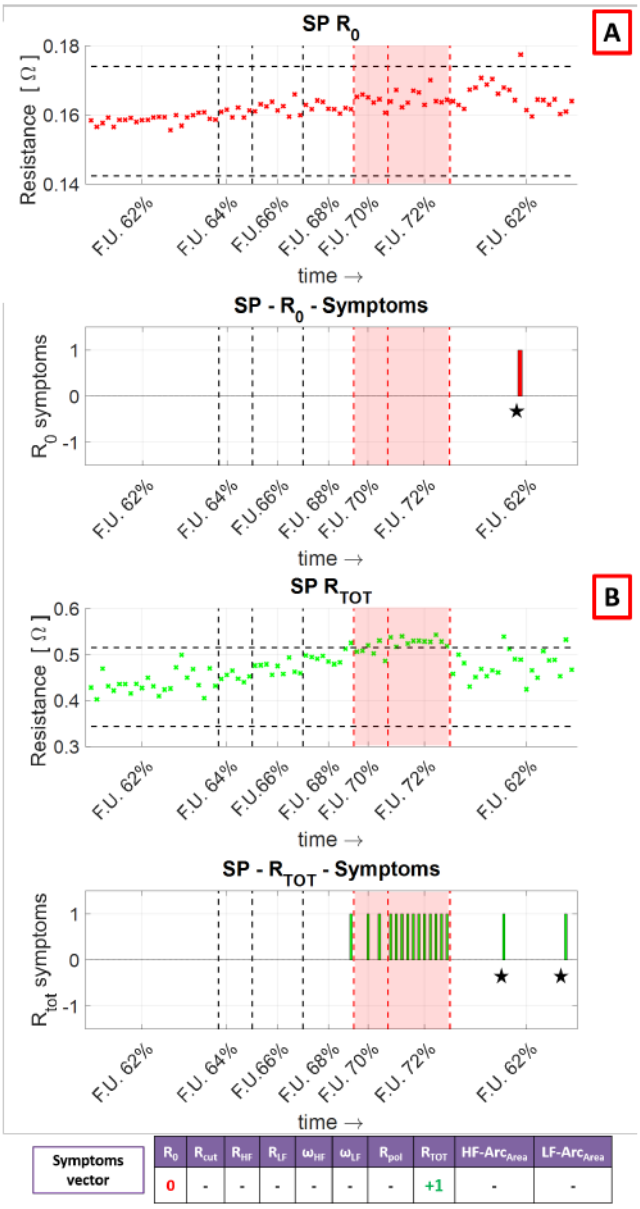


**Figure 3.24:** Validation - SP experimental Campaign - 64 cells stack - On-field Test. The parameters deviations are collected into the symptoms vector. In the Figure, the $R_{CUT}$ and $R_{TOT}$ behaviours are presented.

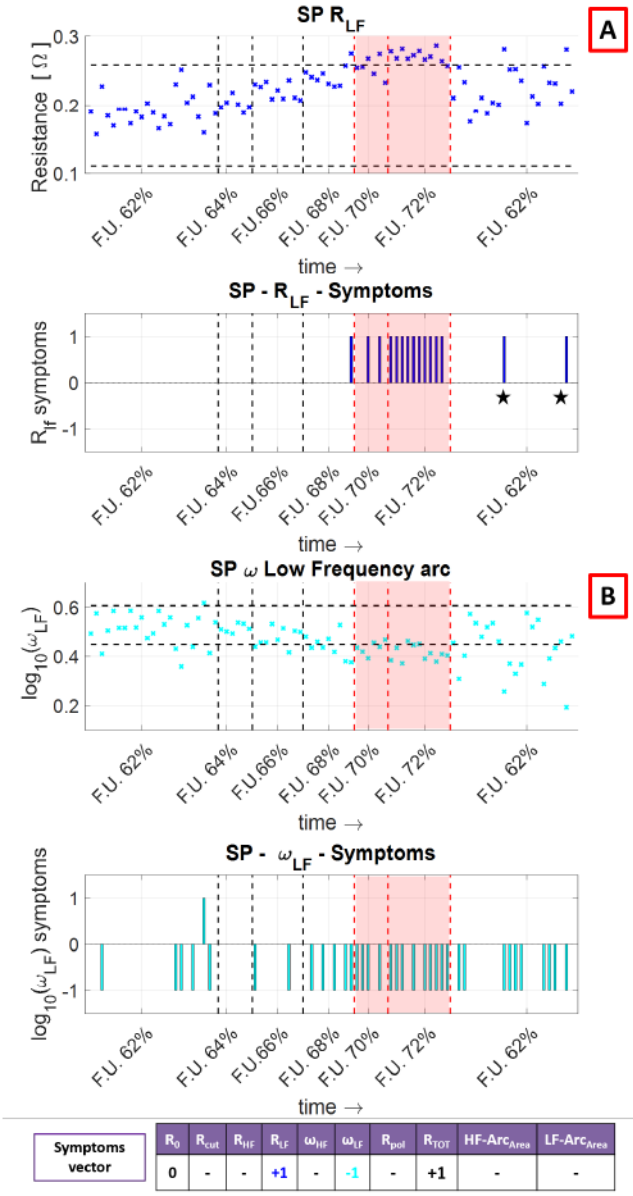


**Figure 3.25:** Validation - SP experimental Campaign - 64 cells stack - On-field Test. The parameters deviations are collected into the symptoms vector. In the Figure, the $R_{LF}$ and low frequency arc characteristic frequency $\omega_{LF}$ behaviours are presented.

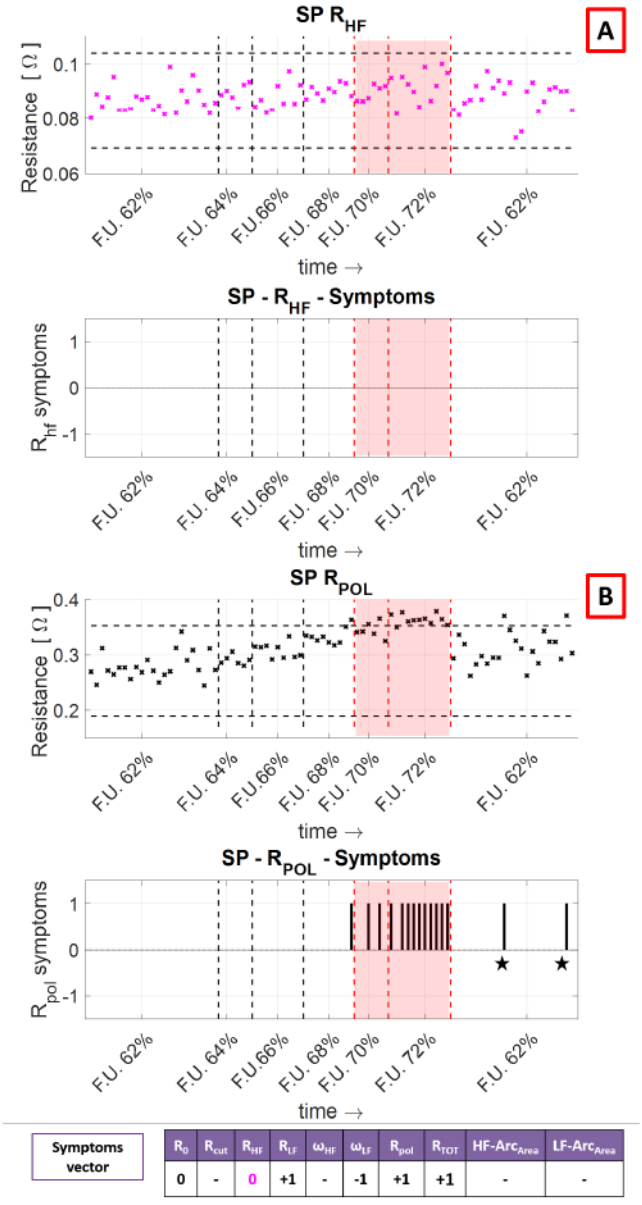


**Figure 3.26:** Validation - SP experimental Campaign - 64 cells stack - On-field Test. The parameters deviations are collected into the symptoms vector. In the Figure, the $R_{HF}$ and $R_{POL}$ behaviours are presented.

The relevant extracted features of the low frequency arc, namely $R_{LF}$ and $\omega_{LF}$, behave as expected during the fuel starvation, thus confirming the trend shown in section 3.4 for the short and full stacks. The limit value for the nominal behaviour is the F.U. 70%. Again, the detrimental effect not decreasing after the return to the nominal condition (f.u. 62%) leads to some outliers in $R_{LF}$ (see black star markers in figure 3.25), whereas the $\omega_{LF}$ presents a very unstable behaviour that makes this parameter not so reliable for the diagnosis. This was expected by looking at the high fluctuation of the EIS measurements at low frequencies.

The fuel starvation does not have a sensible impact on the high frequency region, then the $R_{HF}$ shows a nominal trend, with the related symptom not activated (i.e., $s = 0$). On the other hand, the $R_{POL}$ exceeds the threshold during the malfunctioning (i.e., $F.U. \geq 70\%$). This is due to the increase in the $R_{LF}$, which in turn affects $R_{pol}$, as described by eq. 3.2. Again, even for $R_{pol}$ some outliers can be found in the last measurements and indicated in figure 3.26 by black stars marker.

The comparison of the FSM row defined for the fuel starvation and the symptom pattern monitored for the SP on-field tests is presented in Figure 3.27, where for $F.U. \geq 70\%$ the fuel starvation is correctly detected and isolated.

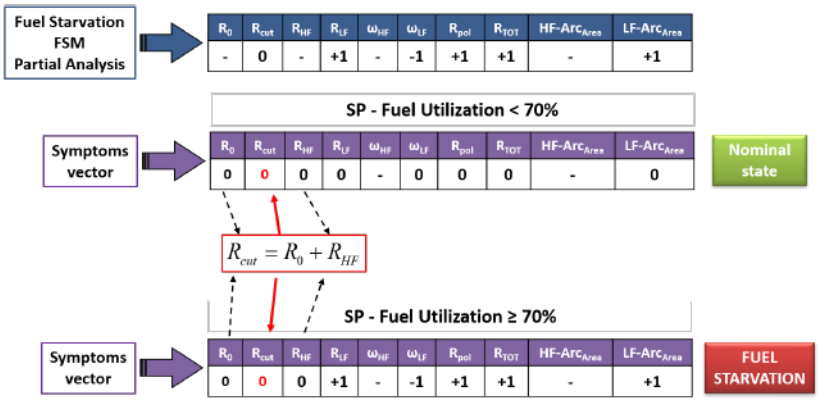


**Figure 3.27:** Validation – SP experimental Campaign - 64 cells stack - On-field Test. Detection and Isolation phase. Comparison of the symptoms vector in nominal and fuel starvation with the Fuel Starvation FSM row.

It is worth making a comment on the numerous outliers found in

the last part of the experiments, that is when the stack is set back to the nominal condition at F.U. 62%, after the starvation test. Since the fault was induced at not very high magnitude, the stack was expected to get back to the nominal condition with a fast, reversible process. However, the detrimental effect do not weaken with the reduction in the fuel utilization, thus leading to a high fluctuation of all extracted parameters around the nominal thresholds; this related anomalous trend is pointed out by the black star markers in figures 3.24, 3.25 and 3.26. This unexpected behaviour of the stack could be ascribed to another malfunctioning, most-likely a leakage, already occurring before the test start with a slight impact on the overall FC State of Health; the high fuel utilization might have increased the magnitude of such phenomenon, whose effect results more evident when the stack is brought back to F.U. 62%. This can be seen, among all parameters, in figure 3.24, where the $R_0$ shows a slight increase (although it should be constant with the increase of fuel utilization) very similar to that one experienced during the CEA "durability" test. Indeed, it is possible to find a resembling behaviour of the extracted parameters with those shown in figures 3.9 and 3.10 and particularly to CEA $R_{cut}$.

After a shut-down for maintenance with a stack replacement, the SP system was restarted and a second test campaign was performed. In this case the diagnostic tool was run on the embedded board integrated in the Bitron box. Its outcome is a User Interface in which on the left side the measured spectrum and its fitting is shown, whereas on the right side a coloured thumb is sketched to immediately inform on the monitored State of Health, as shown in figure 3.28.

Three different conditions are considered:

- **Green Thumb** - Nominal Condition
- **Red Thumb** - Fault isolated (with the specification of the identified malfunctioning)
- **Yellow Thumb** - Alert Possible Unknown condition

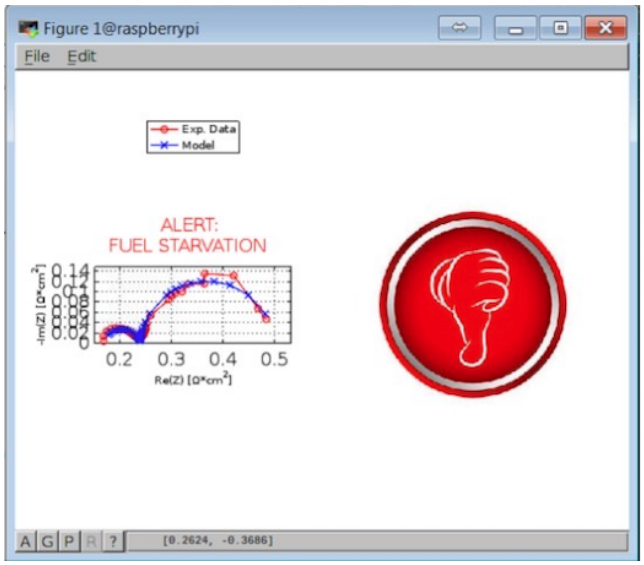


**Figure 3.28:** On-Field test. The diagnostic tool detects fuel starvation problem.

It is worth remarking that such integration on the embedded board required a computational burden reduction, which caused a decay of the algorithm accuracy to lead an increase/reduction of its speed. The next step toward the industrialization requires an accuracy analysis that should define the suitable trade off between costs and performances of the tool, aiming at its future market deployment. Great care should be given to the as much generic as possible application of such tool to be widely spread to Fuel cells, batteries and all electrochemical devices. The final test consisted in around 500 hours measurements at three F.U. levels at 60%, 65% and 72% respectively at 9.3 A, 1000 W, as shown in Figure 3.29. Here the cross markers refer to the EIS and PRBS measurements performed and the related State of Health evaluation analysed by means of the "complete analysis".

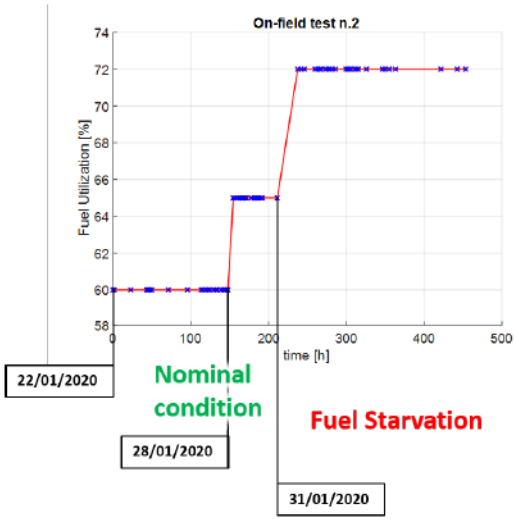


**Figure 3.29:** On-field test n.2 final validation – SP 64 cells stack. Fuel utilization steps.

The on-line application of the tool confirmed the offline analysis (i.e., the first on-field test), as shown in the following, where the diagnostic algorithm embedded in the box proves to be reliable in the on-board Fuel Starvation identification. In this case, the measurement and the algorithm application are automatized and directly performed on-board. This implies the very high difficulties in checking the quality of the measurement before the application of the diagnostic algorithm. Nevertheless, this is a further validation of the tool that should be able to work with significantly dirty spectra collected on board. To provide a visible and immediate feedback on the fuel cell status, the on-field test campaign required the development of a simple Graphic User Interface (GUI), which reports at the end of each EIS tests the acquired Nyquist spectrum along with the identified one via the MGFG algorithm. This allows checking the accuracy of the fitting and its shape. Moreover, as an immediate result of the diagnostic approach, the tool also shows through the aforementioned GUI a graphical object (that is a coloured thumb) describing the detected actual status of the FC along with the identified fault.

Particularly, three different conditions are considered:

- **Green Thumb** - Nominal Condition. In this case, the algorithm does not detect any kind of malfunctioning.
- **Red Thumb** - Fault isolated (with the specification of the identified malfunctioning). Here, the diagnostic tool has found a malfunctioning affecting the cell and the fault has been isolated.
- **Yellow Thumb** - Alert Possible Unknown condition. This condition can be detected when an unknown condition far from the nominal one is detected and when the FC behaviour cannot be associated to the investigated fault. Thus, this unknown condition can be a false alarm (i.e., a sensor malfunctioning or an instantaneous issues) or a not-investigated malfunctioning occurring; in this latter case, the diagnostic algorithm detect a not nominal behaviour but it is not able to identify the issue and then returns a generic alarm.

Figure 3.30 shows the application of the diagnostic tool for the nominal conditions investigates. In this case, almost all the results of the GUI in figure 3.30 show a green thumb, thus revealing the successful application of the tool which is able to monitor the nominal condition of the FC.

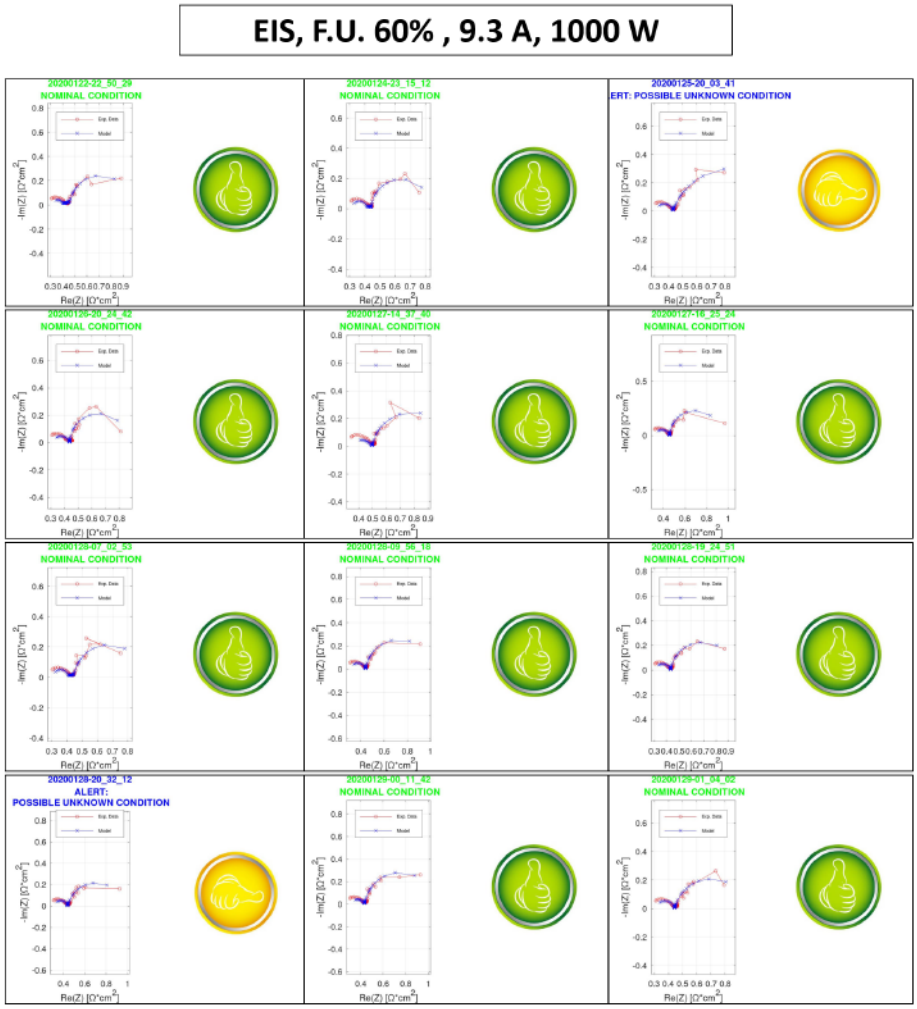


**Figure 3.30:** On-field test n.2 - On-board algorithm outcomes for F.U. 60% - Nominal Condition. The spectrum is acquired via conventional stimuli. Here the yellow thumbs indicates a possible unknown condition. This occurrence can be due either to a false alarm or a condition in which the diagnostic features extracted are on the edge f the defined thresholds. In this case some of the relevant symptoms are activated (i.e., value "1") whereas others are still "0". It usually happens when the FC is slowly moving towards the malfunctioning, due to an increasing drift of the relevant parameters from the nominal conditions.

Only two measurements are not clearly defined as either nominal or faulty condition. Here, some parameters oscillated around the threshold, thus resulting in a symptom pattern different from a zero-vector. These condition can be targeted as "false alarms". At 65% F.U. the stack is still in nominal condition, even though the higher fuel utilization leads some parameters to get close to thresholds, as shown in figure 3.31. This leads to more false alarms since some parameters start changing. The more the false alarms the more likely an incipient fault detection.

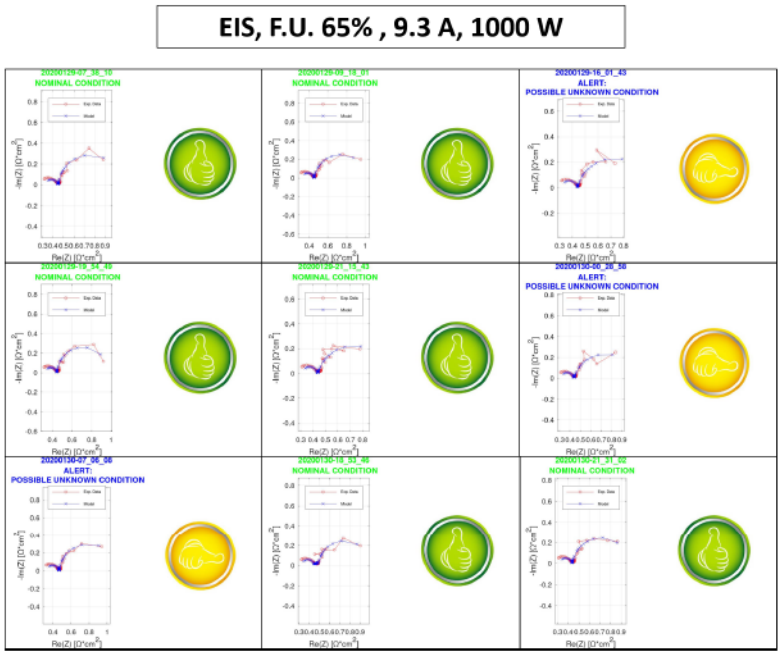


**Figure 3.31:** On-field test n.2 - On-board algorithm outcomes for F.U. 65% - Nominal Condition. The spectrum is acquired via conventional stimuli. The yellow thumbs are the so-called false alarms conditions due to the noise in the measurements. Their occurrence is higher likely due to an incipient malfunctioning (i.e., the fuel starvation).

Figure 3.32 shows the results for the fuel starvation condition. Indeed, when the stack is set at 72% F.U., the diagnostic tool is capable of clearly detect and isolate the fault; indeed it provides an output that shows a red thumb and reports the type of the fault isolated.

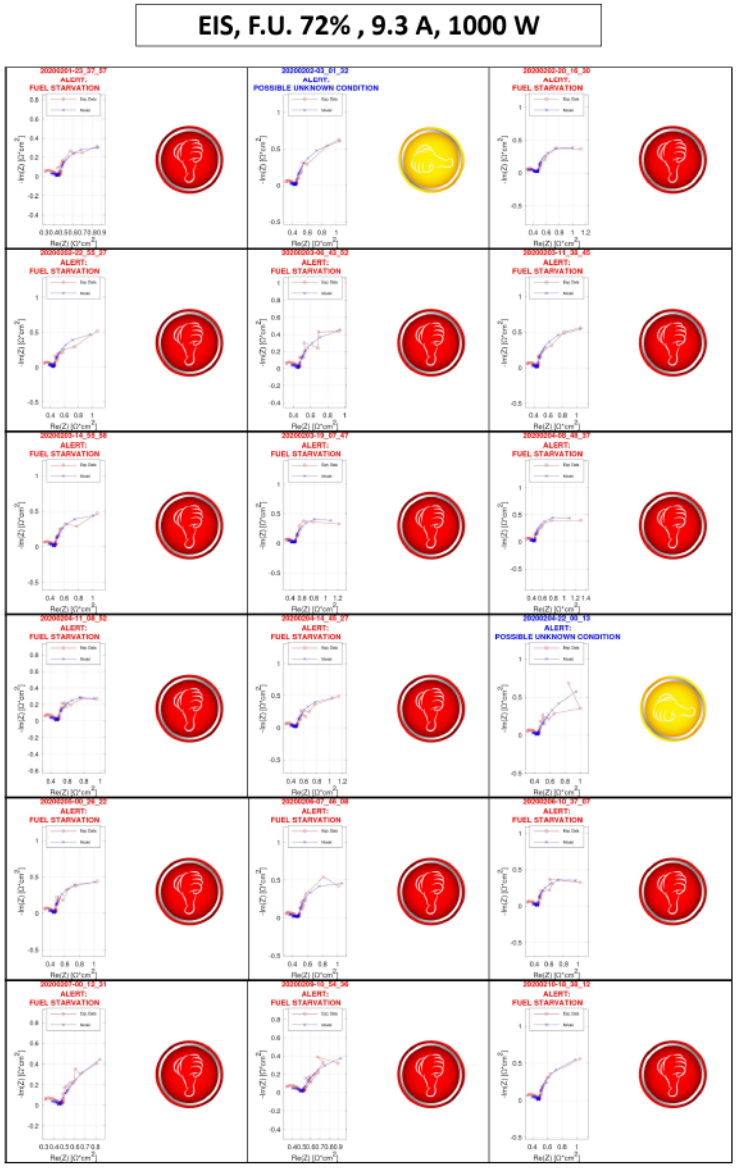


**Figure 3.32:** On-field test n.2 - On-board algorithm outcomes for F.U. 72% - Fuel Starvation. The spectrum is acquired via conventional stimuli. The red thumbs indicates the isolated fault, thus proving the efficacy of the diagnostic algorithm. Some yellow thumbs can be seen, probably due to the oscillation of some parameters around the threshold.

Only two measurements have a not well-defined behaviour, resulting in "false alarms"; for these two cases a not nominal status is detected, but it is not possible to isolate the fault.

The diagnostic tool was also applied on EIS measurement performed by means of a PRBS stimulus, at 60% F.U. – nominal condition – and 72% F.U. – fuel starvation –. The results the diagnostic tool applied to the PRBS measurements are shown in figures 3.33 and 3.34, where both the conditions are clearly identified.

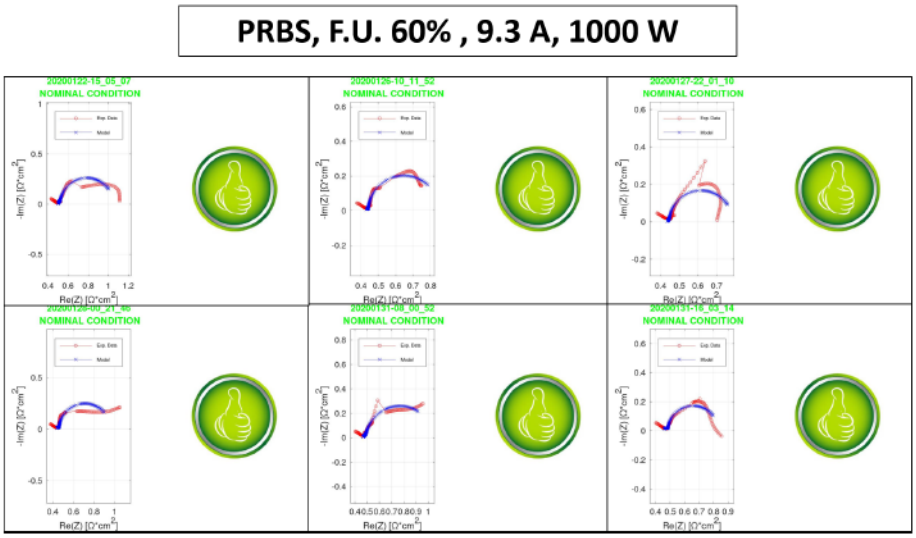


**Figure 3.33:** On-field test n.2 - On-board algorithm outcome for F.U. 60% - Nominal Condition. The spectrum is acquired via PRBS stimuli. Here the yellow thumbs indicates a possible unknown condition. This occurrence can be due either to a false alarm or a condition in which the diagnostic features extracted are on the edge f the defined thresholds. In this case some of the relevant symptoms are activated (i.e., value "1") whereas others are still "0". It usually happens when the FC is slowly moving towards the malfunctioning, due to an increasing drift of the relevant parameters from the nominal conditions.

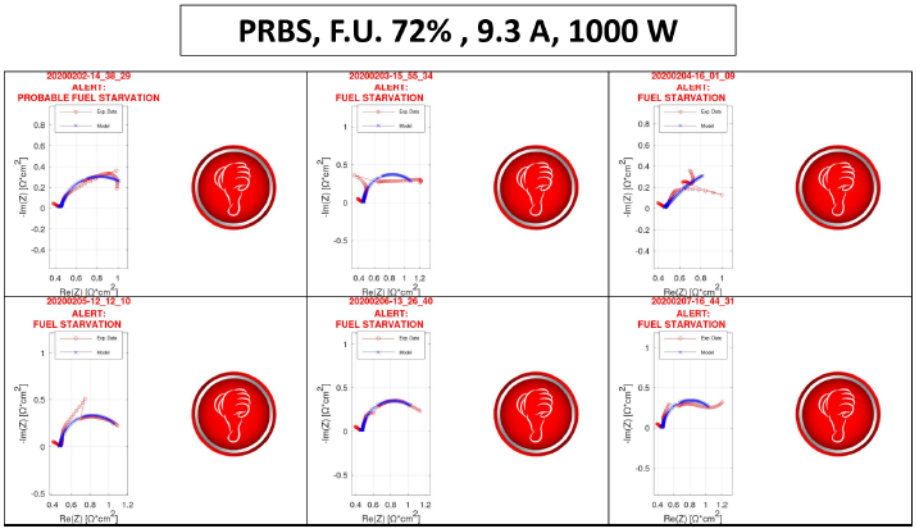


**Figure 3.34:** On-field test n.2 - On-board algorithm outcome for F.U. 72% - Nominal Condition.The spectrum is acquired via PRBS stimuli. Here the yellow thumbs indicates a possible unknown condition likely due to noise in the measurements.

It is worth commenting that the PRBS measurements present a not very smooth spectra with lots of outliers, likely due to the converter response. Further investigations could help in solving this issue. Nevertheless, the algorithm is capable of identifying a proper ECM, thus extracting the features necessary for the detection and isolation. It is worth remarking that even though the spectrum does not show a smooth shape, the algorithm, relying on the physical meaning of each ECM-parameter returns a possible configuration that should represent the FC operation; thus, even though some outliers (particularly at low frequencies) could worsen the spectrum, the algorithm is still able to find a suitable representation of the FC status.

## 3.6 Final Remarks

The Diagnostic approach has been developed and validated against several experimental data collected by the partners of the INSIGHT project, on different sizes and FC set-ups (segmented cells, single cells, short stacks, full stacks), measured with different laboratory instrumentations and by applying different stimuli (both sinusoidal and Pseudo Random Binary Signal based). The diagnostic algorithm proved to be reliable in identifying the ECM related to each measured spectra, with a repetitiveness in the circuital elements that allowed the comparison of the extracted features for State of Health monitoring. The FSM, built on experimental dataset provided by DTU, allowed to correctly detect and isolate the arising fuel starvation in all tested cases, along with some abnormal conditions (either "false alarms" and "general alarms") far from the nominal expected ones. These latter cases lead to the definition of new identified symptoms patterns that could be suitably validated to enrich the malfunctioning detectable by this approach.

From this analysis it emerges that the approach could be valid to monitor the State of Health of the FC during its operations with a not-invasive technique like the EIS. However, this analysis needs to be further improved with ad-hoc tests, aiming at mapping the behaviour of the system and the relevant extracted features at different nominal conditions (considered as reference) and under different malfunctioning. It is clear that the more tests the more reliable and complete the FSM. Moreover, the tests described so far, and particularly the on-field ones, show a strong dependency of symptoms from experimental data; thus, it is fundamental to give strong attention to the quality of the measurement itself to not incur in outliers that could highly reduce the detectability of the faults occurring. Therefore, it could be strongly suggested to improve the frequency of measurements when a possible fault is envisaged, to better understand the persistence of abnormal behaviour over time, clear indication of malfunctioning.

Focusing on the results provided in this work, table 3.4 presents the sum-up of the validated fault detections and the identified rows for the abnormal conditions investigated.

| Partner | Technology | Analysis Type | Perturbation Stimulus | Nominal Condition | Fuel Starvation | Other Conditions |
|---|---|---|---|---|---|---|
| **EPFL** | **Seg. Cell** | *Complete* | *Sinusoidal* | $FU < 90\%$ | $FU \geq 90\%$ | |
| **DTU** | **6-cells short stack averaged cell** | *Partial* | *Sinusoidal* | $FU < 85\%$ | $FU \geq 85\%$ | different nominal condition |
| **CEA** | **6-cells short stack** | *Partial* | *PRBS* | $FU < 82\%$ | $FU \geq 82\%$ | high degradation |
| **VTT** | **64-cells full stack Lab test** | *Complete* | *Sinusoidal* | $FU < 75\%$ | $FU \geq 75\%$ | |
| **SP** | **64-cells full stack On-field test** | *Complete* | *Sinusoidal and PRBS* | $FU < 70\%$ | $FU \geq 70\%$ | |

**Table 3.4:** Resume of the analysis performed and the fuel starvation isolation upon the experimental campaign.

From this table, an interesting remark can be devoted to the fuel utilization limit to distinguish the FC state from nominal to faulty. Table 3.4 shows how this limit reduces with the size of the FC; indeed, a segmented cell can stand high fuel utilization levels up to 90%, the single cell up to $\approx 80\%$, whereas a 64-cells stack suffers form fuel starvation for $F.U. \geq 70\%$. This is expected, due to the path of the fuel within the cell and the distribution of the fuel among the cells. Moreover, this result could suggest a scalability of the approach at different FC sizes and set-ups.

# Chapter 4

# The conventional approach - dynamic modelling

## 4.1 Lumped models - Features and applications

A fast lumped model that reproduces real system behaviour with an acceptable error is useful for the monitoring phase of the main variables during FC operations. Indeed, a reliable simulation can improve the monitoring, providing with reference values (i.e. nominal and unfaulty conditions) that can be compared to real system ones to evaluate real-time residuals [1]. The fault detection and isolation algorithm is thus supported through a real-time estimation of residuals that can turn into arising symptoms of a probable malfunctioning occurring. The combination of conventional signals (i.e. voltage, temperature, pressures, etc.) with EIS measurements could further improve the number of symptoms that can characterize the fault detection phase if their related thresholds are suitably set. Moreover, a reliable model could also help in the design of the Fault Signature Matrix by adding extra features that cannot be directly extracted from measurements. The model described in

[1] It is worth remarking that a residual is a difference between the measure and its reference value. As shown in section 3.3.1 the threshold is set as function of the reference value; thus, if the measure is beyond the threshold (i.e., the residual is higher than the nominal region) the related symptom is activated and the detection phase can be applied.

the following is thus the framework of the Fault Detection and Isolation algorithm and the starting point for the development of both fault mitigation strategies and a lifetime estimation tool. Furthermore, it could be the frame in which information derived from EIS- and ECM-based algorithms are combined along with conventional signals into an aggregate model for control, diagnosis and lifetime estimation.

## 4.2 The dynamic SOFC stack lumped model

A lumped dynamic modelling approach has been adopted to simulate the electrochemistry of the SOFC stack, while guaranteeing a good trade-off between accuracy and computational burden. The model herein presented is a follow-up of previous works [193] and [194], dealing with SOFC systems, developed and validated in the framework of the European Project Diamond. Marra et al. [193] simulates a conventional system, in which all BoP components (i.e. Stack, Postburner, Heat exchanger) are thermally insulated, while Gallo et al. [194] simulates an Integrated System Module (ISM), in which all ancillaries are integrated with the stack in a box and exchange heat through conduction, convection and radiation mechanisms. In both models ([193] and [195]) the system components, including the stack, have been developed by applying the energy conservation principle to each one of them. As a consequence, their dynamic behaviour is represented as a first order time-differential equations system. Even in this case, the same approach has been adopted. A general-purpose mathematical software tool, i.e. MATLAB®, is adopted to develop the simulation code and particularly the SIMULINK environment to perform the dynamic model simulation. The dynamic stack model has been extracted and suitably adapted to estimate the behaviour of a 6-cell short stack made by SolidPower (SP) and tested by DTU and CEA. The dynamic behaviour is herein developed by applying the energy conservation principle, through a a first order time-differential system.

The following assumptions were made:

*i)* negligible pressure drop;

*ii)* negligible variation of gases sensible heat;

*iii)* dynamics of electrochemistry and mass transfer phenomena much faster than thermal one;

*iv)* gases and solid temperature equal at the outlet section;

*v)* outlet gas composition species considered in chemical equilibrium and the fuel supposed to be totally reformed in the anode side of the stack;

*vi)* only one outlet temperature considered as state variable of the gas instead of the anode and the cathode one.

According to these hypotheses, the energy balance reads as follows:

$$K\frac{dT}{dt} = \dot{E}_{in} - \dot{E}_{out} + \dot{Q} - P \tag{4.1}$$

In the energy conservation principle here applied, $K$ is the stack heat capacity, $T$ is the stack outlet temperature, $\dot{E}_{in}$ and $\dot{E}_{out}$ are the inlet and outlet energy flows respectively, $P$ is the electrical power and $\dot{Q}$ is the heat exchanged in case of non-adiabatic conditions. For more information about the thermal exchange among the BoP components, the reader is addressed to [194]. The eq. 4.1 can be detailed as:

$$K_{FC}\frac{dT_{FC,out}}{dt} = \dot{E}_{FC,in} - \dot{E}_{FC,out} - V_{FC}\cdot I_{FC} + \dot{Q} \tag{4.2}$$

where $K_{FC}$ only accounts for the solid part (e.g. cell trilayers and interconnects), it was identified against experimental data in [193] and herein adopted. $\dot{E}_{in}$ and $\dot{E}_{out}$ are the gases energy flows at the inlet and outlet sections of the stack, respectively, calculated according to the following equations:

$$\dot{E}_{FC,in} = \sum \dot{n}_{i,in} \cdot h_i(T_{an,in}) + \sum \dot{n}_{j,in} \cdot h_j(T_{ca,in}) \tag{4.3}$$

$$\dot{E}_{FC,out} = \sum \dot{n}_{i,out} \cdot h_i(T_{an,out}) + \sum \dot{n}_{j,out} \cdot h_j(T_{ca,out}) \quad (4.4)$$

The footers $i$ and $j$ stand for the chemical species at the anode and the cathode side respectively, as follows:

$$\begin{cases} i = [H_2, H_2O, CH_4, CO, CO_2] & anode\ side \\ j = [O_2, N_2] & cathode\ side \end{cases} \quad (4.5)$$

The molar flow rates $\dot{n}_i$ are calculated by solving the following equations systems, which represent the mass balance of the elements/compounds in the anode and cathode sides, respectively:

$$anode: \begin{cases} \dot{n}_{H_2,out} = \dot{n}_{H_2,in} + 3 \cdot \dot{r}_{ref} + \dot{r}_{shift} - \dot{r}_{ox} \\ \dot{n}_{CH_4,out} = 0 \\ \dot{n}_{CO,out} = \dot{n}_{CO,in} + \dot{r}_{ref} - \dot{r}_{shift} \\ \dot{n}_{CO_2,out} = \dot{n}_{CO_2,in} + \dot{r}_{shift} \\ \dot{m}_{H_2,out} + \dot{m}_{H_2O,out} + \dot{m}_{CH_4,out} + \dot{m}_{CO,out} + \dot{m}_{CO_2,out} = \\ \quad = \dot{m}_{H_2,in} + \dot{m}_{H_2O,in} + \dot{m}_{CH_4,in} + \dot{m}_{CO,in} + \dot{m}_{CO_2,in} \\ k_{shift} = \frac{X_{H_2,out} \cdot X_{CO_2,out}}{X_{CO,out} \cdot X_{H_2O,out}} = \frac{\dot{n}_{H_2,out} \cdot \dot{n}_{CO_2,out}}{\dot{n}_{CO,out} \cdot \dot{n}_{H_2O,out}} \end{cases} \quad (4.6)$$

$$cathode: \begin{cases} \dot{n}_{O_2,out} = \dot{n}_{O_2,in} - 0.5 \cdot \dot{r}_{ox} \\ \dot{n}_{N_2,out} = \dot{n}_{N_2,in} \end{cases} \quad (4.7)$$

Considering the methane reforming, water-gas shift and electro-oxidation reactions described in the equation below, the molar flow rates $\dot{n}_i$ are calculated through the evaluation of the reaction rates of each species and considering the aforementioned assumption $(v)$:

$$\begin{cases} CH_4 + H_2O \rightarrow 3H_2 + CO & \text{reforming} \\ CO + H_2O \rightarrow CO_2 + H_2 & \text{water gas shift} \\ H_2 + \frac{1}{2}O_2 \rightarrow H_2O & \text{electro-oxidation} \end{cases} \quad (4.8)$$

where $\dot{r}_{ox}$ is the reaction rate of the electro-oxidation reaction and it can be easily derived through the Faraday's law:

$$\dot{r}_{ox} = \frac{I}{2F} \quad (4.9)$$

These equations can be solved by assuming the equilibrium constant of the water-gas-shift reaction, $k_{shift}$, calculated as function of the anode outlet temperature:

$$k_{shift}(T_{FC,out}) = e^{\frac{-\Delta G_{shift}(T_{FC,out})}{R \cdot T_{FC,out}}} \tag{4.10}$$

where $\Delta G_{shift}$ is the variation of the Gibbs Free Energy of the water gas shift reaction, calculated as follows:

$$\Delta G_{shift}(T) = \Delta H_{shift}(T) - T \cdot \Delta S_{shift}(T) \tag{4.11}$$

where $\Delta H_{shift}$ and $\Delta S_{shift}$ are the enthalpy and the entropy variations associated to the water gas shift reaction (see eq.4.8), respectively. Considering specific molar values, the Gibbs free energy is calculated according to the following equations:

$$\Delta g_{shift}(T) = \Delta h_{shift}(T) - T \cdot \Delta s_{shift}(T) \tag{4.12}$$

$$\Delta h_{shift}(T) = h_{CO_2}(T) \cdot h_{H_2}(T) - h_{CO}(T) - h_{H_2O}(T) \tag{4.13}$$

$$\Delta s_{shift}(T) = s_{CO_2}(T) \cdot s_{H_2}(T) - s_{CO}(T) - s_{H_2O}(T) \tag{4.14}$$

The electrochemistry of the stack is modelled through an Area Specific Resistance (ASR) approach [196]. The cell voltage is thus evaluated as follows:

$$V_{FC} = V_{cell} \cdot n_{cells} = n_{cells} \cdot (V_{Nernst} - J \cdot ASR - V_{off}) \tag{4.15}$$

$$V_{Nernst} = \frac{-\Delta G(T_{FC,out})}{n_{el} \cdot F} - \frac{R \cdot T_{FC,out}}{n_{el} \cdot F} \cdot \ln(\frac{\bar{p}_{H_2O}}{\bar{p}_{H_2} \cdot \bar{p}_{O_2{}^{\frac{1}{2}}}}) \tag{4.16}$$

$$ASR = ASR_0 \cdot e^{\frac{E_a}{R} \cdot (\frac{1}{T_{FC,out}} - \frac{1}{T_0})} \tag{4.17}$$

The electrochemical sub-model accounts for the Nernst potential, polarization losses and the offset voltage $V_{off}$, which can be ascribed to the cell crossover of gases at open circuit (eq. 4.15); $J$ is the current

density. The Nernst potential, $V_{Nernst}$ is calculated through eq. (4.16), where the average values of gas concentrations (i.e. partial pressure) are calculated between the stack inlet and outlet sections. With reference to the ASR approach, $ASR_0$ is the Area Specific Resistance at the reference temperature $T_0$ and $E_a$ is the activation energy. The parameters $ASR_0$, $E_a$, $T_0$ and $V_{off}$ need to be identified against experimental data for a properly characterization of such system.
Usually, during the lab tests, the stack is surrounded by a furnace for a proper regulation of the temperature and to reduce thermal spikes that in a real environment could occur. Thus a related modelling of such effect needs to be considered. Assuming that the used dataset refers from systems surrounded by a furnace, the stack model is thus improved by considering its temperature $T_{furnace}$ and the related dynamics $K_{furnace}$ that affect the stack outlet temperature as well. Particularly, the furnace effect is modelled as a convective exchange whose coefficient $h_{conv}$ needs to be identified against experimental data. The furnace exchange is estimated as:

$$\dot{Q}_{furnace} = h_{conv} \cdot A_{Stack} \cdot (T_{furnace} - T_{Stack}) \tag{4.18}$$

where the $A_{Stack}$ is the surface area of the stack involved into the convective exchange, while $h_{conv}$ is the heat transfer coefficient of the air inside the furnace. Moreover, it is worth remarking that the furnaces pushes the stack to have an overall thermal dynamics notably slower than the isolated case. Thus, for the sake of modelling, the $K_{furnace}$ parameter, properly identified against experimental data, is clearly considered in the dynamics evaluation of the stack as well.

It is worth remarking that, to develop a fast and reliable SOFC stack model, the MATLAB/SIMULINK environment has been chosen. This allowed to apply a model-in-the-loop technique to abstract the Fuel Cell behaviour in a way that the described dynamic lumped model could be used to test, simulate and also be validated by using the measured data from experimental campaign as inputs. Furthermore, such programming environment allowed to have a model ready to be converted in C-language for its possible future control- and diagnostic- oriented applications, to be run in parallel with the real system.

The Parameters identification and the validation of the model has

been tuned up upon experimental data provided in frame of the IN-SIGHT project and measured by DTU on the 6-cells SolidPower short stack fed by Hydrogen/Nitrogen. The test protocol has been defined within the project to infer on the Fuel Starvation effect, performed by changing the $\dot{n}_{H_2}$ during the Fault Starvation test n.1 and varying the load (i.e. current) during the test n.2. Figure 4.1 describes the adopted test plan along with the usage of the data for parameters identification and model validation. For further details about the experiments the reader is addressed to section 3.2.

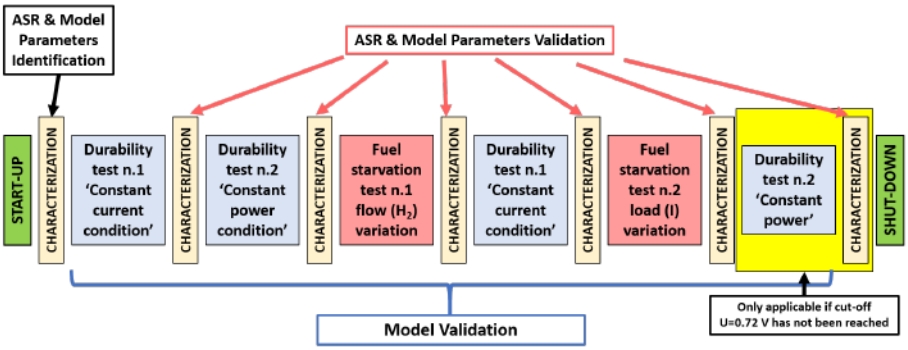


**Figure 4.1:** Test program overview of the experimental data recorded by DTU. The characterization tests are performed at different loads to perform the V-I curves, whereas the durability tests are performed at constant current or power. The two fuel Starvation tests are operated with a F.U. stepwise increase by changing the load or the $\dot{n}_{H_2}$ inlet flow respectively.

It is worth commenting that the first ASR parameter identification has been performed against the first characterization test whereas the other tests are used for their validation. Finally the durability and fuel starvation tests are exploited for the complete model validation.

### 4.2.1 Parameters identification

The parameters identification phase is crucial in any model development process, particularly for a lumped model, where the accuracy in the selection of the lumped parameters and its correct identification guarantees the quality of the representation of the physical processes. Indeed, such parameters might usually lead to uncertainties/inaccuracies

generated by the simplifications made; on the other hand they push the modelling toward the reduction of the computational burden with respect to the physical content of the results; this allows developing a fast model capable of running in parallel with the real system.

The main challenge faced in this dataset handling was the lack of some important measurements within the stack, such as the gas composition, the thickness, the porosity and others; to overcome this issue, a parameters identification procedure was developed, involving both experimental and simulated data.

The model has been was fed with measured data provided in the frame of the INSIGHT project, i.e. mass flow rates, gas compositions and temperatures at stack inlet, voltage and current. The parameter identification procedure entailed three steps, as shown in figure 4.2:

1. Feeding the model with the information related to the input flows and temperatures, current and outlet temperature, the minimization on the Voltage can be performed to identify the ASR parameters (i.e. $ASR_0$, $E_a$, $T_0$ and $V_{off}$) of eq. 4.17. This can be done in stationary conditions, mainly during the characterization tests, whose aim was to produce the V-I curves;

2. Once identified such parameters, the voltage has been modelled, and the minimization routine on the temperature was run; this allowed to identify the thermal dynamics of both stacks and furnace, along with the convective heat exchange $h$ of the surrounding, used to model the furnace effect. For this identification the V-I curves of the characterization tests were used to properly tune the thermal dynamics.

3. Finally, the complete data set has been exploited to validate the model outputs, particularly for voltage and stack outlet temperature.

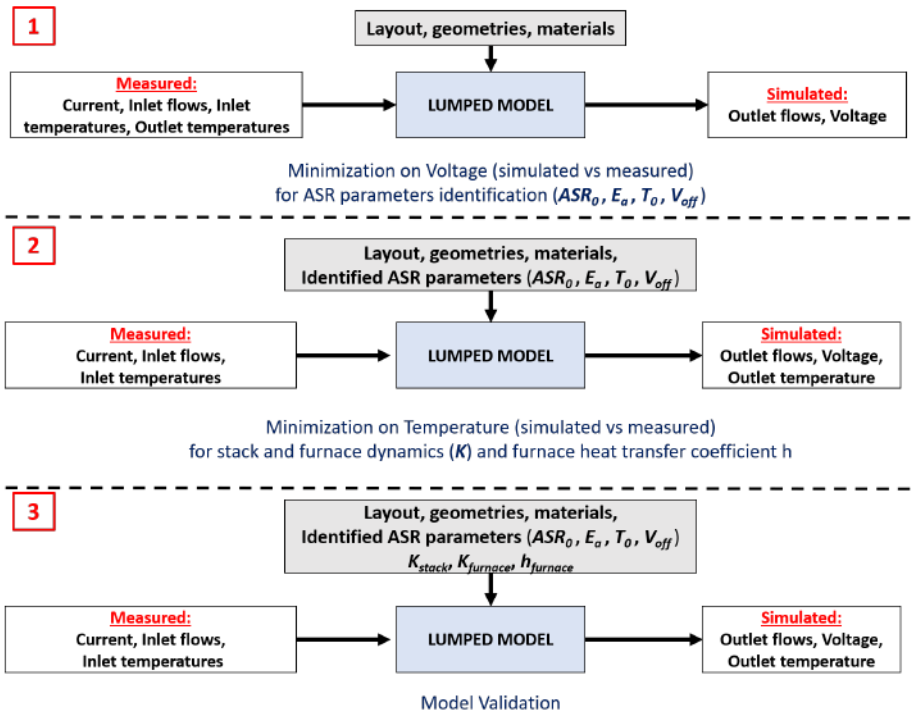


**Figure 4.2:** Identification process scheme. The parameters identification involved three steps, during which the model inputs and the measured/simulated outputs are suitably defined to identify the ASR parameters, the thermal coefficients and to perform the complete model validation.

The minimization problem has been accounted by minimizing the mean squared error (MSE) between the experimental and simulated voltage/temperatures of the stack. So, the minimization is achieved by identifying the parameter values are that bring the error under a defined tolerance value, as follows:

$$MSE = \frac{1}{N}\sum_{N}(X_{measured} - X_{simulated}(\underline{p}))^2 \tag{4.19}$$

where $X$ is the temperature or the voltage, $N$ is the number of the measured/simulated points and $\underline{p}$ is the vector of the parameters to be identified.

As aforementioned, the parameter identification process entailed the exploitation of the V-I experimental curves to clearly identify the parameters for voltage estimation. Figure 4.3 shows the experimental inputs of the real system applied for each characterization test and here reported for the first one, used for the identification of the ASR parameters (phase 1 of figure 4.2). Particularly, the main measurements of the current (figure 4.3 A) ), voltage (figure 4.3 B) ) and the temperatures of the flows at intlet (figure 4.3 C) ) and at the outlet (figure 4.3 D) ) are reported along with the furnace imposed temperature (figure 4.3 D) ). This test lasted about 40 minutes and consisted in a stepwise increase of the load from 4 A to 40 A with a constant inlet flow.

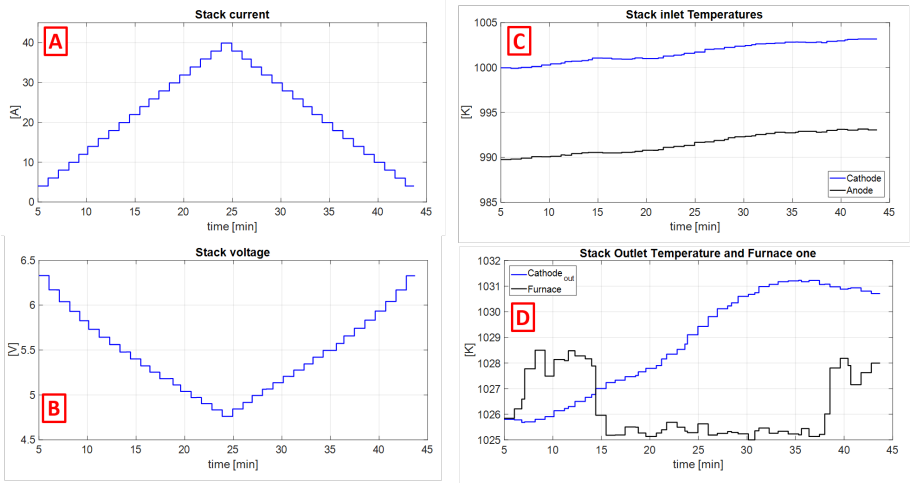


**Figure 4.3:** Stack measurements during characterization test n.1

The ASR-based voltage parameters, namely $ASR_0$, $E_a$, $T_0$ and $V_{off}$, are the identified by minimizing the mean squared error (MSE) between the experimental voltage and the estimated one, defined by the eqq. 4.15-4.17. The Nernst voltage is then simulated according to eq. 4.15, where the inlet flows are measured and the outlet ones are derived by the model fed by all measured variables (i.e., inlet flows, current, voltage, outlet temperature, etc.). Figure 4.4 shows the reliability of the parameters identification. Particularly, figure 4.4 A) shows the comparison between the measured voltage and the simulated one with respect

to the time, whereas figure 4.4 B) presents the V-I curves derived from the measured and simulated voltage respectively. It is worth commenting that in this preliminary stage of the voltage identification, the outlet stack temperature namely $T_{stack,out}$, of eqq. 4.16 and 4.17 is the cathode outlet measured one, according to the hypothesis *vi* of section 4.2.

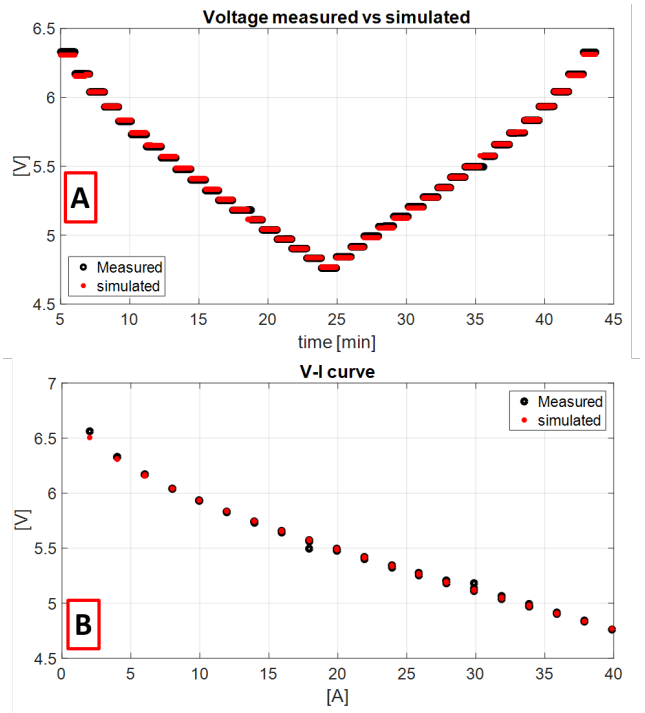


**Figure 4.4:** Voltage model parameters identification. The red markers represent the simulated voltage while the black ones represent the measured ones. A) shows the voltage trend over time whereas B) presents the V-I curve.

To verify the quality of the minimization problem adopted for the parameter identification, a correlation graph is herein presented. It is worth remarking that identification data (circle markers) present a good correlation due to the minimization function adopted for the ASR approach (see eqq. 4.16 and 4.17), while validation data (star markers) show a relative error lower than 1%.

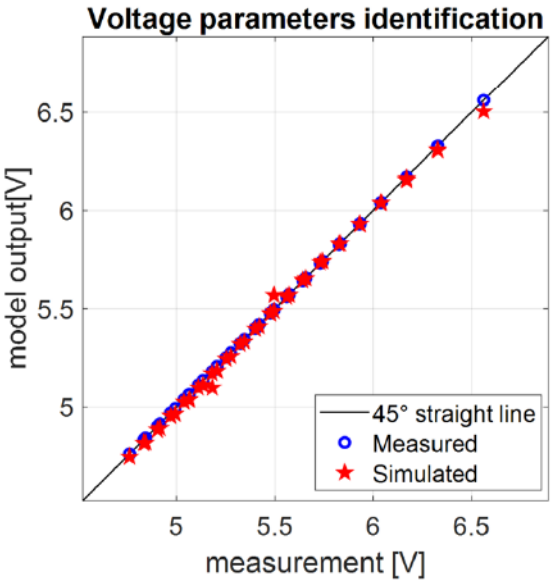


**Figure 4.5:** Correlation graphs of the ASR approach validation.

After the voltage parameters identification and the implementation of the electrochemical model, the $T_{stack,out}$ is simulated through the balance equation described in eq 4.18 along with the voltage. This allows to perform a thorough validation of the model. Here an identification of the $K_{stack}$ is performed to have a good match of the simulated temperature with the measured one over time. It is worth remarking that, due to the hypothesis *vi* of section 4.2 an error in the model is expected; nevertheless, it allows having a good trade-off between accuracy and computational burden, as reported in section 4.1. Figure 4.6 A) shows the stack voltage while Figure 4.6 B) shows the stack outlet temperature, both figures present the comparison of simulated against measured variables.

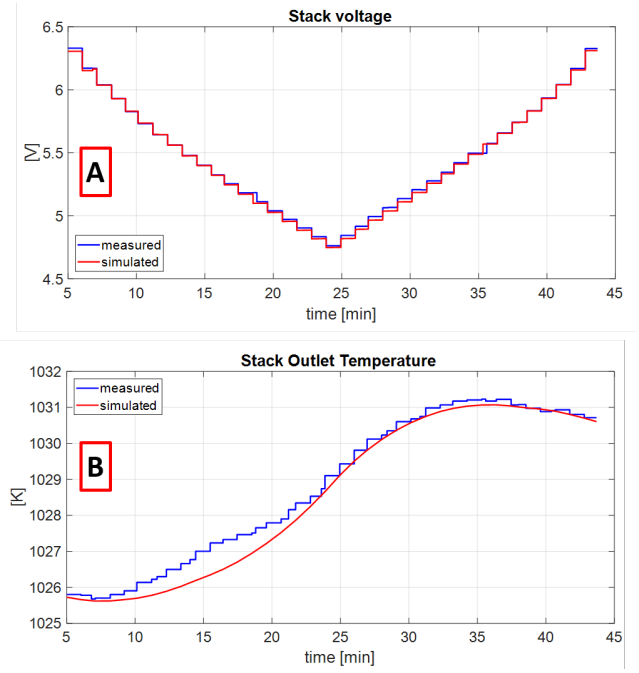


**Figure 4.6:** Parameter validation against the characterization test of voltage (figure A) and stack outlet temperature (figure B). The measured variable is coloured in blue whereas the simulated one is sketched in red.

According to the figure, the simulated stack voltage well fits the experimental data, with a relative error lower than 1%. Looking at the cathode outlet temperature and considering that the flow is kept constant, a step-wise shape similar to that one of the voltage (even if in reverse) is expected; however, the thermal dynamics is highly affected by the furnace, whose lumped heat capacity ($K_{furnace}$) is notably higher than the stack one, thus overlapping the expected behaviour of the temperature and imposing a thermal dynamics of a one order of magnitude higher than that one of the stack.

Table 4.1 resumes the identified values of the lumped dynamic model parameters achieved by means of the process described in figure 4.2. Particularly, the parameters referring to the ASR, the dynamics of the stack and the furnace effect are reported.

| **Parameter** | $\mathbf{K_{stack}}$ | $\mathbf{ASR_0}$ | $\mathbf{E_a}$ | $\mathbf{T_0}$ | $\mathbf{V_{off}}$ | $\mathbf{h_{conv} \cdot A_{stack}}$ |
|---|---|---|---|---|---|---|
| **Value** | $15\ JK^{-1}$ | $0.4795\ \Omega cm^2$ | $59441\ Jmol^{-1}$ | $1003\ K$ | $0.030654\ V$ | $7.25\ WK^{-1}$ |

**Table 4.1:** Identified stack model parameters.

### 4.2.2 Validation and Results

According to the Experimental test protocol presented in Figure 4.1, the model has been tested and validated against experimental data provided by DTU on the 6-cell short stack. The lumped approach adopted ensures a good trade-off between accuracy and computational burden. Indeed, the model simulates more than 800 hours in less than 120 seconds with an error in voltage and temperature less than 1% in nominal conditions. This proves its applicability for the online monitoring of the FC.

Some relevant measures of the DTU dataset are presented in figure 4.7, namely current (A), voltage (B), fuel utilization (C) and temperature (D). Particularly, the experimental dataset used for the validation consisted in the 3 durability tests and the 2 fuel starvation ones as highlighted in different colours in figure 4.1. It is worth nothing that the characterization tests have been used only for the parameters identification and neglected during the long term simulation to avoid modelling interruption due to the shift of the operating condition in OCV mode. Indeed, the model has been built for $i > 0$ and thus not applied for the OCV conditions that are those time intervals filled with grey color in the figure 4.7.

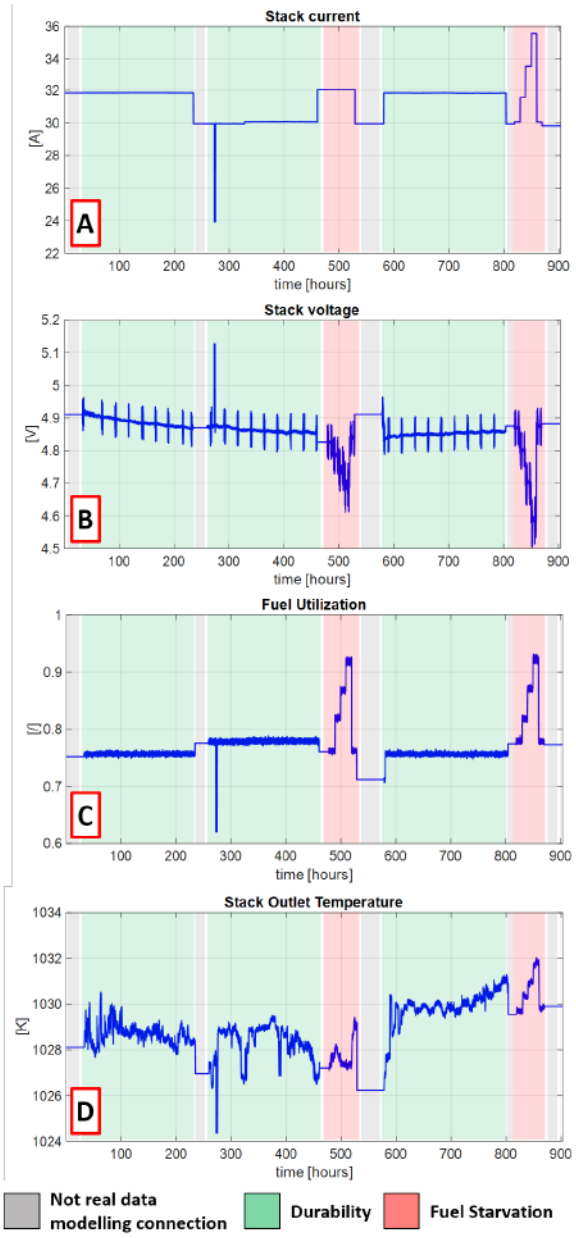


**Figure 4.7:** The experimental data set. A) is the current, B) is the voltage, C) is the Fuel Utilization and D) is the stack outlet temperature. All data shown are measured/set. The data in grey area are not real but added for modelling purposes.

As already presented, the complete test protocol entailed two contiguous "durability" tests at different loads (green areas), a starvation test performed by changing the fuel flow at constant current (red area), followed by a third "durability" test (green area) and, finally, a second starvation test conducted by changing the current at constant fuel flow (red area). Since the OCV conditions have been neglected from measurement, a constant conditions (filled with grey color in figure 4.7) have been added between each tests to merge them without interrupting the simulation; therefore, such data are not representative for the analysis of the results. Moreover, the spikes in voltage (see figure 4.7 B) refer to the EIS measurements performed during the test, and described in section 3.2. Indeed, during an EIS measurement, the perturbation is superimposed on the stable current set point: the FC presents a fluctuation in the voltage, whose frequency and amplitude depends on the stimulus amplitude, the wave form of the imposed signal and on the relaxation times of the main electrochemical processes occurring. For modelling purposes these spikes are not relevant for the monitoring of the stack, since their occurrence is limited in time and, considering the slow thermal dynamics, they have no effect on the other variables; Nevertheless, they can give an hint on the time at which the EIS measurement is performed, so they can graphically link the diagnostic measurement within the experimental campaign. Moreover, it is worth adding a comment on the spike at 280 h. It is an unexpected behaviour of the stack, likely due to an immediate change in the fuel flow; however, such behaviour is instantaneous so not relevant for the analysis as well as does not worsen the modelling results for monitoring and diagnostic purposes.

The experimental campaign has two main aims: to test and validate the model and to infer on degradation and malfunctioning of the system as well. The lumped dynamic model has been applied on the complete available dataset, and the comparison between the experimental data and the results of the lumped dynamic model are presented in Figure 4.8. More than 800 hours of experimental testing have been simulated in less than 2 minutes, proving the feasibility of the application of the lumped approach for on-line monitoring purposes. Particularly, figure 4.8 A) shows the comparison of the measured voltage with the simulated ones, whereas the temperature comparison is presented in figure 4.8 B).

Here the coloured areas distinguish the different tests according to the color used in the previous figures.

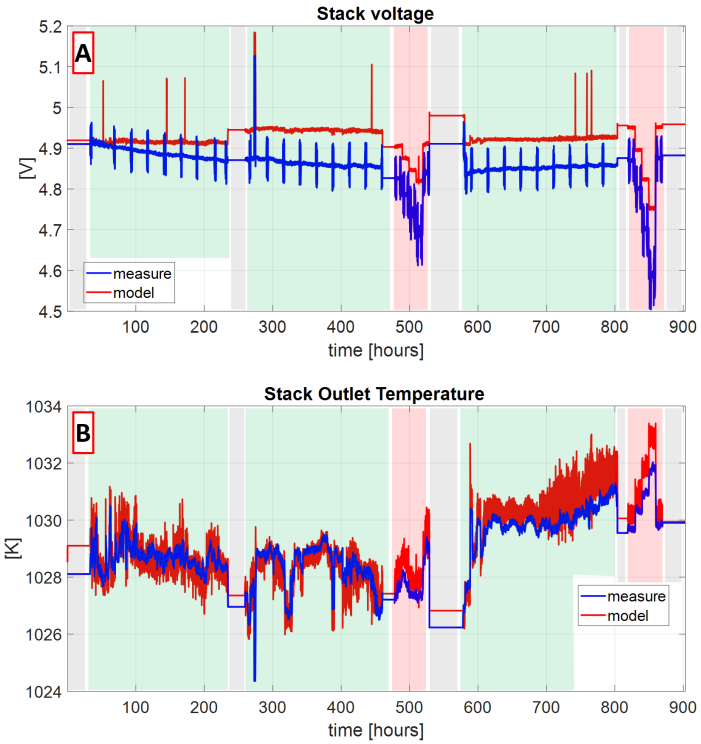


**Figure 4.8:** Comparison of experiments with respect to the model outputs. In A) the voltage comparison is presented whereas B) shows the simulation of the stack outlet temperature with respect to the cathode outlet measured one.

Looking at the voltage, the blue spikes in the measured data refer to the perturbations due to the EIS measurements and thus they should be neglected. On the other hand, the red spikes in the modelling results are related to some mathematical issues occurring in a short time window; they are related to some high non linearities in the solution of the differential equations governing the lumped modelling. Since they are instantaneous they are not reliable and can be easy considered as outliers, thus negligible in the overall analysis of the physical model adherence.

Model parameters have been identified using the V-I curves and the

initial conditions data at t=0 for both voltage and temperature, whose comparison is presented in Figure 4.8 A) and B) respectively. It is worth remarking that, due to the modelling hypothesis described in section 4.2, the representative simulated stack outlet temperature is assumed as an averaged outlet temperature of the two electrodes, lumped state variable of the Stack outlet. This helps in simplifying the stack modelling approach and in sensibly reducing the computational burden of the approach, thus reflecting in a fast model able to provide estimation in a couple of seconds.

From Figure 4.8, it is interesting to note how both the simulated voltage and temperature have a quite good matching with their respectively measurements. For the evaluation of the accuracy of the model outcomes, the percentage error is then calculated as:

$$\epsilon_x = \frac{|x_{measure} - x_{model}|}{x_{measure}} \cdot 100\% \tag{4.20}$$

where x is voltage or cathode/stack outlet temperature.

Figure 4.9 reports the two percentage errors. It is worth commenting that the highest error in voltage estimation (figure 4.8 A) ) is less than 2% with respect to a nominal condition (e.g. during a "durability" test) and less than 5% during an induced faulty condition (e.g. during the two fuel starvation tests). For the temperature comparison of figure 4.8 B), the maximum error is less than 1% in both nominal and faulty conditions, thus proving the reliability of the model on the temperature since it is not highly affected by the changes in the F.U. due to the furnace effect. It is clear that the EIS measurements are not accounted by the model and the perturbation signal imposed for such measurements is not considered in the current value, input of the model; thus, when EIS measurement is performed, a very high percentage error in the model simulation, not relevant for the model validation, is observed.

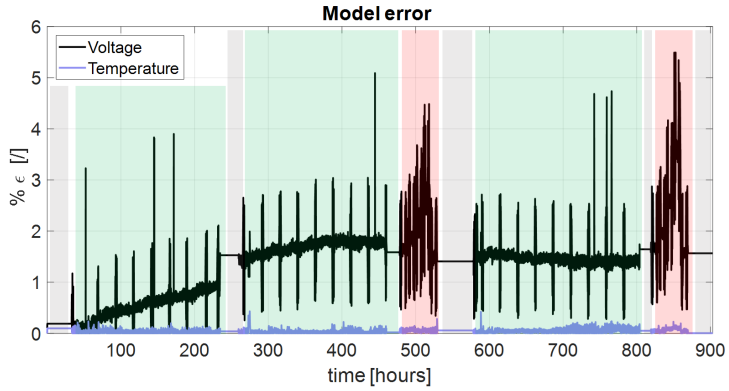


**Figure 4.9:** Percentage model error. The error has been evaluated as the ratio of the difference between real and modelled values with respect to the real ones.

The first "durability" test clearly shows a degradation in the voltage that can be ascribed to a natural ageing of the stack. Its behaviour suggests a linear trend that can be identified by means of linear decreasing function of the time:

$$V_{aging} = r \cdot t \tag{4.21}$$

where $r$ is the natural ageing degradation rate. From the "durability" test n.1, a loss of 0.045V in 200h has been evaluated, so the $r$ can be set to 0.225mV/h. By including the ageing model (4.21) into the voltage sub-model as a further time-dependent loss, the eq. 4.15 becomes:

$$V_{FC} = V_{cell} \cdot n_{cells} = n_{cells} \cdot (V_{Nernst} - J \cdot ASR - V_{off}) - V_{aging}(t) \tag{4.22}$$

The results of the model (4.22) are shown in figure 4.10 that reports the time window 0-220 h ("durability test" n.1). The upper figure A) shows the comparison between the measured voltage, the simulated one without any time-dependent loss and the simulated one with the natural ageing, while B) reports the temperature comparison. The improvement in voltage simulation is evident, whereas the temperature does not present any sensible variation, being its modelling error very limited and

not really affected by a slight change in the voltage due to the furnace effect.

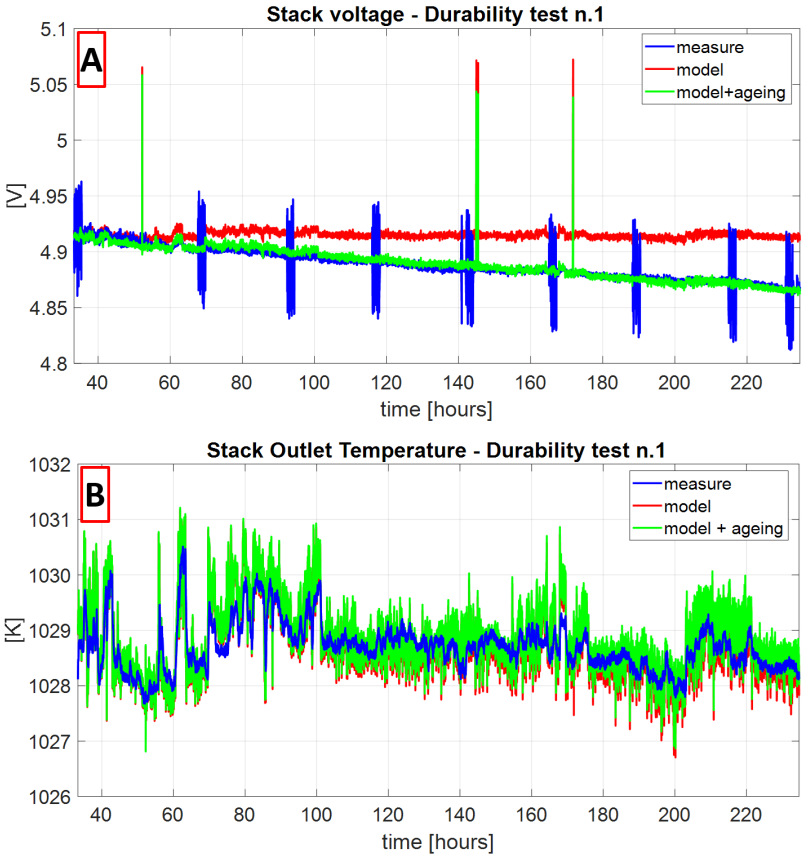


**Figure 4.10:** Natural ageing identification and modelling implementation upon experimental data set "durability test n.1". Here the identified linear degradation rate has been implemented within the model and both voltage (A) and temperature (B) are sketched. Particularly while in red line there is the nominal (i.e. with no degradation) model, in green line the updated model is superimposed on the measurement.

The implementation of such degradation ageing rate on the overall experimental dataset was expected to further reduce the error in simulation. However, the voltage outcome from the updated model sensibly deviated from the measurement, as shown in Figure 4.11, and the related error increased in time. Looking at the figure, it is evident that the identified degradation rate $r$ is relevant in the first part of the experimental data set, but it is not well defined for the entire dataset collected over time. This means that such degradation rate can be ascribed to a local detrimental conditions occurring in stack at the start-up, probably a re-oxidation related to the start up of the system or to a stable condition not yet reached. Consequently, the dataset of the "durability test n.1" is not reliable for the stack modelling and validation because it is not in nominal condition, and then useless for model validation as well.

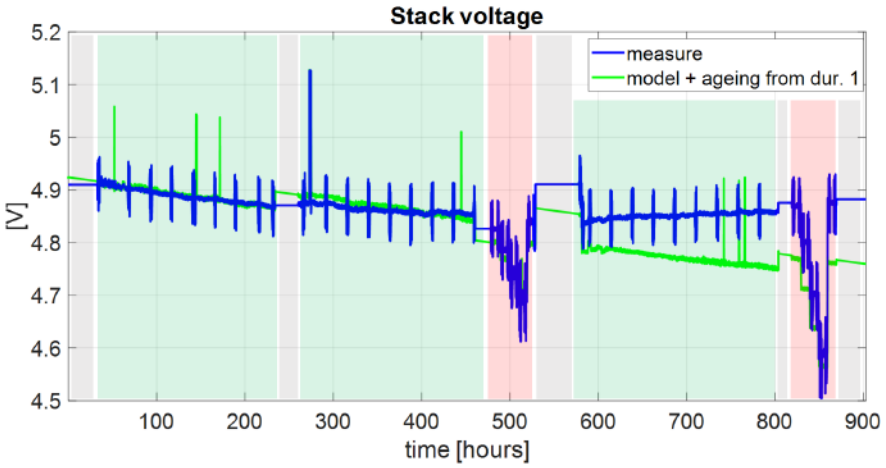


**Figure 4.11:** Voltage estimation from the updated stack model by implementing the ageing degradation rate identified upon "durability" test n.1

To perform the complete validation of the system, the "durability test n.1" has been thus neglected and a re-identification of the voltage model parameter $V_{offset}$ has been done. This allowed to match the new reference voltage without changing the ASR parameters identification performed on the characterization tests already validated. Indeed, this latter validation confirms that the high degradation rate should be related to a dynamic effect on the stack, which shows a strong degradation in the first part of the data-set before reaching a stabilization. Such a behaviour is most likely due to a redistribution of the TPB at the anode side, thus modelled through the $V_{offset}$ parameter.

It is worth commenting that the identified ASR parameters upon the measured V-I curves are not changed, but for the $V_{offset}$, since a unexpected phenomenon occurred, (probably changing the morphology of the anode) and the TPB length, which is directly correlated to the voltage, probably changed as well. Such re-identification is thus necessary due to the new nominal condition achieved, not really related to the operating variables, so much as to the new TPB redistribution at the anode side. Obviously, this is not necessary if a new nominal condition is set upon the changing of the operating variables, since the model is correctly identified on the unfaulty (i.e., healthy) system. On the other hand, if the stack experiences a degradation phenomenon or a malfunctioning, the model will not be able to match the system behaviour if no re-identification of the parameters affected by such degradation phenomenon/fault is performed. The new model validation in terms of voltage and temperature by neglecting the "durability test n.1" is thus presented in Figure 4.12.

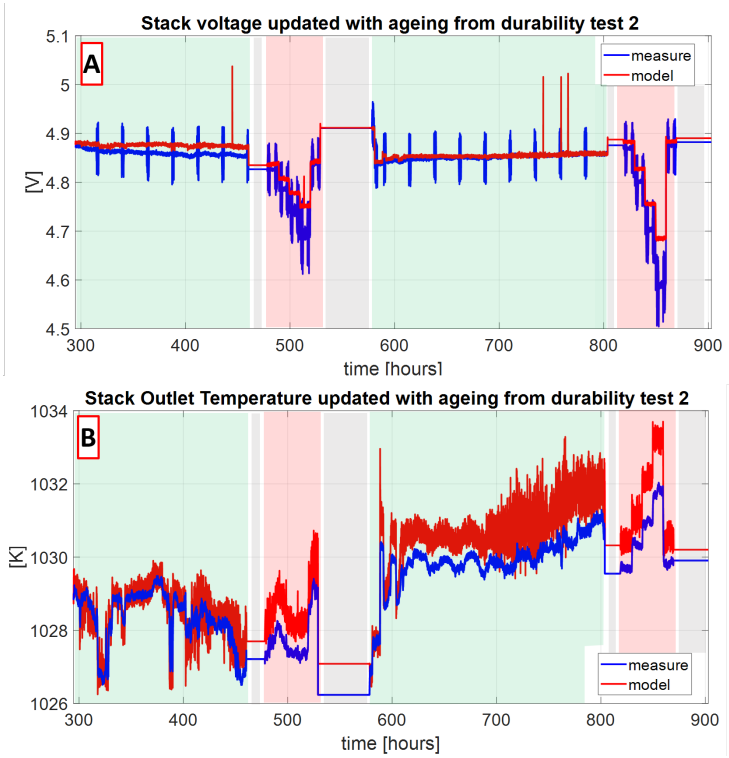


**Figure 4.12:** Dynamic model outputs with re-identified parameters against the updated dataset. It is worth commenting that the model shows a good accuracy with respect to the measured values.

To show the achieved improvement, a comparison of the percentage model errors before and after the re-identification is presented in Figure 4.13, in terms of both voltage (figure A) and temperature (figure B). The improved model with re-identified parameters against the updated dataset presents a percentage error notably lower than the one shown in Figure 4.9, here defined *"complete dataset"*. Indeed, it is possible to note how the error in voltage estimation remarkably decreases with the re-identification process, whereas the temperature one is not really affected by such improvement, whose error is about 0.1% . Particularly, the updated model error is lower than the 0.5%, except when the FC is affected by fuel starvation. In those cases the error is clearly higher, but

it is expected considering the purpose of the lumped dynamic approach: the model has to simulate the nominal expected conditions that can be considered as a reference for the nominal status of the stack. When an unexpected event occurs (i.e. a fuel starvation) the measured data should diverge from the reference modelled value, which simulates the stack in unfaulty conditions. Therefore, an increase in the error of the model during abnormal conditions could trigger the fault detection process thus achieving one of the aim for what such approach has been conceived.

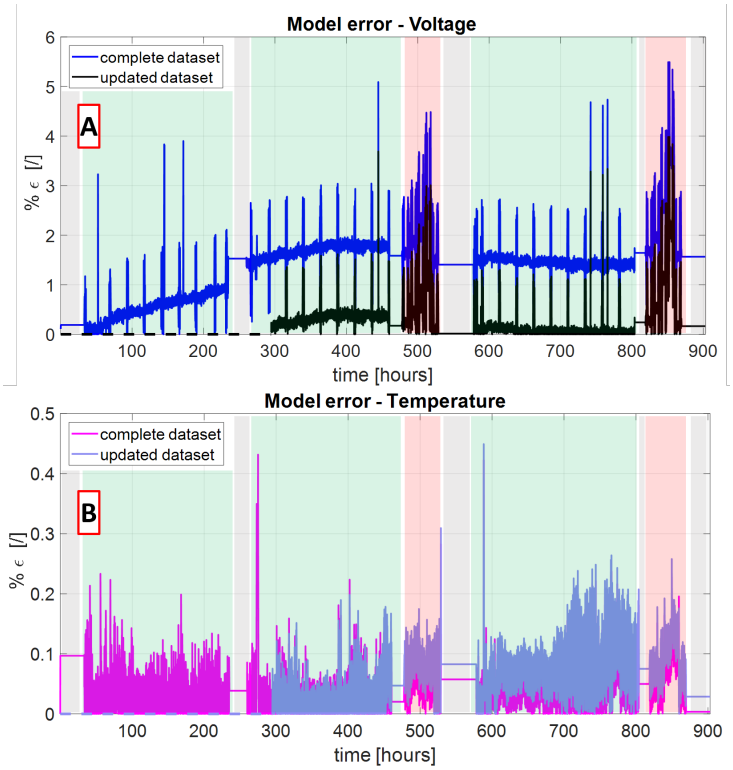


**Figure 4.13:** Percentage model error with re-identified parameters against the updated dataset. The error has been evaluated as the ratio between the difference between real and modelled values with respect to the real measurement, according to eq. 4.20. In the figure the comparison of the errors in voltage (A) and temperature (B) estimation is presented.

The results provided so far demonstrate the model capability of estimating the nominal condition of the 6-cells short stack in terms of voltage and outlet temperature, by feeding it with only information on current, inlet flows and temperature. Furthermore, it is possible to estimate the outlet flows leaving both anode and cathode side, thanks to the eqq. 4.6-4.7; the validation of such variable simulation was not possible due to the lack of proper sensors installed on the real system; however, considering the correlation of the output flows in the Nernst equation (see eq. 4.16) for the voltage sub-model, the reliability of such variables could be confirmed.

### 4.2.3 Results: The Fuel Starvation tests

Once validated the model in nominal conditions it is interesting to study the effect of the fuel starvation through the analysis of the simulations. As described in section 3.2 the DTU experimental campaign contains two fuel starvation tests. The "test n.1" was performed at constant current of 32 A with an increased Fuel Utilization step of 5% by operating on the fuel valve throttle. The second test (named "n.2") was conducted under constant power operating conditions to mimic again the effect of a possible starvation. Here, the constant power mode operations were achieved by regulating the current according to the voltage of the stack and then adjusting the fuel flow to fix the F.U. value. In this case, the fuel starvation was performed by increasing the current during the operation while keeping fixed the fuel flow set point. Both tests were conducted for 50 hours and presented 4 F.U. levels, that are 76.5% (i.e. nominal condition), 82.5%, 87.5%, 92.5%, with a direct return to the nominal condition of 76.5% at the test ending.

- **Fuel starvation test n.1**

  The test was conducted after the "durability test n.2" and required 50 hours. Since the lumped model accounts for inlet flows and temperatures along with the current, the fuel utilization step is properly simulated, as shown in Figure 4.14 A).

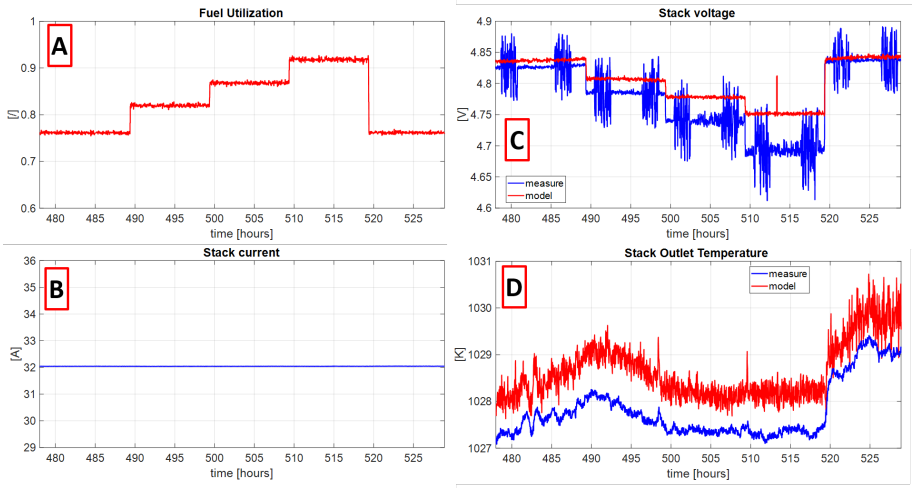


**Figure 4.14:** Fuel starvation test n.1. modelling results. A) Fuel Utilization simulation, B) current, C) comparison (simulated/measured) on the voltage, whereas D) stack outlet temperatures

The voltage estimation presents the same shape of the measured one, but with an evident divergence that can be ascribed to the detrimental effect of the fuel starvation, as shown in figure 4.14 C). Indeed, looking at the figure it is possible to understand that the more is the fuel utilization the more is the divergence between measurement and simulation. On the other hand, the temperature does not appear affected by such condition, as shown in figure 4.14 D) where the model differs from the measurement of just 1 K. This confirms that the model well simulates the dynamics of the stack, while not completely accounting for the electrochemical phenomena within the FC caused by the imposed fuel starvation, resulting in a voltage overestimation. This is expected since the model is conceived to reproduce the nominal behaviour of the stack, with no fault implemented/occurring.

When the fuel starvation is induced, an increase in the error of the model is observed. This allows the detectability of a not expected system condition and could activate an alarm and trigger the fault detection process.

The modelling error (i.e., residual) is shown in Figure 4.15, where the $\Delta V$ presents a stepwise increase with respect to the increasing Fuel Utilization. Such trend is parabolic if compared to the Fuel utilization values, as shown in Figure 4.16, and it can be analysed by exploiting the EIS data collected on such system and used for the FDI algorithm development in Chapter 3.

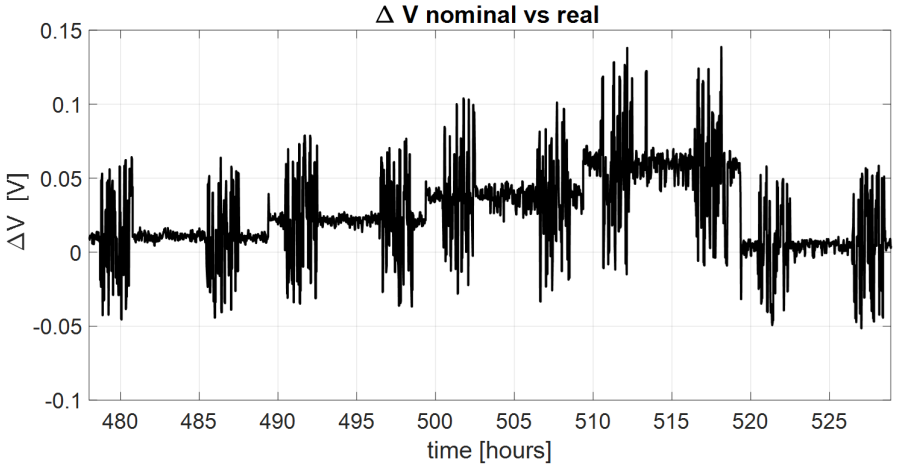


**Figure 4.15:** Stack voltage residual during fuel starvation test n.1. The $\Delta V$ is defined as the absolute value of the difference between measured (faulty) and simulated (nominal) voltage.

Looking at the EIS spectra analysed through the MGFG algorithm and detailed at the low frequency region via *"Partial analysis"* in 3.4, it is interesting to note that the low frequency arc increases at high fuel utilization, as detailed in the FDI paragraph.

Figure 4.16 shows the identified EIS spectra (figure A) along with the extracted relevant ECM parameter trends (figure B). Under fuel starvation, the ECM parameters show an increase of the low frequency element ($R_{LF}$) with a constant behaviour at high frequencies ($R_{CUT}$) and a consequently increase in the total resistance ($R_{TOT}$).

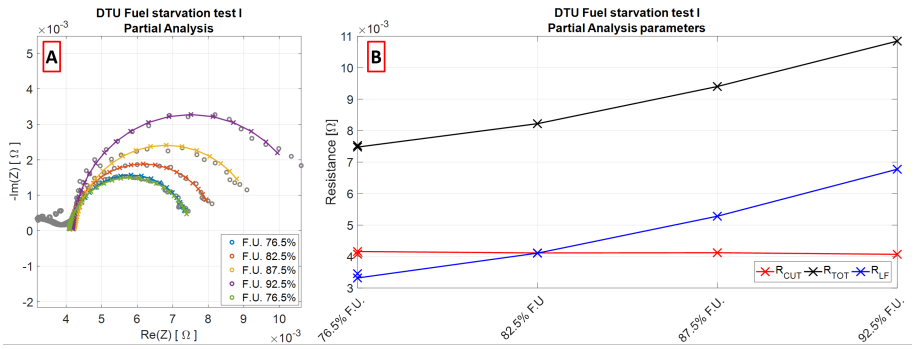


**Figure 4.16:** Fuel Starvation test n.1 - EIS identified spectra (A) and parameter trends (B)

It is possible to state that the increase in $R_{LF}$ immediately reflects in $R_{TOT}$ according to the following equation:

$$R_{TOT} = R_{LF} + R_{CUT} \qquad with \qquad \Delta R_{CUT} \approx 0 \tag{4.23}$$

To investigate a possible correlation between EIS measurements and conventional ones (i.e., voltage, temperature, etc.), the comparison of $R_{TOT}$ trend with voltage residual (nominal/faulty) $\Delta$V is presented in Figure 4.17. It suggests a direct correlation between the considered fault and the evolution of the extracted features by means of the MGFG algorithm.

Therefore, it is evident a link between the electrochemical processes occurring within the Stack and its related voltage measurement.

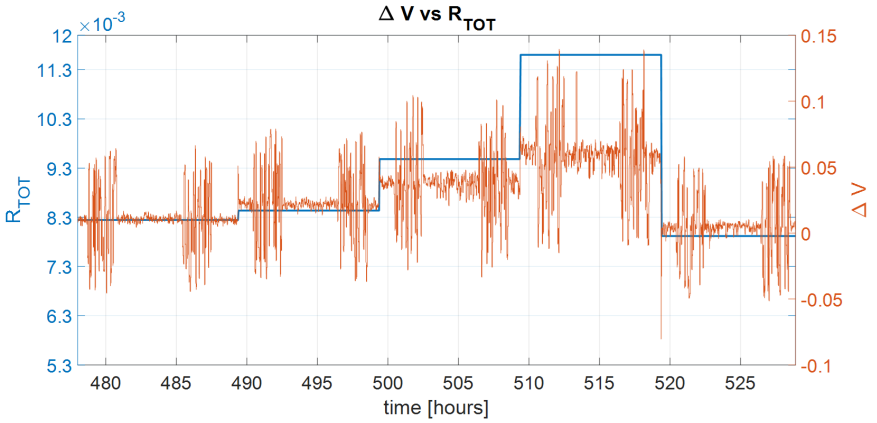


**Figure 4.17:** Fuel starvation test n.1 - Residual voltage (nominal/faulty) vs total resistance trend comparison.

This behaviour suggests a similar dependence of both parameters on the Fuel utilization, likely parabolic, with different coefficients; indeed, if we consider the $R_{TOT}$ at the four F.U. levels it is possible to state that its variation with respect to the F.U. is parabolic.

A similar comment can be done if we average the $\delta V$ for each F.U. step. What does really change is the coefficient that defines the shape of such parabolic trend. Such comment is also confirmed by the fuel starvation test n.2.

This paves the way to further comments and investigations that are described in Chapter 5, where the correlation between the total resistance and the discussed model error is further exploited for RUL estimation.

- **Fuel starvation test n.2**

  The test was conducted after the "durability test n.3" (see figure 4.7) and, even in this case, it required 50 hours. Instead of changing the $H_2$ fuel flow, the fuel starvation test n.2 was performed by varying the load set point. Particularly, the current was set by keeping at constant values both voltage and fuel flow, whose value was defined as function of the nominal conditions.

As already shown in the starvation test n.1, the fuel utilization levels imposed, sketched in figure 4.18 A) are 76.5% (i.e. nominal condition), 82.5%, 87.5%, 92.5%, and a final return to the nominal condition of 76.5% at the test ending, according to a change in current, as shown in figure 4.18 B). Again the voltage estimation presents the same shape of the measured one, with a sensible over-estimation (see figure 4.18 C), while the temperature differs from the nominal one for a couple of degrees, as shown in figure 4.18 D).

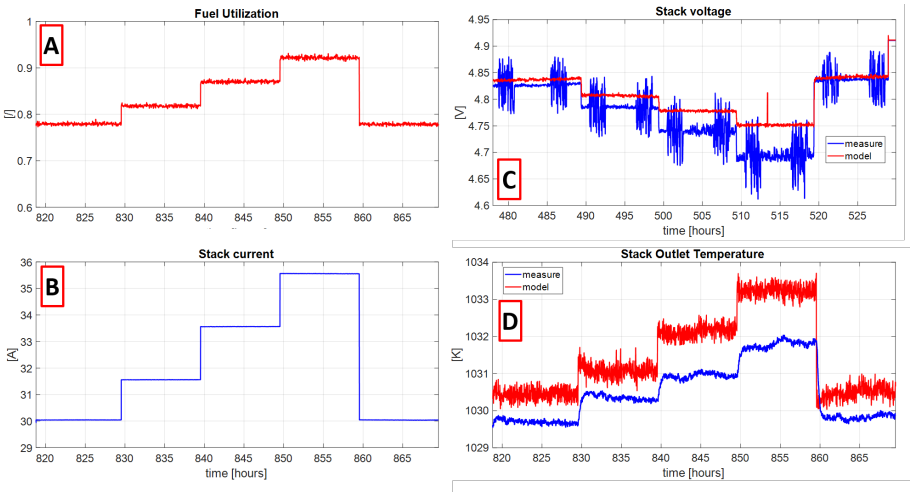


**Figure 4.18:** Fuel starvation test n.2. modelling outcomes. A) shows the Fuel Utilization simulation, B) the current, C)the comparison (simulated/measured) on the voltage, whereas D) shows the stack outlet temperatures

The EIS spectra, analysed through the MGFG Algorithm and detailed at the low frequency region via *"Partial analysis"* (figure 4.19 A) confirms the increase in $R_{LF}$ and $R_{TOT}$ while keeping constant the $R_{CUT}$ (figure 4.19 B).

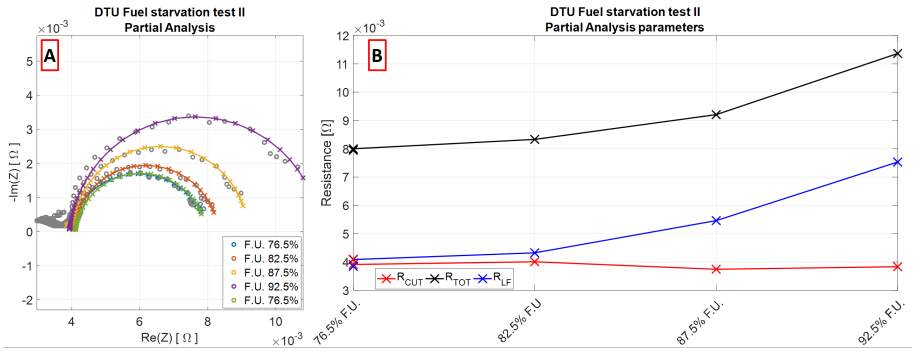


**Figure 4.19:** Fuel Starvation test n.2 - EIS identified spectra (A) and parameter trends (B).

Thus, the comparison of the $R_{TOT}$ trend with respect to the residual voltage (nominal/faulty) $\Delta$V, presented in figure 4.20 A), suggests again the possible correlation between EIS extracted metrics and dynamic measurements; particularly, in this case, the increase of $R_{TOT}$ with the fuel utilization is very similar if compared to the $\Delta$V with respect to that one of the starvation test n.1 and shown in figure 4.20 B).

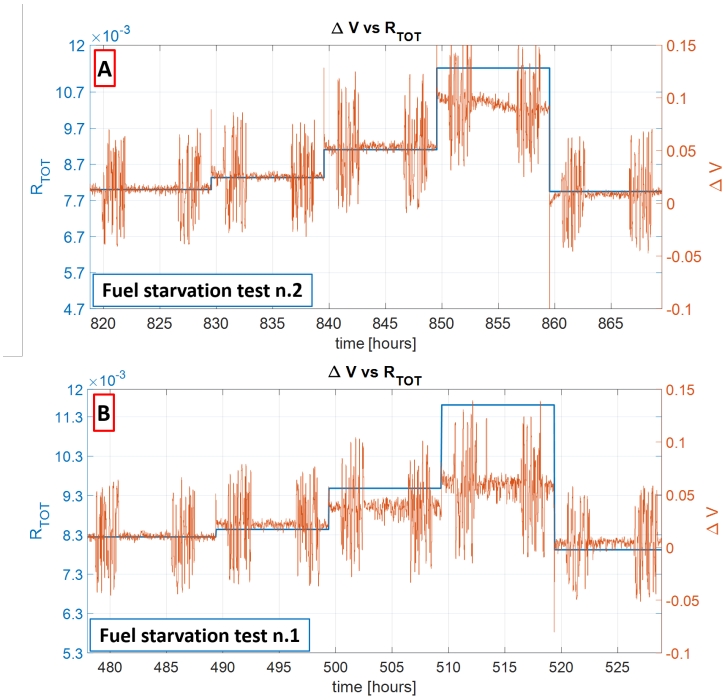


**Figure 4.20:** Residual voltage (nominal/faulty) vs total resistance trend comparison. A) shows the results for fuel starvation test n.2, while B) the ones for the starvation test n.1.

The results provided by the developed lumped model along with the information derived from both conventional measurements and the EIS-based analysis highly suggest their strong dependency for the State of Health monitoring of the FC. By coupling it would be possible to have a clear view on the State of Health of the Stack to perform a lifetime estimation analysis in parallel with a continuous monitoring for diagnostic purposes. Nevertheless, thanks to the flexibility of the EIS technique, a discrete real time updating of the lumped model according to such measurements could be considered to tune the model according the current FC conditions. Moreover, the nominal reference might be updated as function of the operation history and malfunctioning occurring.

# Chapter 5

# Remaining Useful Life

## 5.1 The RUL

The EIS technique is generally applied to gain insight on the State of Health (SoH) of electrochemical devices in a fast and almost not invasive way, to obtain information also on board, as discussed in section 3.5. Indeed, thanks to the information on the several electrochemical phenomena occurring in the cell/stack, on-line diagnosis can be performed during its operation, with no need for conventional manoeuvres (e.g. I-V curves). However, to enhance the lifetime of such systems and their commercialization, a conventional fault detection and isolation algorithm would not be enough. Thus, diagnostic routines should be improved by implementing advanced SoH inference process. Moreover, the combination of diagnostics and mitigation strategies allows extending the Remaining Useful Life (RUL) of such systems, identifying proper countermeasures to cope with the malfunctions occurring within the stack and/or planning the proper maintenance action. A combination of the information derived from conventional measurements along with the in-situ electrochemical ones derived from EIS could help in the real-time natural ageing estimation process. Particularly, from the ECM identified via MGFG algorithm, some characteristic parameters, such as ohmic and total resistances, can be coupled to an Area Specific Resistance (ASR) approach within the lumped model. This allows a real-time tuning of the SoH estimation with updated information on the occurring electro-

chemical process with respect to the nominal (i.e. expected) conditions.

The information derived from the EIS spectrum allows tuning the voltage degradation over time, based on the estimated nominal behaviour provided by the lumped model. Indeed, it will be shown that the time trend of the identified parameters is proportional to the ageing of the cell, if no other abnormal condition occurs. This guarantees an on-line RUL estimation and a more reliable fault diagnosis. The methodology considered for model design consists in a lumped approach, allowing the algorithms to run in parallel with the real system along with the EIS measurements performed at defined intervals according to the monitoring test plan. The features extraction performed through an ECM-based approach allows integrating the real-time information about the system state directly into the voltage estimation.

## 5.2 EIS-based features integration into the lumped model

The stack dynamic model described in Chapter 4 simulates the nominal voltage of the system according to the stack inlet flows and the operating variables, whereas the ECM identified by MGFG Algorithm (introduced in Chapter 3) allows monitoring the changing in the magnitude of the parameters related to electrochemical phenomena via real time measurements.

According to the evidences presented in section 3.4, the $R_{TOT}$ (i.e. the intercept of the Nyquist plot at low frequencies with the Real(Z) axis) is a reliable indicator of the natural ageing of the stack. Indeed, as shown in figure 3.11, a significant degradation in the Fuel Cell shows an increase in both $R_{cut}$ (i.e. the intercept of the Nyquist plot at high frequencies with the Real(Z) axis for the *"partial analysis"*), $R_{LF}$ (i.e. the resistance related to the arc whose characteristic frequency peak is around 10 Hz) and $R_{TOT}$, which is the parameter containing all the losses revealed within the cell.

The variation of the total Resistance ($\Delta R_{TOT}$) can be an indicator of the change in the electrochemistry of the cell and it can be considered as a further voltage loss in the ASR model (see eq. 4.15), as a term ($\eta_{deg}$) related to the degradation, according to the follow equations:

$$\eta_{deg} = i \cdot \Delta R_{TOT} = i \cdot (R_{TOT,t=i} - R_{TOT,t=ref}) \tag{5.1}$$

where the time $t = i$ is the current time of the measurement, whereas $t = ref$ indicates the time of nominal condition taken as reference. As a consequence, the eq. 4.15 can be rewritten as:

$$V_{FC} = V_{cell} \cdot n_{cells} = n_{cells} \cdot (V_{Nernst} - J \cdot ASR - V_{off} - \eta_{deg}) \tag{5.2}$$

### 5.2.1 Algorithm test on experimental data - Data taken from literature

Literature survey proves that the total resistance measured via EIS during long term tests increases with time if no other sudden and unexpected events occur, as reported by Mosbaekaet al. in [197]. According to their measurements, during a long term test of 2500h at steady state operating conditions on a 13-cell stack, the authors found an increase in the ohmic ($R_0$) and polarization ($R_{pol}$) resistances likely linked to the stack degradation rate. Considering the total resistance $R_{TOT}$ as the sum of $R_0$ and $R_{pol}$, its trend seems to be directly correlated to the voltage degradation loss. Thus, improving the ASR approach with an additional degradation term, named $\eta_{deg}$, it is possible matching the natural ageing of the system and thus to perform a RUL estimation as well.

The methodology herein described was preliminary applied to the data presented in [197] to understand its feasibility. In [197] the authors also tested the 13-cells stack during 2500h of operation with 52% fuel utilization and constant current load ($0.1 Acm^{-2}$) at $750C$. EIS measures were taken on a four repeating units with different coatings. Particularly, $\#RU_2$ and $\#RU_4$ presented an expected behaviour with an almost linear increase in both $R_0$ and $R_{pol}$ (and thus $R_{TOT}$ linearly increases as well). Results are shown in figure 5.1, where the evaluation of the nominal behaviour (constant) of the voltage is enriched with the info derived by the EIS-based resistances. The interesting results suggest the effectiveness of such methodology, particularly if applied on-line with real time EIS measurements.

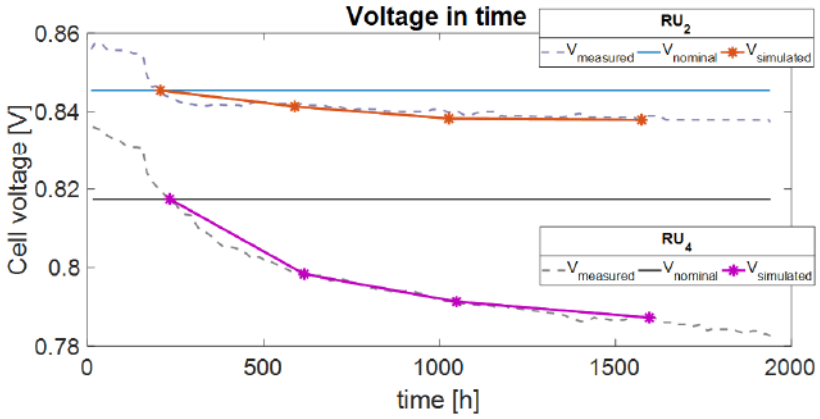


**Figure 5.1:** Voltage simulation coupling ASR approach and EIS features for both $\#RU_2$ and $\#RU_4$. Experimental dataset is taken from [197]. The $V_{simulated}$ is the results of the integration of $\eta_{deg}$ (see eq. 5.2) within the $V_{nominal}$.

Figure 5.1 shows how the nominal voltage ($V_{nominal}$ - blue/black lines), suitably improved with the $\eta_{deg}$ ($V_{simulated}$ - orange/pink lines) according to eq. 5.2, interestingly matches the measured voltage ($V_{measured}$ dashed grey lines). It is worth remarking that the shape of the nominal voltage trend over time is notably affected by the $R_{TOT}$ trend, whose contribution via the improvement of $\eta_{deg}$ allows tuning the simulation of the voltage with a sensible reduction in the modelling error.

The same approach was applied to the experimental work done by Torrel et al. [198] on two fresh cells subjected to a long term degradation test at 700 $C$, running at constant power of 4.5 Wand at two different values of Fuel Utilization. Also in this case, the methodology herein described revealed to be successful, as shown in figure 5.2. Again, the voltage simulation, suitably fixed with the $\eta_{deg}$, revealed to be consistent and replicable on a different experimental test.

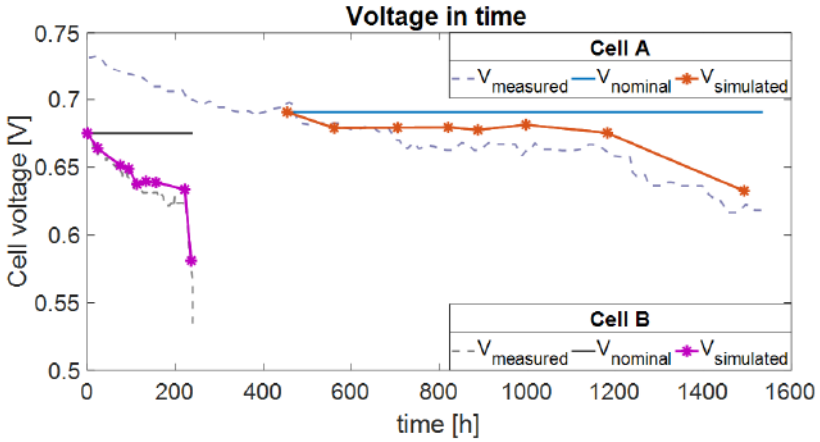


**Figure 5.2:** Voltage simulation coupling ASR approach and EIS features for both Cell A and Cell B. Experimental dataset is taken from [198]

### 5.2.2 Algorithm test on experimental data - Data from INSIGHT project

The proposed methodology was applied on the measurements provided by CEA acquired within the INSIGHT project and described in section 3.4. Particularly, as a further validation, the lumped dynamic model, tested upon experimental data collected by DTU on the 6-cells short stack, was fed up with the data collected by CEA on the same technology to simulate its operation. As shown in Figure 5.3 the voltage (figure A) and the temperatures (figure B) present an acceptable trend resembling to the measured ones. This is achieved just using the lumped model with the data collected by CEA.

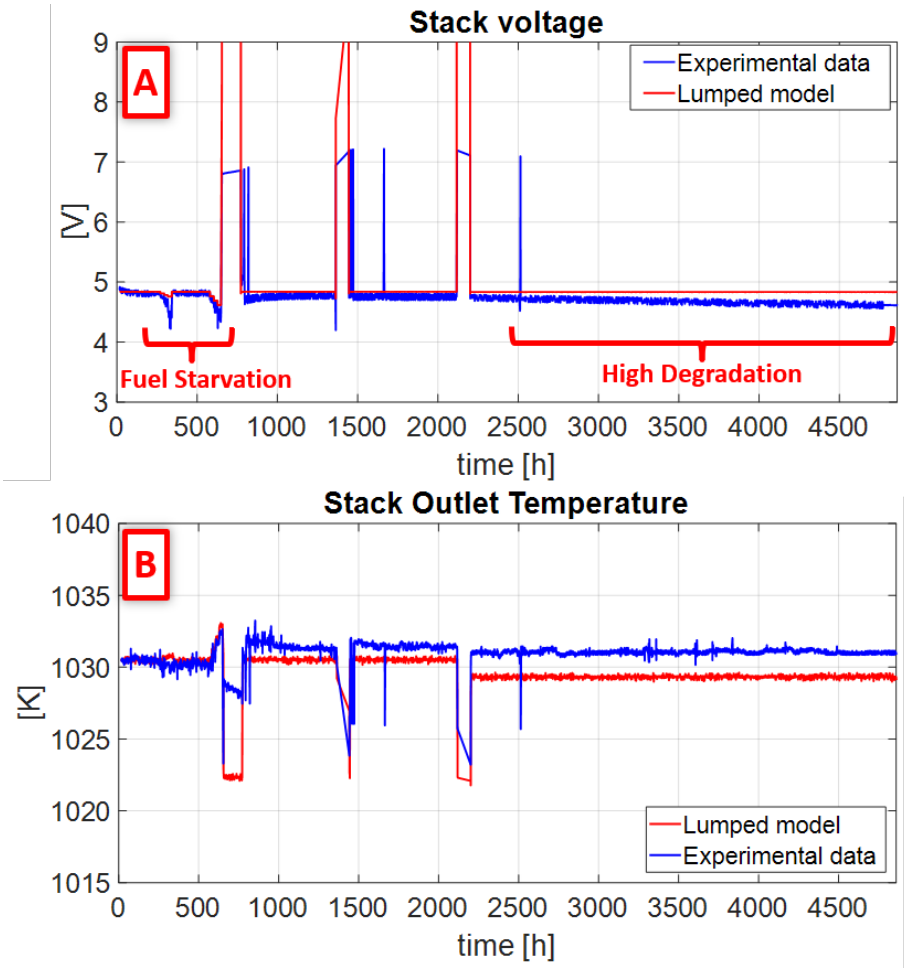


**Figure 5.3:** Model outputs (red lines) vs CEA experiments (blue lines). A) shows the modelled stack voltage with respect to the measured one. B) shows the comparison between modelled stack outlet temperature with the cathode outlet measured one.

The reasons behind the choice of not re-identifying the ASR lumped parameters for the 6-cells short stack upon CEA experiments relies on the fact that the stack were produced by the same manufacturer (Solid-Power) using the same technology. Indeed, as described in section 3.2, SP provided both CEA and DTU with a identical stack for the purpose

of the INSIGHT project .

The obtained results confirmed the robustness of such lumped approach. The only parameter re-tuned was the $V_{OFFSET}$, being it linked to non predictable changes in the boundary conditions. Thus, the lumped model identified upon DTU 6-cells short stack measurements was was run using the input data of the operating experimental data to simulate such conditions measured at CEA on an identical stack provided by the same manufacturer.

The error of the model was analysed and is presented in Figure 5.4, here the error is evaluated as the percentage of the difference of the simulation with respect to the measurement. As shown in section 4.2.2, also in this case the error on temperature is very limited, around the 1%, while the highest error in the voltage estimation is less than 4% with respect to nominal conditions (e.g. during a "durability" test) and less than 10% during an induced faulty condition (e.g. during the two fuel starvation tests).

It is worth noting that in the model the faulty conditions are not simulated then causing the rising of the error. Moreover, after 2500 h (during the long term test after the system shut-down) the error on voltage starts increasing with a linear trend. This is a clear indicator of the natural degradation of the system due to a detrimental phenomena occurrence.

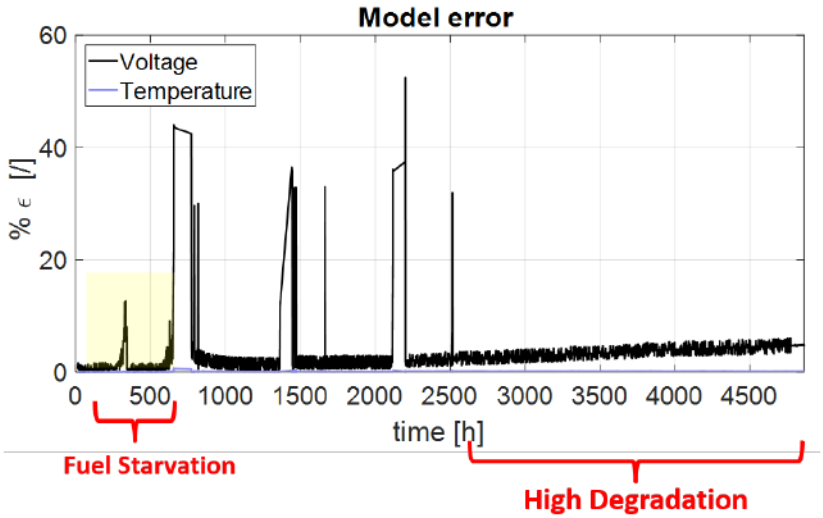


**Figure 5.4:** Model error. The error of the model is the difference between real and and modelled data divided by the real one. It is worth highlighting that the error is evident during the two fuel starvation test performed at 300h and 500h and after 2500h when a clear high degradation occurs.

Such high degradation rate, around $4.62 mV/h$, is mainly due to an abrupt malfunctioning occurred in the cell n.3, which is located in the middle of the short stack tested by CEA. Particularly, this cell was affected by a visible phenomenon occurred after 2000h (before the long term degradation test), when the stack was restarted after a shut-down. After that, a slow and continuous detrimental behaviour is observed and it was also detected by the FDI algorithm as discussed in section 3.4. The CEA test plan accounted for an EIS measurement performed each six hours, so the related ECM features extraction provide useful information on the behaviour of the cells over time. Figure 5.5 shows the $R_{TOT}$ behaviour over time of cell n. 3 compared with the other cells; particularly figure A) shows the complete dataset whereas figure B) is a zoom on the high degradation behaviour occurred after 2500h.

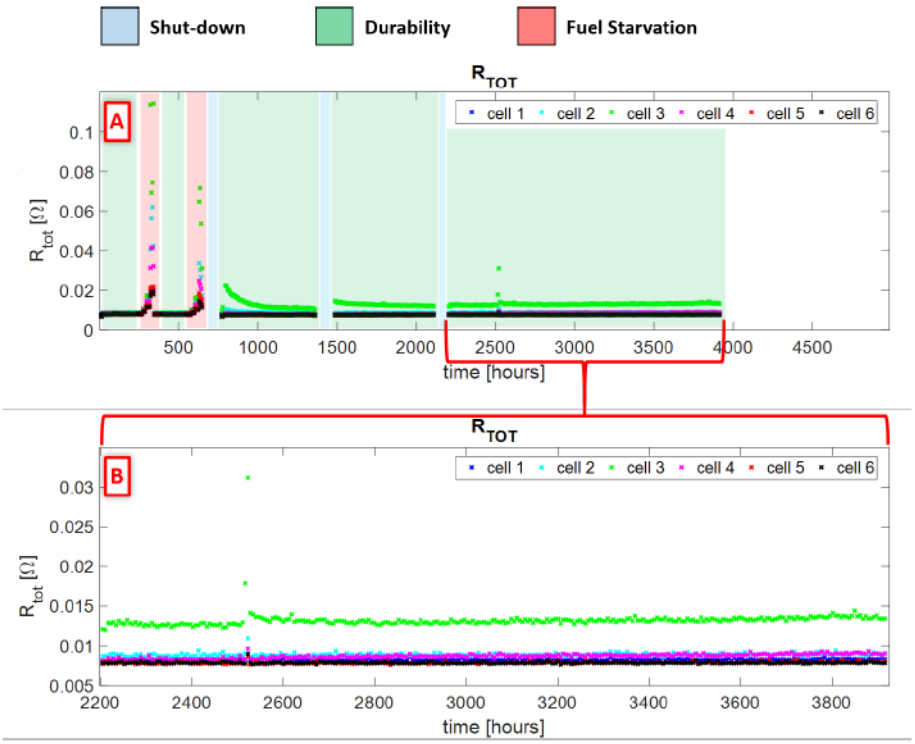


**Figure 5.5:** EIS measurements on the Experimental dataset. The trend of the total resistance for each cell of the short stack is reported in A), whereas B) shows a zoom on the high degradation behaviour after 2500h.

Some comments can be made on the $R_{TOT}$ behaviour; according to the analysis performed in the section related to the FDI algorithm, during the two fuel starvation tests a significant increase in the total resistance (see figure 5.5 A) - red area) is detected. This is expected since the fuel starvation highly affects the anode side with an increase in the low frequency arc of the spectrum, which typically provides useful information on the electro chemistry of the anode. The fault is reversible, as shown in the following durability tests, where the total resistance comes back to its nominal value when the nominal value of the fuel utilization is restored. This is not true for the cell n. 3, which does not comes back to its nominal value after the induced fault; moreover, during the durability test zoomed in figure 5.5 B), a continuous increase

in the total resistance of the cell n. 3 is observed. It is evident that something abnormal occurred after 1500h and it affected the neighbours cells n.2 and 4, whose total resistance slightly increased as well. This high degradation is not expected from the defined nominal conditions and, in turn, it cannot be simulated by the lumped nominal model as it is. However, the integration of such information derived from the EIS measurement can be included to have a better adherence of the simulation to the real data collected. Indeed, the evaluation of the $\eta_{deg}$ in eq. 5.2 could help in tuning the voltage estimation as well as the temperature simulation.

Therefore, by implementing such voltage loss, which can be updated in real-time whenever a EIS measurement is performed, the dynamic model simulation is performed, the dynamic model simulation can be improved by adapting the relevant term in eqq. 5.1 and 5.2. The figure 5.6 A) reports the voltage and the temperature simulated with the dynamic model updated with the $R_{TOT}$ values derived from the EIS data measured during the overall test campaing. Here the experimental voltage is compared to the estimated nominal one, outcome of the *"nominal model"*, along with that one derived from the *"combined model"*, in which $\eta_{deg}$ is integrated into the ASR approach. The same approach is adopted to show the stack outlet temperature results in figure 5.6 B).

It is worth remarking that the simulated voltage well matches the measured one but for the two fuel starvation tests (i.e., at 280 h and 550h). However, it is expected that during a fault the model should be not capable of reproducing the real behaviour. This is also observed in the temperature comparison of Figure 5.6 B), where the combined model simulates a stack temperature higher than the real one, clearly due to the undervoltage estimation.

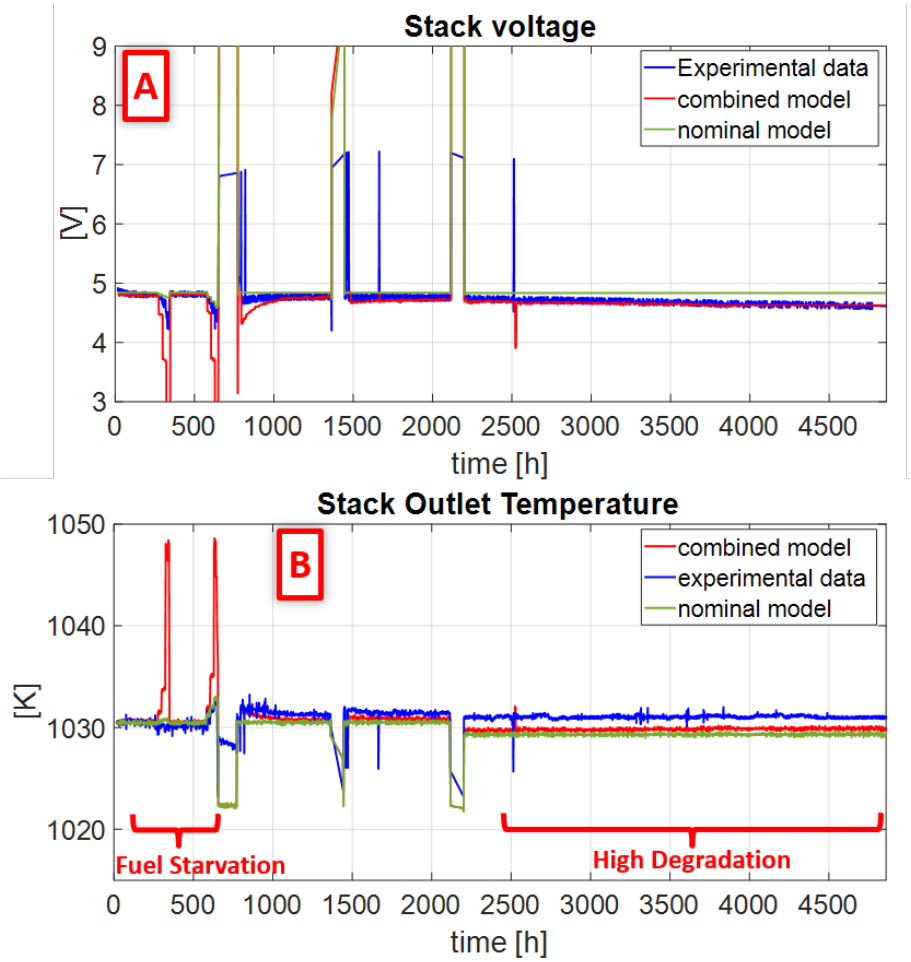


**Figure 5.6:** Comparison of the *"combined model"* (simulated+aging) outputs (red lines), *"nominal model"* ones (green lines) and the experiments (blue lines). A) shows the modelled stack voltages with respect to the measured one. B) shows the comparison between modelled stack outlet temperatures with the cathode outlet measured one.

To better show the accuracy enhancement of the *"combined model"* with the integration of the EIS-based information, the errors of both "nominal" and "combined" model are reported in Figure 5.7. Figure A) sketches the error in voltage estimation and the high degradation

behaviour is zoomed in Figure B); the temperature trends are shown in figure C).

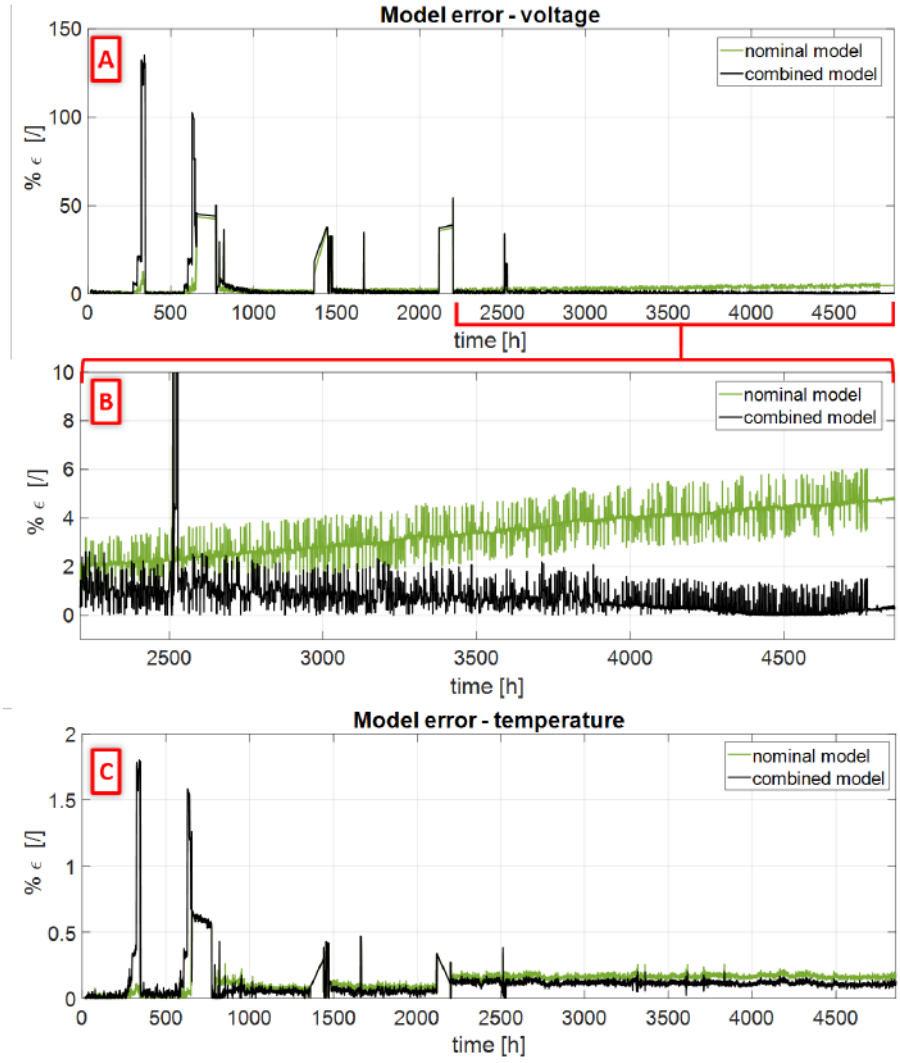


**Figure 5.7:** Percentage model error. The error has been evaluated as the ratio of the difference between real and modelled values with respect to the real ones. A) reports the error on the voltage estimation, B) a zoom on the high degradation behaviour while C) shows the temperature trends.

Figure 5.7 shows the improvement in the accuracy of the *"combined model"* with respect to the nominal one. Indeed, the error in voltage is not higher than 2% during the durability tests. Moreover, as sketched by figure 5.7 B), a very interesting reduction in the percentage error is observed in the *"combined model"*, where the linear increase of such error is avoided thanks to the information derived from EIS measurements; this allows to reach an error lower than 1%. The outlet temperature shows a slight reduction in the percentage error during the durability tests with respect to the classical model, as shown in figure 5.7 C).

On the other hand, it is worth adding a comment on the model response during the fuel starvation tests, where the error in voltage increases up to 120% and, in turn, the error in temperature slightly increases up to the 2%. It is clear that in case of fuel starvation, according to the fault signature matrix developed in section 3.3.2, the total resistance is expected to increase along with the low frequency arc with the fuel utilization; this reflects in a high $\Delta R_{TOT}$ and then in a high degradation loss $\eta_{deg}$.

As a consequence, the error in the voltage estimation reaches very high values from 40% to 120%. The model incapability of matching the measurement during a fault is anything but an issue since it allows individuating a not expected nominal condition. Indeed, this difference between measurement and simulation might trigger the FDI algorithm to infer on the system status aiming at isolating the possible malfunctioning occurring.

Thanks to an alarm raised by such residual in voltage, a specific EIS measurements test could be performed to collect as much information as possible to detect and isolate the fault. On the other hand, if the fault is not so critical the model could be adapted to the new status of the cells/stack by updating the $\eta_{deg}$ in eq. 5.2 to account for the impact of the fault on the evolution of the voltage in time.

## 5.3 RUL estimation

To evaluate the degradation rate and to estimate the remaining useful life (RUL) a first attempt could be done looking at figure 5.8. The graph a the bottom of Figure 5.8 reports the relative variation of the voltage with respect to the initial value, considered as nominal, and evaluated as the average value of the voltage in the time window 0-500h. The stack voltage decreases of about 0.2 V in 4000 h, thus the $r_{deg}$ is about 0.05 mV/h.

It is worth remarking that the degradation process is highly affected by the several system shut-downs, particularly the ones occurred at 500 h and 2000 h.

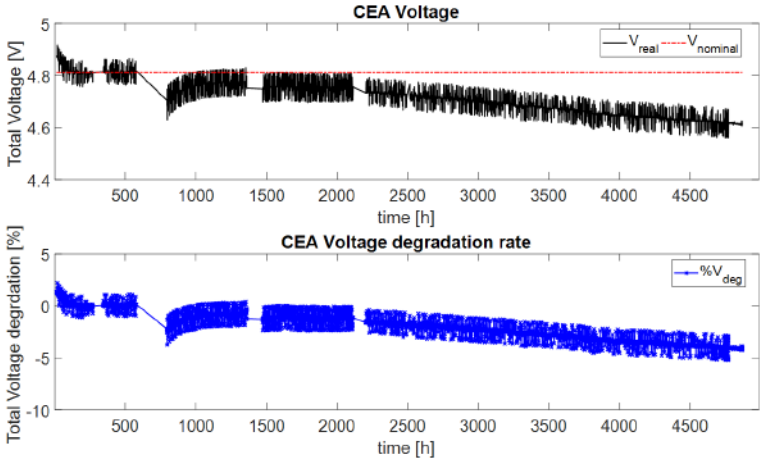


**Figure 5.8:** Stack voltage degradation over time. Comparison between nominal (i.e., expected constant value) and real trends. For sake of completeness the degradation rate estimation is shown in blue line.

Once defined the mathematical trend correlating the extracted EIS-based features and the current to simulate the voltage behaviour, the RUL estimation could be performed. Particularly, the ageing was defined by predicting the total resistance behaviour over time. The mathematical degradation rate function was defined as a linear dependence

on time, as suggested by the experiments. The fitting was performed through a least square error technique.

Once defined the $R_{TOT} = f(t)$, the derived $\eta_{deg} = f(t)$ is thus implemented within the ASR model and the simulation is run for a time window larger than the measured one. By doing so, the estimate of the expected voltage behaviour is performed. Moreover, according to the manufacturer, a proper threshold was set to define the SoH of the stack. In this case, SolidPower suggested to set as not-more-reliable limit value a stack voltage lower than 0.75 V for each cell, which is the value at which that kind of cell is considered broken or not reliable any more. Consequently, the stack threshold on the voltage $V_{Th.,stack}$ is defined as:

$$V_{Th.,stack} = V_{Th.,cell} \cdot n_{cells} = 0.75 \cdot n_{cells} = 4.5V \tag{5.3}$$

The RUL of the stack can thus be defined as the intersection between the threshold $V_{Th.,stack}$ and the voltage; considering the fluctuation in the measurements, a confidence interval analysis is required to select an uncertainty range. It clearly depends on such signal fluctuation and contains all the uncertainties linked to the sensors installed on board as well as all the signal fluctuations due to noise, EIS measurements and other possible interferences. Particularly, prediction intervals can be computed by adopting a linear model with random effects and a Gaussian random noise on measurements, as presented in [101].

The application of the described approach is presented in figure 5.9, where the stack voltage behaviour is predicted along with its detrimental effect; moreover, the probable End of Life (i.e., the time at which the FC is considered not more properly working) is defined along with its uncertainty range.

The choice of predicting the voltage behaviour in time upon EIS evidences was done to increase the robustness of the model. Indeed, the EIS measurements can be performed during the stack operations at fixed time intervals for diagnostic purposes without sensibly changing the current operation; so the derived information could be immediately updated within the lumped model to tune-up the voltage estimation.

On the other hand, if an abnormal condition is envisaged or directly detected, the residual derived from the model might trigger the diagnostic algorithm and then suggest to increase the frequency of the EIS measurements to infer on the FC status.

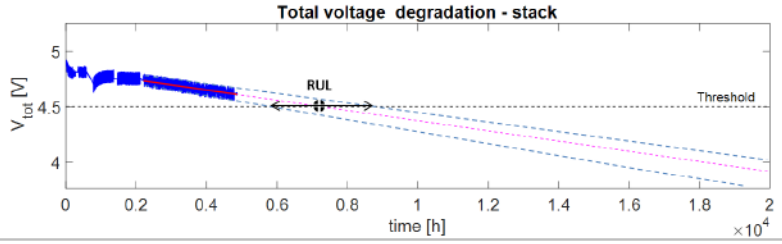


**Figure 5.9:** RUL estimation via stack voltage prediction. The threshold value is set upon the industrial partner information provided, according to eq. 5.3.

The analysis on the voltage degradation for RUL estimation can be specialized for each one of the 6 cells of the stack with a very simple modification in the voltage sub-model. Indeed, considering the estimated voltage equal for each of such cells, what really changes is the $\eta_{deg}$ that can be specialized upon the single EIS measurements.

Through this analysis it is possible to differentiate the degradation at cell level, and to find the worst cell out of the six, where likely the problem occurred. Figure 5.10 shows the voltage behaviour for each one of the 6 cells. It can be observed that the cell n. 3 (green line) has an almost linear decreasing trend, different from the other cells. Furthermore, the cells n. 2 and 4 (cyan and magenta lines respectively) also show a slower decrease with respect other cells.

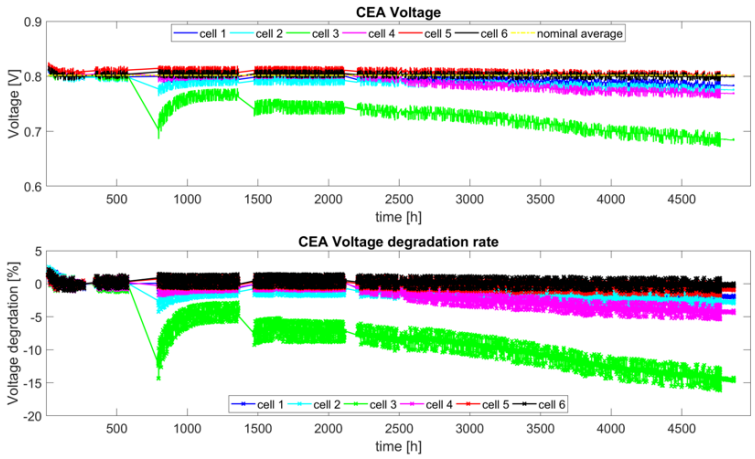


**Figure 5.10:** Cell voltage degradation over time. Comparison between nominal and real trends A) and degradation rate estimation B).

Figure 5.10 clearly shows that the cell n. 3 (in the middle of the stack) likely faced up with a problem (probably a strong re-oxidation) at the restart after the second fuel starvation test (i.e., at 800 h), which worsens after the shut-down at $t = 2000h$; Here, likely a leakage occurred and caused a sensible under-voltage, with a $r_{deg,cell.3} = 0.025mV/h$. Such negative effect propagated within the stack over time and affected the neighbour cells; indeed, cells n.2 and n.4 (cyan and magenta lines) present a degradation rate with a $r_{deg,cell.2} = 0.010mV/h$ and $r_{deg,cell.4} = 0.0075mV/kh$ respectively.

The RUL estimation is thus performed for the 6 cells according to the procedure applied to the complete stack and shown in figure 5.9. The comparison is sketched in figure 5.11, in which the yellow highlighted cell is the one already unreliable at the time of the measurement.

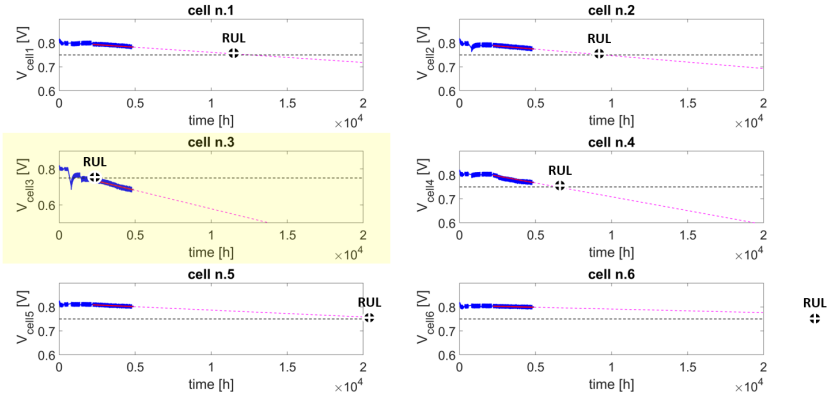


**Figure 5.11:** RUL estimation for each cell of the stack. The worst one – cell n.3 – is highlighted in yellow.

For the sake of comparability, the estimated cells RUL were collected in a histogram plot along with the stack one and shown in Figure 5.12. It is easy to understand how a not proper working cell sensibly affects the entire stack and particularly its adjacent cells. This results in a high lowering of the performance of the stack and in the reduction of the RUL as well. It is worth commenting that cell n.3 shows a negative RUL, since it is the one already unreliable (i.e. broken) at the time of the measurement.

Unfortunately, during the on-field operation environment, the measurements are usually not performed for each cell, particularly the EIS. This choice is necessary to reduce the sensors installed on board and to avoid their invasiveness behaviour. Indeed, for a real system, the measurements are performed on the stack or on cell clusters. This implies that only the RUL of the stack or the clusters could be estimated. However, this approach might be even used to support the maintenance, particularly for the stack replacement operations. If the model is capable of selecting the not-more-reliable cluster, once done the replacement, same still healthy ones could be reused for Life Cycle Assessment (LCA).

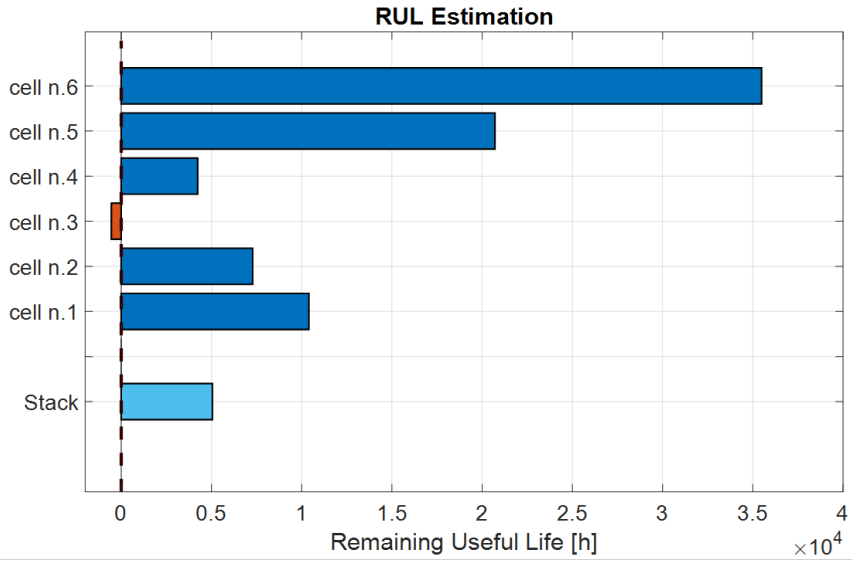


**Figure 5.12:** RUL cells/stack comparison.

In summary, the lumped dynamic model can be coupled to the EIS based information. This allows enhancing the voltage estimation with a real-time information from the monitoring and diagnostic tool. The combination of such information allows refining the real time simulation along with guaranteeing the capability of the model to trigger a more careful monitoring and diagnostic process, when some residuals have a not expected behaviour. The RUL estimation is based on the outcomes of the improved model and on the manufacturer expertise. The proper definition of the stack End of Life allows scheduling the FC maintenance, particularly useful when this technology is used as backup system or for a specific purpose in which the temporary unavailability is an issue.

# Chapter 6

# Mitigation

Mitigation for SOFCs is a new and interesting field whose purpose is to recover from malfunctioning caused by faults occurring within either stack or system components as well as to account for degradation effects. The main objective of mitigation is to extend the lifetime or the availability of the device until maintenance actions will be in place.

The mitigation requires a deep expertise on the phenomena occurring, the physics of the main processes and the effects that they can cause. Indeed, the iterative procedure to mitigate eventual malfunctioning could lead to the occurrence of more critical detrimental effects. Nevertheless, it is not very simple to devise a specific countermeasure for any kind of degradation phenomena detected by the diagnostic procedure.

The work presented in this chapter focuses on a innovative and generalizable approach to apply mitigation strategies to fuel cell powered systems, through the development of a general methodology to choose proper countermeasures.

Signal and model-based approaches are used to preliminary verify the feasibility of such counteractions before applying them on the real system. A reliable mitigation approach needs a robust fault detection and isolation support to clearly determine the problem and its severity. Experimental results, along with heuristic knowledge and industrial partners expertise, are a crucial steps to devise proper actions aiming at reducing or even zeroing the detrimental effects.

Within this work, the analysis derived from the literature and the experimental evidences led to the definition of a general methodology for Fault Mitigation countermeasures. Moreover, the investigated faults (or a general alarm otherwise) and the related diagnostic evidences used to perform detection and isolation allow defining a countermeasure to apply in case of proper isolation, depending on the grade of severity of the isolated malfunctioning.

Furthermore, a study was performed to define a sequence of actions for the design of an on-board mitigation algorithm and to develop a maintenance manual to the user, to suggest the sequence of the operations to be implemented. Here, the diagnostic algorithm and the related features extracted are used in a kind of "reverse mode" to provide information about the feasibility and effectiveness of the applied countermeasure. Particularly, such study was detailed for the Fuel Starvation upon experimental evidences, along with safety limits related to the system and provided by industrial partners.

Finally, a methodology that combines the diagnostic techniques and a mitigated-oriented control approach was defined. A case study on a Fuel Starvation effect due to Hydrogen leakage was performed and a fault mitigation controller was developed to infer on the feasibility of such procedures according to the constraints related to the SOFC functioning. Interesting results paved the way to further work aiming at increasing the TRL of such Monitoring, Diagnostic and Lifetime Tool (MDLT) for commercial purposes along with a prognostic field to be investigated.

## 6.1 The Concept

The fault mitigation application is anything but simple, and the check for the feasibility of any operation is needed to act properly on the real system. The reversibility of a fault highly depends on its nature, and the Fault Detection and Isolation (FDI) approach, coupled with reliable lumped models, could also help in estimating possible countermeasures.

Generally, a reliable model-based fault mitigation strategy requires: i) a model capable of reproducing the system in nominal conditions; ii) a robust FDI method to isolate the fault and identify its magnitude iii) a suitable degradation sub-model and iv) a deep knowledge on the physics

concerned to understand the link between the occurred fault and the variables to be changed. Figure 6.1 sketches the main implementation steps of a fault mitigation strategies. All these phases need to be followed step-by-step in order to have a proper and reliable methodology aiming at facing up with occurring malfunctions and at extending the lifetime of the affected systems.

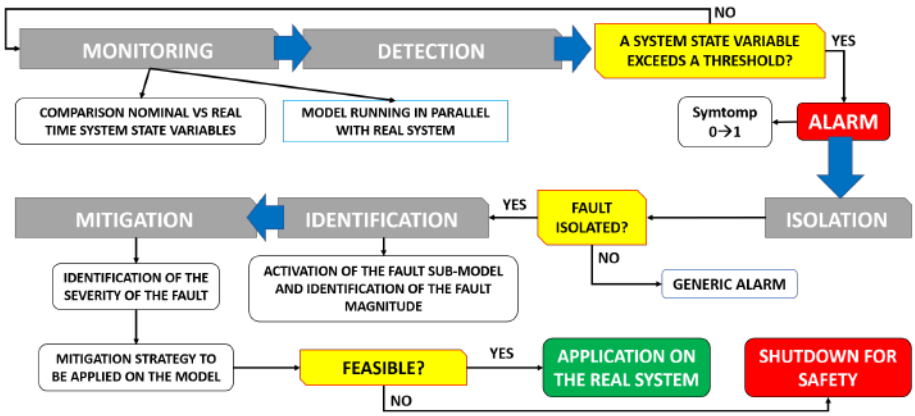


**Figure 6.1:** Main phases of a generic model-based algorithm for Fault Monitoring, Detection, Isolation, Identification and Mitigation. Here all the steps involved are described along with the main if-clauses to consider. The final aim is the evaluation of the feasibility of the mitigation action and its application in case of fault occurred or the shut-down needed otherwise

To better explain the approach adopted, some useful definitions are herein provided:

1. **System Monitoring** Specific features are computed from measurements acquired on the system. During this task only suitable data processing is performed and no inference on system status is made. The monitoring phase allows evaluating the reference conditions for the system state variable considered for each diagnostic algorithm.

2. **Fault Detection** The extracted features are analysed to assess if a faulty event is occurring or not.

3. **Fault Isolation** If a fault is detected, the component(s) affected by the fault are identified and its location is determined. In this case, the diagnostic algorithm has to clearly determine which fault is and where it is located. Then, the faulty RUL ($RUL_F$) can be estimated. Obviously, $RUL_F$ is supposed to be lower than the RUL in unfaulty conditions $RUL_N$.

4. **Fault Identification** At this phase, the fault magnitude and its dynamics are characterized to identify its grade of severity.

5. **Fault Mitigation** According to the severity of the fault (see Figure 6.2), a proper mitigation countermeasure can be applied in order to have a total recovery or to change the operating condition, aiming at stabilizing the detrimental effect by choosing action that are a compromise between the efficiency target needed (or the power) and the RUL.

   If it is not possible and the fault cannot be stabilized, a "Take-Home Operation" could be the most suitable solution to drive the system towards a maintenance procedure, taking time to properly face up with the problem. Moreover, if the detrimental effect is significant that no countermeasure could improve the system condition and no "Take-Home Operation" can be set, an immediate shut-down is the most recommended solution to prevent critical failures.

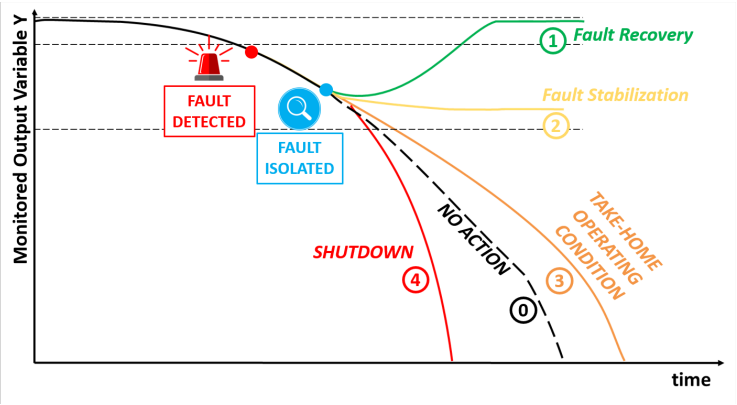


**Figure 6.2:** Fault Mitigation approach. The monitored output variable $Y$ behaviour is the key parameter for the mitigation procedure. The black line (0) is the nominal RUL (No action applied), while coloured lines from 1 to 4 refer to the different mitigation approaches. 1) Is the Fault recovery with the restoring of the nominal condition, 2) is the stabilization of the malfunctioning without the complete restoring, 3) is the take-home operating condition to take useful time to prepare for maintenance, 4) is the immediate shut-down for safety matters

## 6.2 The methodology

The methodology developed in this thesis is conceived to perform the mitigation feasibility by means of the usage of lumped models running in parallel with the real system. According to the scheme of Figure 6.2, the fault mitigation is the further step after the diagnosis. In this section each step of Figure 6.1 is discussed in detail.

### 6.2.1 System Monitoring Phase

The system is monitored by appropriate sensors installed on-board. The output system state vector, defined as $Y$, is the monitoring variable that needs to be continuously observed and analysed to infer on the SoH of the system. Its possible deviations from a defined nominal region might suggest a possible malfunction occurrence. Usually, $Y$ is a set of direct measurements coming from sensors installed on-board or

indirect measurements derived from a combination of information coming from the system. A reliable monitoring approach focuses on several monitoring variables which allow distinguishing different SoH with respect to different conditions (either nominal or faulty). Consequently, $Y$ is a vector (see eq. 6.1) containing several variables (e.g., voltage, temperature, fuel utilization, etc.). The more $Y_i$ elements are present, the more redundant and reliable is the monitoring process.

$$Y = [Y_1, Y_2, ..., Y_n] \tag{6.1}$$

Moreover, all the monitored output variables $Y_i$ depend on system state and control variables. The control variables $u$ are the variables that a controller could modify during the system operation to change the working conditions (e.g., the input flows, recirculation of gases in heat exchangers, etc.), while the system state variables $X$ are variables indirectly evaluated and useful to monitor possible changes. Thus, the condition of the system can be monitored through the variable $Y$, which depends on both state and control variables ($X$ and $u$):

$$Y = f(X, u) \tag{6.2}$$

Based on the objectives of the application and on the relevant system features, some measurements could play the role of $Y$, $X$ and $u$ respectively. For Solid Oxide fuel cell applications and particularly for monitoring and mitigation purposes, the most relevant monitored output variables are voltage, outlet stack temperature, and overall efficiency since they are the clearly independent variables of the process in galvanostatic mode operations. Temperatures (e.g., average stack and outlet cathode temperatures) are instead are representative of the state of the system. On the other hand, the control variables are all the system inputs handled to vary the FC operation; thus the $u$ vector could contain all the input flows (both of the anode and the cathode side) along with the inlet temperatures and the current. Other indirect indicators, which allow defining the system state $Y$, can be considered some indirect measurements like the Fuel Utilization or the reaction rate, whereas other typical parameters not really measurable but that can be derived via modelling approach could be the Triple Phase Boundary ($TPB$) Length, the anode porosity ($\epsilon$) and the tortuosity ($\tau$). Particularly, these latter

parameters, whose variation is strictly connected to several degradation mechanisms, are typically measured via post-mortem analysis on real systems, and usually simulated in the modelling approach to represent the FC operation along with some degradation mechanisms.

Focusing on the meaning of the monitored output variable $Y$ , it could be possible to theoretically split it in two terms: the first one $G$ representative of the theoretical nominal conditions and the second one $D$ standing for the natural ageing of the system during its operation. Therefore, the eq. 6.2 can be rewritten as follows:

$$Y(X,u) = G(X,u) + D(X,u) \tag{6.3}$$

On a real system, it is not possible to measure $G$ and $D$ contributions directly, being them lumped into the measurement, therefore only the overall condition of the system can be derived from the measures. Thus, to account for the change of the nominal condition decoupled from natural ageing, an accurate and reliable model should be developed. For on-board applications, the model is requested to be faster than the real-time so as to provide a rapid feedback on the system behaviour. By doing so, it could be possible to consider and infer on different simulated scenarios before applying the optimal one on the real system.

Defining with $\hat{Y}$ a generic output derived from the model, it can be written:

$$\hat{Y}(X,u) = \hat{G}(X,u) + \hat{D}(X,u) \tag{6.4}$$

A reliable monitoring approach could consider information from measurements taken on the real system in parallel with those coming from the suitably validated model. In nominal conditions the monitored output variables $Y$ and $\hat{Y}$ must satisfy the following equation:

$$\left| Y - \hat{Y} \right| < \epsilon_m \tag{6.5}$$

Where $\epsilon_m$ is the error of the model, which in turns is representative of the chosen model accuracy. During the normal operation in nominal conditions, while performing an on-line monitoring of the system, for each $Y_i$ the following trend sketched in figure 6.3 is obtained.

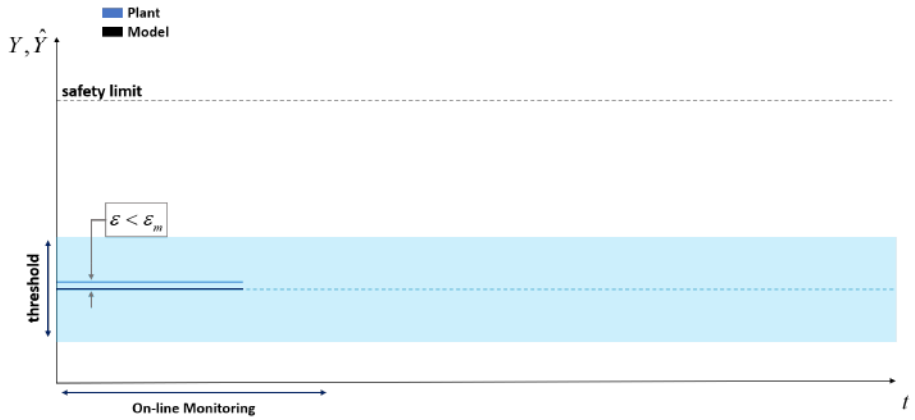


**Figure 6.3:** Y trend Monitoring - Nominal condition.

The cyan area is the threshold range for nominal conditions, suitably set upon experimental data analysis. If the monitored variable is within the threshold area it can be considered as "nominal", while when $Y_i$ falls out of the threshold range, an alarm is activated, as hint of possible malfunction occurrence. In that case, the detection phase starts.

### 6.2.2 Fault Detection Phase

The Fault Detection phase analyses the residual between the model nominal state and the system real state. Indeed, the detection algorithm constantly compares the data measured on the real system $Y_i$ and the simulation output $\hat{Y}_i$. The difference between the real measurement of the state and the modelled nominal condition is called Residual $R$. This is the key parameter of the detection phase, because it allows to identify a possible malfunction in the system when it exceeds the nominal threshold range. Thus, for each monitored variable, a residual $R_i$ can be defined, as:

$$R_i = \left| Y_i - \hat{Y}_i \right| \qquad for\ 1 \leq i \leq n \tag{6.6}$$

As stated in eq. 6.7, considering the semi-height of the nominal threshold associated to the *i-th* variable $\epsilon_{n,i}$ and being it centred around $\hat{Y}_i$ , when the residual $R_i$ is equal or less than $\epsilon_{n,i}$ (i.e., the real state $Y_i$ is

within the threshold area), the generic symptom $s_i$ assumes zero value. On the contrary, when $R_i > \epsilon_{n,i}$ (the real state exceeds the threshold) the generic symptom $s_i$ associated assumes a unitary value.

$$\begin{cases} R_i < \epsilon_{n,i} & s_i = 0 \\ R_i > \epsilon_{n,i} & s_i = 1 \end{cases} \tag{6.7}$$

The symptoms are then collected into a vector, building up the symptoms vector. When this vector contains only zeros, it means that the system is in nominal (i.e., healthy) conditions or nothing is revealed by the detection algorithm (e.g., missed fault). When one or more cells switch from 0 to 1, something is changing and the isolation phase needs to clearly determine which kind of fault is occurring, and then distinguish between a false alarm and a malfunction as well. Figure 6.4 shows the case in which the residual exceeds the threshold and a symptom switches from 0 to 1. From that moment on, the Isolation phase starts aiming at determining the occurring fault.

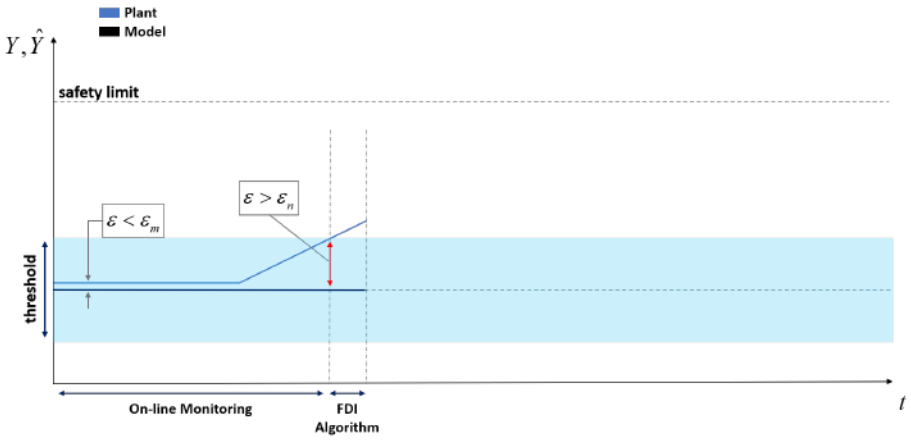


**Figure 6.4:** Y trend Monitoring - fault detected

### 6.2.3 Fault Isolation Phase

The Isolation phase requires the heuristic knowledge of the phenomena to be accounted for in the FDI algorithm and experimental evidences to build the FSM (an example is provided in Table 6.1). When the symptoms vector exactly matches one row of the FSM, the corresponding fault is properly detected and isolated.

| | **STATE OF HEALTH** | | | | | |
|---|---|---|---|---|---|---|
| | $s_1$ | $s_2$ | $s_3$ | $s_4$ | ... | $s_n$ |
| **Fault 1** | 0 | 1 | 1 | 0 | 0 | 1 |
| **Fault 2** | 1 | 0 | 1 | 0 | 0 | 1 |
| **...** | ... | ... | ... | ... | ... | ... |
| **Fault n** | 1 | 1 | 1 | 1 | 0 | 1 |

**Table 6.1:** Example of Fault Signature Matrix (FSM). Here for each fault investigated via ad-hoc experiments the symptoms pattern is collected. During the monitoring phase, if the symptoms vector evaluated on the real system matches one of the rows of the FSM, the corresponding Fault can be isolated.

During the experimental campaign and the related analysis for the FSM design, some faults could have the same row on the FSM. In that case, a redundancy of the symptoms might help in defining the fault univocally (as presented in [103]). Moreover, a "General Alarm" warning addresses the faults not accounted, so as to activate an alarm when the system behaviour diverges from the nominal condition, but the information available are not sufficient to properly isolate a specific fault. When the isolation phase is successfully completed, the fault $F_i$ is clearly isolated. Thus, the model must activate the related fault sub-model, to properly simulate the faulty state, as described below. Once the sub-model is activated, the fault magnitude needs to be identified, in order to set the correct faulty state and to infer on possible mitigation strategies to be adopted depending on the physicist of the malfunctioning and its severity. Therefore, the new monitored variable depends also on the faults occurred, which impact on the performance of the system; this can be modelled as follows:

$$\hat{Y}(X,u) = \hat{G}(X,u) + \hat{D}(X,u) + \hat{F}_i(X,u) \tag{6.8}$$

### 6.2.4 Fault Identification Phase

To perform a proper mitigation strategy, the identification of the fault, its magnitude and its stage is a key-point. Depending on it, mitigation approaches can be different: for instance, if the fault is at a stage in which is totally unrecoverable, trying to apply recovery countermeasures might lead to unsuccessful stabilization of the FC without resolving the problem caused by a detrimental effect. Moreover, a suitable fault identification allows tuning the fault sub-model, and, in turn, the complete model, to have a simulation of the system in that faulty state. The usage of the faulty model is fundamental to infer on different countermeasures to be applied on the system before the direct application on the real system. The fault sub-model depends on characteristic parameters $(A_1, A_2, ..., A_n)$ that need to be properly identified upon real-time measurement:

$$F_i = F(A_1, A_2, ..., A_n) \tag{6.9}$$

Thus, a controller needs to set the optimal values of such parameters to model $\hat{F}_i$, to bring $R_i$ below $\epsilon_m$, satisfying eq. 6.5. In this way, the fault identification is reached, and the model state correctly simulates the faulty condition, as sketched in Figure 6.5.

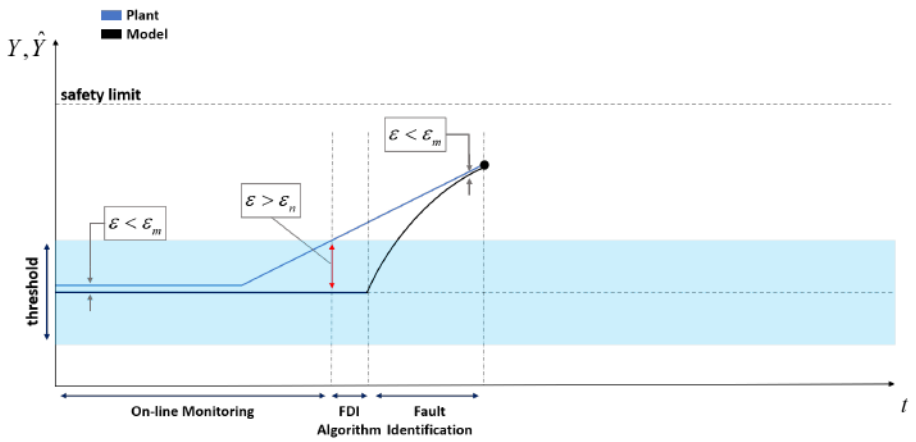


**Figure 6.5:** Y trend Monitoring - Fault identification.

Once the model is set in "Faulty mode" and tuned to simulate the current state of the system, the mitigation approach can take place.

At this stage, all the optimization procedures to define the proper mitigation countermeasure need to be performed on the faulty model, while taking as reference the nominal condition model. By doing so, all the scenarios can be investigated online avoiding to further compromise the health of the real system.

Once the mitigation strategy has been decided and defined, it will be applied to the real system, according to the constraints linked to the application the system is dedicated to (e.g., Auxiliary Power Unit, electric energy production, residential co-generation, etc.).

### 6.2.5 Fault Mitigation Phase

According to Figure 6.2, four different approaches can be adopted depending on the severity of the fault. The issue is to clearly identify such state. Indeed, the detrimental effect of a fault and its irreversibility clearly depend on the intrinsic nature of the malfunction, its magnitude, possible hidden effects or correlation between other occurring phenomena, along with and the quality of the FDI algorithm. Thus, once isolated the fault and identified its magnitude, the crucial step is to single out the optimal countermeasure, as sketched in Figure 6.6, and the related control variables to operate with respect to the constraints.

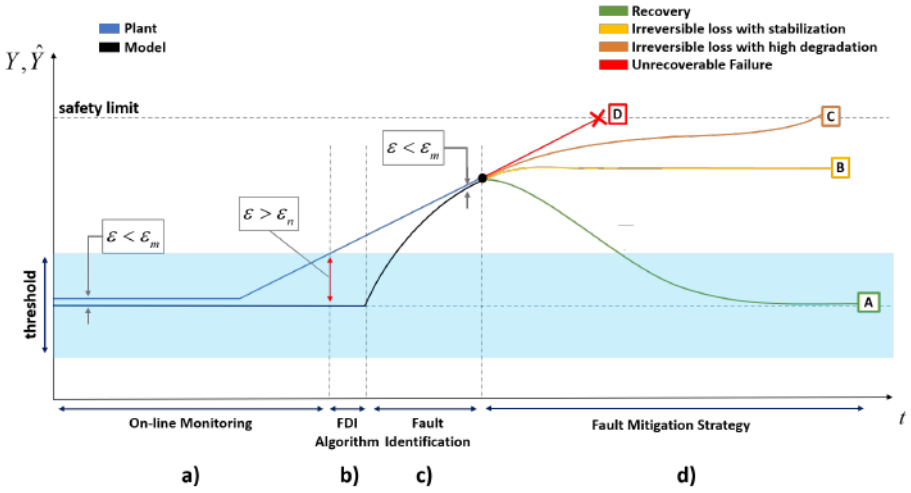


**Figure 6.6:** Qualitative description of model error-related deployment of adopted online monitoring (a) fault detection (b), isolation (b), identification (c) and mitigation (d) algorithms. The following legend clarifies what the main mitigation outcomes shown in Figure are: A) Severity grade 1 - Recovery; B) Severity grade 2 – Stabilization C); Severity grade 3 - Take-Home Condition; D) Severity grade 4 – Shut down for Safety. The trend of the monitored variable of the real plant is sketched in blue line, whereas the corresponding modelled variable is sketched in black. When the phase (c) starts, the model tries to match the plant; at that point the fault identification is then achieved. From that moment, the fault mitigation strategy feasibility can be investigated.

### Severity grade 1 - Recovery

The best case for the mitigation strategy is when the system state can be restored to the nominal condition with minor changes to the RUL. This is possible when the intrinsic nature of the fault allows this kind of countermeasure and when the malfunction is correctly detected and isolated in a reasonable time. One of the most evident examples could be the Sulphur poisoning. At the early stage of such detrimental phenomenon, the Sulphur can be removed through an active regeneration using pure hydrogen $H_2$ as fuel instead of $CH_4$ [62]. Usually, when it comes to recoverable malfunctions, two main countermeasures can be taken. The first one is related to a process that must be enabled to get rid

of contaminants or, in general, the main cause of the detrimental effect, by imposing specific flows or switching to Open Circuit Voltage (OCV) conditions or even to electrolysis mode. On the other hand, a good approach to restore a nominal condition is finding a proper set of new operating variables values, $u_{new}$, that completely recover the detrimental effect, with respect to constraints related to the system operation, such as performances, temperature, load, etc. In this case, the controller behind the mitigation phase needs to identify the optimal set of such $u_{new}$ variables to zeros the fault $F_i$, as stated in the equation below:

$$\begin{aligned} &\exists u_{new} | \hat{F}_i(X, u_{new}) \rightarrow 0 \\ &\hat{G}(X, u_{new}) \approx \hat{G}(X, u) \\ \hat{Y}(X, u) \approx \hat{Y}(X, u_{new}) &= \hat{G}(X, u_{new}) + \hat{D}(X, u_{new}) \end{aligned} \tag{6.10}$$

The identification of the $u_{new}$ can be achieved through a minimization problem, which select a new condition at which the fault $\hat{F}_i$ is reduced to zero according to system constrains (i.e., performance, power, etc.). As a result, once defined the new set $u_{new}$, the system will return to a nominal state $\hat{Y}(X, u)$. It is worth mentioning here that , the time-dependent the term $\hat{D}$, which is representative of ageing phenomena and is thus intrinsically time-dependent, referring to the ageing of components is not recoverable in none of the 4 severity-grade scenarios herein analysed.

**Severity grade 2 - Stabilization**

Sometimes, the minimization problem related to the $u_{new}$ that zeroes the fault $\hat{F}_i$ has no feasible solutions; thus, the complete recovery of the nominal operating conditions is not achievable. In that case, the mitigation process should identify a solution that allows reducing as much as possible the detrimental effect and thus extending the RUL. The goal is to stabilize the $\hat{F}_i$, setting a new condition, different from the nominal one, that has a good compromise between performance and extended life, within the constraints, as described below:

$$\begin{aligned}
&\exists u_{new} | \hat{F}_i(X, u_{new}) \neq 0 \\
&\hat{G}(X, u_{new}) \neq \hat{G}(X, u) \\
&\hat{Y}(X, u) \neq \hat{Y}(X, u_{new}) = \hat{G}(X, u_{new}) + \\
&\qquad + \hat{D}(X, u_{new}) + \hat{F}_i(X, u_{new})
\end{aligned} \tag{6.11}$$

To have a stabilization, from a mathematical point of view, the $u_{new}$ must zeroes the derivative of both the fault and the theoretical nominal conditions $\hat{G}$:

$$\frac{d}{dt} \left| \hat{G}(X, u_{new}) + \hat{F}_i(X, u_{new}) \right| \approx 0 \tag{6.12}$$

**Severity grade 3 - Take-home Condition**

If the stabilization approach fails, the following mathematical relationships applies:

$$\frac{d}{dt} \left| \hat{G}(X, u_{new}) + \hat{F}_i(X, u_{new}) \right| \neq 0 \tag{6.13}$$

In this case, the focus must be the maintenance to replace the damaged component and restart as soon as possible the system. Indeed, a change in the operating conditions would be beneficial in extending the RUL to give the time to prepare the maintenance intervention ($\tau_{ptm}$). Such time can be defined as the time to prepare to the maintenance intervention, that is the time necessary to be ready to apply the maintenance, by also considering the time requested for the shipping of the requested components to change and the possible preliminary actions needed; thus it allows foreseeing the time requested to be ready to solve the problem occurring. The new condition devised is defined as "take-home condition". Usually, a common "take-home condition" is the switching to OCV mode or to a very small load, providing two main benefits. Indeed, interrupting the electrical production without shutting-down the system allows, on the one hand, avoiding the fast degradation correlated to an occurred phenomenon (e.g., an hotspot in the cell which may lead to an anode re-oxidation or a leakage) and, on the other hand, not sensibly

reducing the operating temperature as well. An analysis in the effectiveness of the mitigation application needs to be done regarding the RUL. If the countermeasures allow extending the RUL of the system for a time window at least sufficient to prepare the maintenance (e.g., replacing a stack or changing a stack component), as reported in eq. 6.14, it is worth applying the mitigation.

$$RUL_{new} > RUL_0 \rightarrow RUL_{new} > \tau_{ptm} \tag{6.14}$$

**Severity grade 4 - shut-down for safety**

If the best solution offered by the mitigation approach does not ensure a reasonable increase in the RUL, the system has to be shut-down for safety reasons, even if this implies that the system will not be able to provide energy:

$$\frac{d}{dt}\left|\hat{G}(X, u_{new}) + \hat{F}_i(X, u_{new})\right| \neq 0 \tag{6.15}$$

$$RUL_{new} \leq RUL_0 \qquad or \qquad RUL_0 < \tau_{ptm} \tag{6.16}$$

This does not mean that the mitigation approach has failed. On the contrary, a reliable approach, thanks to its monitoring and detection algorithms, will provide an estimation of the RUL and the identification of the severity of the fault will help the maintenance in the decision making of the component replacement or the entire system changing as well. In Table 6.2, a summary of the mathematical key parameters of such approach are linked to the different stages and objectives of the mitigation strategy. It is worth remarking that this kind of approach requires: *i)* a reliable fast model that allows simulating the nominal conditions, *ii)* validated fault sub-models that can be enabled when the isolation phase reveals the malfunctioning, *iii)* a reliable FDI algorithm and *iv)* a controller capable of identifying the severity grade of the fault. This latter is an open point that needs to be further investigated by means of experimental campaign. One solution could be exploiting the diagnostic algorithms in a reverse mode, in order to apply a mitigation countermeasure, check if the monitoring variable is reversing the trend

and apply the countermeasure. If this does not happen, the controller has to apply a possible countermeasure for the worse severity grade.

| | Recovery A | Stabilization B | Take-home condition C | Shut-down for safety D |
|---|---|---|---|---|
| Severity | 1 | 2 | 3 | 4 |
| $RUL_{new}$ | $>> \tau_{ptm}$ | $>> \tau_{ptm}$ | $> \tau_{ptm}$ | $< \tau_{ptm}$ |
| $\hat{F}_i$ | 0 | $\neq 0$ | $\neq 0$ | $\neq 0$ |
| $\frac{d\hat{F}_i}{dt}$ | 0 | 0 | $\neq 0$ | $\neq 0$ |

**Table 6.2:** Mitigation table for decision making parameters. Here each scenario of Figure 3 is linked to the severity grade of the fault, the RUL, the time to prepare to maintenance and the fault state. Indeed, if the recovery is achieved, the fault has to be set again to zero, otherwise a stabilization (zeroing the derivative of the fault) needs to be achieved. If the fault is not recoverable and even not possible to stabilize, it is fundamental to take time for the maintenance, that is increase the RUL ($RUL_{new}$) to have enough time for the maintenance. If neither this condition is feasible, the shut-down is suggested.

## 6.3 Case Study - The Fuel Starvation

To verify the methodology herein described, a case study of fuel starvation caused by an $H_2$ leakage at the inlet of the SOFC stack is investigated. The aim is to apply the right mitigation strategy and verify its feasibility in order to bring the system back into a recovery condition. This can be achieved only when the fault is correctly detected and isolated in a short time. To reach the goal, the nominal model of a SOFC stack properly validated upon experimental data in section 4.2.2 and the experimental evidences from DTU 6-cells SOFC short stack fuel starvation tests, are here described. As described in the section 4.2.3 the DTU test plan considered two fuel starvation tests performed reducing the inlet fuel flow and increasing the load respectively. Particularly, the former has been used to infer on a possible fuel leakage at the inlet and on the related mitigation countermeasure to apply aiming at restoring nominal system operation. The case study is meaningful even without a real leakage fault at the inlet since the dataset at 77% F.U. (i.e. the

first and the last step of the fuel starvation test) was considered as the nominal reference. By doing so the reduction of the fuel flow is ascribed to the fault (thus causing the fuel starvation) instead of the imposed $H_2$ shortage.

Considering the nature of the fault, the mitigation recovery action is expected to fail while the stabilization is the most likely solution. The chemical species affecting the anode and the cathode in nominal conditions are listed in table 6.3 .

| **ANODE** | | |
|---|---|---|
| | **inlet [mol/s]** | **outlet [mol/s]** |
| **$H_2$** | $1.29 \cdot 10^{-3}$ | $3.06 \cdot 10^{-4}$ |
| **$H_2O$** | $1.29 \cdot 10^{-6}$ | $9.96 \cdot 10^{-4}$ |
| **$CH_4$** | $3.72 \cdot 10^{-6}$ | 0 |
| **CO** | $2.75 \cdot 10^{-6}$ | $6.05 \cdot 10^{-6}$ |
| **$CO_2$** | $2.75 \cdot 10^{-5}$ | $2.52 \cdot 10^{-5}$ |
| **CATHODE** | | |
| | **inlet [mol/s]** | **outlet [mol/s]** |
| **$O_2$** | $3.75 \cdot 10^{-3}$ | $3.25 \cdot 10^{-3}$ |
| **$N_2$** | $1.41 \cdot 10^{-2}$ | $1.41 \cdot 10^{-2}$ |

**Table 6.3:** Molar flows at stack inlet/outlet of SOFC stack model for the Case Study.

The fuel starvation test was performed gradually lowering the inlet hydrogen flow rate from the nominal value to three lower values with a stepwise pattern over time while keeping constant the other parameters. Since, the current was kept constant, the measured cell voltage, showed a stepwise pattern over time according to the reduction of fuel flows towards lower values. Figure 6.7 shows the plant layout with the SOFC stack, pipes and load. Here the fuel flows, named $H_2$ molar flow, $H_2$ leak, $H_2$ after fault, are reported along with the current and voltage trends.

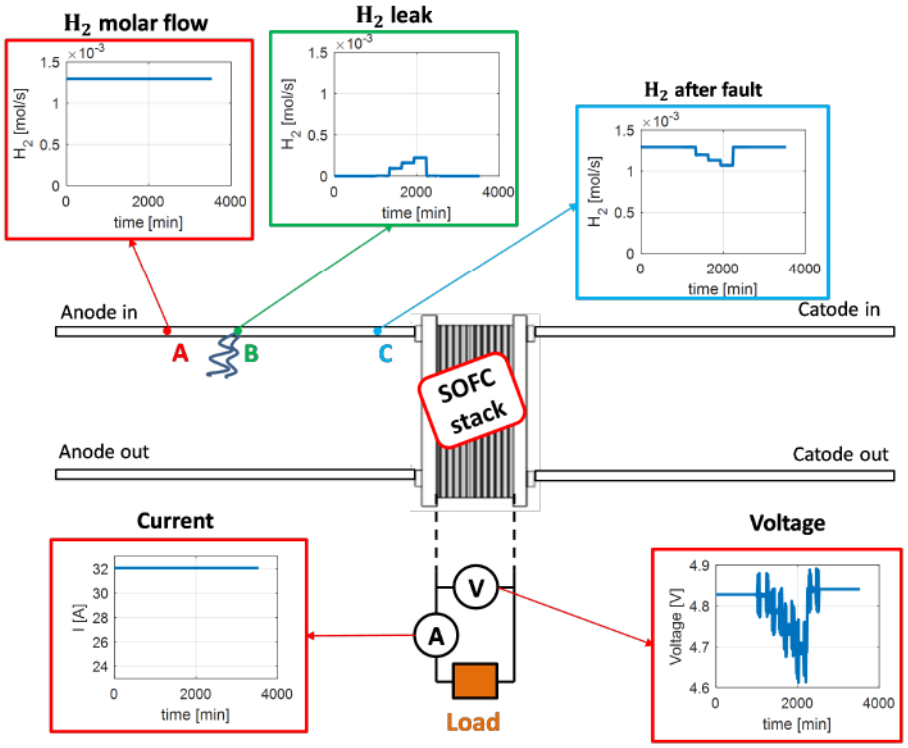


**Figure 6.7:** Plant measurements.The leakage is considered at the stack inlet with a reduction in inlet flow. The current is constant, while the voltage is affected by the change in the flow.

It is clear that $H_2$ molar flow (A) equals the sum of $H_2$ leak (B) and $H_2$ after fault (C). Considering the change in $H_2$, being the current constant, a related change in the voltage trend is thus expected accordingly. It is worth remarking that the high fluctuation of the measurements in a reduced time frame are related to the experimental results provided. Indeed, in that points an EIS measurement was performed for monitoring and diagnostic evaluations. For sake of clarity the inlet/outlet stack temperatures are reported in Figure 6.8.

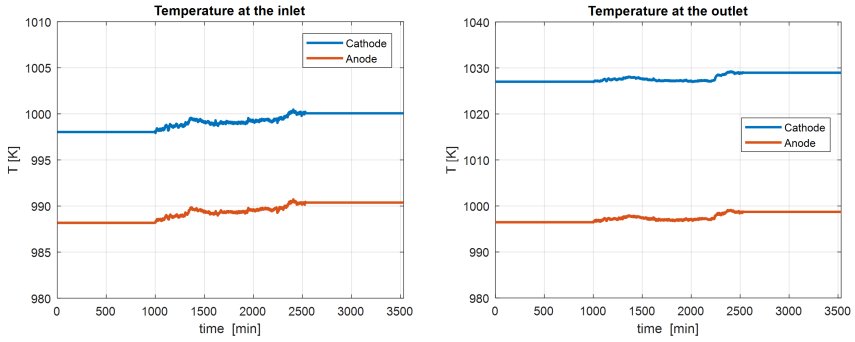


**Figure 6.8:** Plant measurements – a) shows the inlet temperature at the anode (in red) and cathode (in blue) sides of the flows, whereas the b) shows the related outlet temperatures

The outlet temperature is not exactly the one expected from the voltage trend. Indeed, the furnace in which the measured stack was tested presented a sensible and predominant dynamics affecting the outlet stack temperature. To properly apply the afore described mitigation approach is useful to clearly define the model usages for each step. The model is a valid support to reproduce the nominal (i.e., expected) behaviour of the stack to provide a reference value of the real system. Nevertheless, the model, suitably calibrated with the identified fault, could be used to investigate the feasibility of the mitigation approach chosen before its real application. Therefore, the model usage classification is herein provided for each step of the fault mitigation and then resumed in Table 6.4:

1. **Detection & Isolation**. To detect the fault and isolate it through a diagnostic algorithm, it is necessary to use experimental data and the nominal model to monitor continuously the difference between the considered measured and simulated state or output variable;

2. **Identification**. Once the fault is isolated it is necessary to tune the model along with the related degradation sub model to properly match the real measurements and the simulated one. Thus, the fault identification requires the advanced model (that is the nominal model plus the degradation sub-model) and the plant measurements;

3. **Mitigation**. To properly check the mitigation feasibility, the nominal model is the target to reach (for the recovery). Thus, the advanced model is the framework in which the mitigation strategy is implemented, without immediately applying it on the real system for safety matters.

| | **Detection & Isolation** | **Identification** | **Mitigation** |
|---|---|---|---|
| **Nominal Model** | **1** | **0** | **1** |
| **Plant** | **1** | **1** | **0** |
| **Advanced Model** | **0** | **1** | **1** |

**Table 6.4:** Model & Plant measurements usages. "1" stands for "enabled" while "0" stands for "disabled". During the detection&isolation the plant and the nominal model are used, and their measurements/outcomes are compared for the monitoring. During the identification the advanced model is tuned to match its outputs with the plant measurements (it is worth remarking that the isolated fault is occurring). During the mitigation, its feasibility is investigated applying the countermeasure on the advanced model and verifying its results with respect to the nominal (i.e., un-faulty) model before the application on the real system.

### 6.3.1 Fault Detection & Isolation

The use of plant measurements and the nominal model is necessary to perform FDI. The model and the real SOFC stack run simultaneously, the nominal model input is the nominal value of the hydrogen molar flow, while the stack input is the real hydrogen molar flow. The monitored output variable considered for this step is the voltage, when the difference between real voltage ($Y(x,u)$) and nominal voltage ($\hat{Y}(x,u)$) is greater than $\epsilon_n$, the diagnostic algorithm is activated whose task is to detect and isolate the fault. In this sense, the approach discussed in section 3.4 is the required step to trigger the identification procedure. The EIS-based diagnosis (discussed in chapter 3), suitably coupled with the model-based information, is thus devoted to this task.

### 6.3.2 Fault Identification

Once the FDI target is reached, the second step is to correctly identify the magnitude of the malfunction. A degradation sub-model is thus integrated into the nominal model, becoming the *"advanced model"*, to simulate the faulty behaviour. Here, the plant measurements are necessary as reference of the real conditions to be simulated. For the case study herein detailed, the advanced model (i.e., nominal model plus fault sub-model) consists in the estimation of a new hydrogen molar flow at the inlet, using the voltage feedback (difference between nominal and estimated value) and the nominal hydrogen molar flow. Identification is achieved when the difference between the real voltage and the estimated voltage is less than $\epsilon_m$ as described in Figure 6.9.

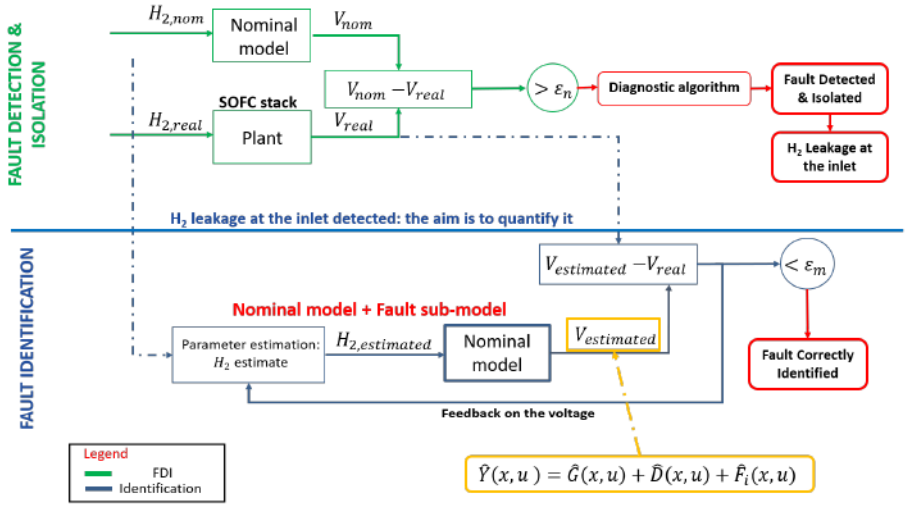


**Figure 6.9:** FDI and Fault Identification - Conceptualization and presentation of main tools (mominal model, fault sub-model) and methods (PID-based input, i.e., $H_2$ molar flow, estimation [199]) adopted. Particularly, at the top of the figure the FDI process is sketched with the identification of the fault: $H_2$ leakage at the anode inlet. At the bottom of the figure the fault identification process is shown: here a $H_2$ estimator (i.e., a very simple fault sub-model) coupled with the nominal model allows identifying the amount of $H_2$ loss; the proper amount of gas leaked is estimated through a feedback on the voltage.

The hydrogen estimation (the *"Parameter estimation"* block in Figure 6.9) consists in a Proportional Integral Derivative (PID) controller, whose task is to set the right amount of $H_2$ at the anode inlet side, to properly match the measured voltage. The identification results are shown and discussed in the following. In Figure 6.10 A) the nominal inlet hydrogen molar flow $H_{2,nominal}$, the real one $H_{2,real}$ and the estimated one $H_{2,estimated}$ are reported. It can be noticed how the estimated flow follows the real one with a reduced error, thus confirming the correct identification performed by the PID. Figure 6.10 B) shows the trend of the voltage over time; also in this case the nominal value $V_{nominal}$, the real value $V_{Real}$ and the estimated value after the identification of the fault $V_{estimated}$ are illustrated. The change in $H_2$ clearly reflects in the voltage and the model manages to achieve a good matching with the real measurements, while maintaining a reduced error, as shown in Figure 6.10 C), where the discrepancies between un-faulty (i.e., nominal) and faulty model are analysed with the following relationship:

$$\epsilon = \frac{V_x - V_{real}}{V_{real}} \cdot 100\% \tag{6.17}$$

It is worth noticing here that $V_x$ in eq. 6.17 corresponds either to nominal or estimated voltage value, respectively. This allows checking if the PID controller sets the right amount of $H_2$ with respect to the occurring fault, thus reducing the error in the voltage estimation from 3.5% (in case of nominal unfaulty model) to about 0.5%.

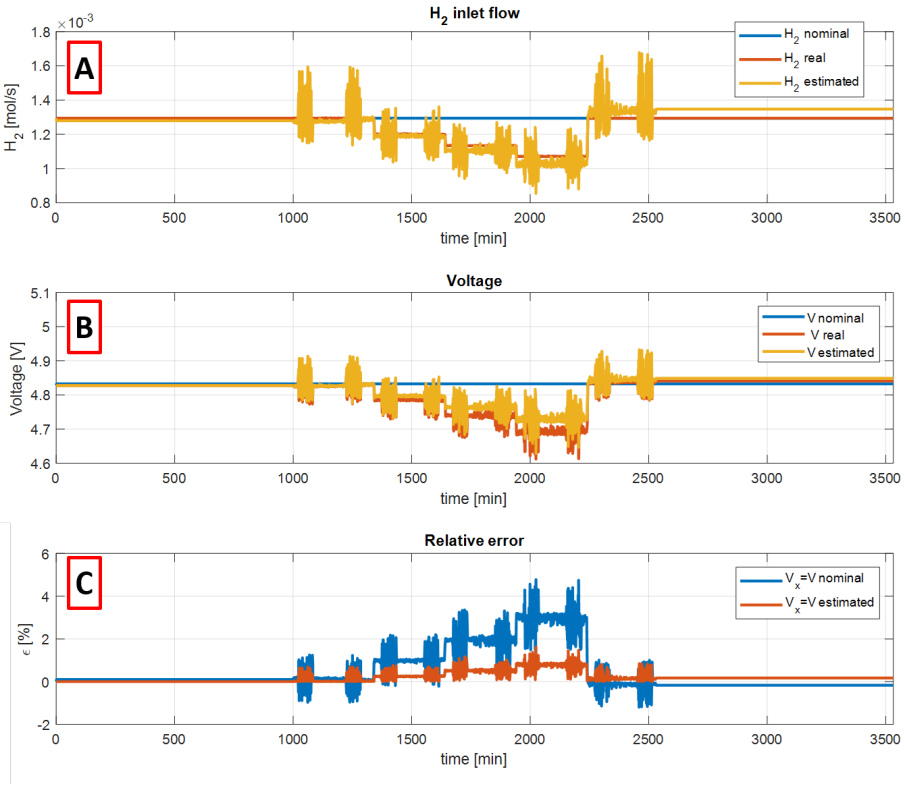


**Figure 6.10:** Nominal (i.e., unfaulty model estimation), experimental (i.e., real) and estimated trajectories of hydrogen molar flow (A) and voltage (B). Analysis of nominal vs. estimated discrepancies (C).

### 6.3.3 Fault Mitigation Application - Recovery

Once identified the fault, its magnitude and then properly tuned the advanced model, the mitigation countermeasure could be simulated via model-based approach to check its feasibility before the real actuation. As seen in paragraph 6.2, the operation of the system is described by different monitored variables $Y_i$ grouped in the vector $Y$. Among many possible variables to consider, the voltage ($V$) and fuel utilization ($F.U.$) are used. For each variable, the right mitigation strategy could be applied based on the severity of the fault. In this case, since the stack

was affected by fuel starvation, the countermeasure is taken on the fuel utilization, being it strongly linked to the hydrogen molar flow at the inlet of the stack, trying to implement a recovery strategy (Fault Recovery n.1 of Figure 6.11). In parallel, the voltage changing is monitored to understand if the countermeasure does not sensibly affect the normal operation of the system.

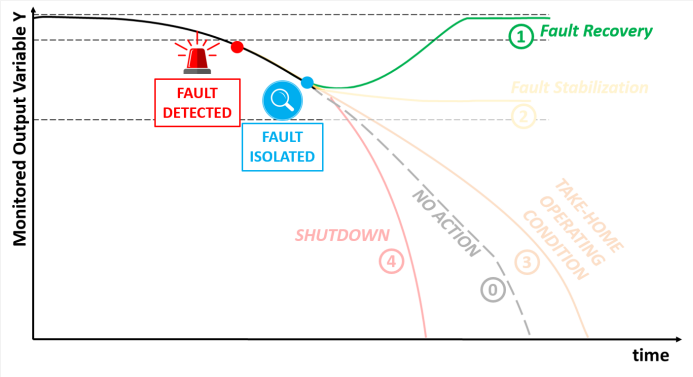


**Figure 6.11:** Fault Mitigation Application – Recovery

The control action suggested when a fuel starvation is detected is to reduce the current accordingly. The mitigation strategy consists in finding new operating conditions $u_{new}$ in order to bring the fuel utilization ($\hat{Y}(X,u)$) back to the nominal operating conditions, satisfying the recovery equation previously described. For this step only the models are used so far, since the feasibility of the approach need to be tested online before its implementation on the real system. The goal is to find a new operating current $I_{estimated}(u_{new})$ according to the information derived from the outputs of both models. Particularly, the current set point identification is carried out via a controller, using the feedback on the $FU$ (difference between nominal $FU_{nominal}$ and mitigated $FU_{mitigated}$ values) and the nominal value of the current. The estimated current is set as an input of the advanced model to mitigate the fault. Mitigation is achieved when the difference between nominal fuel utilization ($FU_{nominal}$) and mitigated fuel utilization ($FU_{mitigated}$) is less than a defined error, $\epsilon_{n1}$, that is similar to the model error (see Figure 6.12).

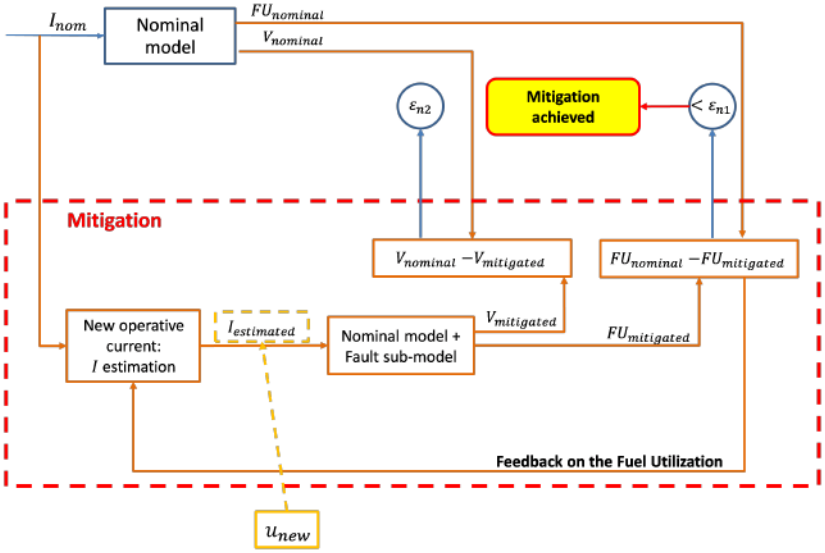


**Figure 6.12:** Fault Mitigation Application – Concept. In this case PID methodology is used in its typical way, i.e., to perform SOFC current adaptation to mitigate, through suitable control actions, the hydrogen leakage fault occurrence.

The current estimation (*"New operative current"* in Figure 6.12) consists in a PID controller conceived to identify the right value of the current set point to match the desired (nominal) fuel utilization (see Figure 6.13 A)). The PID controller was used for the same advantages explained above regarding the fault identification. The constants used for this controller have been found via heuristic procedures. Since the trend of the hydrogen molar flow rate at the inlet presents a reduced stepwise trend, with three lower values than the nominal reference, three different cases have been thus analyzed. The three steps are named "case n.1", "case n.2" and "case n.3", and refers to FU values of 82%, 86% and 90%, respectively, while the nominal condition is at FU equal to 77%. In Figure 6.13 A) the FU trend is reported. Here, both the nominal expected value, the three cases and the related mitigated results are shown. It can be noted that in all cases it is possible to reach the proposed target, that is to bring the considered state variable back to the nominal value. To achieve this latter target, the correct current trajectory is identified

and presented in Figure 6.13 B). It is interesting to note that, as the FU deviation from the nominal value increases, a more marked current set-point reduction is required to bring the fuel utilization back to its nominal value. To check the feasibility of such an action, the voltage trend is monitored and shown in Figure 6.13 C). Here the current reduction leads to a more marked over-voltage. In all cases the voltage presents a higher value with respect to the nominal one. Indeed, it is not possible to completely recover the faulty event though, finding a new acceptable operating condition, the stabilization (Scenario B in Figure 6.6 D) can be considered achieved.

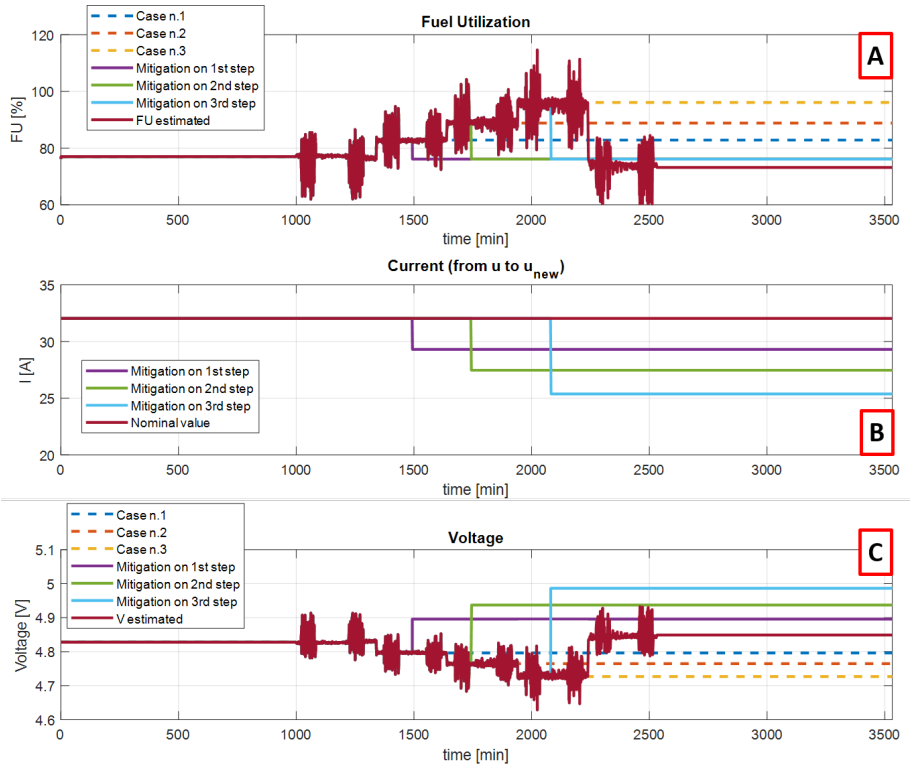


**Figure 6.13:** Mitigation action outcomes, here assessed focusing on fuel utilization (A, simulated state variable), current (B, control variable) and voltage (C, monitored output variable) resulting trajectories.

### 6.3.4 Mitigation feasibility

For the sake of clarity, the changes in current (that is the operating variable), the FU (that is the state variable) and the voltage (that is the monitored variable) are herein investigated.

All the variations are evaluated as percentage of the changing in value with respect to the nominal conditions.

Figure 6.14 A) shows the relative error achieved by the controller on the fuel utilization in the three steps of the case study. The error is described as follows:

$$\epsilon_{FU} = \frac{FU_x - FU_{nominal}}{FU_{nominal}} \cdot 100\% \tag{6.18}$$

where $FU_x$ is the value of either mitigated or estimated (i.e., faulty) cases.

It is interesting to note that in all cases (i.e., induced fault steps) the nominal FU is completely restored to its nominal value (77%).

Figure 6.14 B) shows the related percentage change in current, which is the operating value suitably modified as a counteraction to the malfunctioning. Its deviation is evaluated as follows:

$$\delta_I = \frac{I_{nominal} - I_x}{I_{nominal}} \cdot 100\% \tag{6.19}$$

Again, the footnote "$x$" stands for either the estimated value (i.e., faulty) or the mitigated steps.

In order to check the consequences of such mitigation actions, the voltage change is monitored and presented in Figure 6.14 C). In this case eq. 6.19 turns into:

$$\delta_V = \frac{V_x - V_{nominal}}{V_{nominal}} \cdot 100\% \tag{6.20}$$

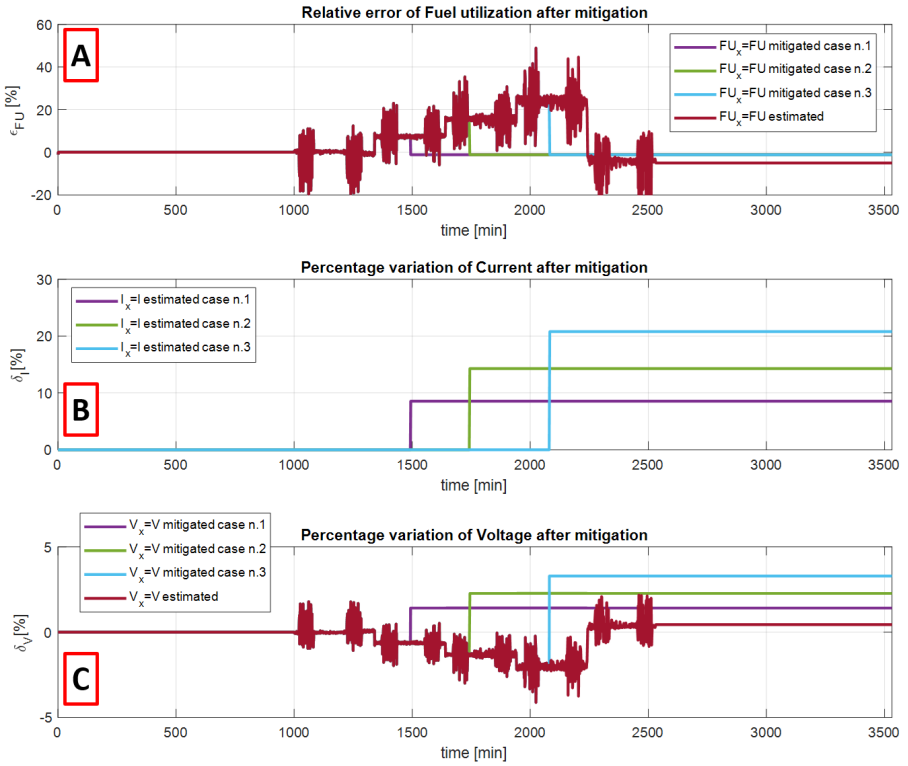


**Figure 6.14:** Feasibility evaluation of the mitigation action played by the change in the control variable I (i.e., operating SOFC current, see Figure 6.13 B). Such an evaluation is based on resulting percentage variation of fuel utilization (A, state variable), current (B, control variable) and voltage (C, monitored output variable).

For sake of comparability, the parameters variations are reported in Table 6.5 along with the nominal conditions.

| | Nominal | Step 1 | | Step 2 | | Step 3 | |
|---|---|---|---|---|---|---|---|
| | | Faulty | Mitigated | Faulty | Mitigated | Faulty | Mitigated |
| **FU** | 77% | 82% | 77% | 88% | 77% | 96% | 77% |
| **V [V]** | 4.83 | 4.79 | 4.89 | 4.76 | 4.94 | 4.72 | 4.99 |
| **I [A]** | 32 | 32 | 29.3 | 32 | 27.5 | 32 | 25.4 |
| $\epsilon_{FU}$ [%] | - | +6.49% | 0 | +14.28% | 0 | +24.67% | 0 |
| $\sigma V$ [%] | - | -0.83% | +1.41% | -1.45% | +2.27% | -2.28% | +3.29% |
| $\Delta I$ [%] | - | 0 | -8.54% | 0 | -14.28% | 0 | -20.78% |

**Table 6.5:** Mitigation feasibility analysis. Nominal, 3-steps faulty and 3-steps mitigation comparison

It is worth remarking that the mitigation action consisted in a progressive reduction in the load, up to the 20% of its nominal value at the third step, and allowed restoring the nominal FU (77%), while causing a change in voltage with an increase up to 3.3%. This confirms the expected impossibility to fully recover the malfunctioning. However, a new stabilized condition is clearly reached. From the results the temperature is missing, since the data set was measured in an operating stack within the furnace, whose dynamics completely overlaps the stack one, resulting in a meaningless measurement.

### 6.3.5 The Mitigation Application - Final remarks

A resume of the proposed procedure is finally presented in Table 6.6. It is worth recalling that in this structure, a nominal model runs in parallel with the real system. This latter is the plant reference for monitoring, detection and isolation purposes, while during the identification of the fault magnitude and the mitigation feasibility phase, the reference is the updated version of the nominal model with the related degradation submodel. Only if the nominal condition is restored, the reference condition can be provided back by the plant as reference for the diagnostic procedure when a new fault occurs and the mitigation approach needs to be applied again.

| | On-line Monitoring | FDI Algorithm | Fault Identification | Fault Mitigation | Real Application |
|---|---|---|---|---|---|
| Nominal model Usage | $\hat{Y}(X,u)$ | | | search $u_{new}$ to have $\hat{Y}(X,u_{new}) \approx \hat{Y}(X,u)$ | $\hat{Y}(X,u_{new})$ |
| Plant Reference | $Y(X,u)$ | | $\hat{Y}(X,u)=\hat{Y}(X,u)+\hat{F}(X,u)$ | | $Y(X,u_{new})$ |
| Fault submodel behaviour | $\hat{F}(X,u)=0$ | | $\hat{F}(X,u)\neq 0$ | search $u_{new}$ to have $\hat{F}(X,u_{new})=0$ | $\hat{F}(X,u_{new})\rightarrow 0$ |
| Mitigation Controller behaviour | No action | | | Test the feasibility of the recovery counteraction | Mitigation achievable Apply operation |

**Table 6.6:** Schematic synthesis of effective real-world deployment of the proposed model-based mitigation procedure, here particularized to the case of successful management of hydrogen leakage fault in an SOFC.

During the monitoring phase, the real system behaviour (i.e., the plant reference) is compared with the nominal model (i.e., the expected condition) to early detect any abnormal condition. When the real measurement diverges from the expected one, the FDI algorithm starts. Once defined the degradation phenomenon ($F(X,u)$), the nominal model evolves into the advanced one (with the enabling of the related degradation sub model to identify the magnitude of the fault). The identification process ends when the advanced model well represents the plant (i.e., faulty) reference with and acceptable error ($\epsilon < \epsilon_m$).

At this point the mitigation feasibility is verified according to proper defined constrains. The approach is completely model-based, since the reference is defined by the nominal model, while the system on which the action is performed is represented by the advanced model (instead of the plant).

Four different scenarios to deal with the malfunctioning are defined:

1. **Recovery** where the nominal condition is fully restored without sensible changes in the operations;

2. **Stabilization** where a new stable operating point is achieved, with a good trade-off between limiting the detrimental effect and saving the stack performances;

3. **Take home condition** where the RUL is slightly increased driving the system towards a condition that reduces the performances but allows preparing for maintenance with no need for shutting down the system;

4. **Shut down for safety** where the degradation is too high to perform any kind of action and the only solution is to immediately turn of the system to avoid components damaging.

## 6.4 The Procedures flowchart

The methodology presented in this work relies on a robust and reliable FDI algorithm and validated degradation sub-models. Their usage allows a continuous monitoring of the FC State of Health for diagnostic purposes. Moreover, their combination allows defining suitable procedures to schedule maintenance actions. However, when a not investigated malfunctioning occurs, the experimental data used for the development of the related sub-models could be not enough to deal with such problem. In that case, or when computational issues does not allow applying the afore described methodology, a generic procedure defined by a synthetic flowchart might help to face up with such not expected conditions. Thus, a procedures flowchart has been herein proposed to manage a system in a critical condition; it is a sequence of actions for the design of an on-board mitigation algorithm or to develop a maintenance manual. Starting from the aforementioned idea of four different mitigation conditions, the procedure flowchart could guide the mitigation algorithm (if automatized) or the user (otherwise) to choose the most suitable action to take, according to the severity of the fault occurring. Here the diagnostic algorithm and the related extracted features can be used in "reverse mode" to provide information on the feasibility and effectiveness of such countermeasure. The main idea is to use the monitoring tools to verify if a slight change in the operating variables, based on the heuristic knowledge of the occurring phenomena, allows reaching a sign of recovery. The Fault Mitigation is the natural next step after the Fault identification. It aims at applying the countermeasures to the identified malfunctioning trying to guide the system through a recovery path towards the nominal state. This would stabilize the detrimental effect and prepare for maintenance, otherwise.

A well-defined mitigation approach should start from the severity grade n. 1, the recoverable fault, which is the best case to have a complete

FC restore, to the grade n.1, the most critical condition. The simplified flowchart herein developed is presented in Figure 6.15.

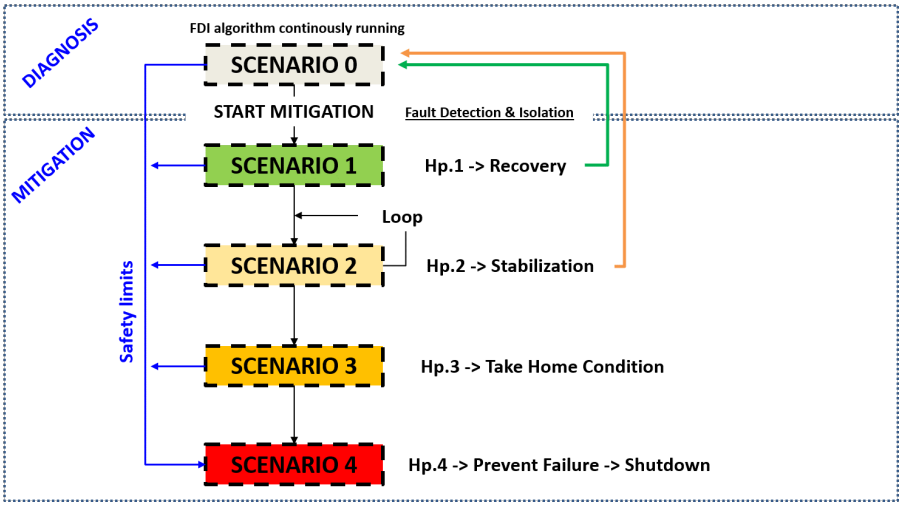


**Figure 6.15:** Simplified mitigation flowchart. The Scenario numbers are the same as those sketched in Figure 6.2

Starting from the Scenario 0, in which the system is considered in nominal conditions, the FDI algorithm runs continuously in background, to monitor possible changes in the expected nominal (i.e., unfaulty) behaviour. When such conditions unpredictably change, an alarm arises, and the investigation procedure starts to infer on system status. Thus, if a fault is detected and isolated, the mitigation phase takes place. Consequently, the system status moves from the Scenario 0 (grey) to the Scenario 1 (green). Here some operations could be applied to drive the system back to its nominal behaviour (or at least in a narrow threshold). Such operations depend on the experimental evidences and on the physics of the detected malfunctioning (i.e., the current reduction is a valuable operation when a Fuel starvation occurs or the injection of pure Hydrogen could be beneficial to restore the system in case of an early stage of sulphur poisoning, etc.). If the operation is successful, the system can return to the Scenario 0, with an updated *"nominal reference condition"*, accounting for the changes occurred after the applied

mitigation operation.

If the recovery fails, the target is to contain the detrimental effect in a defined stabilization range. This can be done by considering the condition as unrecoverable and trying to vary the FC operation in a stabilization loop aiming at stabilizing the effects of the fault, with a good trade-off between performance and RUL. Even in this case, if the stabilization is achieved the system can come back to the Scenario 0 updating the reference conditions that consider the applied actions. If even the stabilization fails, the maintenance could be the only solution to consider.

To avoid the sudden system shut-down, the setting of a take-home condition (Scenario 3) could improve the RUL with respect to that one estimated after the simple shut-down; this could drive the system toward the maintenance in a smoother way, avoiding additional detrimental effects like anode re-oxidation that could occur with a fast operation.

Unfortunately, this theoretical condition is often unfeasible and difficult to set, so the remaining action is the immediate shut-down (Scenario 4). Furthermore, such operation has to be automatically applied when safety limits like high under-voltage or a sensible increase in the cathode outlet temperature are exceeded.

### 6.4.1 The detailed Flowchart

The key value of such flowchart is the Monitoring Index ($MI$), which is a feature (i.e. metrics, parameter, control variable) monitored by the diagnostic algorithm and here exploited to check the quality of the mitigation countermeasure applied. The main idea is to apply the selected strategy in a iterative mode (i.e., a kind of trial and error application), to understand if its application for a short time results in a beneficial effect on the system with the respect to the observed the detrimental trend. Indeed, as shown in Figure 6.16, if the $MI$ (which is already beyond the threshold) changes its trend after the mitigation action and allows predicting a return within such limit, it means that the applied strategy works and the countermeasure can be applied until the recovery/stabilization.

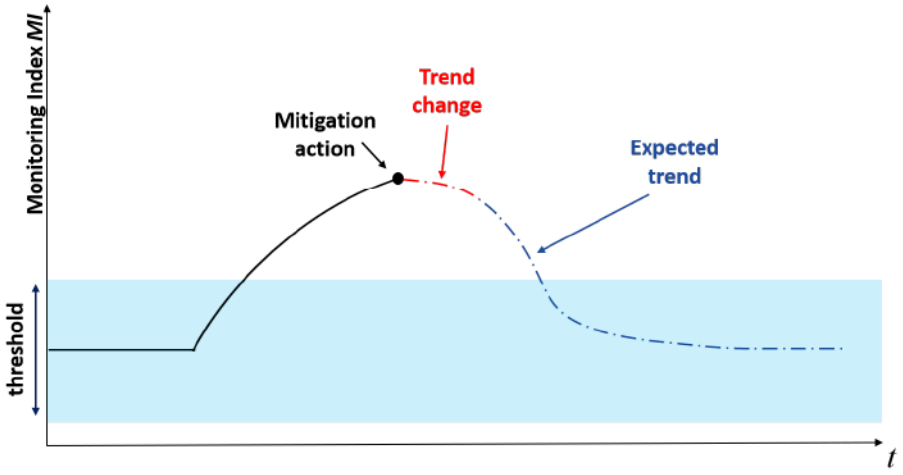


**Figure 6.16:** Monitoring Index application, an example. Here the $MI$ allows checking the feasibility of the mitigation action applied.

To provide an example, if the FDI algorithm reveals the Fuel Starvation occurrence, which means an increase in the $R_{TOT}$, a possible mitigation action can be applied and the $R_{TOT}$ becomes a Monitoring Index; if such operation, applied in a short time window, smooths this increase and changes the $R_{TOT}$ trend toward the nominal state, the operation is feasible and the mitigation can be achieved.

It is worth commenting that it is fundamental to maintain the information of all operations applied, by updating the Monitoring Index value step by step ($MI_{\#Mit,i}$), along with the new reference conditions when achieved. The presented approach could be improved by coupling the Diagnostic algorithm with the Lifetime prediction algorithm. Indeed, the RUL estimation could quantify the advantages of the adopted mitigation procedures, particularly for the Scenarios 3 and 4. Moreover it can help in retuning the FC safety limits of the when a recovery and a stabilization is achieved.

Based on the results from the available data analysed in this work, the mitigation procedure flowchart has been detailed for the fuel starvation and described in figure 6.17.

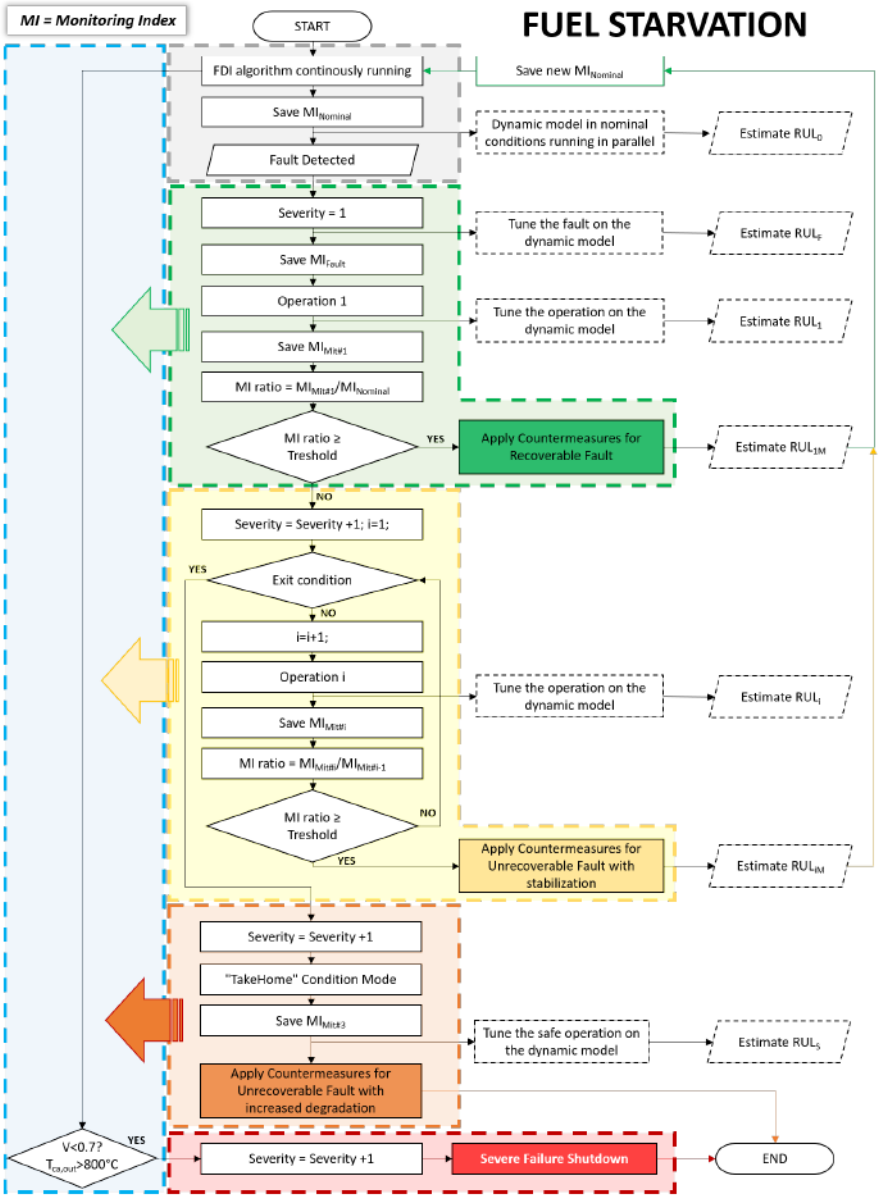


**Figure 6.17:** Procedures Flowchart for the Fuel Starvation. The scheme presented in figure 6.15 is here expanded and detailed.

The suggested procedure to follow for mitigation and described in the flowchart of figure 6.17 lies on the so called *Scenario n.0*, which is the frame of the approach and accounts all the operations related to the FDI algorithm to monitor the Fuel Cell State of Health. When a specific fault is isolated, the procedure starts and the *Scenario n.1* is activated.

- **Scenario 1 – The Recovery stage**

  The main aim of the mitigation is to fully recover the FC driving back the system to its nominal condition. The successful recovery depends on two main factors: the nature of the fault and its early detection. As an example, if a leakage occurs, it is not possible to bring the system back, whereas if a sulphur poisoning is detected at an early stage, an injection of fresh $H_2$ could recover such malfunctioning. Both the aforementioned factors can be summarized in the "fault severity" parameter, which is directly correlated to the Mitigation Scenario. Thus, when the procedure enters the Scenario n.1, the fault severity grade is automatically set to "1" (the least severe one) and the procedure to apply, for the *Scenario n.1* is sketched in figure 6.18.

  Once saved the MI during the fault ($MI_{fault}$), the Operation 1 has to be applied to attempt the recovery. After such operation (like current reduction in case of fuel starvation), the new value of the MI, namely $MI_{MIT\#1}$ has to be compared to the faulty one $MI_{Fault}$ to test the effectiveness of the Operation 1. Indeed, if the ratio between $MI_{MIT\#1}$ and $MI_{Fault}$ is less than 1 (i.e., the Monitoring Index is changing it increasing/decreasing trend, as shown in figure 6.16), the countermeasure for the Recoverable fault can be applied. Finally, when the $MI_{ratio} = MI_{Mit\#1}/MI_{Nominal}$ is less then the Threshold value (whose value is set in table 6.7) the fault can be considered recovered. At this point, the system can be considered as in nominal condition, thus the Scenario n.0 can be set again with a new $MI_{nominal}$. In parallel to such procedure, if the lumped dynamic model described in chapters 4 and 5 is properly tuned, the RUL estimation procedure can be applied to estimate the changes in the lifetime estimation of the FC due to the events occurred; as a consequence $RUL_0$, $RUL_F$, $RUL_1$ and $RUL_{1M}$

will be available for SoH purposes and will give information about the nominal condition, the faulty one after the fault isolation, the new one after the application of the Operation n.1 and the new mitigated condition after the applied countermeasure, respectively.

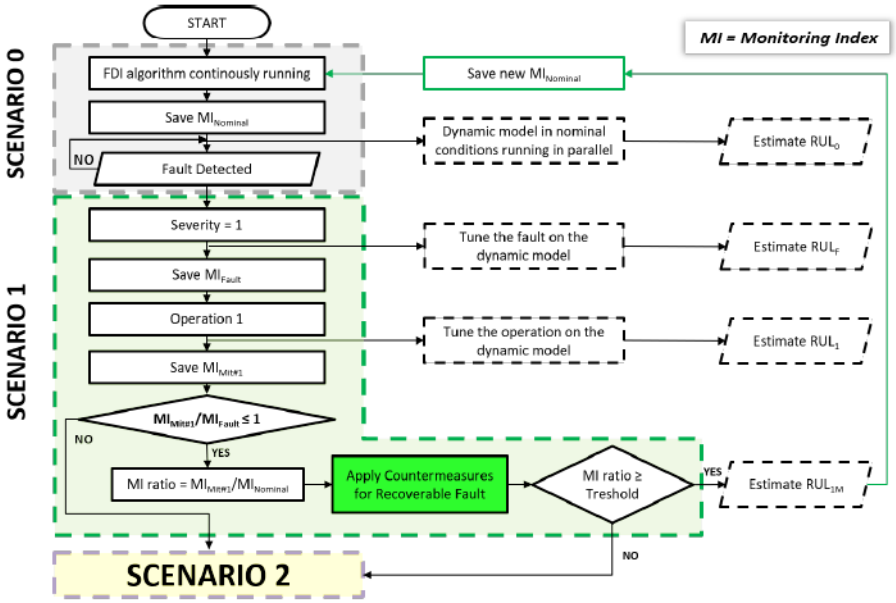


**Figure 6.18:** Scenario 1 – The recovery stage. Here the detailed flowchart for this Scenario is sketched along with the link with Scenarios n. 0 and 2. The specifications for the fuel starvation Monitoring Indexes are detailed in Table 6.7.

Table 6.7 contains the description of the Mitigation Index considered for this scenario, along with the suggested recovery operation and the threshold limits to consider such operation successfully achieved. These latters have been set upon experimental data analysis performed in section 3.3.1. Once applied the current reduction, the monitoring index $MI_{Fault}$ will turn into $MI_{MIT\#1}$. To have an hint of recovery, the $MI_{MIT\#1}$ is expected to move toward the nominal region, according to the following equation:

$$\frac{MI_{MIT\#1}}{MI_{Fault}} \leq 1 \tag{6.21}$$

The MI Threshold parameter, namely $MI_{ratio}$, is defined as the ratio between $MI_{MIT\#1}$ and $MI_{Nominal}$ . To consider the mitigation operation successfully achieved and the fault recovered, the Monitoring index has to come back to the un-faulty area, limited by the thresholds; this means that the FDI algorithm should no longer detect any kind of alarm (i.e., the related symptom value has to turn into 0). If this is not achieved, the recovery attempt fails and the procedure moves toward the Scenario n.2 - the stabilization loop. Table 6.7 shows the Monitoring Index chosen as the most representative for the fuel starvation. Here both power and ECM based features are considered as relevant indicators to monitor the fuel starvation mitigation. The defined values have been defined upon the Threshold definition of section 3.3.1 and here adapted for mitigation purposes. Moreover, same qualitative trends have been added from heuristic knowledge as the $R_0$ and the Pressure drop that have to qualitative monitored to verify their expected behaviour according to the applied mitigation operation (i.e., the $R_0$ is supposed to increase with the current reduction).

| **Severity 1 - Time: system response + time for EIS measurement** | | | | |
|---|---|---|---|---|
| **MI** | Power | *EIS*<br>Area Low Freq. Arc,<br>$\omega_{LF}$, $R_{LF}$, $R_{TOT}$ | $R_0$ | Presssure drop |
| **OPERATION** | Reduce current (with respect to the expected voltage) | | | |
| $MI_{Threshold}$<br>$for$<br>$MI_{ratio} = \frac{MI_{Mit,1}}{MI_{Nominal}}$ | *If operating at fixed current*<br>$Power > 95\%$<br><br>*If operating at fixed flow*<br>$Power < 110\%$ | Area Low Freq. Arc<br>(↓ Qualit.)<br><br>$\omega_{LF} > 88\% \uparrow$<br><br>$R_{LF} < 140\% \downarrow$<br><br>$R_{TOT} < 120\% \downarrow$ | Qualit. | Qualit. |

**Table 6.7:** Scenario Table 1 - Severity 1. Here the suggested monitoring index are reported along with their threshold limits. The mitigation operation is the current reduction. The arrows indicate the expected trend of the related MI (i.e., the down arrow indicates a decreasing expected trend, whereas the up arrow an increasing one).

- **Scenario 2 – The Stabilization loop** If the Recovery strategy is not applicable or it is not able to drive the FC back the nominal condition (i.e., the MI indexes are not within the nominal range set by the defined thresholds), then the Scenario n. 2 is the next step. It consists in a loop of a repeating operation applied at increasing/decreasing magnitudes to stabilize the fault and, in turn the MI index trends. This allows stabilizing the malfunctioning with a new system operation in which a trade-off between the system application purposes (i.e, continuous high performance if applied in a industry or high reliability if used as a APU or UPS, etc.) and RUL is achieved. The Scenario n.2 applies when the fault has a severity grade of "2". The related flowchart is sketched in figure 6.19.

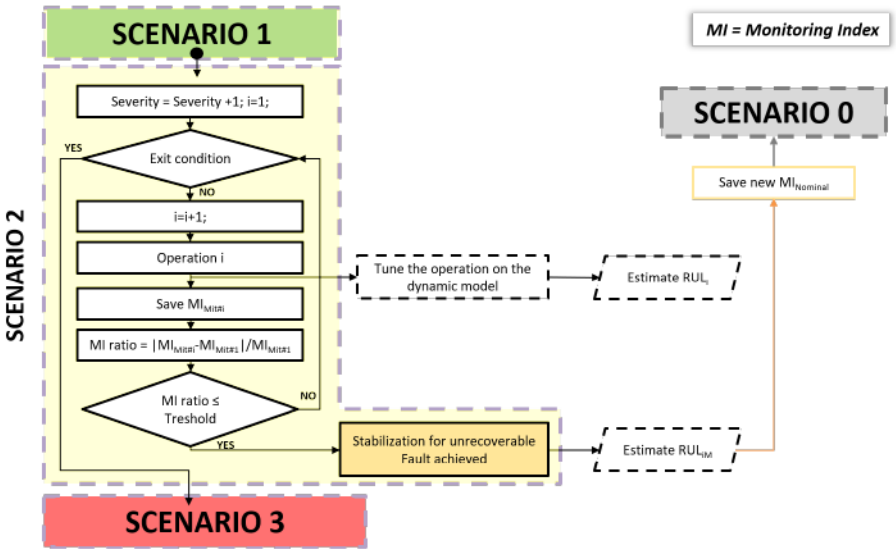


**Figure 6.19:** Scenario 2 - The Stabilization loop. Here the detailed flowchart for this Scenario is sketched along with the link with Scenarios n. 0, 1 and 3. The specifications for the fuel starvation Monitoring Indexes are detailed in Table 6.8.

The suggested approach is very similar to that presented in the previous scenario. The main goal is again that one of recovering the

system nominal condition, but here the aim is to stabilize the fault instead of trying to restore its initial condition (i.e. full recovery). In this case the operation has to be applied in a repeating loop until the stabilization (that is the capability of the application to stop the detrimental effect even though without a reversible process to restore the initial values) is achieved or an exit condition (based on a limit on the voltage) is reached. The stabilization threshold value (reported in Table 6.8) is defined as the 5% variation of the faulty index, $MI_{Fault}$, after the ineffective recovery operation of the Scenario n.1. The exit condition has here defined as a voltage limit value as suggested by the manufacturer (i.e., for a lower value the system can be considered not properly working any more), or it can be defined as a time interval otherwise. In the loop, a floating index $i$ accounts for the applied operations. The $MI_{ratio}$ is here defined as the ratio between the Monitoring Index of the operation $i$ with respect to that one experienced after the recovery attempt $MI_{MIT,1}$, according to the following equation:

$$MI_{ratio} = \frac{|MI_{MIT,i} - MI_{MIT,1}|}{MI_{MIT,1}} \tag{6.22}$$

When such ratio is less than the threshold defined in Table 6.8, the Fault can be considered stabilized and the new $RUL_{iM}$ can be evaluated, thus going back to Scenario n.0. Also in this case the lumped dynamic model described in chapters 4 and 5 could provide information on the RUL, particularly after each application of the operation $i$ ($RUL_i$) and once stabilized the fault if successful ($RUL_iM$).

| **Severity 2 - Stabilization loop Exit condition: Voltage limit exceeded -** $V_{cell} \leq 0.75$ | | | | |
|---|---|---|---|---|
| **MI** | Power | *EIS* Area Low Freq. Arc, $\omega_{LF}$, $R_{LF}$, $R_{TOT}$ | $R_0$ | Presssure drop |
| **OPERATION** | Reduce current (with respect to the expected voltage) | | | |
| $MI_{Threshold}$ $for$ $MI_{ratio} = \frac{\lvert MI_{Mit,i} - MI_{Mit,1} \rvert}{MI_{Mit,1}}$ | $Power \leq 5\%$ | Area Low Freq. Arc ($\downarrow$ Qualit.)<br>$\omega_{LF} \leq 5\% \uparrow$<br>$R_{LF} \leq 5\% \downarrow$<br>$R_{TOT} \leq 5\% \downarrow$ | Qualit. | Qualit. |

**Table 6.8:** Scenario Table 2 - Severity 2. Here the suggested monitoring index are reported along with their threshold limits for the stabilization (5%). The mitigation operation is the current reduction. The arrows indicate the expected trend of the related MI (i.e., the down arrow indicates a decreasing expected trend, whereas the up arrow an increasing one).

As for Table 6.7, Table 6.8 reports the Monitoring Index chosen as the most suitable for the fuel starvation stabilization. The stabilization threshold limit is here imposed at a value of 5% as representative for an acceptable range of stabilization. Moreover, same qualitative trends have been added from heuristic knowledge, like the $R_0$ and the Pressure drop, that can be qualitatively monitored to verify their expected behaviour according to the applied mitigation operation. Indeed, according to the experimental evidences, the $R_0$ is supposed to increase with the current reduction; thus, if the applied countermeasure is the load change (i.e., reduction or increase of the current), when applied such operation, the $R_0$ is expected to change accordingly. If this expected trend is not observed, a feedback on the system on the unsuccessful application of the chosen operation is provided. Moreover, if the stabilization is not achieved after the defined time window or if the voltage limit is exceed, the mitigation should be considered not effective and a maintenance action has to be activated. Therefore, the procedure enters the Scenario n.3, that one dedicated to the planned shut-down.

- Scenario 3/4 – The Take-home condition and Shut-down for safety

The Scenario n.3 is associated to a Severity grade of 3 and aims at finding a soft condition, named "Take-Home Condition" that allows avoiding the immediate shut-down (and its related problems); this solution should keep the system working under a sort of "dummy" mild condition that soften the detrimental effect and guarantees the time necessary to prepare the work needed for maintenance. Such conditions, usually an OCV one, could imply the partial or complete stop of the electrochemical reaction while maintaining the stack at its high working temperature to avoid re-oxidation due to high thermal gradients in a limited time window. In case of fuel starvation, the OCV could be a possible "take-home condition" according to the heuristic knowledge. If neither this condition is feasible or provides good results in terms of RUL ($Rul_S$) compared to the time needed to prepare for maintenance (i.e., $\tau_{ptm}$ as fully described in section 6.2.5), the immediate shut-

down is unavoidable (Severity grade n. 4).

Figure 6.20 describes the flowchart for this procedure.

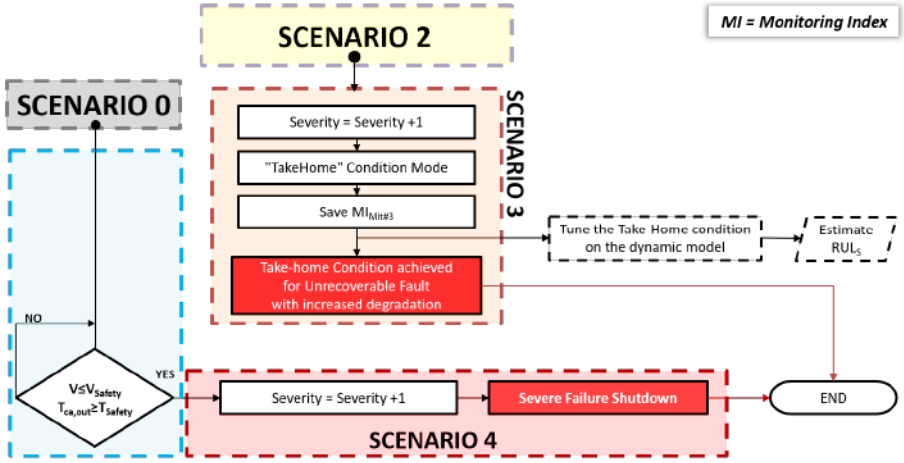


**Figure 6.20:** Scenario 3/4 - Take-Home condition & Shut-down for safety. Here the detailed flowchart for these Scenarios are sketched along with the link with Scenarios n. 0 and 2.

It is worth commenting that a silent check needs to be continuously performed by a sensor on the voltage and the outlet temperature. Indeed, if at any time the stack shows a $V_{cell} \leq V_{safety}$ or a $T_{ca,out} \geq T_{safety}$, the Scenario 4 is automatically enabled and the shut-down immediately actuated accordingly. Such limits were provided by the manufacturer, and in this case are equal to $0.7V$ and 800 °C respectively for the SP 64-cells stack set at 1500W. It is clear that, for the application to other systems or technologies, the safety limits are to be clearly defined by the manufacturers, to clearly define a critical operating limit.

To summarize, fault mitigation for SOFCs is a new and interesting field whose purpose is to manage abrupt malfunctioning within the FC aiming at extending the lifetime. The mitigation requires a deep expertise on the phenomena occurring, the physics of the main processes and the effects that they can cause. In this Chapter a complete methodology

has been proposed to define a procedure to mitigate possible malfunctioning occurring. To achieve its objectives, fault mitigation requires a reliable Fault Detection and Isolation phase along with a useful lifetime estimation routine. Indeed, the combination of dynamic measurements and EIS-based information is fundamental for early detection of possible malfunctioning in the FC, estimate its RUL and define a possible countermeasure to be applied. To pave the way towards the development and application of a complete Monitoring Diagnostic and Lifetime Tool, a flowchart procedure has been presented, in which all the information and tools are exploited for several usages. The further deployment of such tool will allow its industrialization and on-board application to improve the reliability of SOFC system and to facilitate their market deployment.

# Chapter 7

# Conclusions and Outlook

The main aim of this Chapter is to resume the work done in this thesis, highlighting its novelties and advantages. A look on the future perspectives is given as well.

## 7.1 Resuming comments

This thesis focuses on the development and validation of an advanced algorithm to monitor the State of Health of Solid Oxide Fuel Cells. A computational structure for fuel cell diagnosis has been developed and implemented along with a set of strategies for mitigation actions. Lumped dynamic models and Electrochemical Impedance Spectroscopy-based techniques are herein coupled to extract features as relevant parameter for both diagnosis, mitigation and RUL estimation purposes. Moreover, all those approaches are applied to provide helpful guidelines on possible mitigation countermeasures to be actuated in case of faults. A EIS-based fast and generic algorithm, named Matching Geometric Fitting Guess, has been developed for diagnostics in either single cells or stacks. From that, the extracted features are properly selected as sensitive indicators of the cell/stack State of Health (SoH) and then used for Fuel Cell monitoring. The algorithm proved to be fast and reliable on different EIS spectra and FC set-ups with a computational time of about 5 seconds, run on a laptop computer equipped with an Intel Core i7-6700 HQ.

The Diagnostic approach has been validated against several experimental data collected by the partners of the European Project INSIGHT, on different FC set-ups (segmented cells, single cells, short stacks, full stacks), measured with different laboratory instruments and perturbed with different stimuli (based on both sinusoidal and Pseudo Random Binary Signals). The diagnostic algorithm proved to be reliable in identifying the ECM related to each measured spectra, with a repetitiveness in the circuital elements that successfully achieved the comparison of the extracted features for State of Health monitoring. The FSM, built on experimental dataset provided by DTU, allowed to correctly detect and isolate the arising fuel starvation in all the tested cases, along with some abnormal conditions (either "false alarms" or "general alarms") far from the nominal expected ones. These latter cases lead to the definition of new identified symptoms patterns that could be suitably validated to extend the set of detectable malfunctioning. Furthermore, the diagnostic tool proved to successfully work on a commercial SOFC in a real environment, with good results in terms of on-board fuel starvation detection and isolation.

It has been found that the fuel utilization limit (to distinguish the FC state from nominal to faulty) reduces with the size of the FC; indeed, a segmented cell can stand high fuel utilization levels up to 90%, the single cell up to $\approx 80\%$, whereas a 64-cells stack suffers from fuel starvation for $F.U. \geq 70\%$. Indeed, with respect to a single cell, the more the cells the lower the fuel utilization limit. This can be ascribed to the fuel distribution within the each cell of the stack: depending on the fuel path, the gas distribution induces a low reactant flow at the cells at the outlet cells (whose position depends on the stack layout) thus lowering the average F.U. limit of the overall stack.
A stack lumped dynamic model was developed and validated against experimental data on 6-cells short stack. It allows simulating the expected nominal conditions, as unfaulty and nominal reference states for the monitoring. The lumped model, tested and validated on DTU experimental dataset, allows simulating 100 functioning hours in 360 s, on a laptop computer equipped with an Intel Core i7-6700 HQ. A stack ageing submodel was implemented by integrating some ECM-based extracted features, to model the natural ageing of the Fuel Cell. This was also supported by the exploitation of data taken from literature and led to

a Remaining Useful Life (RUL) estimation model, successfully validated upon experimental data from a 6-cells stack tested by CEA. This approach allowed estimating the RUL of each one of the 6-cells of stacks, thus finding the broken one at the time being, as already found in the experimental evidences analysed after the test campaign completion.
Finally, the mitigation was investigated to set a general methodology to define possible countermeasures to apply in case of faults. Here, the lumped model is used to predict the FC behaviour and check the feasibility of the proper counteractions; moreover, it allows choosing the mitigation strategy level to be applied to fulfil: i) full recovery, ii) stabilization, iii) Take-home condition or iv) safety shut-down. The verification of the feasibility of the proposed approach is achieved by testing the methodology for a case study of $H_2$ leakage at inlet, simulating the fuel starvation phenomenon. Furthermore, a procedures flowchart has been proposed to handle the system in a possible critical condition; it is a sequence of actions defined to develop the design of an on-board mitigation algorithm or a maintenance manual to the user. The aim is to guide the mitigation algorithm (if automatized) or the user (otherwise) to choose the most suitable action to take, according to the severity of the fault occurring. Here the diagnostic algorithm and the related extracted features are used in "reverse mode" (i.e., to verify the effectiveness of an operation and instead of diagnosis a malfunctioning, considering the trend of the monitored features with respect to the imposed thresholds) to provide information on the feasibility and effectiveness of the applied countermeasure.

## 7.2 Future perspectives

The interesting results achieved in this work pave the way towards the development of an integrated Monitoring, Diagnostic and Lifetime Tool that could be implemented on SOFC systems for on-board applications. This will help in avoiding incipient malfunctioning and properly schedule maintenance operations. Moreover, the study on the mitigation is intended to provide useful guidelines to handle the detected faults and

to apply proper countermeasures to recover/limit their related negative effects or simply avoiding sudden shut-downs.
The work done aimed at defining a new concept in which monitoring, diagnostics and prognostics are used within a unique frame to assess the Fuel Cell State of Health. Control techniques should be considered as part of this frame when performance optimization, adaptation and recovery tasks are needed to increase both lifetime and availability as well as to reduce maintenance time intervals. Here the development of fast models along with the usage of not-so-invasive techniques like EIS allows analysing the Fuel cell at different levels (i.e., from stack level to cell one), with a possible future improvement through the coupling of the described modelling approach with BoP ancillaries sub-models. This will allow adding more information derived from conventional signals coming from Balance of Plant measurements to the FDI algorithm and help in better distinguishing a fault occurring within the stack or derived from a malfunctioning in one of the ancillaries, to properly counteract to mitigate it.

Future perspectives for the results achieved by this thesis are several and can be split in three macro areas:

- *EIS-based diagnosis*
  The Diagnostic approach could be extended to more faults, with the aim of improving the Fault Signature Matrix. Indeed, the more FSM rows, the more faults than can be isolated, the more reliable the diagnostic approach. Moreover, the investigation of different nominal conditions at different loads, fuel rates and power could lead to the development of a reference condition map, which could characterize the FC and increase the range of applications of such tool. If a large amount of EIS data at different conditions were available, it could be possible to derive useful features behaviour that can be extrapolated to infer on their link to specific parameters like temperatures, flows, etc. It is worth commenting that embedding such tool in a compact device would be a solution for a future portable and versatile diagnostic application that could apply to all electrochemical devices like Fuel Cells, batteries and electrolyzers. The on-field test cases proved the effectiveness of the

tool, already demonstrated for Proton Exchange Membranes (in the frame of the European Project Health-Code), for Solid Oxide Fuel Cells (within the INSIGHT Project), with a interesting open field on batteries. An optimization and industrialization of this concept would enormously impact on the deployment of FC and other electrochemical devices and their future market penetration.

- *Lumped dynamic model*
  The lumped modelling proved to be a reliable solution for the voltage/outlet temperature estimation. It could be a valid support in the design of control and diagnostic strategies and in the real time Fuel Cell monitoring, by running such model in parallel with real system. Moreover, the EIS-based information updated whenever a new measurement is collected, allows tuning the model according to the possible ageing detrimental effect. The model provides useful information on the stack outlet flows, usually difficult to measure with costly and invasive sensors. This will help in a extended diagnostic approach, where the stack is modelled along with its ancillaries. Further improvement could consider the modelling of the BoP elements (see [193] and [194]) to extend the diagnosis at system level.

- *Fault mitigation*
  SOFC fault mitigation is a novel field in which the scientific research is focusing on. This thesis aimed at defining some useful guidelines on this topic and paved the way towards interesting perspectives. Indeed, as shown in table 6.6, the approach could suggest the action to take depending on the malfunctioning occurring. Thus, the procedure flowchart of section 6.4 could be automatized and implemented in a controller that could immediately apply the suggested countermeasure. Furthermore, the Fault Signature Matrix could be extended, accounting for the features for detection, along with the counteractions to the isolated fault according to its severity.

# Nomenclature

## Acronyms

| | |
|---|---|
| AFE | Analog Front End |
| APU | Auxiliary Power Unit |
| ASR | Area Specific Resistance |
| BoP | Balance of Plant |
| CEA | Commissariat à l'énergie atomique et aux énergies alternatives |
| CNLS | Complex Nonlinear Least Square |
| CPE | Constant Phase Element |
| DRT | Distribution of Relaxation Times |
| DTU | Danmarks Tekniske Universitet |
| ECM | Equivalent Circuital Model |
| EIS | Electrochemical Impedance Spectroscopy |
| EoL | End-of-Life |
| EPFL | École polytechnique fédérale de Lausanne |
| FC | Fuel Cell |
| FDI | Fault Detection and Isolation |
| FIB | Focused Ion Beam |
| FSM | Fault Signature Matrix |
| FU | Fuel Utilization |
| GUI | Graphic User Interface |
| HF | High Frequency |
| HSMM | Hidden semi-Mark model |
| ISM | Integrated Stack Module |
| IT | Intermediate Temperature |
| LCA | Life Cycle Assessment |

| | |
|---|---|
| LF | Low Frequency |
| MDLT | Monitoring, Diagnostic and Lifetime Tool |
| MGFG | Matching Geometric Fitting Guess |
| MI | Monitoring Index |
| MSE | Mean Square Error |
| OCV | Open Circuit Voltage |
| PEMFC | Proton Exchange Membrane Fuel Cells |
| PHM | Prognostic and Health Management |
| PRBS | Pseudo Random Binary Signal |
| RUL | Remaining Useful Life |
| SEM | Scanning electron Microscopy |
| SOEC | Solid Oxide Electrolyser Cell |
| SOFC | Solid Oxide Fuel Cell |
| SoH | State of Health |
| SP | SolidPower s.p.a. |
| TEC | Thermal Expansion Coefficient |
| TPB | Triple Phase Boundary |
| TRL | Technology Readiness Level |
| TSR | Thermal Shock Resistance |
| UNISA | University of Salerno |
| VTT | Technical Research Centre of Finland Ltd |

# References

[1] E Weidner, R Ortiz Cebolla, and J Davies. Global deployment of large capacity stationary fuel cells. 2019.

[2] David Chiaramonti and Theodor Goumas. Impacts on industrial-scale market deployment of advanced biofuels and recycled carbon fuels from the eu renewable energy directive ii. *Applied Energy*, 251:113351, 2019.

[3] Hagay Hayun, Roy Wolf, Chen Barad, and Yaniv Gelbstein. Thermal shock resistant solid oxide fuel cell ceramic composite electrolytes. *Journal of Alloys and Compounds*, page 153490, 2019.

[4] Murat Peksen. Numerical thermomechanical modelling of solid oxide fuel cells. *Progress in energy and combustion science*, 48: 1–20, 2015.

[5] M Hanasaki, C Uryu, T Daio, T Kawabata, Yuya Tachikawa, Stephen Matthew Lyth, Yusuke Shiratori, Shunsuke Taniguchi, and Kazunari Sasaki. Sofc durability against standby and shutdown cycling. *Journal of The Electrochemical Society*, 161(9): F850–F860, 2014.

[6] Muhammad Zubair Khan, Muhammad Taqi Mehran, Rak-Hyun Song, Seung-Bok Lee, and Tak-Hyoung Lim. Effects of applied current density and thermal cycling on the degradation of a solid oxide fuel cell cathode. *International Journal of Hydrogen Energy*, 43(27):12346–12357, 2018.

[7] C Schluckner, V Subotić, S Preißl, and C Hochenauer. Numerical analysis of flow configurations and electrical contact positions in

sofc single cells and their impact on local effects. *International Journal of Hydrogen Energy*, 44(3):1877–1895, 2019.

[8] Min Xu, Ting Shuai Li, Ming Yang, Martin Andersson, Ida Fransson, Tara Larsson, and Bengt Sundén. Modeling of an anode supported solid oxide fuel cell focusing on thermal stresses. *International Journal of Hydrogen Energy*, 41(33):14927–14940, 2016.

[9] B Sun, RA Rudkin, and A Atkinson. Effect of thermal cycling on residual stress and curvature of anode-supported sofcs. *Fuel Cells*, 9(6):805–813, 2009.

[10] Pengfei Fan, Guojun Li, Yikai Zeng, and Xiongwen Zhang. Numerical study on thermal stresses of a planar solid oxide fuel cell. *International Journal of Thermal Sciences*, 77:1–10, 2014.

[11] Arata Nakajo, Fabian Mueller, Jacob Brouwer, Daniel Favrat, et al. Mechanical reliability and durability of sofc stacks. part ii: modelling of mechanical failures during ageing and cycling. *International Journal of Hydrogen Energy*, 37(11):9269–9286, 2012.

[12] Trine Klemensø, Charissa Chung, Peter Halvor Larsen, and M Mogensen. The mechanism behind redox instability of anodes in high-temperature sofcs. *Journal of the Electrochemical Society*, 152(11): A2186–A2192, 2005.

[13] Antonin Faes, Aïcha Hessler-Wyser, Amédée Zryd, et al. A review of redox cycling of solid oxide fuel cells anode. *Membranes*, 2(3): 585–664, 2012.

[14] Tatsuya Kawasaki, Junko Matsuda, Yuya Tachikawa, Stephen Matthew Lyth, Yusuke Shiratori, Shunsuke Taniguchi, and Kazunari Sasaki. Oxidation-induced degradation and performance fluctuation of solid oxide fuel cell ni anodes under simulated high fuel utilization conditions. *International Journal of Hydrogen Energy*, 44(18):9386–9399, 2019.

[15] Shuaipeng Shang, Yongjun Lu, Xinlei Cao, Xu Song, Mingliang Shi, and Fenghui Wang. A model for oxidation-induced stress anal-

ysis of ni-based anode-supported planar solid oxide fuel cell. *International Journal of Hydrogen Energy*, 44(31):16956–16964, 2019.

[16] Muhammad Shirjeel Khan, Seung-Bok Lee, Rak-Hyun Song, Jong-Won Lee, Tak-Hyoung Lim, and Seok-Joo Park. Fundamental mechanisms involved in the degradation of nickel–yttria stabilized zirconia (ni–ysz) anode during solid oxide fuel cells operation: A review. *Ceramics International*, 42(1):35–48, 2016.

[17] S Ali Saadabadi, Aditya Thallam Thattai, Liyuan Fan, Ralph EF Lindeboom, Henri Spanjers, and PV Aravind. Solid oxide fuel cells fuelled with biogas: Potential and constraints. *Renewable energy*, 134:194–214, 2019.

[18] Tony Wood and Douglas G Ivey. The impact of redox cycling on solid oxide fuel cell lifetime. In *Solid Oxide Fuel Cell Lifetime and Reliability*, pages 51–77. Elsevier, 2017.

[19] Asseya El-Amiri, Abderrahim Saifi, Ahmed Elhassnaoui, Abdellatif Obbadi, Youssef Errami, and Smail Sahnoun. Control of solid oxide fuel cells damage using infrared thermography. *International Journal of Hydrogen Energy*, 2018.

[20] Benoit Charlas, Henrik Lund Frandsen, Karen Brodersen, Peter Vang Henriksen, and Ming Chen. Residual stresses and strength of multilayer tape cast solid oxide fuel and electrolysis half-cells. *Journal of Power Sources*, 288:243–252, 2015.

[21] Kwangjin Park, Sungoh Yu, Joongmyeon Bae, Hyungsop Kim, and Yoonki Ko. Fast performance degradation of sofc caused by cathode delamination in long-term testing. *International Journal of Hydrogen Energy*, 35(16):8670–8677, 2010.

[22] Marko Nerat and Đani Juričić. Modelling of anode delamination in solid oxide electrolysis cell and analysis of its effects on electrochemical performance. *International Journal of Hydrogen Energy*, 43(17):8179–8189, 2018.

[23] TMM Heenan, X Lu, JB Robinson, F Iacoviello, DJL Brett, and PR Shearing. Thermally driven sofc degradation in 4d: Part ii.

macroscale. *Journal of The Electrochemical Society*, 165(11):F932–F941, 2018.

[24] Salaheddine Kraibaa, Abderrahim Saifi, Asseya El-amiri, Hicham Halloua, Abdellatif Obbadi, Youssef Errami, and Smail Sahnoun. Non-destructive testing of tubular solid oxide fuel cell (sofc) by pulsed thermography. In *2019 International Conference of Computer Science and Renewable Energies (ICCSRE)*, pages 1–7. IEEE, 2019.

[25] Alireza Mohammadzadeh, Seyedeh Kiana Naghib Zadeh, Mohammad Hassan Saidi, and Mahdi Sharifzadeh. Mechanical engineering of solid oxide fuel cell systems: geometric design, mechanical configuration, and thermal analysis. In *Design and Operation of Solid Oxide Fuel Cells*, pages 85–130. Elsevier, 2020.

[26] Salvatore De Angelis, Peter Stanley Jørgensen, Esther Hsiao Rho Tsai, Mirko Holler, Kosova Kreka, and Jacob R Bowen. Three dimensional characterization of nickel coarsening in solid oxide cells via ex-situ ptychographic nano-tomography. *Journal of Power Sources*, 383:72–79, 2018.

[27] Anne Hauch, Peter Stanley Jørgensen, Karen Brodersen, and Mogens Mogensen. Ni/ysz anode–effect of pre-treatments on cell degradation and microstructures. *Journal of Power Sources*, 196 (21):8931–8941, 2011.

[28] YL Liu and Chengge Jiao. Microstructure degradation of an anode/electrolyte interface in sofc studied by transmission electron microscopy. *Solid State Ionics*, 176(5-6):435–442, 2005.

[29] M Trini, A Hauch, S De Angelis, X Tong, P Vang Hendriksen, and M Chen. Comparison of microstructural evolution of fuel electrodes in solid oxide fuel cells and electrolysis cells. *Journal of Power Sources*, 450:227599, 2020.

[30] M Hubert, J Laurencin, P Cloetens, B Morel, D Montinaro, and F Lefebvre-Joud. Impact of nickel agglomeration on solid oxide cell operated in fuel cell and electrolysis modes. *Journal of Power Sources*, 397:240–251, 2018.

[31] Jiang Zhu and Zijing Lin. Degradations of the electrochemical performance of solid oxide fuel cell induced by material microstructure evolutions. *Applied energy*, 231:22–28, 2018.

[32] Muhammad Zubair Khan, Muhammad Taqi Mehran, Rak-Hyun Song, Jong-Won Lee, Seung-Bok Lee, and Tak-Hyoung Lim. A simplified approach to predict performance degradation of a solid oxide fuel cell anode. *Journal of Power Sources*, 391:94–105, 2018.

[33] A Bertei, E Ruiz-Trejo, K Kareh, V Yufit, X Wang, F Tariq, and NP Brandon. The fractal nature of the three-phase boundary: a heuristic approach to the degradation of nanostructured solid oxide fuel cell anodes. *Nano Energy*, 38:526–536, 2017.

[34] Zhenjun Jiao, Naoki Shikazono, and Nobuhide Kasagi. Study on degradation of solid oxide fuel cell anode by using pure nickel electrode. *Journal of Power Sources*, 196(20):8366–8376, 2011.

[35] D Simwonis, F Tietz, and D Stöver. Nickel coarsening in annealed ni/8ysz anode substrates for solid oxide fuel cells. *Solid State Ionics*, 132(3-4):241–251, 2000.

[36] George J Nelson, Kyle N Grew, John R Izzo Jr, Jeffrey J Lombardo, William M Harris, Antonin Faes, Aïcha Hessler-Wyser, Steve Wang, Yong S Chu, Anil V Virkar, et al. Three-dimensional microstructural changes in the ni–ysz solid oxide fuel cell anode during operation. *Acta Materialia*, 60(8):3491–3500, 2012.

[37] Marián Palcut, Lars Mikkelsen, Kai Neufeld, Ming Chen, Ruth Knibbe, and Peter V Hendriksen. Corrosion stability of ferritic stainless steels for solid oxide electrolyser cell interconnects. *Corrosion Science*, 52(10):3309–3320, 2010.

[38] Nima Shaigan, Wei Qu, Douglas G Ivey, and Weixing Chen. A review of recent progress in coatings, surface modifications and alloy developments for solid oxide fuel cell ferritic stainless steel interconnects. *Journal of Power Sources*, 195(6):1529–1542, 2010.

[39] JH Zhu and H Ghezel-Ayagh. Cathode-side electrical contact and contact materials for solid oxide fuel cell stacking: A review. *International Journal of Hydrogen Energy*, 42(38):24278–24300, 2017.

[40] Paul Boldrin, Enrique Ruiz-Trejo, Joshua Mermelstein, Jose Miguel Bermudez Menundez, Tomas Ramirez Reina, and Nigel P Brandon. Strategies for carbon and sulfur tolerant solid oxide fuel cell materials, incorporating lessons from heterogeneous catalysis. *Chemical reviews*, 116(22):13633–13684, 2016.

[41] Kazunari Sasaki and Y Teraoka. Equilibria in fuel cell gases ii. the cho ternary diagrams. *Journal of The Electrochemical Society*, 150 (7):A885–A888, 2003.

[42] Tao Chen, Wei Guo Wang, He Miao, Tingshuai Li, and Cheng Xu. Evaluation of carbon deposition behavior on the nickel/yttrium-stabilized zirconia anode-supported fuel cell fueled with simulated syngas. *Journal of Power Sources*, 196(5):2461–2468, 2011.

[43] A Lanzini, C Guerra, P Leone, M Santarelli, F Smeacetto, S Fiorilli, A Gondolini, E Mercadelli, A Sanson, and NP Brandon. Influence of the microstructure on the catalytic properties of sofc anodes under dry reforming of methane. *Materials Letters*, 164: 312–315, 2016.

[44] Linan Shu, Jaka Sunarso, Siti Salwa Hashim, Junkui Mao, Wei Zhou, and Fengli Liang. Advanced perovskite anodes for solid oxide fuel cells: A review. *International Journal of Hydrogen Energy*, 2019.

[45] Fellipe Sartori Da Silva and Teófilo Miguel de Souza. Novel materials for solid oxide fuel cell technologies: A literature review. *International Journal of Hydrogen Energy*, 42(41):26020–26036, 2017.

[46] Wangxu Yue, Yifeng Li, Yun Zheng, Tong Wu, Chenhuan Zhao, Jia Zhao, Ga Geng, Wenqiang Zhang, Jing Chen, Jianxin Zhu, et al. Enhancing coking resistance of ni/ysz electrodes: In situ characterization, mechanism research, and surface engineering. *Nano Energy*, 2019.

[47] Lei Yang, Zhe Cheng, Meilin Liu, and Lane Wilson. New insights into sulfur poisoning behavior of ni-ysz anode from long-term operation of anode-supported sofcs. *Energy & Environmental Science*, 3(11):1804–1809, 2010.

[48] Shaowu Zha, Zhe Cheng, and Meilin Liu. Sulfur poisoning and regeneration of ni-based anodes in solid oxide fuel cells. *Journal of the Electrochemical Society*, 154(2):B201–B206, 2007.

[49] Jens Foldager Bregnballe Rasmussen and Anke Hagen. The effect of h2s on the performance of sofcs using methane containing fuel. *Fuel Cells*, 10(6):1135–1142, 2010.

[50] Anke Hagen, Gregory B Johnson, and Per Hjalmarsson. Electrochemical evaluation of sulfur poisoning in a methane-fuelled solid oxide fuel cell: Effect of current density and sulfur concentration. *Journal of Power Sources*, 272:776–785, 2014.

[51] Anke Hagen, Jens FB Rasmussen, and Karl Thydén. Durability of solid oxide fuel cells using sulfur containing fuels. *Journal of Power Sources*, 196(17):7271–7276, 2011.

[52] Haruo Kishimoto, Teruhisa Horita, Katsuhiko Yamaji, Manuel E Brito, Yue-Ping Xiong, and Harumi Yokokawa. Sulfur poisoning on sofc ni anodes: thermodynamic analyses within local equilibrium anode reaction model. *Journal of The Electrochemical Society*, 157 (6):B802–B813, 2010.

[53] Anne Hauch, Anke Hagen, Johan Hjelm, and Tania Ramos. Sulfur poisoning of sofc anodes: effect of overpotential on long-term degradation. *Journal of The Electrochemical Society*, 161(6):F734–F743, 2014.

[54] Matthias Riegraf, Atef Zekri, Martin Knipper, Rémi Costa, Günter Schiller, and K Andreas Friedrich. Sulfur poisoning of ni/gadolinium-doped ceria anodes: A long-term study outlining stable solid oxide fuel cell operation. *Journal of Power Sources*, 380:26–36, 2018.

[55] Bingbing Niu, Fangjun Jin, Xin Yang, Tao Feng, and Tianmin He. Resisting coking and sulfur poisoning of double perovskite sr2tife0. 5mo0. 5o6–$\delta$ anode material for solid oxide fuel cells. *International Journal of Hydrogen Energy*, 43(6):3280–3290, 2018.

[56] Francisco J García-García, Francisco Yubero, Agustín R González-Elipe, and RM Lambert. Microstructural engineering and use of efficient poison resistant au-doped ni-gdc ultrathin anodes in methane-fed solid oxide fuel cells. *International Journal of Hydrogen Energy*, 43(2):885–893, 2018.

[57] Wenyuan Wang, Changli Zhu, Kui Xie, and Lizhen Gan. High performance, coking-resistant and sulfur-tolerant anode for solid oxide fuel cell. *Journal of Power Sources*, 406:1–6, 2018.

[58] Shichen Sun, Osama Awadallah, and Zhe Cheng. Poisoning of ni-based anode for proton conducting sofc by h2s, co2, and h2o as fuel contaminants. *Journal of Power Sources*, 378:255–263, 2018.

[59] Yiqian Li, Zhihong Wang, Jingwei Li, Xingbao Zhu, Yaohui Zhang, Xiqiang Huang, Yongjun Zhou, Lin Zhu, and Zhe Lü. Sulfur poisoning and attempt of oxidative regeneration of la0. 75sr0. 25cr0. 5mn0. 5o3- $\delta$ anode for solid oxide fuel cell. *Journal of Alloys and Compounds*, 698:794–799, 2017.

[60] Muhammad Taqi Mehran, Muhammad Zubair Khan, Seung-Bok Lee, Tak-Hyoung Lim, Sam Park, and Rak-Hyun Song. Improving sulfur tolerance of ni-ysz anodes of solid oxide fuel cells by optimization of microstructure and operating conditions. *international journal of hydrogen energy*, 43(24):11202–11213, 2018.

[61] Ho Seong Lee, Hyun Mi Lee, Jun-Young Park, and Hyung-Tae Lim. Degradation behavior of ni-ysz anode-supported solid oxide fuel cell (sofc) as a function of h2s concentration. *International Journal of Hydrogen Energy*, 43(49):22511–22518, 2018.

[62] Davide Papurello, Andrea Lanzini, Sonia Fiorilli, Federico Smeacetto, Rahul Singh, and Massimo Santarelli. Sulfur poisoning in ni-anode solid oxide fuel cells (sofcs): deactivation in single cells and a stack. *Chemical Engineering Journal*, 283:1224–1233, 2016.

[63] Emily M Ryan, Wei Xu, Xin Sun, and Mohammad A Khaleel. A damage model for degradation in the electrodes of solid oxide fuel cells: Modeling the effects of sulfur and antimony in the anode. *Journal of power sources*, 210:233–242, 2012.

[64] Dimitrios K Niakolas. Sulfur poisoning of ni-based anodes for solid oxide fuel cells in h/c-based fuels. *Applied Catalysis A: General*, 486:123–142, 2014.

[65] Chunwen Sun, Rob Hui, and Justin Roller. Cathode materials for solid oxide fuel cells: a review. *Journal of Solid State Electrochemistry*, 14(7):1125–1144, 2010.

[66] K Hilpert, D Das, M Miller, DH Peck, and R Weiss. Chromium vapor species over solid oxide fuel cell interconnect materials and their potential for degradation processes. *Journal of the Electrochemical Society*, 143(11):3642–3647, 1996.

[67] H Yokokawa, T Horita, N Sakai, K Yamaji, ME Brito, Y-P Xiong, and H Kishimoto. Thermodynamic considerations on cr poisoning in sofc cathodes. *Solid State Ionics*, 177(35-36):3193–3198, 2006.

[68] SPS Badwal, R Deller, K Foger, Y Ramprakash, and JP Zhang. Interaction between chromia forming alloy interconnects and air electrode of solid oxide fuel cells. *Solid State Ionics*, 99(3-4):297–310, 1997.

[69] S Taniguchi, M Kadowaki, H Kawamura, T Yasuo, Y Akiyama, Y Miyake, and T Saitoh. Degradation phenomena in the cathode of a solid oxide fuel cell with an alloy separator. *Journal of Power Sources*, 55(1):73–79, 1995.

[70] Elena Konysheva, H Penkalla, E Wessel, Jo Mertens, U Seeling, L Singheiser, and K Hilpert. Chromium poisoning of perovskite cathodes by the ods alloy cr5fe1y2o3 and the high chromium ferritic steel crofer22apu. *Journal of the Electrochemical Society*, 153(4): A765–A773, 2006.

[71] Zhibin Yang, Mengyuan Guo, Ning Wang, Chaoyang Ma, Jingle Wang, and Minfang Han. A short review of cathode poisoning and

corrosion in solid oxide fuel cell. *International Journal of Hydrogen Energy*, 42(39):24948–24959, 2017.

[72] KH Tan, HA Rahman, and H Taib. Coating layer and influence of transition metal for ferritic stainless steel interconnector solid oxide fuel cell: A review. *International Journal of Hydrogen Energy*, 44 (58):30591–30605, 2019.

[73] Sridevi Krishnan, Manoj K Mahapatra, Prabhakar Singh, and Rampi Ramprasad. First principles study of cr poisoning in solid oxide fuel cell cathodes: Application to (la, sr) coo3. *Computational Materials Science*, 137:6–9, 2017.

[74] Dingkai Chen, Basma Mewafy, Fotios Paloukis, Liping Zhong, Vasiliki Papaefthimiou, Thierry Dintzer, Kalliopi M Papazisi, Stella P Balomenou, Dimitrios Tsiplakides, Detre Teschner, et al. Revising the role of chromium on the surface of perovskite electrodes: Poison or promoter for the solid oxide electrolysis cell performance? *Journal of Catalysis*, 381:520–529, 2020.

[75] Xiaoqiang Zhang, Guangsen Yu, Shumao Zeng, Joseph Parbey, Shuhao Xiao, Baihai Li, Tingshuai Li, and Martin Andersson. Mechanism of chromium poisoning the conventional cathode material for solid oxide fuel cells. *Journal of Power Sources*, 381:26–29, 2018.

[76] Jens Foldager Bregnballe Rasmussen, Peter Vang Hendriksen, and Anke Hagen. Study of internal and external leaks in tests of anode-supported sofcs. *Fuel Cells*, 8(6):385–393, 2008.

[77] Zacharie Wuillemin, Nordahl Autissier, Arata Nakajo, M Luong, Daniel Favrat, et al. Modeling and study of the influence of sealing on a solid oxide fuel cell. *Journal of fuel cell science and technology*, 5(1):011016, 2008.

[78] M Rautanen, O Himanen, V Saarinen, and J Kiviaho. Compression properties and leakage tests of mica-based seals for sofc stacks. *Fuel Cells*, 9(5):753–759, 2009.

[79] Jeffrey W Fergus. Sealants for solid oxide fuel cells. *Journal of Power Sources*, 147(1-2):46–57, 2005.

[80] M Stanislowski, E Wessel, K Hilpert, T Markus, and L Singheiser. Chromium vaporization from high-temperature alloys i. chromia-forming steels and the influence of outer oxide layers. *Journal of the Electrochemical Society*, 154(4):A295–A306, 2007.

[81] Martin Bram, Stephan Reckers, Pere Drinovac, Josef Mönch, Rolf W Steinbrech, Hans Peter Buchkremer, and Detlev Stöver. Deformation behavior and leakage tests of alternate sealing materials for sofc stacks. *Journal of Power Sources*, 138(1):111–119, 2004.

[82] A Sorce, A Greco, L Magistri, and P Costamagna. Fdi oriented modeling of an experimental sofc system, model validation and simulation of faulty states. *Applied Energy*, 136:894–908, 2014.

[83] Sanghun Lee, Young-hoon Jang, Ho Yong Shin, Kunho Lee, Minseok Bae, Juhyun Kang, and Joongmyeon Bae. Reliable sealing design of metal-based solid oxide fuel cell stacks for transportation applications. *International Journal of Hydrogen Energy*, 44(57): 30280–30292, 2019.

[84] Young Jin Kim and Min Chul Lee. Evaluation of the thermal and structural stability of planar anode-supported solid oxide fuel cells using a 10× 10 cm2 single-cell test. *International Journal of Hydrogen Energy*, 44(11):5517–5529, 2019.

[85] Bora Timurkutluk, Tolga Altan, Selahattin Celik, Cigdem Timurkutluk, and Yuksel Palacı. Glass fiber reinforced sealants for solid oxide fuel cells. *International Journal of Hydrogen Energy*, 2019.

[86] Robert Gaynor, Fabian Mueller, Faryar Jabbari, and Jacob Brouwer. On control concepts to prevent fuel starvation in solid oxide fuel cells. *Journal of Power Sources*, 180(1):330–342, 2008.

[87] Paulina Pianko-Oprych, Tomasz Zinko, and Zdzisław Jaworski. Cfd modelling of hydrogen starvation conditions in a planar solid

oxide fuel cell. *Polish Journal of Chemical Technology*, 19(2):16–25, 2017.

[88] Grzegorz Brus, Kota Miyoshi, Hiroshi Iwai, Motohiro Saito, and Hideo Yoshida. Change of an anode's microstructure morphology during the fuel starvation of an anode-supported solid oxide fuel cell. *international journal of hydrogen energy*, 40(21):6927–6934, 2015.

[89] Aline Lima da Silva and Nestor Cezar Heck. Thermodynamics of sulfur poisoning in solid oxide fuel cells revisited: The effect of h2s concentration, temperature, current density and fuel utilization. *Journal of Power Sources*, 296:92–101, 2015.

[90] J Laurencin, G Delette, B Morel, F Lefebvre-Joud, and M Dupeux. Solid oxide fuel cells damage mechanisms due to ni-ysz re-oxidation: Case of the anode supported cell. *Journal of power sources*, 192(2):344–352, 2009.

[91] Mario Angeloni, Pilar Lisbona, and Roberto Bove. A pde model for microscopic simulation of solid oxide fuel cells. *Journal of Power Sources*, 201:184–195, 2012.

[92] Qingping Fang, Ludger Blum, Roland Peters, Murat Peksen, Peter Batfalsky, and Detlef Stolten. Sofc stack performance under high fuel utilization. *International journal of hydrogen energy*, 40(2): 1128–1136, 2015.

[93] S Futamura, Yuya Tachikawa, Junko Matsuda, Stephen Matthew Lyth, Yusuke Shiratori, Shunsuke Taniguchi, and Kazunari Sasaki. Alternative ni-impregnated mixed ionic-electronic conducting anode for sofc operation at high fuel utilization. *Journal of The Electrochemical Society*, 164(10):F3055, 2017.

[94] Raffaele Petrone. Electrochemical impedance spectroscopy for the on-board diagnosis of pemfc via on-line identification of equivalent circuit model parameters. 2014.

[95] Zhiwei Gao, Carlo Cecati, and Steven X Ding. A survey of fault diagnosis and fault-tolerant techniques—part i: Fault diagnosis

with model-based and signal-based approaches. *IEEE Transactions on Industrial Electronics*, 62(6):3757–3767, 2015.

[96] Won-Yong Lee, Hwanyeong Oh, Minjin Kim, Yoon-Young Choi, Young-Jun Sohn, and Seung-Gon Kim. Hierarchical fault diagnostic method for a polymer electrolyte fuel cell system. *International Journal of Hydrogen Energy*, 2019.

[97] Catherine Cadet, Samir Jemeï, Florence Druart, and D Hissel. Diagnostic tools for pemfcs: from conception to implementation. *International Journal of Hydrogen Energy*, 39(20):10613–10626, 2014.

[98] Marine Jouin, Rafael Gouriveau, Daniel Hissel, Marie-Cécile Péra, and Noureddine Zerhouni. Prognostics of pem fuel cell in a particle filtering framework. *International Journal of Hydrogen Energy*, 39 (1):481–494, 2014.

[99] Rolf Isermann. *Fault-diagnosis systems: an introduction from fault detection to fault tolerance*. Springer Science & Business Media, 2006.

[100] Raffaele Petrone, Daniel Hissel, MC Péra, Didier Chamagne, and Rafael Gouriveau. Accelerated stress test procedures for pem fuel cells under actual load constraints: State-of-art and proposals. *International Journal of Hydrogen Energy*, 40(36):12489–12505, 2015.

[101] Maurizio Guida, Fabio Postiglione, and Gianpaolo Pulcini. A random-effects model for long-term degradation analysis of solid oxide fuel cells. *Reliability Engineering & System Safety*, 140:88–98, 2015.

[102] Pierpaolo Polverino, Cesare Pianese, Marco Sorrentino, and Dario Marra. Model-based development of a fault signature matrix to improve solid oxide fuel cell systems on-site diagnosis. *Journal of Power Sources*, 280:320–338, 2015.

[103] Pierpaolo Polverino, Marco Sorrentino, and Cesare Pianese. A model-based diagnostic technique to enhance faults isolability in solid oxide fuel cell systems. *Applied Energy*, 204:1198–1214, 2017.

[104] Ivan Arsie, Arturo Di Filippi, Dario Marra, Cesare Pianese, and Marco Sorrentino. Fault tree analysis aimed to design and implement on-field fault detection and isolation schemes for sofc systems. In *Proceedings of the ASME 2010 Eighth International Fuel Cell Science, Engineering and Technology Conference*, pages 14–16, 2010.

[105] Paola Costamagna, Andrea De Giorgi, Alberto Gotelli, Loredana Magistri, Gabriele Moser, Emanuele Sciaccaluga, and Andrea Trucco. Fault diagnosis strategies for sofc-based power generation plants. *Sensors*, 16(8):1336, 2016.

[106] Harumi Yokokawa, Hengyong Tu, Boris Iwanschitz, and Andreas Mai. Fundamental mechanisms limiting solid oxide fuel cell durability. *Journal of Power Sources*, 182(2):400–412, 2008.

[107] GJ Offer and NP Brandon. The effect of current density and temperature on the degradation of nickel cermet electrodes by carbon monoxide in solid oxide fuel cells. *Chemical Engineering Science*, 64(10):2291–2300, 2009.

[108] Arata Nakajo, Fabian Mueller, Jacob Brouwer, Daniel Favrat, et al. Progressive activation of degradation processes in solid oxide fuel cells stacks: Part i: Lifetime extension by optimisation of the operating conditions. *Journal of Power Sources*, 216:449–463, 2012.

[109] LGJ De Haart, J Mougin, O Posdziech, Jari Kiviaho, and NH Menzler. Stack degradation in dependence of operation parameters; the real-sofc sensitivity analysis. *Fuel Cells*, 9(6):794–804, 2009.

[110] V Zaccaria, D Tucker, and A Traverso. A distributed real-time model of degradation in a solid oxide fuel cell, part i: Model characterization. *Journal of Power Sources*, 311:175–181, 2016.

[111] Dong Yan, Lingjiang Liang, Jiajun Yang, Tao Zhang, Jian Pu, Bo Chi, and Jian Li. Performance degradation and analysis of 10-

cell anode-supported sofc stack with external manifold structure. *Energy*, 125:663–670, 2017.

[112] S Göll, RC Samsun, and R Peters. Analysis and optimization of solid oxide fuel cell-based auxiliary power units using a generic zero-dimensional fuel cell model. *Journal of Power Sources*, 196 (22):9500–9509, 2011.

[113] Houssein Al Moussawi, Farouk Fardoun, and Hasna Louahlia. 4-e based optimal management of a sofc-cchp system model for residential applications. *Energy Conversion and Management*, 151: 607–629, 2017.

[114] Dionysios P Xenos, Philipp Hofmann, Kyriakos D Panopoulos, and Emmanuel Kakaras. Detailed transient thermal simulation of a planar sofc (solid oxide fuel cell) using gproms™. *Energy*, 81:84–102, 2015.

[115] Yonggyun Bae, Sanghyeok Lee, Kyung Joong Yoon, Jong-Ho Lee, and Jongsup Hong. Three-dimensional dynamic modeling and transport analysis of solid oxide fuel cells under electrical load change. *Energy conversion and management*, 165:405–418, 2018.

[116] Jawad Hussain, Rashid Ali, Majid Niaz Akhtar, Mujtaba Hassan Jaffery, Imran Shakir, and Rizwan Raza. Modeling and simulation of planar sofc to study the electrochemical properties. *Current Applied Physics*, 2020.

[117] Mustafa Ilbas and Berre Kumuk. Numerical modelling of a cathode-supported solid oxide fuel cell (sofc) in comparison with an electrolyte-supported model. *Journal of the Energy Institute*, 92(3):682–692, 2019.

[118] Tomasz A Prokop, Katarzyna Berent, Hiroshi Iwai, Janusz S Szmyd, and Grzegorz Brus. A three-dimensional heterogeneity analysis of electrochemical energy conversion in sofc anodes using electron nanotomography and mathematical modeling. *International Journal of Hydrogen Energy*, 43(21):10016–10030, 2018.

[119] Jakub Kupecki, Konrad Motylinski, and Jaroslaw Milewski. Dynamic analysis of direct internal reforming in a sofc stack with electrolyte-supported cells using a quasi-1d model. *Applied Energy*, 227:198–205, 2018.

[120] L Barelli, G Bidini, and A Ottaviano. Part load operation of a sofc/gt hybrid system: dynamic analysis. *Applied energy*, 110: 173–189, 2013.

[121] Mario L Ferrari and Aristide F Massardo. Cathode–anode side interaction in sofc hybrid systems. *Applied energy*, 105:369–379, 2013.

[122] Marco Sorrentino and Cesare Pianese. Control oriented modeling of solid oxide fuel cell auxiliary power unit for transportation applications. *Journal of Fuel Cell Science and Technology*, 6(4):041011, 2009.

[123] Hongliang Cao and Xi Li. Thermal management-oriented multivariable robust control of a kw-scale solid oxide fuel cell stand-alone system. *IEEE Transactions on Energy Conversion*, 31(2):596–605, 2016.

[124] M Santarelli, M Cabrera, and M Calì. Solid oxide fuel based auxiliary power unit for regional jets: Design and mission simulation with different cell geometries. *Journal of Fuel Cell Science and Technology*, 7(2):021006, 2010.

[125] F Arpino, M Dell'Isola, D Maugeri, N Massarotti, and A Mauro. A new model for the analysis of operating conditions of micro-cogenerative sofc units. *international journal of hydrogen energy*, 38(1):336–344, 2013.

[126] A Baldinelli, L Barelli, and G Bidini. Upgrading versus reforming: an energy and exergy analysis of two solid oxide fuel cell-based systems for a convenient biogas-to-electricity conversion. *Energy Conversion and Management*, 138:360–374, 2017.

[127] Cheng Bao, Ying Wang, Daili Feng, Zeyi Jiang, and Xinxin Zhang. Macroscopic modeling of solid oxide fuel cell (sofc) and model-

based control of sofc and gas turbine hybrid system. *Progress in Energy and Combustion Science*, 66:83–140, 2018.

[128] Dario Marra, Cesare Pianese, Pierpaolo Polverino, and Marco Sorrentino. *Models for Solid Oxide Fuel Cell Systems*. Springer, 2016.

[129] Raffaele Petrone, Zhixue Zheng, Daniel Hissel, Marie-Cécile Péra, Cesare Pianese, Marco Sorrentino, Mohamed Becherif, and N Yousfi-Steiner. A review on model-based diagnosis methodologies for pemfcs. *International Journal of Hydrogen Energy*, 38(17): 7077–7091, 2013.

[130] Xiao-Zi Riny Yuan, Chaojie Song, Haijiang Wang, and Jiujun Zhang. *Electrochemical impedance spectroscopy in PEM fuel cells: fundamentals and applications*. Springer Science & Business Media, 2009.

[131] Elodie Pahon, Latifa Oukhellou, Fabien Harel, Samir Jemei, and Daniel Hissel. Fault diagnosis and identification of proton exchange membrane fuell cell system using electrochmical impedance spectroscopy classification. 2014.

[132] Yanghua Tang, Jiujun Zhang, Chaojie Song, Hansan Liu, Jianlu Zhang, Haijiang Wang, Sean Mackinnon, Tim Peckham, Jing Li, Scott McDermid, et al. Temperature dependent performance and in situ ac impedance of high-temperature pem fuel cells using the nafion-112 membrane. *Journal of the Electrochemical Society*, 153 (11):A2036–A2043, 2006.

[133] Qiu-An Huang, Rob Hui, Bingwen Wang, and Jiujun Zhang. A review of ac impedance modeling and validation in sofc diagnosis. *Electrochimica Acta*, 52(28):8144–8164, 2007.

[134] A Nechache, M Cassir, and A Ringuedé. Solid oxide electrolysis cell analysis by means of electrochemical impedance spectroscopy: A review. *Journal of Power Sources*, 258:164–181, 2014.

[135] Aziz Nechache, Aurore Mansuy, Marie Petitjean, Julie Mougin, Fabrice Mauvy, Bernard A Boukamp, Michel Cassir, and Armelle

Ringuedé. Diagnosis of a cathode-supported solid oxide electrolysis cell by electrochemical impedance spectroscopy. *Electrochimica acta*, 210:596–605, 2016.

[136] X Changjun and Q Shuhai. Drawing impedance spectroscopy for fuel cell by eis. *Procedia Environmental Sciences*, 11:589–596, 2011.

[137] Xiaozi Yuan, Jian Colin Sun, Haijiang Wang, and Jiujun Zhang. Ac impedance diagnosis of a 500w pem fuel cell stack. *Journal of Power Sources*, 2(161):929–937, 2006.

[138] Shuab Khan, SM Aijaz Rizvi, and Shabana Urooj. Equivalent circuit modelling using electrochemical impedance spectroscopy for different materials of sofc. In *2016 3rd International Conference on Computing for Sustainable Global Development (INDIACom)*, pages 1563–1567. IEEE, 2016.

[139] Daniel Hissel and Marie-Cécile Pera. Diagnostic & health management of fuel cell systems: Issues and solutions. *Annual Reviews in Control*, 42:201–211, 2016.

[140] L Barelli, E Barluzzi, and G Bidini. Diagnosis methodology and technique for solid oxide fuel cells: a review. *International Journal of hydrogen energy*, 38(12):5060–5074, 2013.

[141] Tae-Hee Lee, Ka-Young Park, Ji-Tae Kim, Yongho Seo, Ki Buem Kim, Sun-Ju Song, Byoungnam Park, and Jun-Young Park. Degradation analysis of anode-supported intermediate temperature-solid oxide fuel cells under various failure modes. *Journal of Power Sources*, 276:120–132, 2015.

[142] Ph Hofmann and KD Panopoulos. Detailed dynamic solid oxide fuel cell modeling for electrochemical impedance spectra simulation. *Journal of power sources*, 195(16):5320–5339, 2010.

[143] Huayang Zhu, Alexander Kromp, Andre Leonide, Ellen Ivers-Tiffée, Olaf Deutschmann, and Robert J Kee. A model-based interpretation of the influence of anode surface chemistry on solid oxide fuel cell electrochemical impedance spectra. *Journal of The Electrochemical Society*, 159(7):F255–F266, 2012.

[144] M Fadaei and R Mohammadi. A comprehensive simulation of gas concentration impedance for solid oxide fuel cell anodes. *Energy Conversion and Management*, 106:93–100, 2015.

[145] Michael Lang, Corinna Auer, Andreas Eismann, Patric Szabo, and Norbert Wagner. Investigation of solid oxide fuel cell short stacks for mobile applications by electrochemical impedance spectroscopy. *Electrochimica Acta*, 53(25):7509–7513, 2008.

[146] D Montinaro, AR Contino, A Dellai, and M Rolland. Determination of the impedance contributions in anode supported solid oxide fuel cells with (la, sr)(co, fe) o3- $\delta$ cathode. *International Journal of Hydrogen Energy*, 39(36):21638–21646, 2014.

[147] C Comminges, QX Fu, Muhammad Zahid, N Yousfi Steiner, and O Bucheli. Monitoring the degradation of a solid oxide fuel cell stack during 10,000 h via electrochemical impedance spectroscopy. *Electrochimica Acta*, 59:367–375, 2012.

[148] SS Shy, CM Huang, HH Li, and CH Lee. The impact of flow distributors on the performance of solid oxide fuel cell—part ii: Electrochemical impedance measurements. *Journal of power Sources*, 196(18):7555–7563, 2011.

[149] Javier Ignacio Gazzarri and O Kesler. Electrochemical ac impedance model of a solid oxide fuel cell and its application to diagnosis of multiple degradation modes. *Journal of power Sources*, 167(1):100–110, 2007.

[150] Davide Papurello, Andrea Lanzini, Davide Drago, Pierluigi Leone, and Massimo Santarelli. Limiting factors for planar solid oxide fuel cells under different trace compound concentrations. *Energy*, 95: 67–78, 2016.

[151] Pietro Tanasini, Marco Cannarozzo, Paola Costamagna, Antonin Faes, J Van Herle, A Hessler-Wyser, and C Comninellis. Experimental and theoretical investigation of degradation mechanisms by particle coarsening in sofc electrodes. *Fuel Cells*, 9(5):740–752, 2009.

[152] Masaru Kubota, Takeou Okanishi, Hiroki Muroyama, Toshiaki Matsui, and Koichi Eguchi. Microstructural evolution of ni–ysz cermet anode under thermal cycles with redox treatments. *Journal of The Electrochemical Society*, 162(4):F380–F386, 2015.

[153] Helge Schichlein, Axel C Müller, Michael Voigts, Albert Krügel, and Ellen Ivers-Tiffée. Deconvolution of electrochemical impedance spectra for the identification of electrode reaction mechanisms in solid oxide fuel cells. *Journal of Applied Electrochemistry*, 32(8): 875–882, 2002.

[154] Anne Hauch and Mogens B Mogensen. Testing of electrodes, cells, and short stacks. In *Advances in Medium and High Temperature Solid Oxide Fuel Cell Technology*, pages 31–76. Springer, 2017.

[155] Alexander Kromp. *model-based Interpretation of the performance and degradation of reformate Fueled Solid oxide Fuel Cells*. KIT Scientific Publishing, 2013.

[156] André Leonide, Volker Sonn, André Weber, and Ellen Ivers-Tiffée. Evaluation and modeling of the cell resistance in anode-supported solid oxide fuel cells. *Journal of The Electrochemical Society*, 155 (1):B36, 2007.

[157] Andre Leonide, Yannick Apel, and Ellen Ivers-Tiffee. Sofc modeling and parameter identification by means of impedance spectroscopy. *ECS Transactions*, 19(20):81–109, 2009.

[158] Alexandra Weiß, Stefan Schindler, Samuele Galbiati, Michael A Danzer, and Roswitha Zeis. Distribution of relaxation times analysis of high-temperature pem fuel cell impedance spectra. *Electrochimica Acta*, 230:391–398, 2017.

[159] J Ross Macdonald and E Barsoukov. Impedance spectroscopy: theory, experiment, and applications. *History*, 1(8):1–13, 2005.

[160] Yanxiang Zhang, Yu Chen, Mufu Yan, and Fanglin Chen. Reconstruction of relaxation time distribution from linear electrochemical impedance spectroscopy. *Journal of Power Sources*, 283: 464–477, 2015.

[161] Hiroki Nara, Tokihiko Yokoshima, and Tetsuya Osaka. Technology of electrochemical impedance spectroscopy for an energy-sustainable society. *Current Opinion in Electrochemistry*, 2020.

[162] Xiaojuan Wu and Boyang Zhou. Fault tolerance control for proton exchange membrane fuel cell systems. *Journal of Power Sources*, 324:804–829, 2016.

[163] Xiao-long Wu, Yuan-Wu Xu, Tao Xue, Dong-qi Zhao, Jianhua Jiang, Zhonghua Deng, Xiaowei Fu, and Xi Li. Health state prediction and analysis of sofc system based on the data-driven entire stage experiment. *Applied energy*, 248:126–140, 2019.

[164] Wu Xiao-long, Xu Yuanwu, Xue Tao, Zhao Dongqi, Jiang Jianhua, Deng Zhonghua, Fu Xiaowei, and Li Xi. Standby and shutdown cycles modeling of sofc lifetime prediction. *Energy Procedia*, 158: 1573–1578, 2019.

[165] Xiaojuan Wu, Liangfei Xu, Junhao Wang, Danan Yang, Fusheng Li, and Xi Li. A prognostic-based dynamic optimization strategy for a degraded solid oxide fuel cell. *Sustainable Energy Technologies and Assessments*, 39:100682, 2020.

[166] Xiaojuan Wu, Qianwen Ye, and Junhao Wang. A hybrid prognostic model applied to sofc prognostics. *International Journal of Hydrogen Energy*, 42(39):25008–25020, 2017.

[167] Boštjan Dolenc, Pavle Boškoski, Martin Stepančič, Antti Pohjoranta, and Đani Juričić. State of health estimation and remaining useful life prediction of solid oxide fuel cell stack. *Energy Conversion and Management*, 148:993–1002, 2017.

[168] Fei Jia, Liejin Guo, and Hongtan Liu. Mitigation strategies for hydrogen starvation under dynamic loading in proton exchange membrane fuel cells. *Energy Conversion and Management*, 139: 175–181, 2017.

[169] A Moradi Bilondi, M Abdollahzadeh, MJ Kermani, H Heidary, and P Havaej. Numerical study of anode side co contamination effects

on pem fuel cell performance; and mitigation methods. *Energy conversion and management*, 177:519–534, 2018.

[170] Yunfeng Zhai and Jean St-Pierre. Tolerance and mitigation strategies of proton exchange membrane fuel cells subject to acetylene contamination. *International Journal of Hydrogen Energy*, 43(36): 17475–17479, 2018.

[171] B Shabani, M Hafttananian, Sh Khamani, A Ramiar, and AA Ranjbar. Poisoning of proton exchange membrane fuel cells by contaminants and impurities: Review of mechanisms, effects, and mitigation strategies. *Journal of Power Sources*, 427:21–48, 2019.

[172] Diankai Qiu, Linfa Peng, Xinmin Lai, Meng Ni, and Werner Lehnert. Mechanical failure and mitigation strategies for the membrane in a proton exchange membrane fuel cell. *Renewable and Sustainable Energy Reviews*, 113:109289, 2019.

[173] Md Aman Uddin, Ashish N Aphale, Boxun Hu, Ugur Pasaogullari, and Prabhakar Singh. In-cell chromium getters to mitigate cathode poisoning in sofc stack. *ECS Transactions*, 78(1):1039–1046, 2017.

[174] Xiaojuan Wu and Danhui Gao. Optimal fault-tolerant control strategy of a solid oxide fuel cell system. *Journal of Power Sources*, 364:163–181, 2017.

[175] Shenglong Yu, Tyrone Fernando, Tat Kei Chau, and Herbert Ho-Ching Iu. Voltage control strategies for solid oxide fuel cell energy system connected to complex power grids using dynamic state estimation and statcom. *IEEE Transactions on Power Systems*, 32 (4):3136–3145, 2017.

[176] I Sreedhar, Bhawana Agarwal, Priyanka Goyal, and SA Singh. Recent advances in material and performance aspects of solid oxide fuel cells. *Journal of Electroanalytical Chemistry*, page 113315, 2019.

[177] Jakub Kupecki, Konrad Motylinski, Agnieszka Zurawska, Magdalena Kosiorek, and Leszek Ajdys. Numerical analysis of an sofc stack under loss of oxidant related fault conditions using a dynamic

non-adiabatic model. *International Journal of Hydrogen Energy*, 2019.

[178] Ruofan Wang, Zhihao Sun, Uday B Pal, Srikanth Gopalan, and Soumendra N Basu. Mitigation of chromium poisoning of cathodes in solid oxide fuel cells employing cumn1. 8o4 spinel coating on metallic interconnect. *Journal of Power Sources*, 376:100–110, 2018.

[179] A Lanzini, P Leone, C Guerra, F Smeacetto, NP Brandon, and M Santarelli. Durability of anode supported solid oxides fuel cells (sofc) under direct dry-reforming of methane. *Chemical engineering journal*, 220:254–263, 2013.

[180] Raffaele Petrone, Cesare Pianese, Pierpaolo Polverino, and Marco Sorrentino. Method and apparatus for monitoring and diagnosing electrochemical devices based on automatic electrochemical impedance identification. *International Patent Number WO2016/071801*, 2016.

[181] Bernard A Boukamp and Aurélie Rolle. Analysis and application of distribution of relaxation times in solid state ionics. *Solid state ionics*, 302:12–18, 2017.

[182] P Caliandro, A Nakajo, S Diethelm, et al. Model-assisted identification of solid oxide cell elementary processes by electrochemical impedance spectroscopy measurements. *Journal of Power Sources*, 436:226838, 2019.

[183] Xiaoming Ge, Changjing Fu, and Siew Hwa Chan. Double layer capacitance of anode/solid-electrolyte interfaces. *Physical Chemistry Chemical Physics*, 13(33):15134–15142, 2011.

[184] Dino Klotz, André Weber, and Ellen Ivers-Tiffée. Practical guidelines for reliable electrochemical characterization of solid oxide fuel cells. *Electrochimica Acta*, 227:110–126, 2017.

[185] Liu Zhen Bian, Zhi Yuan Chen, Li Jun Wang, Fu Shen Li, and Kuo Chih Chou. Electrochemical performance and carbon deposition of anode-supported solid oxide fuel cell exposed to h2co

fuels. *International Journal of Hydrogen Energy*, 42(20):14246–14252, 2017.

[186] Andrej Debenjak, Pavle Boškoski, Bojan Musizza, Janko Petrovčič, and Đani Juričić. Fast measurement of proton exchange membrane fuel cell impedance based on pseudo-random binary sequence perturbation signals and continuous wavelet transform. *Journal of Power Sources*, 254:112–118, 2014.

[187] Andrej Debenjak, Janko Petrovčič, Pavle Boškoski, Bojan Musizza, and Đani Juričić. Fuel cell condition monitoring system based on interconnected dc–dc converter and voltage monitor. *IEEE Transactions on Industrial Electronics*, 62(8):5293–5305, 2015.

[188] Julie Mougin, Bertrand Morel, Alexandra Ploner, Priscilla Caliandro, Jan Van Herle, Pavle Boškoski, Boštjan Dolenc, Marco Gallo, Pierpaolo Polverino, Antti Pohjoranta, et al. Monitoring and diagnostics of sofc stacks and systems. *ECS Transactions*, 91(1): 731–743, 2019.

[189] Juan José Giner-Sanz, EM Ortega, and Valentín Pérez-Herranz. Application of a montecarlo based quantitative kramers-kronig test for linearity assessment of eis measurements. *Electrochimica Acta*, 209:254–268, 2016.

[190] A Nakajo, G Rinaldi, P Caliandro, G Jeanmonod, L Navratilova, M Cantoni, et al. Evolution of the morphology near triple-phase boundaries in ni–yttria stabilized zirconia electrodes upon cathodic polarization. *Journal of Electrochemical Energy Conversion and Storage*, 17(4), 2020.

[191] Joel Padulles, GW Ault, and JR McDonald. An integrated sofc plant dynamic model for power systems simulation. *Journal of Power sources*, 86(1-2):495–500, 2000.

[192] Arata Nakajo, Zacharie Wuillemin, Patrick Metzger, Stefan Diethelm, Günter Schiller, Daniel Favrat, et al. Electrochemical model of solid oxide fuel cell for simulation at the stack scale i. calibration procedure on experimental data. *Journal of the Electrochemical Society*, 158(9):B1083–B1101, 2011.

[193] Dario Marra, Marco Sorrentino, Antti Pohjoranta, Cesare Pianese, and Jari Kiviaho. A lumped dynamic modelling approach for model-based control and diagnosis of solid oxide fuel cell system with anode off-gas recycling. *ECS Transactions*, 68(1):3095–3106, 2015.

[194] Marco Gallo, Dario Marra, Marco Sorrentino, Cesare Pianese, and Siu Fai Au. A versatile computational tool for model-based design, control and diagnosis of a generic solid oxide fuel cell integrated stack module. *Energy conversion and management*, 171:1514–1528, 2018.

[195] Marco Gallo, Dario Marra, Marco Sorrentino, Cesare Pianese, and Siu Fai Au. Development of a dynamic model for diagnosis and control of an integrated stack module based on solid oxide fuel cells. *Energy Procedia*, 105:1936–1941, 2017.

[196] Dario Marra, Marco Sorrentino, Cesare Pianese, and Antonio Mennella. A one-dimensional modelling approach for planar cylindrical solid oxide fuel cell. In *ASME 2015 13th International Conference on Fuel Cell Science, Engineering and Technology collocated with the ASME 2015 Power Conference, the ASME 2015 9th International Conference on Energy Sustainability, and the ASME 2015 Nuclear Forum*, pages V001T05A005–V001T05A005. American Society of Mechanical Engineers, 2015.

[197] Rasmus Rode Mosbæk, Johan Hjelm, R Barfod, J Høgh, and Peter Vang Hendriksen. Electrochemical characterization and degradation analysis of large sofc stacks by impedance spectroscopy. *Fuel Cells*, 13(4):605–611, 2013.

[198] M Torrell, A Morata, P Kayser, M Kendall, K Kendall, and A Tarancón. Performance and long term degradation of 7 w microtubular solid oxide fuel cells for portable applications. *Journal of Power Sources*, 285:439–448, 2015.

[199] Marco Sorrentino, Matteo Acconcia, Davide Panagrosso, and Alena Trifirò. Model-based energy monitoring and diagnosis of telecommunication cooling systems. *Energy*, 116:761–772, 2016.

**SOLIDpower SA**
Av. des Sports 26
1400 Yverdon-les-Bains
Switzerland
Tel. +41 24 426 10 81
info.ch@solidpower.com
www.solidpower.com

Dear madam/sir

Marco Gallo and I know each other from the European project INSIGHT. Within this project, Marco and I collaborated on the development of a diagnostic tool for advanced monitoring and fault detection for a combined heat and power system based on solid oxide fuel cells that is commercialized by SOLIDpower. Within the project, it was Marco's responsibility to develop some of the diagnostic algorithms and to take a leading role in the implementation of routines developed by him and other project partners in the monitoring tool.

During the execution of the project, I have always appreciated the contributions from Marco. I remember a project workshop at the end of the year 2017 that was organized in order to discuss in detail about the pros and cons of each diagnostic routine, and to develop a strategy to exploit the routines to their best extent. Marco took the lead during this meeting, where he was able to process input from everyone in documents that formed the basis of several deliverables that came from his hand later on, and to reflect on the input from others in calm, sensible way.

Therefore, I can highly suggest the work performed by Marco within the INSIGHT project and the interesting results achieved during these years.

Please refer to my contact details in the header of this letter if you require further information.

Sincerely,

Jan Pieter Ouweltjes

Grenoble, 12/11/19

Reference : LITEN/DTBH/STHB/2019-LTH-JM

Object: Support letter

To whom it may concern,

As leader of the Hydrogen Technologies Laboratory at CEA/LITEN, my team and I are collaborating with several research groups across Europe in the field of hydrogen and fuel cells. I am personally coordinating several European projects, and in particular INSIGHT project, dealing with the development of monitoring and diagnostics tools using signal analysis, and their implementation in real Solid Oxide Fuel Cell (SOFC) systems.

In the frame of this project, I have the opportunity to collaborate with Marco Gallo, who is, with the team at University of Salerno, deeply involved in the Work Package dealing with Monitoring and Diagnostic Tools since the beginning of the project. In this frame, Marco Gallo took the responsibility of several tasks and presented the achievements of University of Salerno at all technical meetings. Marco Gallo's directly and strongly contributed to one of the main achievements of the project, that is to say the development of a diagnostic algorithm for Detection and Isolation of faults (FDI) at single cell and stack level based on Electrochemical Impedance Spectroscopy (EIS), with the support of a dynamic lumped model for the parameters identification with reduced computational efforts. Thanks to those tools, allowing a fault detection as early as possible, it was finally possible to propose mitigation strategies. This methodology has proven its efficiency, and has consequently being implemented with success on a hardware device for use in real SOFC system. The demonstration of the in-field operation is in progress.
It is a pleasure to work with Marco Gallo, who is strongly committed in both the scientific aspects and the team work, internally at University of Salerno but also with the other partners of the project.
In summary, Marco Gallo is reliable and has a multidisciplinary professional profile with a good technical background. Consequently, I strongly support his candidacy for the final PhD evaluation.

Should you have any further questions, feel free to contact me.

Sincerely,

Julie Mougin, Head of Hydrogen Technologies Laboratory

Commissariat à l'énergie atomique et aux énergies alternatives
17 rue des Martyrs | 38054 Grenoble Cedex
T. +33 4 38 78 30 18 | F. +33 4 38 78 53 96
www-liten.cea.fr
Établissement public à caractère industriel et commercial | RCS Paris B 775 685 019

DTBH
STHB/LTH

# Acknowledgements

The activity of the presented work has been developed in the frame of the INSIGHT EU project. This project has received funding from the Fuel Cells and Hydrogen 2 Joint Undertaking under grant agreement No 735918. This Joint Undertaking receives support from the European Union's Horizon 2020 research and innovation programme and Hydrogen Europe and N.ERGHY.